Sulfur and Sulfur Isotope Distribution between Fluids and Silicate Melts: An Experimental Investigation

Von der Naturwissenschaftlichen Fakultät

der Gottfried Wilhelm Leibniz Universität Hannover

zur Erlangung des Grades

Doktor der Naturwissenschaften

Dr. rer. nat.

genehmigte Dissertation

von

Dipl.-Geow. Adrian Fiege

geboren am 27. September 1982 in Hessisch Lichtenau

2013

ABSTRACT

The distribution of Sulfur (S) and S-isotopes between fluid and silicate melt upon decompression was investigated experimentally. Synthesized volatile-bearing (H_2O-S±Cl) andesitic or basaltic glasses were used as starting material. The MgO content in the basaltic melts was varied from ~1 to ~10 wt% to study the influence of small changes in melt composition on S (-isotope) fluid-melt distribution at constant Fe content. The initial H_2O content in the melt ranged from ~3 to ~8 wt%. However, most starting glasses initially contain ~6 wt% H_2O. Additionally, ~140 to ~2700 ppm S and 0 to ~3600 ppm Cl were added to the system. The experiments were performed in internally heated pressure vessels (IHPV). Experiments with andesitic melt composition were conducted at constant temperature (T) of ~1030°C while T ranges from ~1050 to ~1250°C for basaltic compositions. The oxygen fugacity (fO_2) was varied from $\log(fO_2/\text{bar})$ = QFM to QFM+4.2 (QFM: quartz-fayalite-magnetite buffer). Pressure (p) was released continuously, typically from ~400 to ~70 MPa. The decompression rate (r) ranged between ~0.0005 to ~0.2 MPa/s for andesitic systems while a constant r of ~0.1 MPa/s was applied for experiments with basaltic compositions. The samples were annealed at final p-T conditions for 0 to 72 h (= t_A) to allow to investigate the fluid-melt equilibration process after decompression.

Experiments with andesitic composition performed under oxidizing conditions (> QFM+3) and directly quenched after decompression (t_A = 0 h; fluid-melt disequilibrium) revealed a strong increase of the $S_{(fluid)}/S_{(melt)}$ ratio ($S_{(fluid)}$ = wt% S in the fluid; $S_{(melt)}$ = wt% S in the melt) with increasing r, from ~30 at 0.02 MPa/s to ~300 at 0.2 MPa/s. Consistent with this observation, $S_{(fluid)}/S_{(melt)}$ was found to decrease by a factor of ~6 during annealing after fast decompression (~0.1 MPa/s); i.e. S was resorbed by the andesitic melt. Such a kinetically controlled transient degassing of S upon fast decompression was not observed at lower fO_2 (~QFM+1 to ~QFM+1.5) in andesitic systems and was completely absent (i.e. independent of fO_2) in basaltic systems, e.g. $S_{(melt)}$ remained almost constant with varying t_A.

The data showed that near-equilibrium conditions between fluid and melt were achieved shortly after decompression; i.e. within ~2 h in basaltic systems and within ~5 h in andesitic systems. The fluid-melt partitioning coefficients of S ($D_S^{fl/m}$) decreased significantly with increasing fO_2; e.g. from ~220 at QFM+1 to ~35 at ~QFM+4 in andesitic systems at 1030°C. Data obtained for basaltic composition indicated a slight positive correlation between $D_S^{fl/m}$ and T in the range of 1150 to 1250°C at both oxidizing (QFM+4; $D_S^{fl/m} \approx$ 50 to 80) and intermediate (QFM+1.5; $D_S^{fl/m} \approx$ 90 to 210) redox conditions. On the other hand, varying the initial H_2O and S content in the melt had an insignificant effect on $D_S^{fl/m}$. Moreover, the influence of Cl on $D_S^{fl/m}$ was small in andesitic systems containing up to 1000 ppm Cl and negligible in basaltic systems containing up to 3600 ppm Cl. A comparison of the obtained data with previously published results showed that under oxidizing conditions (> QFM+3; i.e. when S^{6+} was the only S species), bulk melt composition, ranging from basaltic through andesitic to rhyolitic, has a minor effect on $D_S^{fl/m}$. In contrast, such changes in melt composition strongly affected $D_S^{fl/m}$ under reducing conditions (~QFM to ~QFM+1; i.e. when S^{2-} became abundant). However, changes in MgO content in reduced basaltic systems had only a minor effect on $D_S^{fl/m}$.

The S-isotope composition of selected glasses before and after decompression was determined using secondary ion mass spectrometry (SIMS). Gas-melt isotopic fractionation factors $\alpha_{g\text{-}m}$ were estimated via mass balance calculations. The obtained data indicated no detectable effect of r and t_A on $\alpha_{g\text{-}m}$. The results showed that the S-isotope fractionation between fluid and silicate melt is significantly larger than indicated by previous models, at least for reducing conditions. For instance, a fluid-melt fractionation of ~ +3.7 ‰ under reducing conditions and of ~ -1.5 ‰ under oxidizing conditions can be induced by closed system degassing at ~1040°C. A new model is proposed which allows one to calculate $\alpha_{g\text{-}m}$ for a given fO_2 in systems with andesitic to basaltic melt composition.

KURZZUSAMMENFASSUNG

Anhand von Druckentlastungs-Experimenten wurde die Verteilung von Schwefel (S) und S-Isotopen zwischen fluider Phase und silikatischer Schmelze untersucht. Als Ausgangsmaterial dienten synthetisierte, H_2O-S±Cl-haltige andesitische und basaltische Gläser. Der MgO-Gehalt in den basaltischen Schmelzen wurde variiert (~1 bis 10 Gew%) um den Einfluss von kleinen Änderungen in der Schmelzzusammensetzung auf die S (-Isotopen) Verteilung zwischen Fluid und Schmelze bei konstantem Fe-Gehalt zu untersuchen. Der initiale H_2O-Gehalt bewegte sich zwischen ~3 und ~8 Gew%, wobei die meisten Ausgangsgläser einen H_2O-Gehalt von ~6 Gew% aufwiesen. Außerdem wurden ~140 bis ~2700 ppm S sowie 0 bis 3600 ppm Cl dem System initial hinzugefügt. Die Experimente wurden in intern beheizten Gasdruckanlagen durchgeführt. Die Andesit-Experimente wurden bei einer konstanten Temperatur (T) von ~1030°C durchgeführt, während für Basalt-Experimente eine T zwischen 1050 und 1250°C eingestellt wurde. Die Sauerstoff-Fugazität (fO_2) lag zwischen log(fO_2/bar) = QFM und QFM+4.2 (QFM: Quarz-Fayalit-Magnetite Puffer). Der Druck (p) wurde kontinuierlich abgelassen, i.d.R. von ~400 bis ~70 MPa. Die Druckentlastungsrate (r) variierte für andesitische Systeme von ~0.0005 bis ~0.2 MPa/s und lag für Basalt-Experimente bei einem konstanten Wert von ~0.1 MPa/s. Die Proben wurden für 0 bis 72 h (= t_A) bei finalen p-T Bedingungen getempert um die Gleichgewichtseinstellung zwischen Fluid und Schmelze zu untersuchen.

Andesit-Experimente, welche unter oxidierenden Bedingungen (> QFM+3) durchgeführt und direkt nach der Dekompression abgeschreckt wurden (t_A = 0 h; Ungleichgewicht zwischen Fluid und Schmelze), zeigten einen starken Anstieg des $S_{(fluid)}/S_{(melt)}$ Verhältnisses ($S_{(fluid)}$ = Gew% S im Fluid; $S_{(melt)}$ = Gew% S in der Schmelze) mit steigender r, von ~30 bei 0.02 MPa/s bis ~300 bei 0.2 MPa/s. In Übereinstimmung mit dieser Beobachtung wurde eine Abnahme von $S_{(fluid)}/S_{(melt)}$ um etwa das Sechsfache während des Temperns, nach schneller Dekompression (~0.1 MPa/s) entdeckt; d.h. S wird von der andesitischen Schmelze resorbiert. Eine derartige, kinetisch kontrollierte, vorübergehende Entgasung von S während einer schnellen Dekompression wurde bei niedrigeren fO_2 (~QFM+1 to ~QFM+1.5) in andesitischen Systemen nicht beobachtet und fehlte vollständig (unabhängig von fO_2) in basaltischen Systemen; d.h. $S_{(melt)}$ blieb nahezu konstant mit variierender t_A.

Die Daten zeigen, dass Gleichgewichtsbedingungen zwischen Fluid und Schmelze kurz nach der Dekompression erreicht wurden; d.h. innerhalb von ~2 h in basaltischen und innerhalb von ~5 h in andesitischen Systemen. Der Verteilungskoeffizient von S zwischen Fluid und Schmelze ($D_S^{fl/m}$) sank signifikant mit steigender fO_2; z. B. von ~220 bei QFM+1 bis zu ~35 bei ~QFM+4 in andesitischen Systemen bei 1030°C. Eine schwach positive Korrelation zwischen $D_S^{fl/m}$ und T wurde für Basalte im T-Bereich von 1150 bis 1250°C sowohl für oxidierende (QFM+4; $D_S^{fl/m} \approx$ 50 bis 80) als auch für intermediäre (QFM+1.5; $D_S^{fl/m} \approx$ 90 bis 210) Redox-Bedingungen beobachtet. Änderungen des initialen H_2O-Gehalts hatten keinen nennenswerten Effekt auf $D_S^{fl/m}$. Der Einfluss von Cl auf $D_S^{fl/m}$ in andesitischen Systemen mit bis zu 1000 ppm Cl war klein und vernachlässigbar in basaltischen Systemen mit bis zu 3600 ppm Cl. Ein Vergleich der Daten mit bisher publizierten Ergebnissen zeigte, dass Änderungen in der Schmelzzusammensetzung, von basaltisch über andesitisch bis rhyolitisch, unter oxidierenden Bedingungen einen unwesentlichen Effekt auf $D_S^{fl/m}$ haben. Hingegen zeigten derartige Änderungen in der Schmelzzusammensetzung einen starken Einfluss auf $D_S^{fl/m}$ unter reduzierenden Bedingungen (~QFM bis ~QFM+1). Änderungen des MgO-Gehalts in reduzierten basaltischen Systemen hatten jedoch einen nur geringfügigen Effekt auf $D_S^{fl/m}$.

Das $^{34}S/^{32}S$ Verhältnis wurde in den Gläsern ausgewählter Experimente mit Sekundärionen Massenspektrometrie (SIMS) bestimmt. Die Fraktionierungsfaktoren α_{g-m} (Gas-Schmelze) wurden mittels Massenbilanz berechnet. Die ermittelten Daten deuteten keinen nachweisbaren Effekt von r und t_A auf α_{g-m} an. Die Ergebnisse zeigten jedoch, dass die S-Isotopen-Fraktionierung zwischen Fluid und Schmelze erheblich größer ist als von bisherigen Modellen prognostiziert, zumindest für reduzierende Bedingungen. Beispielsweise kann in einem geschlossenen System bei ~1040°C unter oxidierenden Bedingungen eine Fraktionierung von ~ -1.5 ‰ durch Entgasung induziert werden, während unter reduzierenden Bedingungen sogar eine Fraktionierung von ~ +3.7 ‰ erreicht werden kann. In dieser Arbeit wird ein neues Modell vorgeschlagen, welches die Berechnung von α_{g-m} bei bestimmter fO_2 in Systemen mit andesitischer bis basaltischer Schmelzzusammensetzung ermöglicht.

Schlagwörter: Schwefel, Basalt, Andesit, Druckentlastungsexperimente, Kinetik vulkanischer Entgasung, Fluid-Schmelz Verteilung von Schwefel, Schwefel-Isotopen-Fraktionierung

DANKSAGUNG

TABLE OF CONTENTS

TABLE OF CONTENTS

III

CHAPTER I-A[1]

KINETIC VS. THERMODYNAMIC CONTROL OF DEGASSING OF H₂O-S±CL-BEARING ANDESITIC MELTS

ABSTRACT

The sulfur (S) distribution between andesitic melts and fluids, both under near-equilibrium conditions and during fast decompression (disequilibrium conditions), has been experimentally investigated. Isothermal decompression experiments were conducted at ~1030°C and variable oxygen fugacity (fO_2; $\log(fO_2/\text{bar})$ from ~QFM+0.8 to ~QFM+4.2; QFM = quartz-fayalite-magnetite buffer) in internally heated pressure vessels (IHPV) using synthetic, H₂O- and S-bearing andesitic melts (~4 to 8 wt% H₂0, ~140 to 2700 ppm S). Selected glasses were doped with chlorine (Cl; 500 to 1000 ppm) to study the influence of Cl on S partitioning. The starting pressure varied from 300 to 500 MPa, and pressure (p) was released continuously to reach 150, 100, 70, or 30 MPa. The decompression rate (r) ranged from 0.0005 to 0.17 MPa/s and samples were either directly quenched to preserve disequilibrium conditions or annealed for various times (annealing time (t_A) = 1 to 72 h) at final p and 1030 °C to achieve near-equilibrium conditions.

The directly quenched experiments revealed a strong increase of the $S_{(fluid)}/S_{(melt)}$ ratio ($S_{(fluid)}$ = wt% S in the fluid; $S_{(melt)}$ = wt% S in the melt) with increasing r, from ~30 at 0.02 MPa/s to ~300 at 0.2 MPa/s at oxidizing conditions ($\log(fO_2/\text{bar}) >$ QFM+3), i.e., when sulfate (S^{6+}) was the only S species. After fast decompression (~0.1 MPa/s) subsequent annealing for > 5 h resulted in a decrease of $S_{(fluid)}/S_{(melt)}$ by a factor of ~6, i.e., S was resorbed by the melt. In contrast to oxidizing conditions, the S content in the melt remained almost constant with varying r and was independent of t_A at low fO_2 (QFM+1 to QFM+1.5), when sulfide (S^{2-}) became abundant. Thus, the different behaviors of S^{2-} and S^{6+} during kinetically-controlled degassing need to be considered when modeling the volatile release of ascending magma.

The addition of > 500 ppm Cl to the system slightly increased the $S_{(fluid)}/S_{(melt)}$ under near-equilibrium conditions by a factor of ~2 at QFM+1.8. Furthermore, $Cl_{(fluid)}/Cl_{(melt)}$ (wt% Cl in fluid / wt% Cl in melt) showed a positive correlation with initial Cl content of the melt and ranged from 1 to 13, largely independent of r and t_A. The interaction between S and Cl as well as the dependence of $Cl_{(fluid)}/Cl_{(melt)}$ on Cl content in the melt may have a significant influence on S/Cl ratios in volcanic gasses.

1. INTRODUCTION

S is the third most abundant volatile in silicate melts after H_2O and CO_2. Because of its polyvalent character, S can be involved in various chemical and biogeochemical processes (Faure, 1986; Hawthorne et al., 2000). Under geologically relevant conditions S is dissolved as S^{6+} or S^{2-} in silicate melts and released as SO_2 and H_2S to volcanic gases during magma ascent (Symonds et al., 1994; Wilke et al., 2011). Degassing of SO_2 and H_2S from magmatic systems to the atmosphere has a major influence on atmospheric chemistry (Arthur, 2000; Oppenheimer et al., 2011). Volcanic eruption can release large amounts of S-rich aerosols to the stratosphere (Jugo et al., 2010) and SO_2 has an especially high potential for climate impact (e.g. Bluth et al., 1992; Mandeville et al., 2009). Magmas typically contain several volatiles and, hence, the release of S is controlled by partitioning between the fluid and the melt. Experimental results on the partitioning of S between hydrous silicate melts and (complex multi-component) fluids are still scarce (see review of Webster and Botcharnikov, 2011; and references therein). The available data are mainly based on hydrothermal experiments in which fluid-saturated melts were at equilibrium (or near-equilibrium) with a fluid phase.

Experimental studies have shown that the potential of a melt to dissolve S depends largely on its composition, e.g. much higher amounts of S can be incorporated in mafic melts than in silicic melts (see reviews of Baker and Moretti, 2011; Webster and Botcharnikov, 2011). Information about S and other volatile contents of magmas come primarily from melt inclusions in minerals and glasses from submarine pillow lavas. Consistent with the experimentally observed trend, the S content of arc

magmas decreases by an order of magnitude or more from basalt to rhyolite (see review of Wallace and Edmonds, 2011). The crucial role of fO_2 on S partitioning is evidenced by recent studies. In a simple Fe-free haplogranitic system equilibrated with an H_2O-S fluid Keppler (2010) observed a strong negative correlation between fO_2 and the partitioning coefficient of S between fluid and melt ($D_S^{fl/m}$ = S$_{(fluid)}$/S$_{(melt)}$ at equilibrium conditions). $D_S^{fl/m}$ was found to decrease from 468 $\pm$ 32 at Co-CoO buffer to 47 $\pm$ 4 at 0.5-1 log units above Ni-NiO buffer and $D_S^{fl/m}$ remained constant with further increase of fO_2 to the hematite-magnetite buffer. Moreover, Zajacz et al. (2012) found that $D_S^{fl/m}$ decreased from about 170 (S^{2-}-dominated) to about 20 (S^{6+}-dominated) in andesitic systems (1000°C, 200 MPa).

Results on the effect of p on S partitioning are controversial. Keppler (2010) found that $D_S^{fl/m}$ is largely independent of p (50 to 300 MPa) under oxidizing conditions. The experiments conducted by Lesne et al. (2011) on a more complex H_2O-CO_2-Cl-S-bearing basaltic system indicate a minor influence of p on S partitioning in the p range of 100 to 300 MPa. In contrast, $D_S^{fl/m}$ increases remarkably with decreasing p at $p < 100$ MPa. On the other hand, results of Teague et al. (2008) for andesitic melts equilibrated with H_2O-Cl-S-bearing fluids imply that $D_S^{fl/m}$ strongly decreases with p, from ~2000 at 800 MPa to ~200 at 200 MPa (at 1250-1300°C; fO_2 not reported). However, the experimental dataset of Teague et al. (2008) is not large enough to determine a robust trend.

The effect of T on S partitioning is poorly elaborated since often only small T ranges have been experimentally accessible. According to Keppler (2010), in oxidized haplogranitic systems $D_S^{fl/m}$ is largely independent of T in the range of 750 to 850°C. Zajacz et al. (2012) also observed a minor influence of T in andesitic systems and over a larger T range (750 to 1000°C).

Dissolved H_2O in the melt is known to strongly affect melt properties; however, its effect on $D_S^{fl/m}$ is poorly understood, because in experimental studies a change in H_2O content is usually associated with a change in fO_2 (Scaillet et al., 1995). A variation of $D_S^{fl/m}$ between 6 and 816 was determined by Webster and Botcharnikov (2011) in the range of 0.8 to 7.8 wt% H_2O using the dataset of Moune et al. (2009) for a basaltic andesite (1050°C, 300 MPa). Roughly constant fO_2 close to the QFM buffer was maintained in the experiments of Moune et al. (2009) by varying the H_2-pressure in the vessel.

The little information available indicates a rather small influence of Cl on the fluid-melt distribution of S. In rhyodacitic melts Botcharnikov et al. (2004) found that the addition of Cl has only a minor effect on $D_S^{fl/m}$ (experiments conducted at 850°C, 200 MPa, and Ni-NiO). The observed slight negative correlation of Cl content and $D_S^{fl/m}$ was attributed to non-ideal mixing in the fluid. Experimental data of Beermann (2010) for a trachybasaltic melt revealed an weak increase of $D_S^{fl/m}$ with Cl content from ~160 at ~0.05 wt% Cl to ~240 at ~3 wt% Cl at QFM+0.7 (hereafter differences of log(fO_2/bar) to the QFM buffer (Schwab and Küstner,1981) are given to specify fO_2).

It is worth noting that the partitioning coefficient of chlorine between fluid and melt ($D_{Cl}^{fl/m}$) shows a detectable positive correlation with S content in rhyodacitic, phonolitic, and basaltic melts (Botcharnikov et al., 2004; Webster et al., 2009; Beermann et al., 2011). The different trends of $D_S^{fl/m}$ and $D_{Cl}^{fl/m}$ are useful for interpreting volcanic gas signatures. Keppler (2010), for example, revealed that the $D_{Cl}^{fl/m}$ (in contrast to $D_S^{fl/m}$) in haplogranitic systems strongly increases with p, implying that variations in the SO₂/HCl ratio of volcanic gases may indicate p changes in a magma chamber. Furthermore, Lesne et al. (2011) noted a preferential release of S over Cl from basaltic melts at low p (150 to 25 MPa). Thus, the authors expect a sharp increase in the S/Cl ratios in the released vapor phase concomitant to a sharp drop in the S/Cl ratios of the melt upon decompression in a shallow magma reservoir.

In summary, the dataset on $D_S^{fl/m}$ (and $D_{Cl}^{fl/m}$) is still patchy and the influence of melt degassing kinetics on S partitioning in magmatic systems at geologically relevant conditions is poorly understood. In order to elucidate the role of melt degassing kinetics on S partition data, we performed decompression experiments on andesitic melts with systematic variations of r and t_A after decompression. If the experimental charge is directly quenched after decompression ($t_A = 0$), the distribution of volatiles between melt and fluid may be far away from equilibrium. On the other hand, if decompression is followed by long term annealing at constant T and p, equilibrium or at least near-equilibrium conditions can be achieved and the determined S$_{(fluid)}$/S$_{(melt)}$ ratios represent $D_S^{fl/m}$, i.e. a thermodynamic quantity.

2. EXPERIMENTAL PROCEDURE

The experimental strategy is based on a rapid exchange of volatiles between fluid pools and the melt. Due to high melt viscosity (η) a large fraction of the bubbles formed by decompression remain within the melt on the timescale of the experiments and act as local sinks and sources for volatiles. Hence, fluid-melt partitioning of volatiles can be rapidly re-adjusted in the melt due to short distances between fluid pools. On the other hand, volatile diffusivities in melts differ strongly, i.e. H_2O diffuses much faster than Cl and S (see Watson, 1994; Behrens and Stelling, 2011). This may induce a kinetic fractionation of volatiles during degassing. Depending on the time-pressure path of the experiment, partitioning of volatiles between fluid and melt may be controlled by kinetics (fast decompression) or thermodynamics (long term annealing after decompression).

Isothermal decompression experiments were conducted at $1030 \pm 10°C$ and variable fO_2 (QFM+0.8 to QFM+4.2) in IHPV. The experimental approach comprises a three step procedure.

In the *first step* a synthetic anhydrous glass with andesitic composition close to the Krakatau andesite was prepared by melting a mixture of oxide (Al_2O_3, SiO_2, TiO_2, Fe_2O_3, MgO, Mn_2O_3) and carbonate (Na_2CO_3, $CaCO_3$, K_2CO_3) powders in a $Pt_{90}Rh_{10}$ crucible at 1600°C for 2 h. The crucible was quenched in a water bath; the resulting glass was ground and melted again to improve homogeneity (~2 h, 1600°C). Table 1 lists the composition of the obtained anhydrous starting glasses measured by electron microprobe (EMP, for details see Section 3.1.1).

In the *second step* volatile-bearing [H_2O, S, $\pm Cl$] glasses were synthesized at 1030°C and high p (~450 MPa or ~500 MPa; see Table 2) under fluid-undersaturated conditions in IHPV at variable fO_2 (from QFM+0.8 to QFM+4.2) for 12 to 16 h. Gold (Au) was chosen as capsule material because it is the only known metal which does not react with S (or Fe) at high p-T conditions (capsule size for synthesis: length: 30 mm; inner diameter: 6.0 mm; wall thickness: 0.2 mm). H_2O was added as deionized H_2O and Cl as 10 wt% HCl_{aq}. Anhydrite ($CaSO_4$), gypsum ($Ca[SO_4] \times 2H_2O$), barite ($BaSO_4$) or natural pyrrhotite ($Fe_{1-x}S$; originating from Sudbury, Canada) served as S sources. The mixture composed of glass powder- H_2O - $\pm$hydrochloric acid - S-bearing mineral was added stepwise into the Au capsules and compressed by a piston to minimize entrapped air (added volatile contents: ~4 to ~8 wt% H_2O, ~140 to ~2700 ppm S, 0 to ~1000 ppm Cl).

In the *third step* decompression experiments were conducted in IHPV using smaller Au capsules (length: 20 mm; diameter: 4.0 mm; wall thickness: 0.2 mm). One hundred to 200 mg of the synthesized glass were ground, placed in a capsule, and compressed using a piston to minimize entrapped air. This technique results in the formation of cylindrical melt pools with typical diameter and height of ~4 mm and minimizes the influence of the capsule wall on the fluid-melt system in the center of the capsule. The experiments were initially annealed for 5 to 60 min at 1030°C and 500, 400, or 300 MPa for homogenization. Subsequently, p was released continuously with different r (= 0.0005 to 0.17 MPa/s) to 150, 100, 70, or 30 MPa). For experiments at redox conditions < QFM+4, a novel type of high-p low-flow metering valve was used to release the Argon (Ar) gas p from the IHPV. The valve is equipped with a piezoelectric nano-positioning system to allow continuous decompression (for details see Nowak et al., 2011). The r for experiments conducted at oxidizing conditions (log(fO_2/bar) $\geq$ QFM+4) was adjusted by slowly opening a conventional high-p valve because the IHPV used for oxidizing conditions are not equipped with a high-p low-flow metering valve. After decompression, samples were either isobarically quenched (rapid-quench technique) to preserve non-equilibrium conditions or annealed for various times (t_A = 0 to 72 h) at final p-T conditions before quenching to approach near-equilibrium between andesitic melt and aqueous fluid. Table 2 lists the conditions of the conducted syntheses and experiments.

Table 1: Composition (wt%) of the anhydrous andesite and three representative volatile-bearing starting glasses determined by EMP or FTIR spectroscopy (H_2O)

Sample ID	SiO_2	TiO_2	Al_2O_3	FeO_{tot} (a)	MnO	MgO	CaO	Na_2O	K_2O	H_2O	SO_3 (b)	Cl (c)	Total
Anhydrous	64.79	1.28	15.62	4.94	0.23	1.40	4.92	3.92	1.80	-	-	-	98.91
andesite	*0.59*	*0.07*	*0.22*	*0.33*	*0.04*	*0.06*	*0.20*	*0.25*	*0.07*	-	-	-	*0.78*
AH	61.23	0.85	14.69	4.52	0.21	1.34	4.80	3.69	1.69	6.61	0.32	-	99.90
	0.63	*0.04*	*0.08*	*0.28*	*0.09*	*0.08*	*0.15*	*0.28*	*0.10*	*0.03*	*0.01*	-	*0.81*
GYMClA	60.65	0.83	14.92	4.33	0.17	1.41	5.19	3.43	1.65	6.29	0.67	0.05	99.59
	0.34	*0.02*	*0.18*	*0.07*	*0.02*	*0.03*	*0.06*	*0.26*	*0.03*	*0.24*	*<0.01*	*<0.01*	*0.49*
QFMClA	60.83	0.79	14.92	4.63	0.15	1.33	4.47	4.05	1.57	6.58	0.07	0.10	99.50
	0.43	*0.03*	*0.15*	*0.12*	*0.07*	*0.03*	*0.05*	*0.23*	*0.02*	*0.13*	*<0.01*	*<0.01*	*0.42*

Notes: Data in *italic*: 1 σ standard deviations based on EMP analysis; number of EMP analyses: 20; (a) FeO_{tot}: total Fe concentration in the glass given as FeO; (b) SO_3: total S concentration in the glass given as SO_3; (c) Cl is considered as an additional component to the other constituents.

Table 2: Experimental results. All syntheses and experiments were conducted at 1030 ± 10 °C. Most partially degassed samples contain Au-globules.

Sample ID	p_S [MPa]	t_I [min]	r [MPa/s]	p_E [MPa]	t_A [min]	ΔQFM	$Fe^{3+}/\Sigma Fe$ → corr.	$S^{6+}/\Sigma S$	S [ppm]	H_2O [wt%]	Cl [wt%]	$D_S^{fl/m}$	$D_{Cl}^{fl/m}$	Comments
ASD	500	xx	xx	500	o. n.	3.4 (a)	nd	nd	1207 ±23	4.83 ±0.35	xx	xx	xx	xx
ASD-1	300	60	0.08	100	300	4.2 (a)	nd	1.03	868 ±82	4.22 ±0.16	xx	62 ±6	xx	Fe-oxides
ASD-2	300	60	0.11	100	2880	4.2 (a)	nd	1.05	980 ±21	4.07 ±0.15	xx	30 ±1	xx	Fe-oxides
AH	500	xx	xx	500	o. n.	3.7 (a)	0.34	nd	1266 ±140	6.61 ±0.03	xx	xx	xx	xx
AH3	500	60	0.16	71	1083	4.2 (a)	0.25	>0.80	720 ±236	3.56 ±0.05	xx	24 ±9	xx	xx
AH4	500	60	0.17	71	d. r. q.	4.2 (a)	0.12	nd	130 ±50	3.97 ±0.29	xx	317 ±130	xx	NQ
GY	500	xx	xx	500	o. n.	3.7 (a)	0.41	nd	1426 ±180	6.96 ±0.06	xx	xx	xx	xx
GY4	500	60	0.17	71	d. r. q.	4.2 (a)	0.13	nd	120 ±35	2.92 ±0.02	xx	216 ±83	xx	NQ
GYC	500	xx	xx	500	o. n.	3.7 (a)	0.38	1.03	1376 ±60	6.50 ±0.37	xx	xx	xx	xx
GYC-1	505	40	0.09	65	60	4.2 (a)	0.34	>0.74	380 ±85	2.49 ±0.07	xx	64 ±15	xx	xx
GYC-2	505	5	0.16	71	d. r. q.	4.2 (a)	0.39	nd	375 ±100	3.64 ±0.07	xx	90 ±25	xx	xx
GYC-3	402	5	0.05	70	d. r. q.	4.2 (a)	0.10	nd	636 ±116	3.34 ±0.07	xx	36 ±7	xx	xx
AHC	450	xx	xx	450	o. n.	3.9 (a)	nd	0.98	2703 ±65	7.95 ±0.48	xx	xx	xx	xx
AHC-1	450	40	0.08	71	120	4.2 (a)	nd	>0.89	916 ±50	3.58 ±0.05	xx	41 ±3	xx	xx
AHC-2	451	40	0.08	71	1200	4.2 (a)	nd	>0.85	951 ±50	3.48 ±0.05	xx	38 ±2	xx	Fe-oxides
AHC-3	414	40	0.08	73	900	1.2 (b)	nd	>0.52	315 ±80	3.60 ±0.06	xx	159 ±41	xx	xx
AHC-4	403	5	0.02	71	d. r. q.	4.2 (a)	nd	nd	1190 ±27	3.60 ±0.08	xx	27 ±1	xx	xx
SD1	502	xx	xx	502	o. n.	3.6 (a)	0.39	>0.85	1223 ±71	5.79 ±0.48	xx	xx	xx	xx
SD1-300	405	5	0.10	34	d. r. q.	2.8	0.18	nd	146 ±64	2.02 ±0.15	xx	190 ±87	xx	NQ
SD1-700	410	5	0.10	70	d. r. q.	3.2	0.27	(>0.66)	170 ±35	3.90 ±0.15	xx	310 ±72	xx	xx
SD1-1000	389	5	0.10	100	d. r. q.	3.4	0.13	(>0.67)	274 ±62	4.97 ±0.35	xx	379 ±97	xx	xx
SD1-1500	404	5	0.10	150	d. r. q.	2.8	0.28	>0.86	834 ±117	5.39 ±0.16	xx	107 ±19	xx	xx
GYB	500	xx	xx	500	o. n.	3.6 (a)	0.31	0.98	1451 ±70	6.33 ±0.79	xx	xx	xx	xx
GYB-1	420	60	0.07	74	1087	1.72	nd	0.71	405 ±95	3.08 ±0.09	xx	77 ±21	xx	xx
GYB-3	420	60	0.07	74	1087	1.72	nd	(0.47)	260 ±70	3.78 ±0.06	xx	172 ±52	xx	xx

Table 2: Experimental results. *Continuation*

Sample ID	p_S [MPa]	t_I [min]	r [MPa/s]	p_E [MPa]	t_A [min]	ΔQFM	Fe³⁺/ΣFe → corr.	S⁶⁺/ΣS	S [ppm]	H₂O [wt%]	Cl [wt%]	$D_S^{fl/m}$	$D_{Cl}^{fl/m}$	Comments
SD2	500	xx	xx	500	2 days	3.3 (a)	nd	nd	1167 ±20	4.55 ±0.09	xx	xx	xx	xx
SD2-1	410	5	0.10	70	d. r. q.	2.13	nd	0.96	329 ±86	3.82 ±0.28	xx	313 ±85	xx	xx
SD2-2	413	5	0.05	70	d. r. q.	1.27	nd	0.05	318 ±75	3.53 ±0.09	xx	294 ±81	xx	NQ
SD2-3	404	5	0.02	70	d. r. q.	1.03	nd	nd	202 ±38	3.74 ±0.09	xx	527 ±100	xx	xx
SD2-4	402	5	0.10	70	d. r. q.	1.49	nd	(0.97)	279 ±115	3.74 ±0.13	xx	354 ±147	xx	xx
SD2-5	413	5	0.10	70	60	2.6	nd	(0.91)	241 ±90	3.66 ±0.12	xx	392 ±147	xx	xx
SD2-5b	405	5	0.10	71	60	1.80	nd	(0.22)	190 ±35	3.46 ±0.39	xx	434 ±94	xx	xx
SD2-6	405	5	0.10	70	300	1.64	nd	(0.57)	175 ±20	3.52 ±0.13	xx	501 ±61	xx	xx
GYCIA	508	xx	xx	502	o. n.	0.65	nd	0.09	1018 ±188†	6.56 ±0.24	0.103 ±0.002	xx	xx	re-melted (d)
GYCIA-1	412	5	0.10	70	d. r. q.	1.7	nd	(0.37)	184 ±60	3.73 ±0.06	0.089 ±0.009	155 ±60	6 ±2	xx
GYCIA-2	404	5	0.10	70	66	1.9	nd	(0.47)	148 ±60	3.56 ±0.28	0.081 ±0.007	188 ±87	9 ±4	NQ
GYCIA-3	407	5	0.10	70	300	1.8	nd	(0.29)	112 ±52	3.61 ±0.07	0.073 ±0.010	262 ±136	15 ±7	xx
GYCIA-4	415	5	0.10	70	4323.5	1.8	nd	(0.35)	92 ±48	1.98 ±0.03	0.073 ±0.009	214 ±121	10 ±5	xx
GYCIA-5	401	5	0.10	71	63	1.9	nd	(0.20)	124 ±48	3.84 ±0.09	0.078 ±0.008	253 ±112	12 ±5	xx
GYMCIA	495	xx	xx	478	o. n.	0.76	nd	0.23	1043 ±143†	6.29 ±0.24	0.051 ±0.001	xx	xx	re-melted (d)
GYMCIA-1	412	5	0.10	70	d. r. q.	1.7	nd	0.33	356 ±112	3.64 ±0.07	0.047 ±0.008	71 ±27	3 ±1	xx
GYMCIA-3	407	5	0.10	70	300	1.8	0.15 →0.17	(0.65)	128 ±36	3.62 ±0.06	0.044 ±0.006	257 ±89	6 ±2	xx
GYMCIA-4	415	5	0.10	70	4323.5	1.8	nd	(0.25)	108 ±48	3.61 ±0.06	0.046 ±0.006	311 ±151	4 ±2	xx
GYMCIA-5	401	5	0.10	71	63	1.9	nd	(0.25)	176 ±44	3.59 ±0.06	0.045 ±0.008	176 ±60	5 ±2	xx
RED	495	xx	xx	495	o. n.	0.11	nd	0.03	1623 ±242†	6.71 ±0.18	xx	xx	xx	re-melted (d)
RED-1	402	5	0.10	70	60	1.00	nd	(0.33)	172 ±56	3.77 ±0.09	xx	273 ±98	xx	xx
RED-2	413	5	0.10	71	d. r. q.	1.19	nd	(0.30)	284 ±116	3.45 ±0.10	xx	139 ±60	xx	xx
RED-3	412	5	0.10	70	300	1.13	nd	(0.25)	200 ±56	3.56 ±0.06	xx	215 ±69	xx	xx
RED-4	405	5	0.10	70	1204.5	1.1	nd	0.46	330 ±25	3.39 ±0.41	xx	113 ±24	xx	xx
QFMA	522	xx	xx	524	4 days	0.44	0.30 →0.35	(0.03)	137 ±15	6.47 ±0.13	xx	xx	xx	xx
QFMA-1	431	5	0.10	70	d. r. q.	0.8 (c)	0.09 →0.11	(0.33)	42 ±8	3.51 ±0.10	xx	77 ±17	xx	xx
QFMA-2	424	5	0.05	71	d. r. q.	0.98	0.09 →0.10	(0.36)	37 ±8	3.56 ±0.10	xx	92 ±22	xx	xx
QFMA-3	424	5	0.02	70	d. r. q.	0.77	0.11 →0.12	(0.37)	42 ±7	3.17 ±0.09	xx	68 ±13	xx	xx
QFMA-4	412	5	0.01	70	d. r. q.	0.94	0.16 →0.17	(0.27)	29 ±8	3.64 ±0.10	xx	133 ±39	xx	xx
QFMA-5	400	5	0.0005	71	d. r. q.	0.51	0.28 →0.28	(0.16)	bd	3.71 ±0.05	xx	xx	xx	xx

Table 2: Experimental results. *Continuation*

Sample ID	p_S [MPa]	t_I [min]	r [MPa/s]	p_E [MPa]	t_A [min]	ΔQFM	Fe³⁺/ΣFe → corr.	S⁶⁺/ΣS	S [ppm]	H₂O [wt%]	Cl [wt%]	D_S^{flm}	D_{Cl}^{flm}	Comments
QFMCIA	508	xx	xx	509	6 days	0.38	nd	(0.04)	260 ±19	6.58 ±0.13	0.104 ±0.002	xx	xx	xx
QFMCIA-1	431	5	0.10	70	d. r. q.	0.8 (c)	nd	(0.27)	60 ±14	3.47 ±0.09	0.094 ±0.003	105 ±27	3 ±1	xx
QFMCIA-2	424	5	0.05	71	d. r. q.	0.98	nd	(0.30)	68 ±26	3.35 ±0.09	0.094 ±0.002	87 ±35	3 ±1	xx
QFMCIA-3	424	5	0.02	70	d. r. q.	0.77	nd	(0.28)	52 ±16	3.48 ±0.10	0.095 ±0.002	127 ±41	2 ±1	xx
QFMCIA-4	412	5	0.01	70	d. r. q.	0.94	nd	(0.23)	69 ±15	3.57 ±0.06	0.097 ±0.003	92 ±22	2 ±1	xx
QFMCIA-5	400	5	0.0005	71	d. r. q.	0.51	nd	(0.08)	bd	3.70 ±0.06	0.101 ±0.003	xx	1 ±1	xx

Notes: *Sample ID:* starting glasses are written in *italic*; p_S: start pressure; t_I: initial annealing time before decompression; r: decompression rate – error of decompression rate ≤ 0.01 MPa/s; p_E: final pressure after decompression / before rapid quench; t_A: annealing time at final conditions; *ΔQFM:* Nominal oxygen fugacity determined using the *Shaw*-membrane technique or (a) intrinsic redox conditions determined by Berndt et al.(2002), see text – (b) experiments without *Shaw*-membrane; fO_2 calculated using the initially loaded H₂ pressure – (c) *Shaw*-membrane defect; calculated average value of the experiments QFM(Cl)A-2 to -5; Fe²⁺/ΣFe: analytical error < 0.12 (2 σ); S⁶⁺/ΣS: error probably > 0.1, values in parenthesis refer to samples with very low sulfur content in the melt (<300 ppm) leading to (very) noisy XANES spectra (see text); *italic* font indicates that the S⁶⁺/ ΣS ratios should be equal to 1; *Comments:* solid phases in the melt were identified by EDX analyses (EDX: electron dispersive X-ray; Cameca SX-100 EMP Oxford EDX system). (d): Starting glass contained quench related S-globules and was re-melted for ~1 h at ~1030°C and 500 MPa to improve homogeneity.

xx: not relevant or 0; o. n.: over night (12 to 16 h); d. r. q.: direct rapid quench; nd: not determined / no measurement conducted; bd: below detection limit; NQ: normal quench, cooling rate ~150°C/min.

The fO_2 prevailing in all experiments was indirectly adjusted via the fH_2 in the p vessel. H_2 diffuses through the capsule wall and controls fO_2 by reaction with H_2O ($H_2 + \frac{1}{2} O_2 \leftrightarrow H_2O$). To adjust reducing conditions Ar and H_2 were loaded in different ratios into the vessel, and the prevailing fH_2 during the experiment was continuously recorded using a *Shaw*-membrane (Berndt et al., 2002). After quenching the sample using the rapid quench device, the final p-T conditions were maintained in the vessel for several h to measure the prevailing fH_2 at the end of the experiment. It is worth noting that p reduction involves a decrease of fH_2 in the vessel inducing oxidation of the samples (see Section 5.1 for details). However, in most experiments the final H_2-pressure was even lower – typically by a factor of 1.1 to 2.5 – than expected from the initially loaded H_2, indicating that H_2 is preferentially lost through the valve during decompression. In some experiments (series SD1) with high initial H_2-pressure the H_2 loss was particularly pronounced (up to factors of ~12). On the other hand, experiments with low initial H_2-pressure typically showed a higher final H_2-pressure than expected (by a factor of 1.8 to 3.1). This is attributed to a "memory" effect of the autoclave, i.e. H_2 stored in the metal wall of the autoclave during previous experiments under high fH_2 is released. A correlation between the observed deviation (measured vs. expected H_2) and r or t_A was not observed.

Some synthesis and decompression experiments were carried out in vessels without a *Shaw*-membrane using pure Ar gas as p medium (containing H_2 as an impurity). The intrinsic redox conditions in these IHPV were determined to be about QFM+3.9 for H_2O saturated conditions (water activity $a(H_2O) = 1$; Berndt et al., 2002; Wilke et al., 2002; Schuessler et al., 2008). The following equation was used to calculate fO_2 in the capsule ($fO_2{}^{capsule}$) for $a(H_2O) < 1$ (e.g. Jugo et al., 2010):

$$\log\left(fO_2^{capsule}\right) = \log\left(fO_2^{aH_2O=1}\right) + 2 \cdot \log\left(a(H_2O)\right)$$

(1)

The $a(H_2O)$ was close to one, at least at the end of the decompression experiments, because these systems all contain an H_2O-rich free-fluid phase and the bulk S and Cl concentration is relatively low (Table 2). The $a(H_2O)$ of the starting glasses were calculated from the amount of H_2O dissolved in the silicate glasses using the approach of Burnham (1979). If not specified differently, the reported values

of fO_2 refer to the final H_2-pressure in the vessel measured with the *Shaw*-membrane or to the intrinsic redox conditions of the vessel.

3. ANALYTICAL METHODS

3.1 Glass composition

3.1.1 EMP and Fe-colorimetric analyses

The andesitic glass samples were analyzed using a Cameca SX-100 EMP to determine the glass composition (15 keV acceleration voltage, 20 µm beam size). The counting time varied from 4 s for Na up to 10 or 30 s for all major constituents (Si, Al, Ca, K, Ti, Fe, Mg, Mn). The counting time was increased to 240 s for S and to 120 s for Cl to improve the counting statistics. The applied beam current was 5 nA (Na), 10 nA (Si, Al, Ca, K, Ti, Fe, Mg, Mn) and 35 nA (S, Cl), resulting in detection limits of ~32 ppm for S and ~50 ppm for Cl. NIST U. S. National Institute of Standards and Technology) standard 610 and 620 glasses were measured before and after each EMP session to evaluate the accuracy of the measurements, especially of the S content. The S content as well as that of the main constituents (e.g. SiO_2, Al_2O_3) are within quoted NIST standard errors. However, Na_2O was often notably lower than expected. This deviation arises most likely from Na migration during EMP measurements (Morgan and London, 1996; 2005) or possibly from the loss of small amounts of Na to the fluid phase upon degassing. The EMP settings were slightly adjusted for the measurement of S in the QFMA and QFMClA experimental series because the S contents of the partially degassed samples of both series are close to the detection limit. Increasing the beam current to 100 nA reduced the detection limit to about 21 ppm. The bulk $Fe^{3+}/\Sigma Fe$ ratio of selected starting glasses and experimental run products was determined by colorimetric wet-chemical analyses (vanadate method) following the approach of Schuessler et al. (2008). Typically 6 - 13 mg of sample was used in these analyses.

3.1.2 H_2O determination

The H_2O content of hydrous starting glasses was measured by Karl-Fischer titration (KFT). Raw data were corrected by an increment of 0.10 wt% H_2O to account for unextracted water in the samples after analyses, determined to be 0.10 ± 0.05 wt% H_2O (Behrens, 1995; Leschik et al., 2004). Run products

were analyzed by infrared spectroscopy using doubly polished glass chips with thickness ranging from 120 to 300 μm, depending on the translucency of the samples. Sample thickness (d) was determined using a digital micrometer (precision ~2 μm). Near infra-red (NIR) spectra were collected with a Bruker IFS 88 FTIR spectrometer equipped with a Bruker IRscope II IR microscope. A tungsten light source, a CaF_2 beam splitter, and a mercury-cadmium-tellur (MCT) narrow range detector were used in the measurements. For each spectrum, 100 scans were accumulated with spectral resolution of 4 cm^{-1}; 3 to 5 spots were analyzed on each sample. The peak height (absorbance) of the bands at 4500 cm^{-1} and 5200 cm^{-1} was used to determine the concentration of OH groups and molecular H_2O, respectively, via the Lambert-Beer law:

$$c(H_2O) = \frac{1802 \cdot A(H_2O)}{d \cdot \rho} \cdot \frac{1}{\varepsilon(H_2O)} \tag{2}$$

$$c(OH) = \frac{1802 \cdot A(OH)}{d \cdot \rho} \cdot \frac{1}{\varepsilon(OH)} \tag{3}$$

where $c(OH)$ and $c(H_2O)$ are the concentrations [wt%] of water dissolved as OH groups and as molecular H_2O respectively, d is the thickness of the section [cm] and ρ the density of the glass [g/L]. A refers to the absorbance and ε to the linear molar absorption coefficient [L mol^{-1} cm^{-1}] of the respective NIR combination bands of H_2O molecules (~5200 cm^{-1}) and OH groups (~4500 cm^{-1}). The total water content is the sum of $c(H_2O)$ and $c(OH)$.

The ρ of the andesitic glasses was calculated from the glass composition using the Gladstone-Dale rule (Gladstone and Dale, 1863). Mandeville et al. (2002) have shown that the Gladstone-Dale rule is applicable to hydrous andesitic glasses. The authors compared the calculated densities to empirically determined densities using the float-sink method in sodium polytungstate reference solutions and determined a deviation of ±0.03 g/cm^3. The densities of our glass samples estimated using the Gladstone-Dale rule show a deviation of < 1 % from the densities derived from the linear relation given by Ohlhorst et al. (2001) for dacitic composition (~65 wt% SiO_2 in the dry glass).

A tangential baseline correction was applied to determine the heights of the water bands. Calibrations of the absorption coefficients for dacitic and andesitic compositions using the same baseline correction

were published by Ohlhorst et al. (2001) and Mandeville et al. (2002). The applicability of these calibrations was tested by plotting normalized absorbances of both NIR bands against each other (Fig. 1a). The data points (listed in Table 3) plot in between the lines defined by the absorption coefficients for Krakatau andesite and Fe-free andesite from Mandeville et al. (2002) and close to the calibration for Unzen andesite from Ohlhorst et al. (2001). An influence of the fO_2 was not observed (see Fig. 1a). Hence, the difference from the calibration of Mandeville for the Krakatau andesite is probably due to small variations in melt composition (e.g. Fe content) and cooling rate at the end of the experiment.

We performed a regression of the data shown in Fig. 1a to determine the absorption coefficients best applicable to the decompression samples. Molar absorption coefficients of $\varepsilon(5200 \text{cm}^{-1}) = 1.27 \pm 0.07$ L mol^{-1} cm^{-1} for the molecular H_2O band and $\varepsilon(4500 \text{cm}^{-1}) = 0.84 \pm 0.07$ L mol^{-1} cm^{-1} for the OH group band were obtained. It is noteworthy that this calibration is poorly constrained for very low H_2O contents, i.e. the OH concentration may have a large error. However, the total H_2O content is well reproduced in the range of 2 to 8 wt% (Fig. 1b); i.e. the deviation of H_2O content is typically < 0.3 wt% between IR and KFT data.

Table 3: Data for calibration of NIR absorption coefficients and concentrations of hydrous species in the glasses.

Sample ID	fO_2 [ΔQFM]	H_2O [wt%] KFT [a]	d [cm]	ρ [g/L]	A(OH)	A(H_2O)	c(OH)	c(H_2O)
ASD	3.4	4.84 ± 0.07	0.0133	2460	0.033	0.061	2.15	2.67
AH	3.7	6.28 ± 0.10	0.0105	2429	0.028	0.076	2.36	4.26
GY	3.7	6.40 ± 0.08	0.0100	2427	0.028	0.077	2.43	4.53
GY-C	3.7	6.88 ± 0.09	0.0146	2427	0.034	0.111	2.06	4.45
AH-C	3.9	8.11 ± 0.13	0.0194	2412	0.043	0.196	1.98	5.97
SD1	3.6	6.27 ± 0.11	0.0310	2438	0.070	0.202	1.98	3.81
GY-B	3.6	6.01 ± 0.12	0.0147	2427	0.028	0.116	1.68	4.64
SD2	3.3	4.16 ± 0.07	0.0422	2456	0.106	0.172	2.19	2.36
GYClA	0.7	6.32 ± 0.10	0.0199	2434	0.051	0.146	2.28	4.29
GYMClA	0.8	6.93 ± 0.10	0.0194	2425	0.050	0.132	2.26	4.00
RED	0.1	6.41 ± 0.11	0.0194	2436	0.052	0.144	2.36	4.35
QFMClA	0.4	6.48 ± 0.10	0.0290	2422	0.076	0.211	2.30	4.28
SDR-2 [b]	1.5	2.47 ± 0.07	0.0419	2468	0.075	0.073	1.55	1.00
AND70 [c]	2.6	3.80 ± 0.10	0.0285	2494	0.069	0.076	2.10	1.53

Notes: (a) H_2O content measured by KFT; (b) glass sample was synthesized for the KFT–NIR calibration but not used for decompression experiments; (c) H_2O solubility experiments conducted at 70 MPa and 1030 °C, average of 4 experiments for NIR and 2 experiments for KFT; see Section 4.2.1.
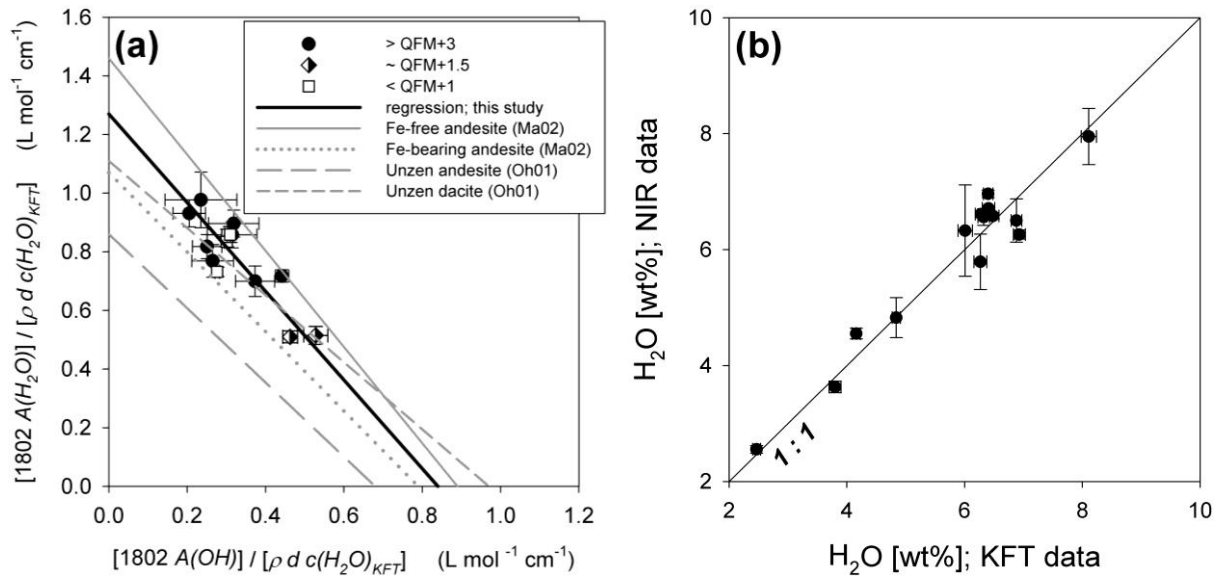
Fig. 1a-b: a) Calibration plot for the absorption coefficients of the OH and H_2O combination bands in the NIR. Data points and regression are for Krakatau dacitic andesite.
b) Comparison of H_2O contents determined by IR spectroscopy with KFT data for Krakatau dacitic andesite.
Ma02: Mandeville et al. (2002); Oh01: Ohlhorst et al. (2001)

3.2 S Speciation in the melt

XANES analyses were performed at the S K-edge (ca. 2.47 keV) using the SUL-X beamline at the ANKA synchrotron radiation source (Karlsruhe Institute of Technology, Germany) to determine the S speciation in the andesitic glasses. The ANKA storage ring operates at a beam energy of 2.5 GeV and a beam intensity of 200 mA. The SUL-X beamline uses a wiggler as radiation source. A beam size of about 300μm×150 μm was applied to evaluate the bulk S speciation in the andesitic glasses. The spectra were collected in fluorescence mode from 2.45 to 2.55 keV. Mainly quick-XAFS scans were performed to avoid irradiation damage (XAFS: X-ray absorption fine structure; relevant details for quick-XAFS: continuously running bragg axis; 400 to 800 motorsteps/s; measuring 0.2 s/datapoint; scanning once). The energy of the monochromator was calibrated to the white line of sulfate in scotch tape (2481.4 eV). The spectra energies were corrected to the white line of the gypsum spectrum (2482.84 eV) to allow an estimation of fO_2 in our experiments based on the model of Jugo et al. (2010); see Section 4.1.

4. RESULTS

The bulk composition of all volatile-bearing starting glasses and experimental glasses is close to the anhydrous andesite if H_2O, S, and Cl are subtracted and oxides normalized to 100 wt% (Table 1). The H_2O contents are in the range of 4.8 to 7.0 wt% H_2O, except for SD2 with ~4.5 wt% H_2O and AHC with ~8 wt% H_2O (Table 3). Most of the glasses synthesized for decompression experiments were homogenous, bubble-free, and crystal-free. However, three samples (GYClA, GYMClA and RED) contained minor amounts of S-bearing globules indicating that either the dissolution of the added gypsum was incomplete or the solubility of S was exceeded. Differences in degassing kinetics and initial fluid composition are expected for globule-bearing and globule-free glasses, i.e. an S-rich fluid can be easily formed by diffusion of H_2O to the globules in the former case while slow diffusion of S in the melt and homogeneous bubble nucleation have major control in the latter case.

In order to determine the bulk S content, ~20 mg of the globule-bearing glasses were powdered, mixed with ~100 mg of anhydrous andesite and adequate amounts of H_2O, and re-melted for > 6 h in Au capsules at the same conditions as used for the initial syntheses. Afterwards, the S content of the diluted glasses was analyzed by EMP, and the bulk S content of the undiluted GYClA, GYMClA, and RED glasses was estimated by mass balance calculations. In a second approach to quantifying the S contents of the globule-bearing starting glasses, pieces from the GYClA-1, GYMClA-1, and RED-2 decompression experiments were re-melted at 1030°C and 500 MPa for a short term (~30 min). The re-melted GYClA-1 and GYMClA-1 samples are pure glasses with bulk S contents similar to those inferred from the dilution experiments. The average of the two values (*re-melting* and *dilution*) for the bulk GYClA and GYMClA S contents was used in mass balance calculations, e.g. to determine $D_S^{fl/m}$. The re-melted RED-2 sample contains S-bearing globules indicating that the RED starting material was $Fe_{1-x}S$ saturated. Hence, the S content based on the dilution experiment was used to estimate the total S content.

All decompression products were homogeneous (except for SD1-300) and most were crystal-free (Table 2). Bubbles produced during decompression are common in all run products (Fig. 2). After decompression, the H_2O concentration in the glasses significantly decreased with decreasing final *p*

(see results of SD1 experiments; Section 4.2.1) and ranged (with a few exceptions, see Table 2) from 3.1 to 4.2 wt% H_2O at a final p of 70 MPa corresponding to a relative loss of 40% to 58% H_2O. The initial S content in the starting glasses ranged from ~140 to ~2700 ppm and decreased in the partially degassed samples at 70 MPa down to contents of ~30 to ~1200 ppm, corresponding to a relative variation of 56% to 96%. Cl was added to three starting glasses and the initial bulk Cl content was either ~510 ppm (GYMClA) or ~1035 ppm (GYClA, QFMClA). The Cl content in the partially degassed glasses was only slightly lower than in the starting glasses and ranged from ~440 to ~1000 ppm at 70 MPa (for details see Table 2).
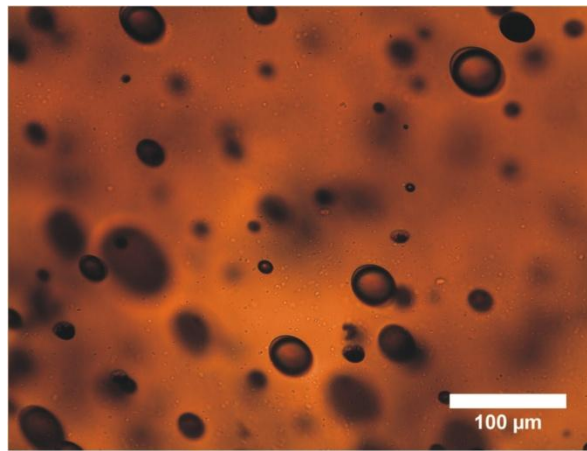
Fig. 2: Microscopic images of sample AHC-1 (decompression experiment conducted at 1030°C and ~QFM+4.2 with r ~ 0.1 MPa/s, t_A ~ 2 h). Bubble sizes range from about ~2 to ~70 μm in diameter.

4.1 Speciation of S and redox state of Fe

Fig. 3a and 3b show S-XANES spectra of selected starting glasses and partially degassed samples covering a redox range from ~QFM+0.5 up to ~QFM+4. The spectra of the oxidized samples (e.g. GYC; Fig. 3a) show a prominent, sharp peak at ~2482 eV which is related to S^{6+} in glass. The spectra of samples conducted at $\leq$ QFM+1 show only a small (e.g. GYClA) or no S^{6+} peak (e.g. QFMA) but a broad hump with a center at about 2478 eV corresponding to S^{2-}. In addition, a sharp peak at about 2472 eV, which also originates from S^{2-}, occurs in most glasses processed at $\log(fO_2/\text{bar}) <$ QFM+2 . Fleet (2005) attributed such an S^{2-} peak in Fe-bearing glasses to the predominance of Fe mono-sulfide units; however, the exact assignment of this feature is still pending (Wilke et al., 2011). In general, an increasing fO_2 leads to a decrease of the S^{2-} features and an increase of the S^{6+} peak and vice versa. The

XANES spectra indicate that the S in the andesitic melt is fully reduced at $\log(fO_2/\text{bar}) <$ QFM+0.5 and completely oxidized at $\log(fO_2/\text{bar}) >$ QFM+2.8. This observation is in agreement with earlier studies (e.g. Jugo et al., 2010; Botcharnikov et al., 2011). No systematic differences were observed for XANES spectra recorded in the center and near the rims of the melt, i.e. no redox gradients are visible. A method to estimate fO_2 in glasses using the peak intensities of S^{6+} and S^{2-} in XANES spectra [$fO_2(XANES)$] was proposed recently by Jugo et al. (2010). The method, calibrated on basaltic glasses, is based on the assumption that mixtures of end-member glasses with either fully oxidized or fully reduced S species can be used as reference samples to determine the proportion of species in glasses with mixed S oxidation state. The authors found the following relationships for basaltic glasses:

$$S^{6+}/\Sigma S = -C \cdot ln\{[(I(S^{6+})/SI - A] / B\} \tag{4}$$

$$with \quad A = 1.2427; B = -0.94911; C = 0.81354 \quad and \quad \Sigma I = I(S^{6+}) + I(S^{2-})$$

where $S^{6+}/\Sigma S$ is the molar ratio of S^{6+} and total S (ΣS) in the melt and $I(S^{6+})$ and $I(S^{2-})$ are the integrated intensities for spectral ranges characteristic of S^{6+} and S^{2-}. The energy interval for the integration proposed by Jugo et al. (2010) is 2481.5 to 2484 eV for S^{6+} and 2475.7 to 2480 eV for S^{2-} in basaltic glasses (see Fig. 2). According to Jugo et al. (2010) the following relationship describes the $S^{6+}/\Sigma S$ ratio as a function of fO_2 for basalt:

$$S^{6+}/\Sigma S = 1/(1 + 10^{(2.1 - 2 \cdot \Delta QFM)}) \tag{5}$$

where ΔQFM is fO_2 expressed as log units above QFM. We used this concept to estimate the local fO_2 in the glasses (denoted as $fO_2(XANES)$). This evaluation is based on a specific calibration for andesitic glasses determined by Max Wilke (pers. comm.) and applied in Botcharnikov et al. (2011).

The derived $S^{6+}/\Sigma S$ ratios are listed in Table 2 and displayed in Fig. 4 as a function of the nominal fO_2. Spectra of glasses with low S content ($<$ 300 ppm, grey shaded symbols in Fig. 4) are often very noisy and background features in the high and low energy ranges are not well resolved (e.g. QFMA-5 and

GYClA-4 in Fig. 3b) so the determination of peak areas is poorly constrained. Notably, presuming equal concentrations of S^{2-} and S^{6+} in the glass, the S^{2-} features in XANES spectra are less prominent than the S^{6+} features. As a consequence, in S-poor glasses the S^{2-} contribution is often overestimated by the integral method, i.e. a noticeable intensity in the S^{2-} range is obtained although the typical spectral features of S^{2-} are missing (e.g. GYC-1 in Fig. 3b). For such glasses the $S^{6+}/\Sigma S$ ratio in Table 2 represents a lower limit and these data are not considered in Fig. 4.

Another limitation of the integral method is that variations in peak shape in the S^{2-} region due to changes in coordination of S^{2-}, i.e. the sharp S^{2-} peak at ~2472 eV visible in some spectra, are ignored. Additionally, for highly vesiculated samples, where the beam size was much larger than the average distance between vesicles, it cannot be excluded that bubbles (and quench products in the bubbles) contribute to the spectra.

Considering all mentioned uncertainties related to the method of Jugo et al. (2010) and the low S content in some glasses, the $S^{6+}/\Sigma S$ derived from XANES data show good correlation with the nominal fO_2 in the melt (Fig. 4a). However, the XANES data generally indicate a (slightly) lower fO_2 in the capsule when compared to the nominal fO_2 in the vessel. This deviation may originate from the compositional, p, and T effects on S speciation in silicate melts (see e.g. Fig.13 in the review of Baker and Moretti, 2011).

Further information about the fO_2 inside the capsule was obtained from the bulk $Fe^{3+}/\Sigma Fe$ ratios listed in Table 2. As noted by Sossi and O'Neill (2011) the vanadate method for determination of Fe^{2+}/Fe^{3+} ratio is sensitive to reducing agents in the glass, i.e. S^{2-}. The authors observed an apparent increase of Fe^{2+} consistent with a stoichiometric reduction of 8 moles Fe^{3+} by 1 mole S^{2-} (see also Appendix of Sossi et al., 2012). As a first approximation the measured $Fe^{3+}/\Sigma Fe$ data were corrected using the $S^{6+}/\Sigma S$ ratios determined by XANES and total S contents of the glasses based on EMPA. This correction was applied only if clear evidence of S^{2-} features were observed in the XANES spectra (see above, this Section).

In general, the $Fe^{3+}/\Sigma Fe$ ratios of the starting glasses and of the experiments with long term annealing after decompression (near-equilibrium; $t_A \geq 5$ h) are close to the predictions made by the empirical calibrations of Kress and Carmichael (1991) and the thermodynamic model of Moretti (2005),

although some scatter of the data is obvious (Fig. 4b). Different p cannot explain these variations, since our data show no systematic correlation to p. Possible explanations are: *i)* the material for analyses was taken from outer parts of the sample and may be not representative of the whole sample and *ii)*, in the case of the most oxidizing experiments under intrinsic conditions, the fH_2 is unbuffered and experiments were performed in two different vessels.

The $Fe^{3+}/\Sigma Fe$ ratios of samples without or with short annealing after decompression are systematically below the trends predicted by the computation models. However, there is no direct evidence for more reducing conditions in the melt interiors relative to the prevailing vessel atmosphere during decompression. All samples contain a large fraction of bubbles and the major part of the S species is located in the bubbles. These species may act as reducing agents for Fe^{3+} in the glass during digestion. Fluid components are not considered in the correction of the $Fe^{3+}/\Sigma Fe$ data and, hence, Fe^{2+} is possibly overestimated.
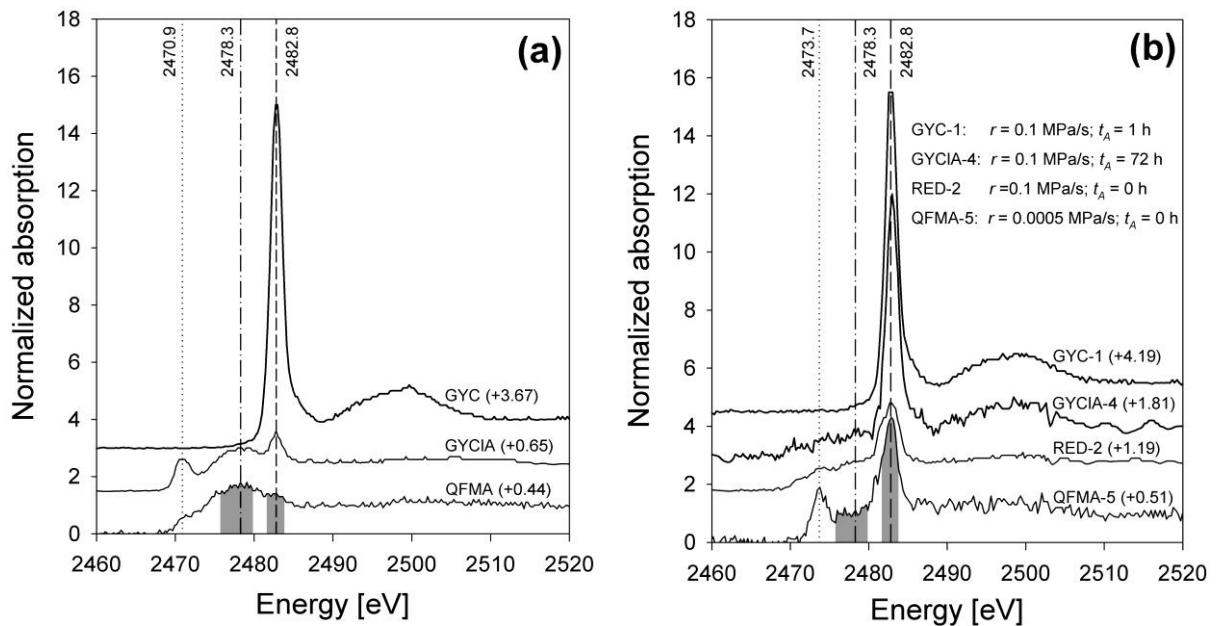
Fig. 3a-b: S Kα XANES analyses of selected samples. **a)** Starting glasses. **b)** Decompression experiments. The normalized absorption is plotted as a function of the excitation energy. The nominal fO_2 is given in parentheses (e. g. +3.67 → QFM+3.67). The vertical lines mark the positions of the three observed S peaks (sharp S^{2-} peak at 2470.9 eV to 2473.7 eV; broad S^{2-} peak centered at 2478.3 eV; sharp S^{6+} peak at 2482.8 eV). The energy intervals used for the determination of $S^{6+}/\Sigma S$ ratio following the approach of Jugo et al. (2010) are illustrated by grey shaded areas for the spectra on bottom.
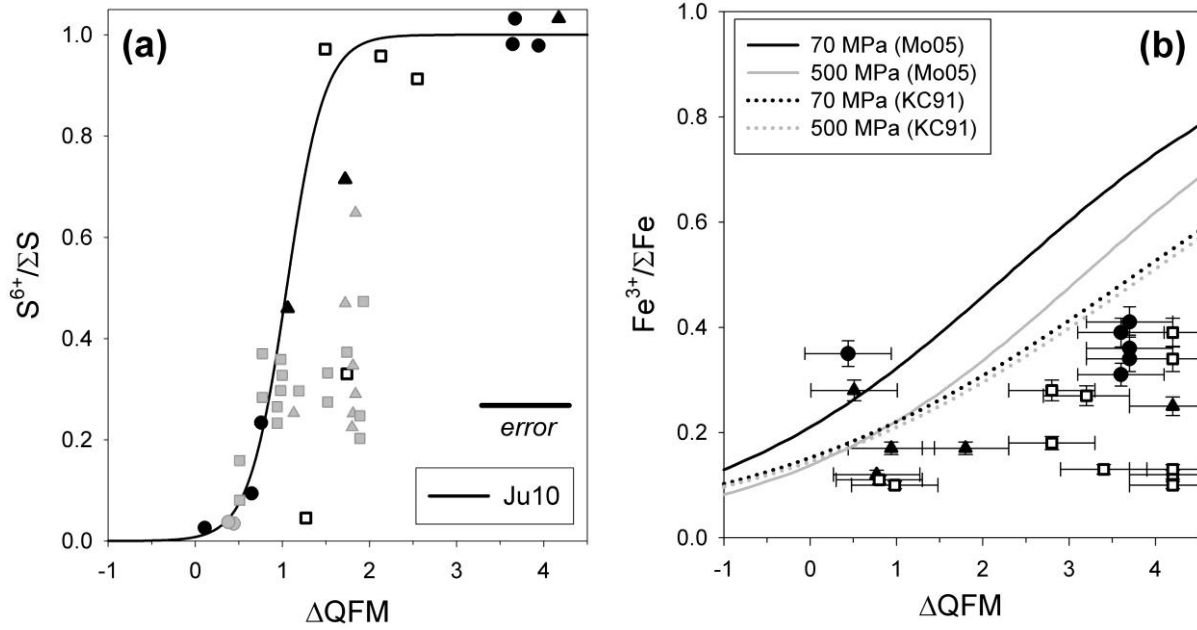
Fig. 4a-b: a) $S^{6+}/\Sigma S$ plotted against the nominal fO_2. The solid line was calculated using equation 5 derived by Jugo et al. (2010; Ju01) for basaltic composition. Samples with low S content (< 300 ppm) are indicated by grey symbols. **b)** $Fe^{3+}/\Sigma Fe$ plotted against the nominal fO_2. Trends for $Fe^{3+}/\Sigma Fe$ vs. ΔQFM at 70 and 500 MPa are based on the models of Moretti (2005; M05) and Kress and Carmichael (1991; KC91).

4.2 Partitioning of H_2O, S, and Cl

The distribution of S and Cl between fluid and melt under fluid-melt equilibrium can be described by the partitioning coefficients $D_S^{fl/m}$ and $D_{Cl}^{fl/m}$, respectively, where

$$D^{fl/m} = X_{(fluid)}/ X_{(melt)} \tag{6}$$

and $X_{(fluid)}/ X_{(melt)}$ is the concentration in wt% of S or Cl in the fluid and in the melt, respectively. In this study, the concentration of S, Cl, and H_2O in the fluid phase was determined by mass balance calculation using the measured S, Cl, and H_2O content in the glasses before (contents in the starting glasses) and after (contents in the partially degassed samples) decompression. It is emphasized that the $X_{(fluid)}/X_{(melt)}$ ratio derived from the decompression experiments does not necessarily represent equilibrium conditions. In the following the term $D^{*fl/m}$ is used to describe the distribution of volatiles between melts and fluid for such kinetic experiments whereas $D^{fl/m}$ refers to near-equilibrium conditions.

4.2.1 Evolution of H₂O contents during decompression and annealing

The experimental SD1 series was designed to investigate the distribution of H_2O and S between fluid and melt at various final p (150, 100, 70, and 30 MPa) under oxidizing conditions (~QFM+3). Samples were directly quenched after decompression ($r \approx 0.1$ MPa/s). Fig. 5a shows clearly that the H_2O content of the glasses, measured by IR spectroscopy, decreases with final p in the range of 30 to 150 MPa and is systematically higher than predicted by the computation models of Newman and Lowenstern (2002; VolatileCalc model) and Witham et al. (2012; SolEx model). A comparison of all decompression experiments with a final $p = 70$ MPa reveals that the H_2O content in these partially degassed glasses is largely independent of r, t_A, and fO_2, ranging from 2.0 to 4.2 wt% H_2O with an average of 3.54 ± 0.37 wt%. The solubility calculations are applicable to rhyolitic and basaltic systems, and the question is whether the deviation from the solubility data is due to differences in fluid-melt composition or related to kinetic effects during decompression. In order to clarify this point, we performed a set of H_2O solubility experiments with the Krakatau andesite at 1030°C and 70 MPa for 48 h under oxidizing conditions (~QFM+2.6). In two capsules glass powder was used as starting material and two others contained a single glass piece each. Post-experimental glasses were bubble-rich in the first case and bubble-free in the second case. Identical H_2O contents detected by IR of 3.63 ± 0.10 wt% for all four glasses give confidence that the data represent equilibrium H_2O solubilities. KFT measurements on the bubble-free glasses support the IR data (see Table 3), demonstrating that H_2O solubility in the Krakatau andesite is higher than in rhyolite and basalt at this *p-T* condition (1030°C, 70 MPa). Hence, we conclude that the H_2O contents of the decompressed samples are close to the equilibrium values for the applied r (0.0005 to 0.17 MPa/s).

4.2.2 Evolution of S contents during decompression and annealing

Fig. 5b indicates that most of the S dissolved in an oxidized melt is released to a fluid phase upon decompression in a p range of 150 to 100 MPa, in quite good agreement with the predictions of the *SolEx* model of Witham et al. (2012) although the model was calibrated for basaltic melts. Comparison of Fig. 5a and 5b reveals that S is released earlier than H_2O during decompression, i.e. the H_2O content in the melt decreases significantly below 100 MPa when most S has been released to the

fluid phase. This trend is confirmed in Fig. 5c, which shows the influence of final p on $D*_S^{fl/m}$. These

findings indicate that S- and H_2O-degassing are controlled by different mechanisms.
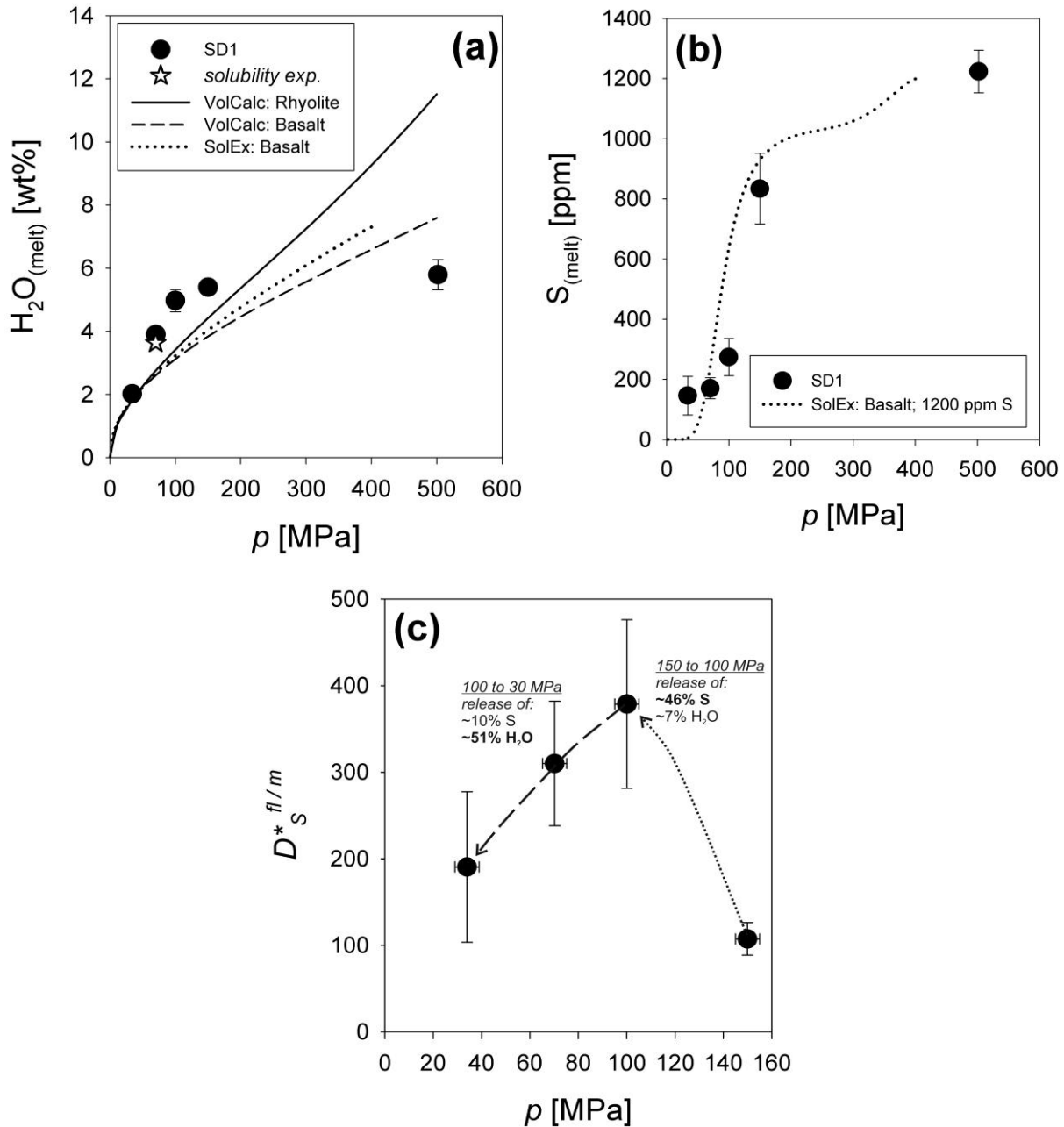
Fig. 5a-c: Influence of final p on **a)** H_2O content of the melt, **b)** S content of the melt and **c)** $D*_S^{fl/m}$ at 1030°C and ~QFM+3 ($r \sim 0.1$ MPa/s). Calculated solubility of H_2O and S in basaltic and/or rhyolitic melts is plotted for comparison, using recent solubility models (see below). The *star* marks the water solubility in the Krakatau andesite experimentally determined at 1030°C, 70 MPa and QFM+2.6 (see text).
Details about **a)** and **b)**: the H_2O and S data at 500 MPa correspond to the initial concentration in sample SD1.
Details about **c)**: Given percentages refer to the amount of S or H_2O released from the melt within the p ranges from 150 to 100 MPa (*dotted line*) when S is predominantly degassing and 100 to 30 MPa (*dashed line*) when degassing of H_2O dominates over S.
VolCalc (VolatileCalc model of Newman and Lowenstern, 2002); *SolEx* (SolEX model of Witham et al., 2012); applied parameters: 7.3 wt% H_2O, 1200 ppm S, closed system, PI parameterization.

In contrast to the H_2O content, the S content in the melt at the final $p = 70$ MPa is often highly variable and depends e.g. on r, t_A, and fO_2. Under oxidizing, S^{6+} dominated conditions ($\log(fO_2/\text{bar}) > \text{QFM}+3$; Fig. 6a), a strong increase of $D^*_S{}^{fl/m}$ by a factor of ~10 with increasing r ($D^*_S{}^{fl/m} = 288 \pm 40$ at 0.17 MPa/s and $D^*_S{}^{fl/m} = 27 \pm 1$ at 0.02 MPa/s; $t_A = 0$ h) is observed. By contrast, experiments at slightly reducing conditions of ~QFM+1.5 (10-20% S^{2-} in the melt) show an increase of $D^*_S{}^{fl/m}$ by a factor of ~1.7 with decreasing r over a slightly smaller range of r ($D^*_S{}^{fl/m} = 317 \pm 35$ at 0.1 MPa/s and $D^*_S{}^{fl/m} = 527 \pm 100$ at 0.02 MPa/s; $t_A = 0$ h). At more reducing conditions (~QFM+0.8; $S^{2-} > S^{6+}$) the influence of r on $D^*_S{}^{fl/m}$ seems to be negligible; $D^*_S{}^{fl/m}$ ~100 over a wide range of r (0.01 to 0.10 MPa/s; $t_A = 0$ h; Fig. 6b). Significantly higher values of $D^*_S{}^{fl/m}$ were estimated with $r = 0.0005$ MPa/s at ~QFM+1 but the S contents of these two experimental glasses (QFMA-5 and QFMClA-5) are below the detection limit of the EMP, and the data have high uncertainty. Moreover, Fig. 7a indicates a significant influence of fO_2 on the fluid-melt distribution of S at $t_A = 0$ h (fluid-melt disequilibrium) for a constant r of ~0.1 MPa/s. A strong increase of $D^*_S{}^{fl/m}$ from 77 ± 17 to 354 ± 147 is observed in the range of QFM+0.8 to QFM+1.5. However, $D^*_S{}^{fl/m}$ remains almost constant at higher fO_2 (average $D^*_S{}^{fl/m} \approx 300$).

The influence of t_A on $D^*_S{}^{fl/m}$ and, thus, of fluid-melt equilibration processes on the fluid-melt distribution of S is illustrated by Fig. 8. Fig. 8a displays the results under oxidizing conditions ($\log(fO_2/\text{bar}) > \text{QFM}+3.2$) for different combinations of initial and final p: 500 and 70 MPa (AH3, AH4, GY3, GY4, GY-C-1, GY-C-2, AH-C-1, AH-C-2), 400 and 70 MPa (SD1-700), or 300 and 100 MPa (ASD-1, ASD-2). Differences in initial and final p as well as slight variations of r (see Table 2) exert no significant effect on the evolution of $D^*_S{}^{fl/m}$ with increasing t_A. Quenching directly after decompression ($t_A = 0$ h) yielded an average "initial" $D^*_S{}^{fl/m}$ of 244 ± 106. Annealing for 5 h at final p-T conditions leads to a strong decrease of $D^*_S{}^{fl/m}$ to values below 70. Further annealing up to $t_A = 48$ h has no significant effect on the fluid-melt partitioning of S implying that near-equilibrium distribution was achieved. On the basis of all data for $t_A \geq 5$ h a "final" $D_S{}^{fl/m}$ of 39 ± 16 is derived for oxidizing conditions at 70 MPa and 1030°C. A relaxation trend was fitted to the data using the estimated "initial" and "final" $D_S{}^{fl/m}$ values (A_0 and A_1, see caption, Fig. 8a) and a relaxation time $\tau = 0.8$ h. The

good correlation of the regression with the data confirms that (near-) fluid-melt equilibrium conditions (equals ~ 6 times τ) are reached after ~5 h annealing.

A different trend for $D*_S^{fl/m}$ as a function of t_A is observed under more reducing conditions of ~QFM+1.1 to ~QFM+2.2 (Fig. 8b). In general, these $D*_S^{fl/m}$ values have higher uncertainties than those under oxidizing conditions (> QFM+3.2). Experiments containing > 6 wt% initial H_2O in the melt – an H_2O content which is comparable to the H_2O concentration of experiments shown in Fig. 6a and 8a for oxidizing conditions – reveal an almost constant $D*_S^{fl/m}$ of 164 ± 65 for t_A ranging from 0 to 19 h at QFM+1.1 to QFM+1.7. On the other hand, samples with lower initial H_2O content (~4.6 wt%) are characterized by higher $D*_S^{fl/m}$ values of ~400 at QFM+1.7 to QFM+2.2 with no significant change upon annealing for $t_A \leq 5$ h.

The contrasting trends for oxidizing and reducing conditions are also evident when comparing disequilibrium values ($D*_S^{fl/m}$; $t_A = 0$ h; Fig 7a) to near-equilibrium values ($D_S^{fl/m}$; $t_A \geq 5$ h; Fig. 7b) as a function of the nominal fO_2. In contrast to the results at disequilibrium conditions, $D_S^{fl/m}$ decreases remarkably from ~220 to ~50 with increasing $\log(fO_2/\text{bar})$ from ~QFM+1 to ~QFM+2 at near-equilibrium conditions. However, comparable to disequilibrium data, $D_S^{fl/m}$ seems to be independent of fO_2 as soon as $\log(fO_2/\text{bar}) > \text{QFM}+2$ (average $D_S^{fl/m} \approx 35$). Moreover, our results for near-equilibrium conditions correlate well with the fluid-melt partitioning data of Zajacz et al. (2012) for andesitic systems. The slight differences may refer to differences in melt compositions (e.g. starting glasses of Zajacz et al. (2012) contain ~55 to 60 wt% SiO_2), p, and/or T.
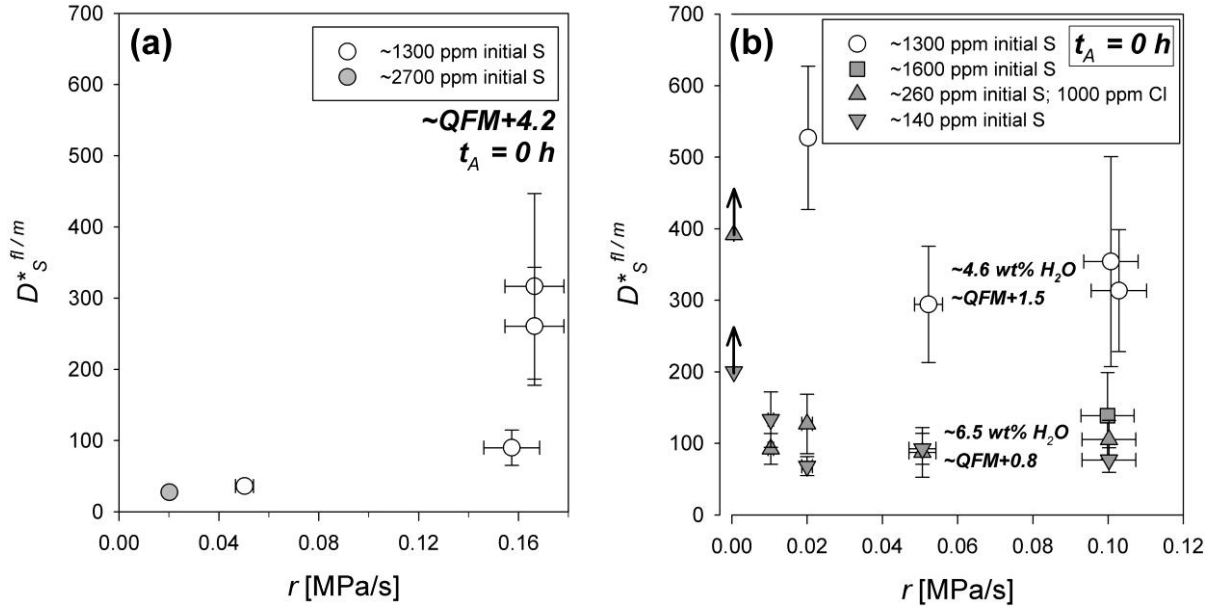
Fig. 6a-b: Influence of *r* on $D^*_S{}^{fl/m}$ for samples quenched directly after decompression. **a)** Oxidizing conditions, log(fO_2/bar) > QFM+3 and **b)** reducing conditions, log(fO_2/bar) ranging from about QFM+0.8 to QFM+1.5. An effect of initial H_2O content (~4.6 and ~6.5 wt%) is evident for reducing conditions. The experiments conducted with an *r* of 0.0005 MPa/s (QFMA-5 and QFMClA-5) contain S below the EMP detection limit. The black arrows indicate that $D^*_S{}^{fl/m}$ represent the lower limit in this case.
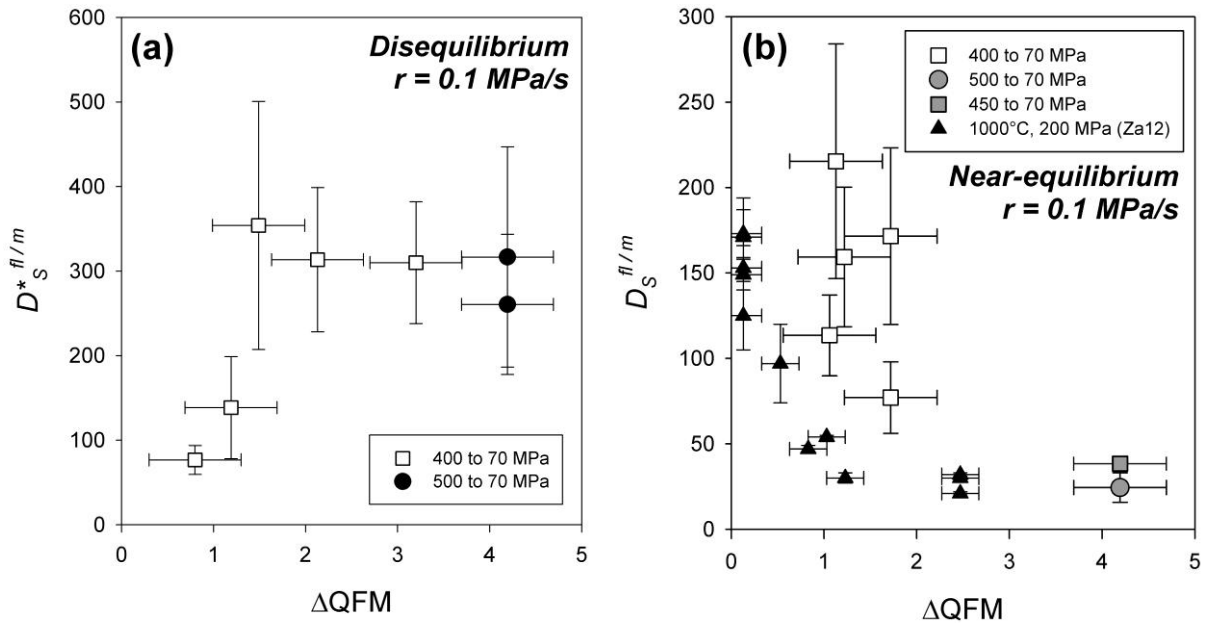
Fig. 7a-b: $D_S{}^{fl/m}$ against ΔQFM. **a)** Fluid-melt disequilibrium conditions. Samples were directly rapid-quenched after decompression ($t_A = 0$ h). **b)** Fluid-melt near-equilibrium conditions ($t_A \geq 5$ h). $D_S{}^{fl/m}$ values of Zajacz et al. (2012; Za12) for andesitic systems based on experiments conducted at 1000°C, 200 MPa and variable fO_2 are plotted for comparison.
Only experiments with initial H_2O contents of ~6 wt% are shown.
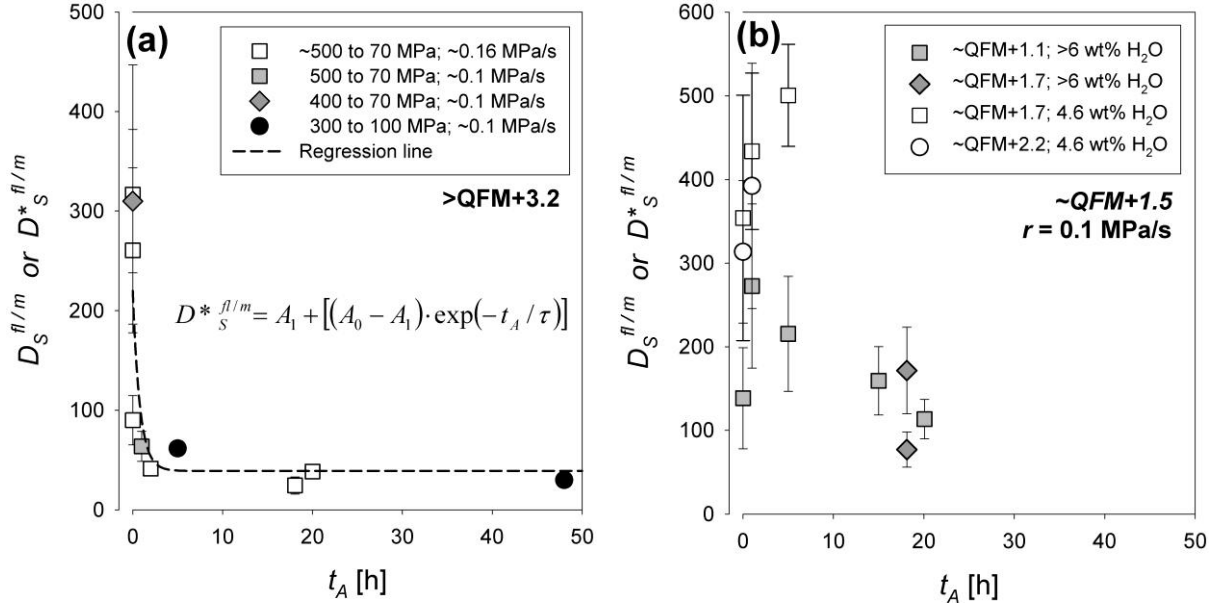
Fig. 8a-b: Dependence of $D_S^{fl/m}$ on t_A at **a)** oxidizing conditions (> QFM+3.2) and **b)** more reducing conditions (~QFM+1 to ~QFM+2).
A) Includes a regression line. The parameters for the equation of the fitted regression are:
$A_0 = 244$ (~initial $D*_S^{fl/m}$); $A_1 = 39$ (~final $D*_S^{fl/m}$); $\tau = 0.8$ h (relaxation time); t_A in h

4.2.3 Evolution of Cl contents during decompression and annealing

Cl was added to three starting glasses: GYClA (~500 ppm), GYMClA (~1000 ppm), and QFMClA (~1000 ppm). The Cl contents in the decompression experiment glasses are slightly lower than the Cl contents of the starting glasses. The $D*_{Cl}^{fl/m}$ are 1 or 2 orders of magnitude smaller than those of S (ranging from 1 to 13). Fig. 9a and 9b indicate that r (Fig. 9a) and t_A (Fig. 9b) have a minor effect on the fluid-melt partitioning of Cl ($D*_{Cl}^{fl/m} \approx D_{Cl}^{fl/m}$). It is worth noting that the determined $D*_{Cl}^{fl/m}$ values are close to the equilibrium values predicted by previous studies, e.g., by Webster (1992) for a haplogranitic system (e.g. $D*_{Cl}^{fl/m} \approx 9$ at 993°C, 910 ppm initial Cl, 194 MPa).

Parameters which affect Cl partitioning are in particular the fO_2 and the initial Cl content. $D*_{Cl}^{fl/m}$ increases remarkably from 2 ± 1 to 10 ± 3 (average $D*_{Cl}^{fl/m}$ values) with increasing fO_2 (from QFM+0.8 to QFM+1.8). This effect is probably related to the decreasing Fe^{2+}/Fe^{3+} ratio and, thus, changes in melt polymerization which has a significant influence on Cl solubility in silicate melts (Metrich and Rutherford, 1992). Doubling the initial Cl content (from 500 to 1000 ppm) leads to a significant increase of $D*_{Cl}^{fl/m}$ from 4 ± 1 to 10 ± 3 at QFM+1.8, in accordance with observations of Webster (1992) for haplogranitic systems.
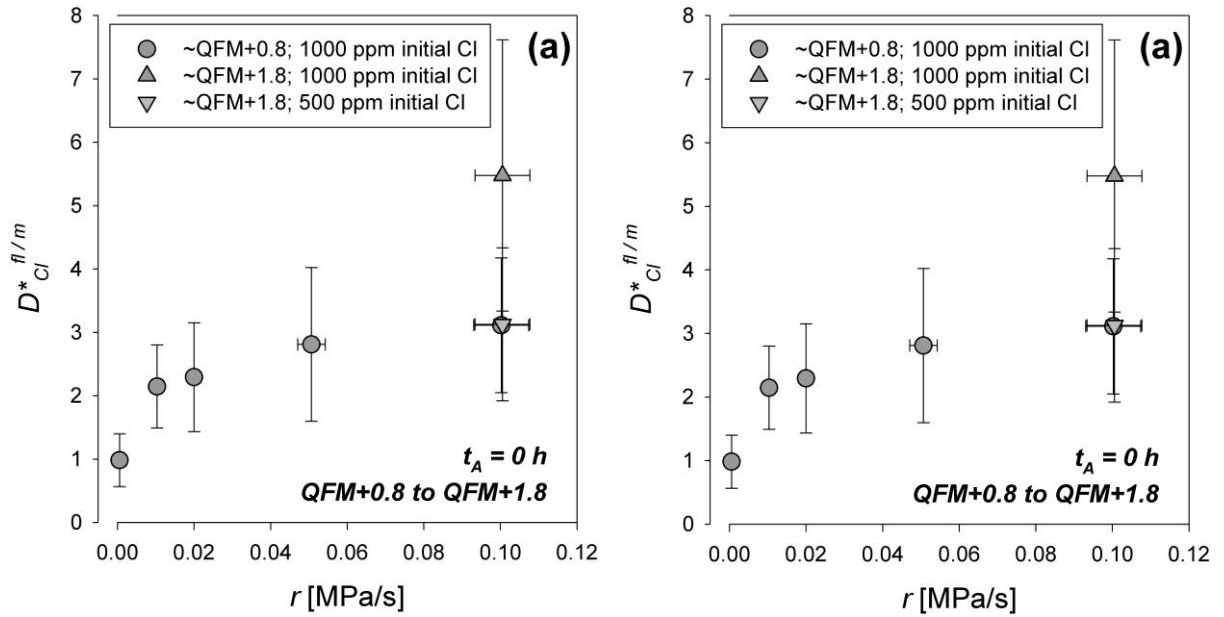
Fig. 9a-b: Partitioning of Cl between fluid and andesitic melt. **a)** Influence of r on $D_{Cl}^{fl/m}$ at QFM+0.8 and QFM+1.8. **b)** Influence of t_A on $D_{Cl}^{fl/m}$ at QFM+1.8.

5. DISCUSSION

5.1 Oxygen fugacity

The fO_2 plays a crucial role in distributing S between fluid and melt (e.g. Keppler, 2010; Webster and Botcharnikov, 2011; Zajacz et al., 2012) and, thus, the estimation of fO_2 should be discussed critically. As demonstrated in various studies, the prevailing fO_2 within a noble metal capsule can be accurately predicted when the H_2-pressure in the vessel is known by direct measurements using a *Shaw-membrane* or can be reasonably estimated by experience (e.g. Scaillet et al., 1992; Berndt et al., 2002; Wilke et al., 2002). A prerequisite for this estimate is that equilibrium between the p medium and the interior of the capsule has been achieved.

Decompression affects the fO_2 inside the capsule in several ways. First, p release automatically induces a decrease of fH_2 in the vessel and, as a consequence, an increase of the fO_2 within the capsule, i.e., by ~0.7 log units for p reduction from 400 to 70 MPa at 1030°C. As mentioned in Section 2, the reduction of fH_2 in the vessel can be even larger due to a preferential loss of H_2 through the valve upon decompression. Another complication arises from the history of the vessel. Even at room temperature H_2 diffuses into the metallic parts of an autoclave and, depending on duration and H_2 p in previous experiments, H_2 can be either released or consumed by the vessel during an experiment. Measurements

with a *Shaw*-membrane at the end of experiments can only yield information about the total change in fH_2; the sensor is too sluggish to resolve the timescale of fH_2 variation in the vessel.

The redox conditions inside the capsule are additionally influenced by volatiles dissolved in the melts which approach saturation during decompression. For instance, the $a(H_2O)$ in the melt will increase gradually upon decompression until $a(H_2O) \sim 1$ is reached at about 150 to 200 MPa (see Fig. 5c). This accounts for a slight oxidation of the samples by ~ 0.3 log units (assuming initial H_2O content of 6 wt% in the melt). Reactions within the released fluid phase, i.e. dissociation of sulfate ($SO_4^{2-} \rightarrow SO_2 + 0.5\ O_2 + O^{2-}$), can cause further oxidation of the melt. The stability of sulfate in the fluid strongly relies on fluid density, i.e., the potential of fluid components to form a complex with charged particles. Decompression also affects the relationship between the $Fe^{3+}/\Sigma Fe$ ratio of Fe in the melt and the fO_2. The model of Moretti (2005) predicts for a p reduction from 500 to 70 MPa a decrease in fO_2 by ~ 0.9 log units for andesite at 1030°C and constant $Fe^{3+}/\Sigma Fe$ ratio (Fig. 4b).
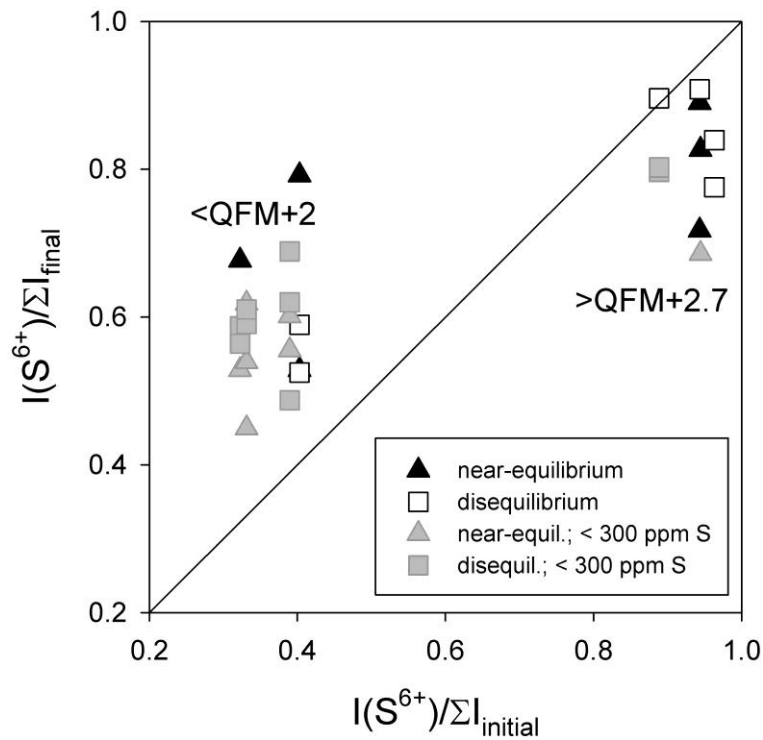
Fig. 10: Integrated S-XANES peak intensity ratios of the decompression experiments ($I(S^{6+})/\Sigma I_{final}$) in comparison to the starting glasses ($I(S^{6+})/\Sigma I_{intial}$). Samples with low S content (< 300 ppm) are indicated by grey symbols.

Considering the complexity of the processes involved, the overall effect of decompression on melt fO_2 is difficult to predict, although a tendency towards higher fO_2 is evident at least for intermediate to reducing conditions from comparing the final and initial abundance of S^{6+} in the glasses (Fig. 10). For oxidizing conditions (> QFM+2.7) the S intensity ratio ($I(S^{6+})/\Sigma I$) of the run products is typically below that of the starting materials, but this is probably an artifact related to low S contents in the partially degassed melts after decompression and/or to limitations of the integral method used to estimate $I(S^{6+})/\Sigma I$ (see Section 4.1) .

The rate of readjustment between sample and vessel is determined by H_2 permeation through the capsule wall as well as by transport and reactions of H_2 and H_2O in the melt. Thus, crucial parameters are H_2 diffusion and solubility in the capsule wall and andesitic melt, H_2O diffusion in the melt, the amount of polyvalent elements in the melt (here mainly Fe and S), and the dimensions of the melt pool. The H_2 transport through the Au wall is not the limiting factor due to the high permeability of Au for H_2 at 1030°C, i.e. sufficient amounts of H_2 required for redox-equilibration between the vessel and melt interior are transported through the capsule wall within minutes (Chou, 1987). Gaillard et al. (2003) observed that the growth of a reduction layer in rhyolitic melts is controlled by the solubility and the diffusivity of H_2 in the melt weighted by the concentration of the sink (Fe^{3+}; also S^{6+} in our experiments), while redox-exchange reactions (e.g. $H_2 \leftrightarrow 2\,H^+ + 2\,e^-$ and $2\,Fe^{3+} + 2e^- \leftrightarrow 2\,Fe^{2+}$) and H_2O dissociation reactions are rather fast. The minimum time (t) required for redox-equilibration of the melt can be estimated using diffusivity data for H_2 in silicate melts. Based on the diffusion equation fitted by Zhang and Ni (2010) to the H_2 diffusion data of Shelby (1977) and Shang et al. (2009), t required for equilibration of the melt with respect to fH_2, is on the order of 1 h for our experimental conditions. This estimate is consistent with the minimum t_A to achieve a stable $D_S^{fl/m}$ (Fig. 8).

5.2 Kinetics of degassing

As pointed out previously, the H_2O and Cl content in the melt can rapidly adjust to changing conditions during decompression while the S content is sensitive to r and t_A. The major reason is the slow diffusivity of S species in the melt compared to the other volatiles (Zhang et al. 2010; Behrens

and Stelling 2011). In Section 5.2.1 and Section 5.2.2 the degassing kinetics of S-bearing melts are discussed for oxidizing and intermediate to reducing conditions using plots of the S content in the partially degassed melts against r and t_A (Fig. 11). No detectable influence of the bulk S content in the system on the distribution of S between fluid and melt could be found in the range from 1150 to 2700 ppm S in the melt. Under reducing conditions even very low initial S contents of ~140 ppm in the melt gave consistent results. These findings are in agreement with the results of Keppler (2010) for haplogranitic melts.
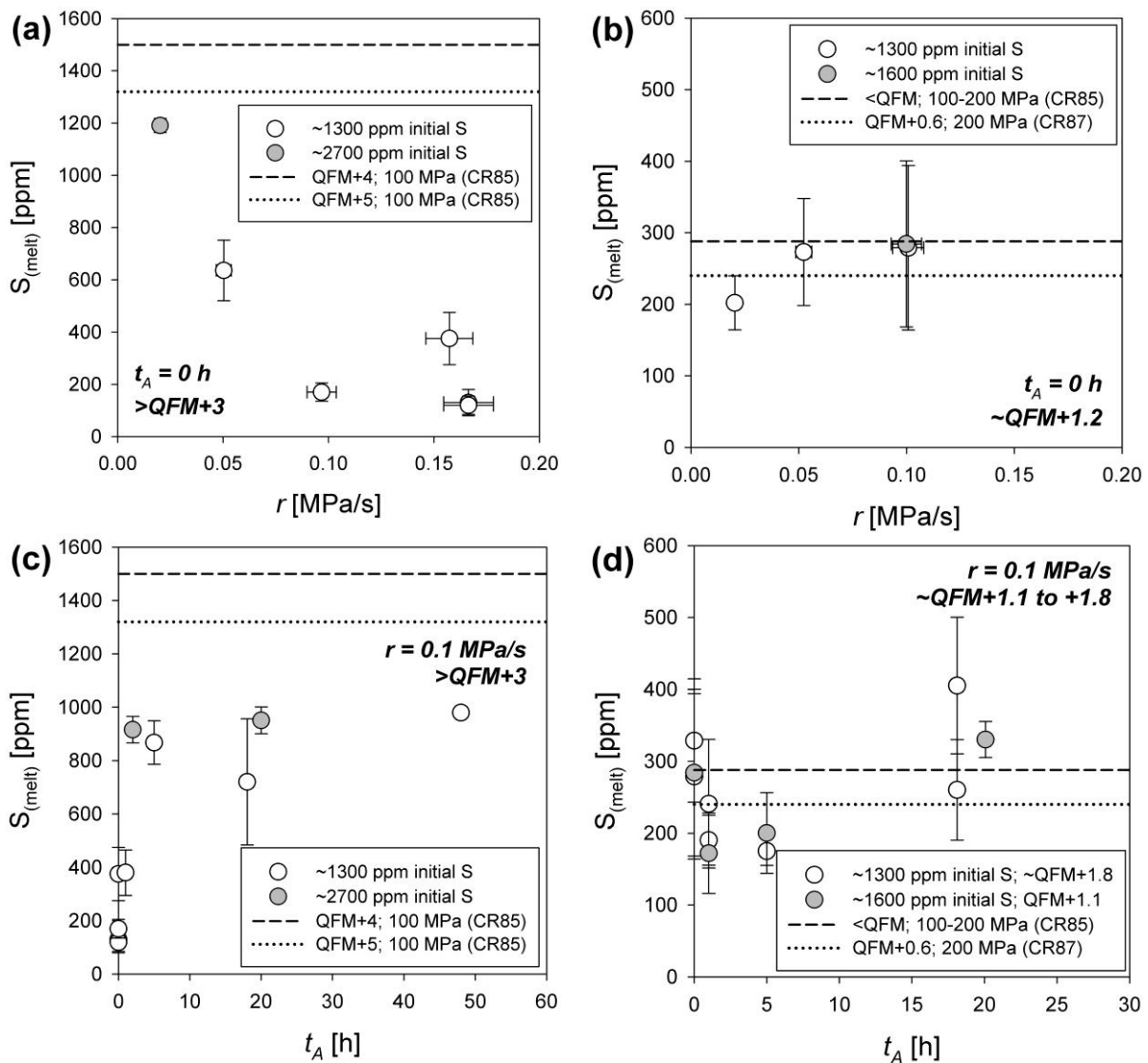
Fig. 11a-d: S contents in the partially degassed samples plotted against r or t_A.
a) S [ppm] vs. r at log(fO_2/bar) > QFM+3. **b)** S [ppm] vs. r at an average log(fO_2/bar) of QFM+1.2. **c)** S [ppm] vs. t_A at log(fO_2/bar) > QFM+3. **d)** S [ppm] vs. t_A at log(fO_2/bar) of QFM+1.1 to QMF+1.8.
CR85: S solubility of Carroll and Rutherford (1985), dacitic melt, H_2O saturated ; CR87: S solubility of Carroll and Rutherford (1987), dacitic melt, 4.6 to 5.4 wt% H_2O

5.2.1 S degassing under oxidizing conditions (> QFM+3)

The amount of S released upon decompression under oxidizing conditions (> QFM+3) decreases continously with decreasing r (Fig. 11a). About 70 to 90% of the S initially present in the melt (1200 to 2700 ppm at 1030°C) is released to the fluid phase during fast decompression (~0.17 MPa/s) from ~500 to 70 MPa. At the lowest r = 0.02 MPa/s the remaining S content in the melt of ~1200 ppm is close to the S solubility. Carroll and Rutherford (1985) found S contents of 1300 to 1500 ppm in nearly H_2O saturated (andesitic) dacite coexisting with anhydrite at > QFM+4, 100 MPa, and 1025°C (indicated by the dashed lines in Fig. 11a). Taking the p dependence of S solubility into account (e.g. Carroll and Rutherford, 1985; Lesne et al., 2011), values slightly below 1300 ppm are expected for a melt in equilibrium with anhydrite at 70 MPa.

The variation of S content and, thus, of the $D*_S^{fl/m}$ as a function of r at oxidizing redox conditions (Fig. 6a) is interpreted to reflect a transient distribution of S between fluid and melt. Upon decompression volatiles (here H_2O, S, ± Cl) are exsolved from a melt to a fluid phase. Fluid bubbles will nucleate and volatiles must migrate to fluid pools to allow bubble growth. The fluid composition will change upon decompression, depending on the initial volatile budget and on the solubility and mobility of volatiles. The transport of S (as sulfate and sulfide ions) and H_2O in a silicate melt without convection fluxes is controlled by diffusion. Sulfide and sulfate must be charge-compensated by alkali ions and/or alkaline earth ions and, hence, S fluxes will be coupled to these mobile cations. In particular Ca^{2+} shows high affinity for sulfate as demonstrated by Delmelle et al. (2011). For the experimental glasses of this study a sulfate-to-Ca^{2+} coupling is not hypothesized because of the low abundance of S.

Anhydrite solubility in hydrous fluid strongly increases with p in the studied p-T range (Newton and Manning, 2005). The initially formed high-density fluid has a high capacity for dissolving sulfate, but with continuing decompression the density of the fluid decreases and at a final p of 70 MPa the S solubility in the fluid becomes very low. At high r the fluid is initially S-undersaturated and sulfate diffuses from the melt to the bubbles. Further decompression induces saturation of the fluid in anhydrite (i.e. anhydrite crystallizes within the fluid) and back-diffusion of S into the anhydrite-undersaturated melt. Thus, S contents in the melts after fast decompression are far below the level expected for fluid-melt equilibrium. Consistent with this scenario, anhydrite crystals up to 10 µm in

length were observed by microscopy and identified by Raman spectroscopy within bubbles produced during experiments decompressed at a high rate ($r \geq 0.1$ MPa/s) and annealed for ≤ 2 h (see Appendix I for details).

The t required to transport sulfate to the fluid pools upon initial decompression as well as for the back-diffusion of sulfate into the melt when low p is achieved is controlled by sulfate diffusivity in the melt and the distance between the fluid pools. Microscopic investigations indicate that the distance between two bubbles in samples directly quenched after fast decompression (~0.1 MPa/s) is typically about 20 µm. Sulfate diffusion is controlled by melt η, and sulfate diffusivity in the melt can be estimated using the Eyring relationship $D_\eta = k{\cdot}T / \lambda{\cdot}\eta$; D_η = diffusivity [m^2/s], k = Boltzmann constant and λ = jumping distance, assumed to be ~0.3 nm (Behrens and Stelling 2011). The η of the andesitic melt at 1030°C is calculated for 6 wt% H_2O ($\approx$ initial content, prior to decompression) and 3.6 wt% H_2O in the melt ($\approx$ final content, after decompression) to be 190 Pa·s and 550 Pa·s, respectively, using the computation model of Hui and Zhang (2007). With the derived diffusivities for initial ($3.15{\times}10^{-13}$ m^2/s) and final H_2O contents ($1.09{\times}10^{-13}$ m^2/s) the t required for a diffusion distance [$x = (2{\cdot}D{\cdot}t)^{0.5}$] of 20 µm is initially ~10 min and finally ~30 min. It is noteworthy that the model of Giordano et al. (2008) predicts slightly higher melt η values, indicating that e.g. the back-diffusion of sulfate into the melt may take up to ~60 min. These timescales are consistent with the observed variations in S content of the melt with r and t_A (Fig. 8 and 11), supporting the idea that S diffusion in the melt is the rate-controlling parameter under oxidizing conditions.

5.2.2 S degassing under reducing to intermediate conditions

As for the experiments at oxidizing conditions, most of the S initially present in the melts (~1150 to ~1600 ppm) is incorporated into the fluid after fast decompression. However, contrary to what occurs under oxidizing conditions, the S content in the melt is not affected by the r (Fig. 11b) and post-decompression annealing (Fig. 11d) under reducing (~QFM+1.1) to intermediate (~QFM+1.8) redox conditions. This trend is also observed for Cl-bearing systems (see results of GYClA and GYMClA experiments, Table 2), indicating that Cl has no remarkable influence on the degassing kinetics of S at intermediate to reducing redox conditions. The average S content measured in the glasses after

decompression (~300 ppm) is similar to the S solubility in H_2O saturated (andesitic) dacite melts coexisting with pyrrhotite at ~QFM, 1025°C and 100 to 200 MPa (Carroll and Rutherford, 1985).

These observations point to distinct differences in the degassing mechanisms under oxidizing and reducing conditions. The diffusivity of sulfide in silicate melt is similar to that of sulfate (Behrens and Stelling, 2011). Thus, differences between the transport rates of sulfide and sulfate to the fluid pools upon decompression are not expected. Considering the evolution of the S contents in the melt during annealing after decompression (Fig. 11d), there appears to be no driving force for back-diffusion of S from the fluid into the melt at low p. It is worth noting that no crystalline precipitates were found within bubbles in any of the experiments performed at $\leq$ QFM+1.8. These observations can be explained by good miscibility of S species (i.e. H_2S, HS^-) and hydrous components in the fluid under intermediate to reducing conditions. Due to the absence of a back-diffusion process at the end of decompression over the range of r applied in this study, the calculated $D*_S^{fl/m}$ values represent near-equilibrium conditions at the end of decompression.

5.3. Partitioning of S and Cl between fluid and melt

5.3.1 Influence of fO_2 on $D_S^{fl/m}$

Decompression experiments (rate: ~0.1 MPa/s) conducted under oxidizing conditions (QFM+3) and close to fluid-melt equilibrium ($t_A > 5$ h; Fig. 8a) indicate a $D_S^{fl/m}$ of 39 ± 16 for a final p ~70 MPa. This $D_S^{fl/m}$ is similar to data obtained by Lesne et al. (2011) for basaltic compositions ($D_S^{fl/m} \approx 67$ at 1150°C, 100 to 300 MPa, and QFM+1.7 to QFM+3.0) and to the results of Keppler (2010) for haplogranitic systems ($D_S^{fl/m} \approx 50$ at 850°C, 200 MPa, and QFM+5). Keppler (2010) also noted a minor effect of p in the range of 50 to 300 MPa on $D_S^{fl/m}$ in haplogranitic systems. In contrast, preliminary experiments of Teague et al. (2008) conducted at 1250 to 1300°C (fO_2 unknown) using andesitic melt indicate an increase of $D_S^{fl/m}$ by a factor of 10 with increasing p from 200 to 800 MPa. Furthermore, the data Lesne et al. (2011) obtained for basaltic systems (1150°C, ~QFM+1.7 to ~QFM+3.1) indicates a minor influence of p on $D_S^{fl/m}$ in the range of 100 to 400 MPa but a strong increase of $D_S^{fl/m}$ by up to two orders of magnitude in the p range of 100 to 25 MPa. Hence, we suggest

that a $D_S^{fl/m}$ of ~50 is applicable over a wide range of silicate melt compositions and over a p range of at least ~70 to ~400 MPa, under oxidizing conditions.

Our experiments with $t_A \approx 20$ h (near-equilibrium) and $r \approx 0.1$ MPa/s, performed at QFM+1.5 (Fig. 8a), yielded a $D_S^{fl/m}$ of ~150 at a final p ~70 MPa, indicating an increase of $D_S^{fl/m}$ with decreasing fO_2 (from ~QFM+3 to ~QFM+1.5) by a factor of about 3. This observation is consistent with findings Keppler (2010) made for Fe-free haplogranitic melts at 850°C and 200 MPa. Keppler (2010) determined an increase of $D_S^{fl/m}$ from ~50 to ~470 with fO_2 decreasing from QFM+5.1 to QFM-0.9. The strong dependence of $D_S^{fl/m}$ on fO_2, illustrated in Fig. 7b, is also largely in agreement with earlier findings of e.g. Zajacz et al. (2012). The slight differences between our data and the results of Zajacz et al. (2012) may arise from small differences in melt compositions, in p, and/or uncertainties in fO_2 determination.

5.3.2 Influence of Cl content on S distribution between fluid and melt

Fig. 12 shows that $D_S^{fl/m}$ increases by a factor of ~2 at QFM+1.8 if 500 ppm Cl is added to the system and remains constant with further increase in bulk Cl content to 1000 ppm. An average $D_S^{fl/m}$ of 261 ± 40 was calculated for Cl-bearing andesitic melts (500 to 1000 ppm Cl). The data of Zajacz et al. (2012) indicates that this trend may be extrapolated to bulk Cl contents of ~2600 ppm, but at higher Cl contents $D_S^{fl/m}$ decreases slightly with bulk Cl content (e.g. $D_S^{fl/m}$ ~90 at ~2 wt% Cl). A weak negative correlation between $D_S^{fl/m}$ and bulk Cl content in rhyodacitic systems at ~QFM+0.6, 850°C, and 200 MPa was inferred by Webster and Botcharnikov (2011) based on equilibrium experiments conducted by Botcharnikov et al. (2004). The authors suggested that the effect of Cl content on $D_S^{fl/m}$ might be related to changes in activity coefficients of S species in the fluid-melt system. They assumed that extraction of cations such as Ca, Na, and K may change the fluid composition and, thus, the activities of the S and Cl components in the fluid phase. Beermann (2010) proposed that the extent of cation extraction is largely dependent on S speciation and thus on fO_2. This dependence on fO_2 is suggested to be less significant at fairly reducing conditions. Hence, the discrepancy between these results and the results of Webster and Botcharnikov (2011) may be due to differences in fO_2 and/or melt composition.
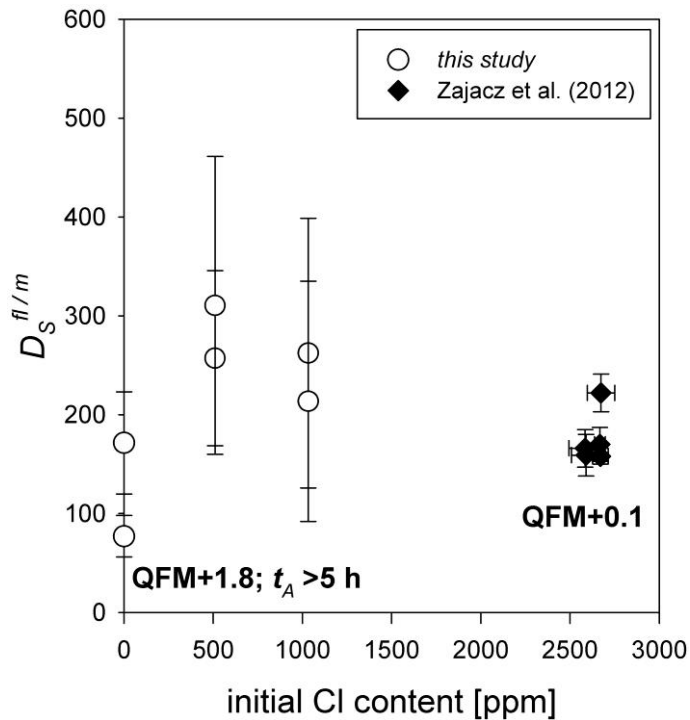
Fig. 12: Dependence of $D_S^{fl/m}$ on Cl content of the starting glass. Data from Zajacz et al. (2012) are for andesitic systems at 1000°C, 200 MPa and log(fO_2/bar) of ~QFM+0.1.

On the other hand, experiments conducted at slightly more reducing conditions (~QFM+0.8) and with $t_A = 0$ h, representing fluid-melt disequilibrium conditions, indicate that Cl has only a minor effect on $D*_S^{fl/m}$ (Fig. 6b). Considering that the effect of Cl-S interaction is probably small for systems with low S content (Keppler, 2010), the differences may refer to the significantly lower bulk S concentration (~260 ppm) in the starting glass (QFMClA) of the disequilibrium experiments. Thus, it is suggested that the observed $D_S^{fl/m}$ dependence on bulk Cl content at QFM+1.8 is applicable to S-enriched systems containing >260 ppm to ~2600 ppm S and is probably relevant for various redox conditions.

We suggest that the observed dependence can be explained by the negative correlation between Cl and S concentrations found by Webster et al. (2009) in phonolitic and trachytic melts at 200 MPa and 896 to 1022 °C. The authors proposed that the correlation reflects the dependence of S and Cl on their reciprocal solubilities in the studied melt which is in agreement with previous observations in rhyodacitic (Botcharnikov et al., 2004) and phonolitic melts (Webster et al., 2006). Assuming a strong interaction of Cl and S in the fluid and in the melt, Cl is expected to influence $D_S^{fl/m}$ and S is expected to influence $D_{Cl}^{fl/m}$. Webster and Botcharnikov (2011) noted a positive correlation between S content and $D_{Cl}^{fl/m}$ based on recent studies on rhyodacitic to basaltic systems (Botcharnikov et al., 2004;

Webster et al., 2009; Beermann et al., 2011), and estimated a maximum increase of $D_{Cl}^{fl/m}$ by 25 to 30 % if the melt is saturated with an S-bearing phase. Thus, the observed increase of $D_{Cl}^{fl/m}$ with increasing fO_2 (QFM+0.8 to QFM+1.8; Fig. 9a and 9b) may not only refer to variations in fO_2 but also to increasing initial S content (260 ppm at QFM+0.8 and ~2600 ppm at QFM+1.8).

5.4. Implications for volcanic systems

Experimental studies on the distribution of S and Cl between fluid and silicate melt indicate the high potential of the Cl/S ratio in volcanic gases to improve the forecasting of volcanic eruptions (e.g. Botcharnikov et al., 2004; Keppler, 2010). Fig. 13a shows the molar Cl/S ratio in the melt plotted against the molar Cl/S ratio in the fluid phase of all our Cl-bearing experiments in comparison to the results of Botcharnikov et al. (2004) for a rhyodacitic melt (850°C, 200 MPa, ~QFM+0.6) and Zajacz et al. (2012) for andesitic systems (1000°C, 200 MPa, ~QFM+0.1). The positive correlation of $Cl/S_{(fluid)}$ with $Cl/S_{(melt)}$ found by Botcharnikov et al. (2004) for $Cl/S_{(melt)}$ ratios ranging from 13 to 45 in rhyodacitic melts is basically confirmed by our data and also by the results of Zajacz et al. (2012) for lower $Cl/S_{(melt)}$ ratios (~1 to ~16) in andesitic melts. However, the data from this study with $Cl/S_{(melt)}$ ratios < 15 follow a linear trend rather than an exponential one as suggested by Botcharnikov et al. (2004).

Fig. 13b illustrates that K_d values ($K_d = [(Cl/S)_{fluid}/(Cl/S)_{melt}]$) of our samples and of Botcharnikov et al. (2004) are in very good agreement for $Cl/S_{(melt)}$ molar ratios ranging from 0 to 20 with an average K_d of 0.029 ± 0.013, indicating that a linear correlation between $Cl/S_{(fluid)}$ and $Cl/S_{(melt)}$ is applicable to $Cl/S_{(melt)} \leq 20$. The small deviations observed between our data and the data of Zajacz et al. (2012) point to slight compositional effects on the K_d; e.g. the andesite studied by the authors is less evolved than the Krakatau andesite and bulk volatile contents added to the capsules and within the experimental glasses of Zajacz et al. (2012) are significantly higher than in our experiments. The kinetic parameters (r, t_A) have no notable effect on K_d in our study. Hence, the $Cl/S_{(melt)}$ molar ratio can be used to determine the $Cl/S_{(fluid)}$ of a coexisting fluid phase, even if equilibrium between fluid and melt phases is not achieved.
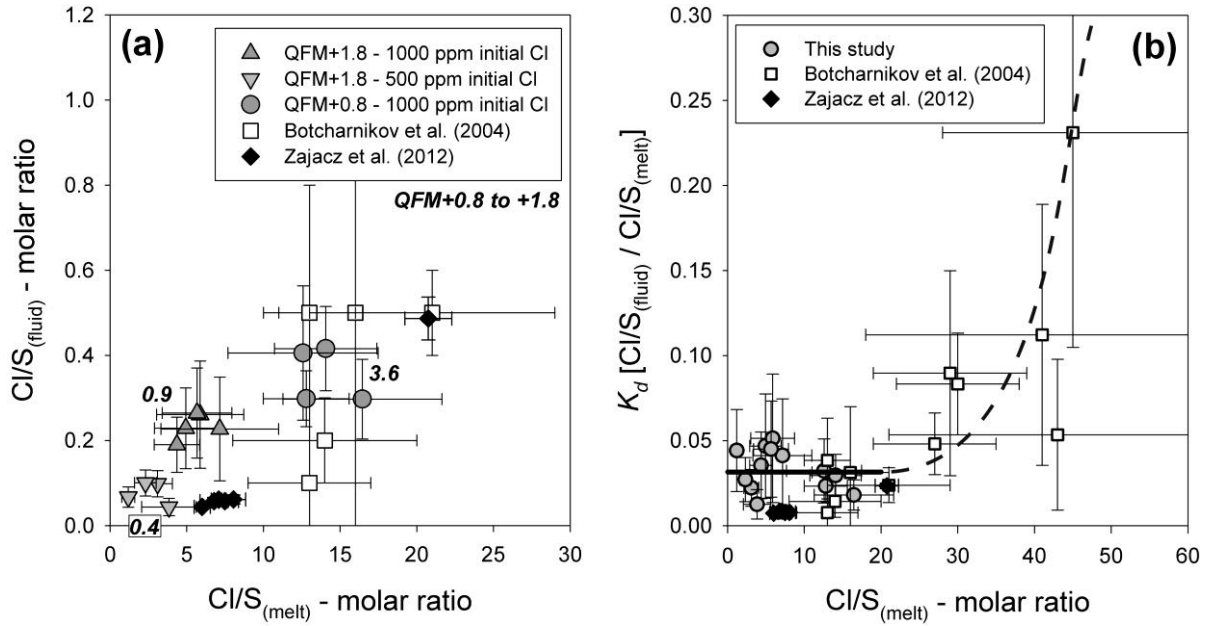
Fig. 13a-b: Evolution of the Cl/S ratio in the fluid and in the melt. **a)** Cl/S$_{(fluid)}$ vs. Cl/S$_{(melt)}$ − molar ratios. **b)** K_d values vs. Cl/S$_{(melt)}$ molar ratio. The **bold** numbers in **a)** correspond to the initial molar Cl/S ratios in the melts of the three experimental series. The *Solid line* represents the average K_d value calculated using the experimental data from this study (Cl/S$_{(melt)}$ ≤ 20). The *Dashed line* indicates the trend for Cl/S$_{(melt)}$ > 20, based on data from Botcharnikov et al. (2004).
This study: Krakatau andesite (70 MPa; 1030°C; log(fO_2/bar): QFM+0.8 or QFM+1.8)
Botcharnikov et al. (2004): Mt. Unzen rhyodacite (850°C; 200 MPa; ~QFM+0.6)
Zajacz et al. (2012): Andesite (1000°C, 200 MPa, ~QFM+0.1).

Based on the results presented in this study the evolution of the S/Cl ratio in a fluid phase upon equilibrium or fractional degassing of an andesitic melt can be modeled. For this purpose, a few assumptions have to be made to allow an estimation of $D_S^{fl/m}$ (fluid-melt equilibrium) and $D*_S^{fl/m}$ values (fluid-melt disequilibrium) for given fO_2.

A main assumption is that the S-Cl fluid-melt distribution can be described by constant K_d values, i.e. Cl/S$_{(melt)}$ ≤ 20 (see above, this Section). Moreover, considering that $D_S^{fl/m}$ = 39 ± 16 at QFM+4.2 in Cl-free systems and that $D_S^{fl/m}$ increases by a factor of ~2.1 if 500 to 1000 ppm Cl is added to the system (Fig. 12), a $D_S^{fl/m}$ of ~81 can be estimated for Cl-bearing oxidized systems (QFM+4.2). Similarly, a $D*_S^{fl/}$ of ~513 is calculated for Cl-bearing oxidized systems using the average $D*_S^{fl/m}$ values of 244 ± 104 determined in Cl-free experiments directly quenched after decompression (fluid-melt disequilibrium). In addition, an average $D_S^{fl/m}$ of 261 ± 40 is determined for Cl-bearing melts at QFM+1.8 using data listed in Table 2.

As a first approximation we assume a simple linear relationship between $\log(fO_2/\text{bar})$ and $D_S^{fl/m}$ in the range of QFM+1.8 to QFM+4.2 (see Fig. 7). Using the two $D_S^{fl/m}$ values for QFM+1.8 (~261) and QFM+4.2 (~81) the following equation for Cl-bearing andesitic systems can be derived by simple linear interpolation (applicable for: ~500 to ~2600 ppm Cl; QFM+1.8 to QFM+4.2):

$$D_S^{fl/m} \approx \text{-}75 \cdot \Delta\text{QFM} + 396 \tag{7}$$

Additionally, the data shown in Fig. 9b (experimental series GYMClA) is used to determine an average $D_{Cl}^{fl/m}$ of 10 ± 3 for andesitic melts containing ~1000 ppm Cl. We assume that this $D_{Cl}^{fl/m}$ is applicable to a wide range of fO_2 (QFM+1.8 to QFM+4.2) in andesitic melts containing initially ~1000 ppm Cl and >300 to ~1600 ppm S. Table 4 lists the $D_S^{fl/m}$ and $D^*{}_S^{fl/m}$ values used for calculating the degassing trends.

The following equations were applied to model the evolution of the S/Cl mass ratio during equilibrium and fractional degassing, respectively (see also Keppler, 2010).

$$c_{fl} = \frac{c_{initial} \cdot D^{fl/m}}{(1-\alpha) + D^{fl/m} \cdot \alpha} \qquad equilibrium\ degassing \tag{8}$$

$$c_{fl} = D^*{}^{fl/m} \cdot c_{initial} \cdot (1-\alpha)^{\left(D^*{}^{fl/m}-1\right)} \qquad fractional\ degassing \tag{9}$$

where c_{fl} is the concentration of S or Cl in the fluid phase (in ppm), $c_{initial}$ is the initial S or Cl content in the melt (in ppm) and α is the mass fraction of fluid released. Here, *equilibrium degassing* describes a degassing scenario in which the fluid released from a magma is in equilibrium with the melt prior to separation, while *fractional degassing* occurs when the fluid released from a magma is separated immediately after release, without fluid-melt equilibration.

Fig. 14a shows the evolution of the S/Cl mass ratio in a magmatic fluid upon *equilibrium degassing* at QFM+1.8, +2.8, and +4.2. The degassing trends indicate that fluids released from magmas at intermediate redox conditions (QFM+1.8) are characterized by very high S/Cl ratios in the first fluid fraction formed upon decompression. By contrast, the first fluid released under oxidizing conditions

(> QFM+2.8) shows significantly lower S/Cl ratios. The data show that a sharp increase in the S/Cl$_{(fluid)}$ mass ratio detected in volcanic gases can be induced by decompression, especially under reducing conditions. In addition, changes in redox conditions in a degassing magma reservoir may also be reflected by significant changes in the S/Cl$_{(fluid)}$ ratio. Such oxidizing or reducing events could be related to intrusions of e.g. a primitive basaltic melt into the magma chamber. Thus, both scenarios may indicate a possible forthcoming eruption. It is emphasized that the application of the model is probably limited to andesitic systems.

The degassing trends plotted in Fig. 14b indicate that S/Cl$_{(fluid)}$ mass ratios in volcanic gases released from a magma upon fast ascent (~*fractional degassing*) can be up to a factor of ~6 higher than those released by slowly ascending magma (~*equilibrium degassing*). Thus, variations detected in the S/Cl$_{(fluid)}$ mass ratio of volcanic gases may also help to distinguish between *equilibrium* and *fractional degassing* (calculation assuming a fast decompression of ~0.1 MPa/s, a log(fO_2/bar) of ~QFM+4.2, and disequilibrium conditions; see Table 4). *Fractional degassing* may be more relevant for magmas with high ascent rates in conduits and, thus, for predicting hazardous explosive eruptions. Fig. 14b shows that dramatic variations of fluid composition should be observed with very small p changes in oxidized systems, if *fractional degassing* occurs and considering that the fluid composition does not change significantly after a degassed fluid fraction of 2%. Furthermore, changes in decompression style may induce distinct variations in S/Cl$_{(fluid)}$, an important finding which is linked to the observed transient exsolution of a large amount of S upon fast decompression from an oxidized andesitic melt; this finding may help to improve monitoring of volcanic activities.

Table 4: $D_S^{fl/m}$ and $D*_S^{fl/m}$ values used for the calculation of degassing trends

ΔQFM	$D_S^{fl/m}$ or $D*_S^{fl/m}$	Degassing process
4.2	81	*near-equilibrium*
2.8	186 (a)	*near-equilibrium*
1.8	261	*near-equilibrium*
4.2	513	*disequilibrium*

Notes: (a) calculated using equation 7
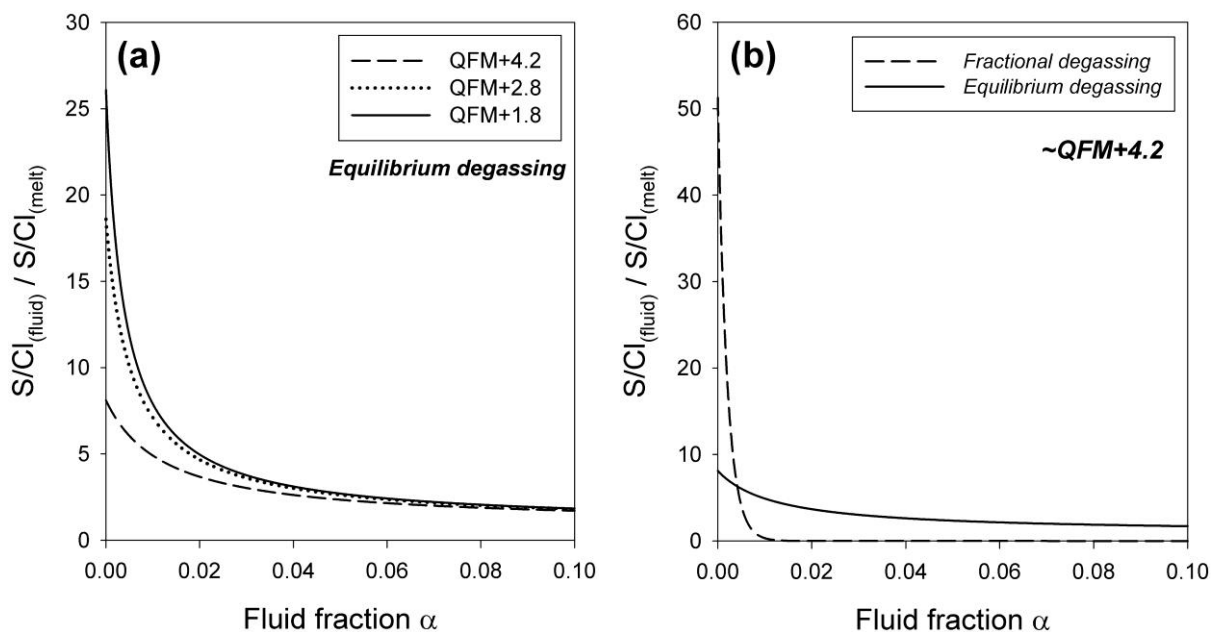
Fig. 14a-b: Modeling of S/Cl mass ratio in a magmatic fluid upon decompression. **a)** Evolution of the fluid phase during *equilibrium degassing* at variable fO_2 (QFM+1.8 to QFM+4.2). **b)** Comparison of *equilibrium* and *fractional degassing* at QFM+4.2.

6. CONCLUSION

The experimental approach applied in this work provides first insights into the partitioning of S and Cl between fluid and melt in a H_2O-S-Cl-bearing andesitic system upon degassing at disequilibrium conditions.

An average $D*_S^{fl/m}$ of 300 was determined for Cl-free andesitic melts decompressed quickly (from ~400 to ~70 MPa; rate: ~0.1 MPa/s) and quenched rapidly after decompression (fluid-melt disequilibrium conditions preserved) under intermediate to oxidizing conditions (~QFM+1.5 to ~QFM+4). Thus, a sharp increase in the relative S concentration may be detected in Cl-free volcanic gases released and extracted from a fast ascending magma (*fractional degassing*). In contrast, at near-equilibrium conditions $D_S^{fl/m}$ decreased with increasing fO_2 from ~150 at QFM+1.5 to ~40 at ~QFM+4. The strong decrease of $D*_S^{fl/m}$ from ~300 to ~40 under oxidizing conditions with further annealing after fast decompression may be related to a transient exsolution of S and the formation of solid S^{6+}-bearing phases within the vapor phase upon decompression. These S-bearing phases are dissolved again with further annealing after decompression leading to an increase of the S

concentration in the melt and, thus, a decrease of $D^*_S{}^{fl/m}$. The formation of such phases upon fast decompression becomes negligible at intermediate to reducing redox conditions.

A ~2-fold increase of $D_S{}^{fl/m}$ was observed if 500 ppm Cl was added to an S-enriched system (>> 300 to ~3000 ppm S). In contrast, the effect of Cl concentration on $D^*_S{}^{fl/m}$ (disequilibrium) seems to be negligible, at least in S-poor systems. Moreover, no influence of t_A or r on $D_{Cl}{}^{fl/m}$ was observed (i.e. $D^*_{Cl}{}^{fl/m} \approx D_{Cl}{}^{fl/m}$).

The observed dependences of the S and Cl fluid-melt distribution at fluid-melt disequilibrium and near-equilibrium on e.g. fO_2 and initial volatile content, respectively, need to be considered for volcanic degassing scenarios. For instance, $D_S{}^{fl/m}$ derived from commonly conducted equilibrium experiments may not be adequate to describe *fractional degassing* S processes. Hence, our results may help to interpret volcanic gas signatures (e.g. HCl/SO$_2$) and may enhance volcanic hazard mitigation.

CHAPTER I-B

BUBBLE FORMATION DURING DECOMPRESSION OF ANDESITIC MELTS

ABSTRACT

Bubble formation in andesitic melts during continuous decompression (from ~400 to ~70 MPa) was investigated experimentally at 1030°C and oxygen fugacities (fO_2) of log(fO_2/bar) = QFM+0.8 or QFM+1.8 (QFM: quartz-fayalite-magnetite buffer). The experiments were conducted in internally heated pressure vessels (IHPV). One set of experiments was carried out at variable decompression rate (r), ranging from 0.0005 to 0.1 MPa/s. These samples were directly quenched after decompression to allow us to investigate the influence of r on bubble formation. A second set of experiments was performed at a constant r of 0.1 MPa/s. These samples were annealed for t_A = 0 to 72 h at final p-T conditions after decompression in order to study changes in vesiculation during magma storage ($\approx$ annealing) at shallow depths (~2 to 3 km) after fast ascent. Back scattered electron (BSE) images of the samples were analyzed to determine bubble number densities (BND).

The BND was found to increase strongly with increasing r, from ~$10^{2.2}$ mm^{-3} at 0.0005 MPa/s to ~$10^{4.5}$ mm^{-3} at 0.1 MPa/s. Moreover, after fast decompression (r ~ 0.1 MPa/s) BND decreased significantly with t_A, from ~$10^{4.5}$ mm^{-3} at t_A = 0 h to ~$10^{2.8}$ mm^{-3} at t_A = 72 h. A comparison of the derived BND values with recently published data (Cichy et al., 2011; Nowak et al., 2011) showed clearly the essential role that decompression style (continuous, multi-step or single step) plays for bubble formation.

The presented results provide important insights on the bubble formation in ascending magmas. The data can help to improve models for the estimation of magma ascent rates via BND values determined e.g. for natural pumices.

Keywords: Bubble formation, bubble number density, andesite, continuous decompression

1. INTRODUCTION

A good knowledge of bubble forming processes in magmatic systems is a pre-requisite to improve our understanding of hazardous, explosive eruptions and pyroclastic flows (see review of Sparks et al., 1994). However, experimental data at geologically relevant conditions in magmatic systems are rare, especially at low r; i.e. r is typically > 0.02 MPa/s for experimental studies (e.g. Cichy et al., 2011; Gondé et al., 2011), while r is often < 0.02 MPa/s in natural systems, depending on eruptive style (e.g. Cashman, 2004). The experimental approach chosen in this study (decompression experiments; see Chapter I-A) results in the formation of bubble-bearing, crystal-free run products. The compiled experiments cover a wide range of r (0.0005 to 0.1 MPa/s) and t_A (0 to 72 h) and, thus, may help to improve our knowledge on (homogeneous) bubble nucleation processes in ascending magmas.

In order to investigate the effect of r and t_A on bubble formation, bubble number densities (BND; i.e. the number of bubbles per volume) were calculated for selected decompression experiments (GYClA, GYMClA, QFMA and QFMClA; see Table 2 of Chapter I-A). The experimental series QFMA and QFMClA (0.0005 to 0.1 MPa/s; 0 h) were chosen to explore the influence of r on BND, while GYClA and GYMClA (0.1 MPa/s; 0 to ~72 h) were selected to evaluate possible changes in vesiculation during annealing after (fast) decompression. The selected experiments are characterized by a similar initial water (H_2O) content of about 6.5 wt%, while the initial sulfur (S) content ranges from ~140 to ~1050 ppm and chlorine (Cl) varies from 0 to 1000 ppm (see Chapter I-A for further details).

2. EXPERIMENTAL PROCEDURE AND ANALYTICAL METHOD

The experimental procedure is described in Chapter I-A, Section 2. Details on the experimental series GYClA, GYMClA, QFMA and QFMClA, chosen for BND studies are listed in Table 2 of Chapter I-A.

2.1 Estimation of bubble number densities (BND)

BSE images of the experimental series GYClA, GYMClA, QFMA and QFMClA (collected by electron microprobe) were analyzed using the public computer program ImageJ (http://rsb.info.nih.gov/ij/) to study bubble formation upon magma degassing. The program allows us

to determine e.g. total area, average size, area fraction as well as width and length of the bubbles. Moreover, the (average) minor and major axis as well as the angle of the ellipsoid fitted to the bubbles are estimated and used for subsequent *BND* estimations. Two BSE images of each experiment were analyzed to determine the *BND* following the method described in Cichy et al. (2011). The images were taken at different magnifications and on different locations of the samples to minimize possible truncation effects (see Section 3.1 and e.g. Armienti, 2008). The image sizes range between ~600 × ~400 µm and ~2500 × ~1850 µm (resolution: ~0.5 to ~2.5 µm/pixel). Noteworthy, BSE images were chosen for *BND* analyses because a higher contrast between bubbles and melt can be achieved when compared, for instance, to reflected-light microscopic images.

The geometric information derived from ImageJ analyses was used to estimate the *BND* of the selected samples following the method of Noguchi et al. (2008); see also Cichy et al. (2011) and Nowak et al. (2011). However, the performed ImageJ analyses provide only 2D information about the bubble distribution. Hence, the estimation of the *BND* involves as a final step the 3D correction using the CSD-Corrections 1.4 software (http://depcom.uqac.ca/~mhiggins/csdcorrections.html). For the correction, the roundness factor calculated by ImageJ (ranging from 0.6 to 0.9) was applied and the aspect ratio was set to 1 - 1.1 - 1.2 (short axis - intermediate axis - long axis). The methods used in CSD-Corrections 1.4 are described in Higgins (2000, 2002) as well as in Higgins and Chandrasekharam (2007). *BND* values were estimated with both, bubbles at the edges of the image excluded and included.

3. RESULTS AND DISCUSSION

Fig. 1 shows a typical microscopic image of a partially degassed andesitic glass (GYClA-3) under plane polarized light. The size of the bubbles range from a few microns up to ~80 µm, a typical feature of fast decompressed (~0.1 MPa/s) samples with 0 to ~2 h annealing at final conditions.

Comparison of BSE images indicate that the amount of bubbles decreases while the size of bubbles increases with decreasing r from 0.1 to 0.0005 MPa/s (e.g. QFMClA series; Fig. 2). A comparable trend is observed with increasing t_A after fast decompression (~0.1 MPa/s; e.g. GYMClA). The bubbles appear often elongated and show a preferred orientation (flow structures) − especially in

experiments with low r (< 0.02 MPa/s) and/or long term annealing after decompression (t_A > 5 h) – indicating that convection may occur during the experimental runs. Noteworthy, no significant influence of the S and the Cl content in the system, ranging ~140 to ~1000 ppm S and from 0 to ~1000 ppm Cl, on bubble formation was detected (see Fig. 3).
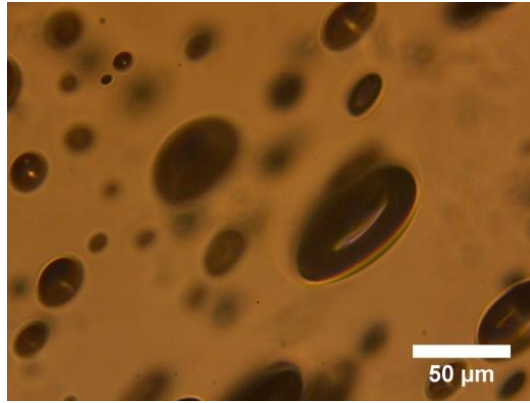
Fig. 1: Microscopic images of sample GYClA-3 (r ~ 0.1 MPa/s; t_A = 5 h). Bubble sizes range from about ~5 to ~80 µm in diameter.

3.1 Accuracy of the BND estimation

As mentioned previously, the method applied for the estimation of *BND* values may result in truncation effects which can affect *BND* values significantly (e.g. Armienti, 2008). Such truncation effects either arise from the resolution of the BSE image (left-hand truncation) or from the image size (right-hand truncation).

In case of left-hand truncation the number of bubbles with a size close to resolution limit is reduced. However, the resolution of the BSE images used in this study was found to be sufficient to detect bubbles with a diameter of ≥ 1 µm and microscopic investigations indicate that the amount of bubbles with a diameter < 1 µm is negligible. Thus, a reduction of the number density of the smallest bubbles is unlikely, i.e. left-hand truncation can be ruled out.

Right-hand truncation effects occur when the largest bubbles in the sample are excluded or are underrepresented in the analyzed area of the sample. This would result in a flattening of the size distribution on nearly horizontal trends at large size ranges, however, such trends were not observed; i.e. right-hand truncation is unlikely (see Fig. I-C.1 in the Appendix I for bubble size distribution plots of selected samples).

The *BND* values derived from the analyses of the same image but with bubbles at the edges of the image excluded or included differ by less than 0.12 log units. The *BND* values obtained from the two images of one sample differ typically by < 0.8 log units, indicating a quite homogeneous distribution of the bubbles within the samples. The mean of all four analyses (2 images; bubbles at the edges included or excluded) are listed in Table 1 and used for interpretation and discussion in the following sections.
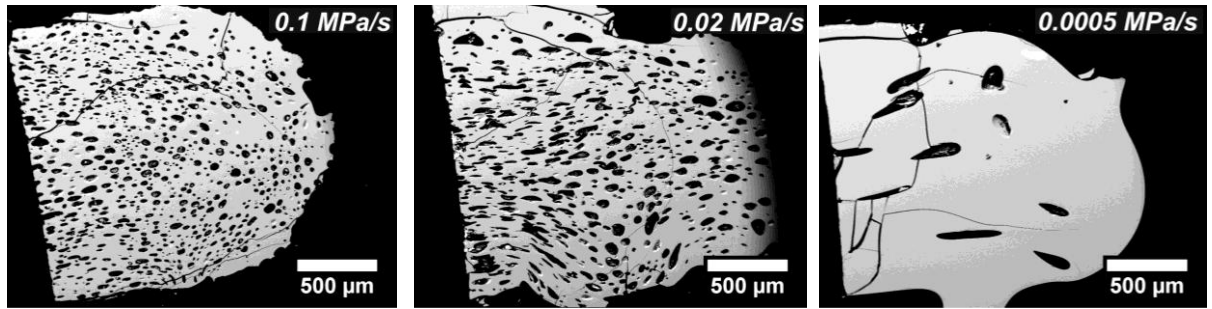
Fig. 2: BSE images of QFMClA-1 (*left*), QFMClA-3 (*center*) and QFMClA-5 (*right*). Values for *r* are displayed in the upper right corner of each image. Decreasing *r* leads to a decreasing number of bubbles and an increasing size of bubbles. Some bubbles are elongated and show a preferred orientation (flow structures).

Table 1: Bubble number densities (*BND*).

Sample ID	log ($BND \times$ mm^3) (a)	r [MPa/s]	t_A [h]	Sample ID	log ($BND \times$ mm^3) (a)	r [MPa/s]	t_A [h]
GYClA-1	4.82 ± 0.31	0.10	-	QFMA-1	4.54 ± 0.38	0.10	-
GYClA-2	4.65 ± 0.31	0.10	1.10	QFMA-2	4.49 ± 0.21	0.05	-
GYClA-3	3.91 ± 0.53	0.10	5.00	QFMA-3	4.39 ± 0.13	0.02	-
GYClA-4	3.03 ± 0.40	0.10	72.06	QFMA-4	4.23 ± 0.43	0.01	-
GYClA-5	4.92 ± 0.43	0.10	1.05	QFMA-5	2.10 ± 0.40	0.0005	-
GYMClA-1	4.40 ± 0.58	0.10	-	QFMClA-1	4.22 ± 0.44	0.10	-
GYMClA-3	3.12 ± 0.16	0.10	5.00	QFMClA-2	4.34 ± 0.26	0.05	-
GYMClA-4	2.47 ± 0.40	0.10	72.06	QFMClA-3	4.32 ± 0.53	0.02	-
GYMClA-5	3.69 ± 0.14	0.10	1.05	QFMClA-4	3.52 ± 0.22	0.01	-
				QFMClA-5	2.32 ± 0.68	0.0005	-

Notes: (a): logarithmized *BND* values [mm^3]; provided error: standard deviation (1 sigma) of the four analyses performed (2 BSE images; bubbles at the edges included/exclude; see Section 2.1); - : $t_A = 0$ h

3.2 Influence of r on BND

The *BND* data of experiments with varying *r* and constant $t_A = 0$ h is shown in Fig. 3a and is compared with experimental results of Cichy et al. (2011). The authors investigated the vesiculation during decompression (from 300 to 50 MPa) in a partly crystallized rhyodacitic system at 850°C and *r* ranging from 0.0002 to 20 MPa/s. It is emphasized, that the differences in *T* should have an insignificant effect on *BND* at given *r* (Hamada et al., 2010). For the samples of the experimental series QFMA and QFMClA (this study) a roughly linear increase of log(*BND* × mm^3) with log(*r* × s/MPa) is observed (Fig. 3a; *BND* values given in Table 1). In contrast, Cichy et al. (2011) observed a minimum of log(*BND* × mm^3) at $r \approx 0.02$ MPa/s. Noteworthy, the experiments of Cichy et al. (2011) were conducted to investigate decompression-induced degassing and crystallization and all experiments contain significant amounts of crystalline phases (including Fe-Ti microlites). According to Hurwitz and Navon (1994), microlites (especially Fe-Ti oxides) are important bubble nucleation sites and, thus, may also explain the trend observed by Cichy et al. (2011); i.e. heterogeneous bubble nucleation processes are studied by Cichy et al. (2011), while homogeneous nucleation is assumed for our experiments. However, the microlite number densities (*MND*) determined by Cichy et al. (2011) for their experiments do not show any clear dependence on *r* (*MND* $\approx 10^{5.5}$ mm^{-3} in the range of 0.0002 MPa/s to 20 MPa/s), making this explanation rather unlikely. On the other hand, Cichy et al. (2011) applied a multi-step decompression technique to conduct experiments with $r \leq 0.01$ MPa/s. Nowak et al. (2011) revealed a significant influence of decompression style on *BND* for rhyodacitic melt at 1050°C. The authors show that the multi-step decompression technique leads to *BND* values which are more than one log unit higher than those obtained for continuous decompression. Thus, the presented data is in agreement with the observations of Nowak et al. (2011) and the non-linear trend found by Cichy et al. (2011) can probably be assigned to variations in decompression style.
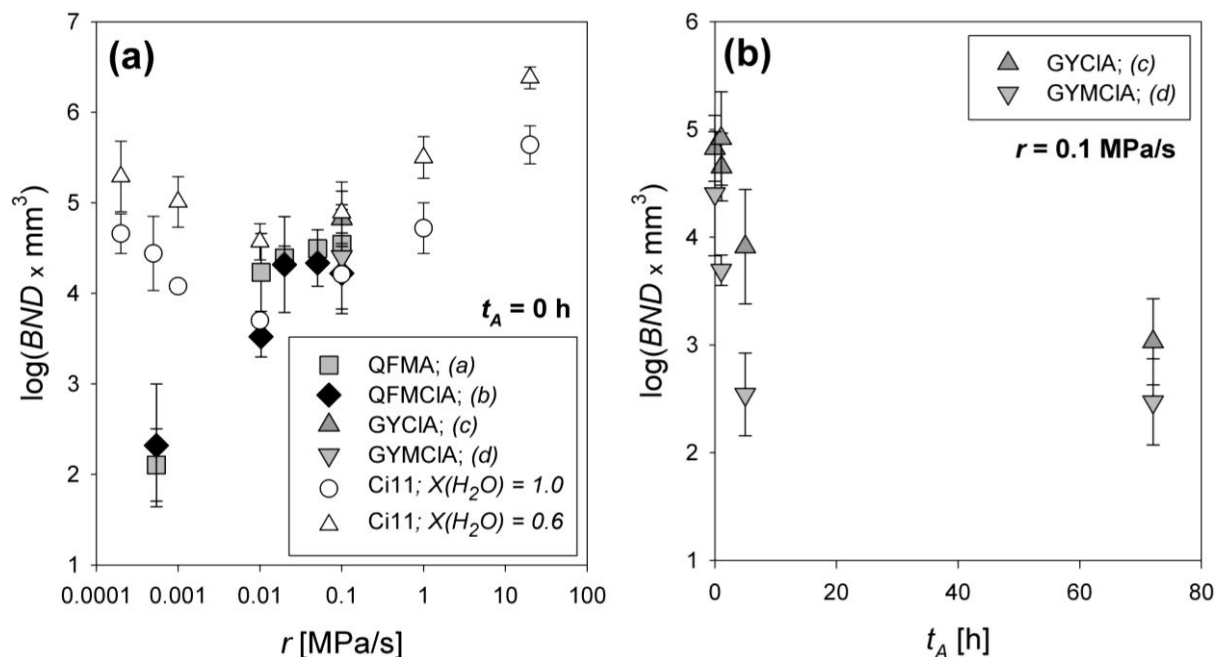
Fig. 3a-b: Bubble formation. **a)** log($BND \times$ mm^3) vs. *r* (*logarithmic scaling*). Samples of the experimental series QFMA, QFMClA, GYClA and GYMClA which have been directly quenched after decompression ($t_A = 0$ h) are plotted together with the results of Cichy et al. (2011; Ci11) on rhyodacitic melt compositions (experiments of Cichy et al. (2011) with $r \geq 0.1$ MPa/s were conducted with continuous decompression technique, while those $r \leq 0.01$ MPa/s are carried out using a multi-step approach). **b)** log($BND \times$ mm^3) vs. t_A at constant $r = 0.1$ MPa/s (experimental series: GYClA and GYMClA).
Horizontal error bars are smaller than symbol size. *(a)*: QFMA experiments: ~140 ppm initial S, Cl-free, ~QFM+0.8; *(b)* QFMClA: ~240 ppm initial S, ~1000 ppm initial Cl, ~QFM+0.8; *(c)* GYClA: ~1000 ppm initial S, ~1000 ppm initial Cl, ~QFM+1.8; *(d)* GYMClA: ~1000 ppm initial S, 500 ppm initial Cl, ~QFM+1.8.

3.3 Influence of t_A on BND

The influence of t_A on *BND* was studied at QFM+1.8 (experimental series GYClA and GYMClA; *BND* values listed in Table 1) and at a constant *r* of ~0.1 MPa/s. Fig. 3b indicates that log($BND \times$ mm^3) decreases significantly within the first ~5 h of annealing. Further annealing after decompression has a minor effect on *BND*; i.e. *BND* values obtained from one experimental series for $t_A = 5$ h and for $t_A = 72$ h, respectively, are identical within error. The observed sharp decrease of log($BND \times$ mm^3) with increasing t_A at QFM+1.8 (see Fig. 3b) is probably linked to the very fast decompression ($r \sim 0.1$ MPa/s). It is assumed that a fast decompression of the andesitic melt leads to a high supersaturation pressure Δp, thus, the gas (H$_2$O-S±Cl) pressure in the melt is significantly larger than the ambient *p* in the vessel (Sparks et al., 1994). Furthermore, as a consequence of the high Δp, the critical radius size of the bubble nucleus/embryo is lowered, leading to the domination of bubble nucleation over bubble growth and/or coalescence upon decompression. The resulting significant

decrease of the *BND* by about 1 log unit within the first few hours of annealing indicates that coalescence and/or bubble growth become more important than nucleation. For distinguishing between bubble growth and coalescence upon further annealing, a closer look at the fluid concentrations in the melt may be useful. In fact, H_2O (determined by FTIR spectroscopy) and Cl (determined by EMP analyses) contents of the partially decompressed andesitic melts remain almost constant during further annealing at final conditions. The slight variations in H_2O (3.56 to 3.84 wt%; except GYMClA-4: 1.98 wt%) and Cl (420 to 470 ppm for GYMClA series; 730 to 890 ppm for GYClA series) concentration in the melt are independent of t_A. By contrast, minor amounts of S are still released from the melt to the fluid phase with further annealing (e.g. GYClA series: S_{melt} decreases from ~180 ppm to 90 ppm upon annealing). Nevertheless, most of the volatiles are exsolved upon decompression. Thus, it is supposed that coalescence dominates over bubble growth upon further annealing at final conditions. However, Lautze et al. (2011) noted that diffusive coarsening, also known as Ostwald ripening, should be the dominant mechanism leading to a decreasing *BND* with increasing t_A. Hence, in addition to volatile diffusion, other processes (e.g. convection fluxes), may influence the bubble formation in the decompression experiments of this study.

4. IMPLICATIONS TO NATURAL SYSTEMS

Toramaru (2006) developed a method which allows one to estimate *r* based on *BND* data of natural pumices. The new data is used in combination with the results of Cichy et al. (2011) to test the model. The following equation, based on the numerical simulations of Toramaru (2006) and provided by Hamada et al. (2010), was applied to estimate the *BND* for a diffusion-controlled (andesitic) system and 6.5 wt% initial H_2O content in the melt (similar to the initial H_2O contents of the experiments investigated in this Chapter; see Table 2 in Chapter I-A):

$$BND \approx 34 \cdot C_{SAT} \cdot \left(\frac{16 \cdot \pi \cdot \sigma_{LB}^3}{3 \cdot k \cdot T \cdot P_{SAT}^2}\right)^{-2} \cdot \left(\frac{\Omega_L \cdot P_{SAT}}{k \cdot T}\right)^{-\frac{1}{4}} \cdot \left(\frac{P_{SAT}^2 \cdot k \cdot T \cdot C_{SAT} \cdot D_{H2O}}{4 \cdot \sigma_{LB}^2 \cdot r}\right)^{-\frac{3}{2}} \tag{1}$$

where C_{SAT} is the H$_2$O content at the saturation pressure expressed as the number of H$_2$O-molecules per unit volume of liquid, σ_{LB} is the surface tension of the bubble-liquid interface in N/m, k is the Boltzmann constant (1.38×10^{-23} J/K), T the temperature in K, P_{SAT} is the H$_2$O saturation pressure in Pa, Ω_L is the molecular volume of H$_2$O in the liquid (fixed to 3×10^{-29} m^3), D_{H2O} is the H$_2$O diffusivity in the melt in m^2/s and r is the decompression rate in Pa/s.

The value for σ_{LB} is estimated using equation 6 in Bagdassarov et al. (2000) as well as the relationship provided by the authors for the influence of H$_2$O solubility on σ_{LB}. In a first approximation, P_{SAT} is assumed to be the p at which a H$_2$O activity $a(H_2O)$ of ~1 is reached in the andesitic system upon decompression. Thus, P_{SAT} strongly depends on the initial H$_2$O content in the melt (here: 6.5 wt%). Assuming that the S and Cl contents in the andesitic system are too low to affect $a(H_2O)$ to a significant extend, P_{SAT} is estimated to be 3.23×10^8 Pa at 1030°C and an initial H$_2$O content in the melt of 6.5 wt% using the model of Burnham (1979). Subsequently, C_{SAT} at $P_{SAT} = 3.23\times10^8$ Pa was calculated to be 4.82×10^{27} m^{-3} for an initial H$_2$O content of 6.5 wt%, using the model of Ochs and Lange (1999) to estimate the density of the melt (ρ_{melt}) at 70 MPa and 1030°C ($\rho_{melt} = 2.217$ g/cm^3). Furthermore, the relationship provided by Behrens et al. (2004) for the estimation of the H$_2$O diffusivity in dacitic melts as a function of T and H$_2$O content in the melt is used to calculate D_{H2O}. Assuming an initial H$_2$O content in the melt of 6.5 wt% (prior to decompression) and a final H$_2$O content of 3.6 wt% (after decompression; see also Chapter I-A, Section 5.2.1), D_{H2O} is estimated to decrease from 2.03×10^{-11} m^2/s to 1.12×10^{-11} m^2/s during decompression. The average value of 1.58×10^{-11} m^2/s was used for the *BND* calculations.

D_{H2O} was also estimated using the relationship for andesitic systems provided by Behrens et al. (2004) and the general model developed by Zhang and Ni (2010), which uses the cation mole fractions of Si, Al, Na and K in the melt and is applicable to a wide range of melt compositions (equation 26 in Zhang and Ni, 2010). These two H$_2$O diffusivity models yield ~2.5 to ~4.8 times higher D_{H2O} values when compared to the H$_2$O diffusivity model of Behrens et al. (2004) for dacitic melts and the higher D_{H2O} would result in ~0.6 to ~0.8 log units lower *BND* values at given r. However, the equation of Behrens et al. (2004) for dacitic melts was chosen for further calculations because of the similar melt composition in comparison to the Krakatau andesite.

Fig. 4 shows clearly that $\log(BND \times \text{mm}^3)$ of experiments quenched directly after continuous decompression [this study and Cichy et al. (2011)] increases linearly with $\log(r \times \text{s/MPa})$, in accordance with the trend predicted by the Toramaru (2006) model. However, the slopes differ significantly. The most apparent explanation for the observed discrepancies is that convection fluxes (which are not considered by the Toramaru (2006) model) within the capsule are influencing the vesiculation processes. In fact, microscopic investigation as well as the collected BSE images indicate that convection processes probably play a minor role for samples decompressed at $r \geq 0.05$ MPa/s (i.e. flow structures are rare) but may become important at lower r (i.e. flow structures are commonly observed; see Fig. 2 and Section 3). Considering that convection processes are to be expected within a magma chamber and along a conduit during magma ascent (e.g. Shaw, 1965; Turner and Campbell, 1986; Witham, 2011), the presented result indicate that the effect of convection on *BND* certainly needs to be considered when modeling bubble nucleation for natural systems.
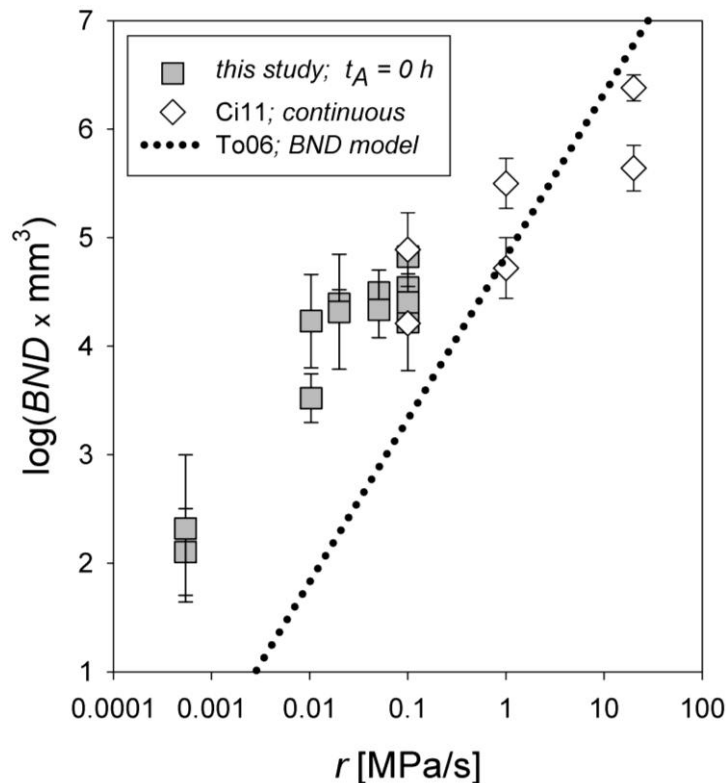
Fig.4: Experimental results of this study and of Cichy et al. (2011) are compared with the trend predicted by the model of Toramaru (2006).
Ci11: Continuous decompression experiments of Cichy et al. (2011);
To06: Calculated using the model of Toramaru (2006).
Horizontal error bars are smaller than symbol size.

Furthermore, experiments annealed for ≥ 5 h after fast decompression ($r \sim 0.1$ MPa/s) show ≥ 1 log unit lower *BND* values (see Fig. 4, Section 3.3) than those quenched directly after fast decompression. This indicates that a good knowledge about possible storage times during magma ascent is required to allow an accurate estimation of *r* on basis of natural pumice samples. Hence, a larger experimental dataset is needed to calibrate the Toramaru (2006) model and to include the influence of storage time at certain depth(s) on bubble formation in an ascending magma.

5. CONCLUSION

The presented results on bubble formation upon magma decompression clearly show the high importance of decompression style on *BND* and, thus, confirm the observations of Nowak et al (2011) based on preliminary decompression experiments. The observed differences between continuous and multi-step decompression may arise from a high Δp induced by instantaneous *p* drops of 50 MPa during multi-step decompression experiment and leading to a predomination of bubble nucleation (Nowak et al., 2011). In respect to continuous decompression, as stated by Nowak et al. (2011), nucleation may require a certain Δp and bubble growth will dominate over nucleation processes upon further decompression caused by favorable energetics (e.g. review of Sparks et al., 1994; Nowak et al., 2011). Nevertheless, the increase of $\log(BND \times \text{mm}^3)$ with decreasing multi-step decompression rate at $r < 0.01$ MPa/s observed by Cichy et al. (2011) needs to be clarified by further investigation, e.g. the large number of crystals present in the rhyodacitic melts of Cichy et al. (2011), leading to heterogeneous bubble nucleation, could also explain the discrepancies.

Furthermore, the data indicates a strong influence of t_A after decompression on *BND*, i.e. even short storage times interrupting magma ascent for a few hours, may affect *BND* significantly. This knowledge is important for the interpretation of natural (pumice) samples derived, for instance, from explosive Plinian eruptions.

CHAPTER II

SULFUR ISOTOPE FRACTIONATION BETWEEN FLUID AND ANDESITIC MELT

ABSTRACT

Decompression experiments were conducted to investigate the fractionation of sulfur isotopes between fluid and melt upon magma degassing. Synthetic glasses with a composition close to that of Krakatau andesite were used as starting material. The starting glasses contained 4.55 to 7.95 wt% H_2O, ~140 to 2700 ppm sulfur (S), and 0 to 1000 ppm chlorine (Cl). The experiments were carried out in internally heated pressure vessels (IHPV) at 1030°C and oxygen fugacities (fO_2) ranging from QFM+0.8 log units up to QFM+4.2 log units (QFM: quartz-fayalite-magnetite buffer). The decompression experiments were conducted by releasing pressure (p) continuously from ~400 MPa to final p of 150, 100, 70 and 30 MPa. The decompression rate (r) ranged from 0.01 to 0.17 MPa/s. The samples were annealed for 0 to 72 h (annealing time, t_A) at the final p and quenched rapidly from 1030°C to room temperature (T).

The decompression led to the formation of a S-bearing aqueous fluid phase due to the relatively large fluid-melt partitioning coefficients of S. Secondary ion mass spectrometry (SIMS) was used to determine the isotopic composition of the glasses before and after decompression. Mass balance calculations were applied to estimate the gas-melt isotopic fractionation factor α_{g-m}.

The SIMS analyses indicated no detectable effect of r and t_A on α_{g-m}. However, SIMS data revealed a remarkable increase of α_{g-m} from ~0.9985 ± 0.0007 at >QFM+3 to ~1.0042 ± 0.0042 at ~QFM+1. Noteworthy, the isotopic fractionation at reducing conditions was about an order of magnitude larger than predicted by previous works. Based on our experimental results and on existing models for S-speciation in fluid and silicate melt a new model predicting the effect of fO_2 on α_{g-m} (or $\Delta^{34}S_{g-m}$) in andesitic systems at 1030°C is proposed. Our experimental results as well as our modeling provide essential knowledge for the interpretation of S-isotope signatures in natural samples (e.g. melt inclusions or volcanic gases).

CHAPTER II

1. INTRODUCTION

Sulfur is a major volatile in volcanic systems and large amounts are released from magmas as a fluid phase upon decompression. Thus, a good knowledge of the behavior of S and S-isotopes during degassing as well as during magma-fluid interactions is required to improve our understanding of volcanic processes and e.g. help monitoring and forecasting of volcanic eruptions. Sulfur is a polyvalent element and can be dissolved as S^{2-} and S^{6+} in silicate melts (e.g. Jugo et al., 2010; Metrich and Mandeville, 2010; Wilke et al., 2011), while the most relevant species in a fluid phase at magmatic conditions are SO_2 and H_2S (e.g. Katsura and Nagashima, 1974; Gerlach and Nordlie, 1975; Moretti et al., 2003). Sulfur has four naturally occurring stable isotopes: ^{32}S (natural abundance: 95.04%), ^{34}S (4.20%), ^{33}S (0.75%), ^{36}S (0.01%); de Laeter et al. (2003). While considerable progress has been made in the past decades on the characterization of the partitioning of S between fluid and silicate melt at geologically relevant conditions (high p and T) and under fluid-melt equilibrium conditions (e.g. Keppler, 1999, 2010; Webster and Botcharnikov, 2011; Zajacz et al., 2012) as well as on the kinetics of S degassing (Chapter I-A), experimental data on fluid-melt S-isotope fractionation is scarce.

S-isotope fractionation between a silicate melt and a coexisting fluid phase depends on T and on the speciation of S in both phases (e.g. Mandeville et al., 2009; Mandeville, 2010). Ohmoto and Rye (1979) revealed the order $SO_4^{2-} > SO_3 > SO_2 > S^0 > H_2S > S^{2-}$ for the retention of ^{34}S in a S-bearing compound; i.e. release of S to a fluid phase from a melt where SO_4^{2-} predominates as dissolved S enriches the melt in ^{34}S because of the greater tendency of oxidized S compounds to retain ^{34}S. Hence, the magnitude of S isotope fractionation is strongly controlled by the redox conditions in the system (e.g. Mandeville, 2010). At oxidizing conditions the degassing of S upon decompression is dominated by SO_4^{2-} species in the melt and SO_2 in the fluid, while under reducing conditions the prevailing species are S^{2-} in the melt and H_2S in the fluid (e.g. Nagashima and Katsura, 1973; Carroll and Rutherford, 1988; Burgisser and Scaillet, 2007; Jugo et al., 2010). Thus, S-isotope composition in the melt will progressively become heavier with S-degassing at oxidizing conditions and become lighter at reducing conditions. In theory, S-isotope fractionation is approximately proportional to the relative

mass difference of the considered S-isotope pairs (e. g. ~2 amu difference between ^{34}S and ^{32}S) and proportional to $1/T^2$ (T in K, Mandeville, 2010).

The application of S-isotope to the understanding of high T magmatic processes has, with a few exceptions, remained stagnant for the past three decades. Fundamental experimental and theoretical studies or compilation by Richet et al. (1977), Sasaki et al. (1979), Ohmoto and Rye (1979), Ohmoto and Lasaga (1982), Sakai et al.(1982), Allard (1983), Ueda and Sakai (1984), Miyoshi et al. (1984) and Taylor (1986) provide the only relevant data so far. The only existing experimental study conducted at magmatic T (800 to 1000°C), investigating the fractionation pairs SO_4^{2-} - S^{2-} and SO_4^{2} - H_2S, was performed using molten salt (e.g. Na_2SO_4 and Na_2S; Miyoshi et al., 1984). The T dependence for the fluid-melt fractionation of S-isotope has been summarized by Taylor (1986) and the equations provided in this study were used by de Hoog et al. (2001) to develop a model for S-isotope fractionation between fluid and melt. However, this model has not been tested experimentally at geologically relevant conditions and remains questionable. The absence of experimental calibration is related to the difficulties to determine quantitatively the S-isotopic composition in silicate glasses. However, recent advances in the micro-analytical measurement of S-isotopes in silicate glasses using SIMS allow us to analyze the S-isotope composition in silicate glasses with S content of a few hundreds of ppm and with a precision of ~0.5 ‰ (Mandeville et al., 2008). Thus, it is now technically possible to determine isotope fractionation factors based on experimental samples carried out under magmatic conditions.

The present study is focused on the experimental investigation of S-isotopes fractionation between fluid and silicate melt. Considering that fluid phases in magmatic systems are generated upon magma ascent (degassing), decompression experiments were conducted to simulate natural case studies. Based on our experimental results and on existing models for S-speciation in fluid and silicate melt a model predicting the isotopic distribution of S between andesitic melts and coexisting fluids is proposed.

2. EXPERIMENTAL PROCEDURE

Selected S-bearing glasses obtained from decompression experiments conducted by Fiege (Chapter I-A) were used in this study. The isothermal decompression experiments were carried out at constant T (1030 ± 10°C) and variable fO_2 (QFM+0.8 to QFM+4.2) in IHPV and the applied experimental approach is described in detail Chapter I-A.

The experimental strategy involves three steps: In the *first step* synthetic anhydrous glasses with an andesitic composition close to the Krakatau andesite (Table 1) were prepared by melting a mixture of oxide and carbonate powders at 1600°C and 1 atm. In the *second step* ten volatile-bearing (H_2O, S, Cl) glasses were synthesized at high p (~500 MPa) and at 1030°C under fluid-undersaturated conditions in IHPV. These starting glasses were bubble-free and contained different amounts of H_2O (4.55 to 7.95 wt%) and S (260 to 2700 ppm, see Table 2). Three glasses contained also Cl (0.05 and 0.1 wt% Cl; Table 2). The isotopic composition of the starting glasses covers a wide range from $\delta^{34}S \approx$ -32 ‰ to about +23 ‰. The different $\delta^{34}S$ were obtained by adding different S sources, either with known (IAEA standards: synthetic barite; see below) or with unknown S-isotope composition (natural anhydrite, natural pyrrhotite or synthetic gypsum). The starting glasses GYClA, GYMClA and RED contained some S-bearing globules after the first high p annealing. Hence, a portion of these materials was re-melted to dissolve the globules and improve homogeneity (see Chapter I-A for details concerning the re-melting procedure). In the *third step,* the volatile-bearing glasses were heated at 1030 °C ± 10°C and isothermal decompression experiments were conducted in IHPV by releasing p continuously from 400, 450 or 500 MPa to lower p (150 to 30 MPa) with different r ranging from ~0.02 to ~0.2 MPa/s. After decompression, the samples were either rapidly quenched to preserve eventually non-equilibrium conditions or annealed for various times (t_A = 1 to 72 h) at the final p-T conditions before quenching. The annealing at 1030°C after decompression was performed to approach near-equilibrium conditions between melt and fluid.

The nominal fO_2 prevailing in each experiment was either *i)* determined using the *Shaw*-membrane technique (e.g. Berndt et al., 2002; and references therein) or *ii)* estimated based on the known intrinsic redox conditions in the IHPV (Berndt et al., 2002; Wilke et al., 2002; Schuessler et al., 2008).

Table 1: Composition of the anhydrous andesitic starting glass determined by electron microprobe or FTIR spectroscopy (H_2O).

[wt%]	SiO_2	TiO_2	Al_2O_3	FeO	MnO	MgO	CaO	Na_2O	K_2O	H_2O	SO_3	Cl	Total
Anhydrous	64.79	1.28	15.62	4.94	0.23	1.40	4.92	3.92	1.80	-	-	-	98.91
andesite	*0.59*	*0.07*	*0.22*	*0.33*	*0.04*	*0.06*	*0.20*	*0.25*	*0.07*	-	-	-	*0.78*

Notes: Error in *italic*:1 σ standard deviations based on microprobe analysis; number of EMP analyses: 20

3. ANALYTICAL APPROACH

3.1 Determination of major element and volatile concentrations in glasses

The starting materials and the glasses of the decompression experiments were already characterized in a previous study aimed at investigating the distribution of volatiles in fluid and melt during decompression and subsequent annealing at final *p-T* conditions (Chapter I-A). Details on the analytical techniques (electron microprobe and near infra-red spectroscopy) can be found in the Appendix II-A and II-B.

3.2 SIMS, data processing and determination of the fluid-melt isotopic fractionation of S

The S-isotope composition ($\delta^{34}S$; see below for details on the delta notation) of the andesitic glasses was determined by *in situ* SIMS using the Cameca IMS 1280 of the Northeast National Ion Microprobe Facility (NENIMF) at Woods Hole Oceanographic Institution (WHOI). The measurements were conducted using a Cs+ primary beam with 10 μm in diameter, 10 kV accelerating voltage and 1-2 nA beam current. The secondary ions are collected at 10 kV accelerating voltage, 150 μm field of view and a mass resolution power (MRP) of 5500. The energy slit is centered and opened to 40-60 V. This method of high precision *in situ* SIMS analysis of S isotopes in glasses down to a few hundreds of ppm bulk S has been established recently at WHOI (Mandeville et al., 2008). Mandeville et al. (2008) demonstrated that by operating the Cameca IMS 1280 at mass resolving power of 5500 ($M/\Delta M$), it is possible to avoid interferences from $^{29}Si^1H$ and $^{31}P^1H$ with ^{30}Si and ^{32}S in glass. The authors have shown that *in situ* $\delta^{34}S$ measurements (15×15 micron area) with a precision of ±0.4 to 0.6 ‰ can be conducted in silicate glasses containing about 500 to 1600 ppm S.

Table 2. Experimental results. All syntheses and experiments were conducted in IHPVs at 1030 ± 10 °C.

Sample ID	p_S [MPa]	t_I [min]	r [MPa/s]	p_E [MPa]	t_A [min]	ΔQFM	$S^{6+}/\Sigma S$	H_2O [wt%]	Cl [wt%]	S [ppm]	%S degass.	$\delta^{34}S_{melt}$ [‰]	$\delta^{34}S_{fluid}$ [‰]	α_{g-m}	n (SIMS)	Comments B
AH	500	xx	xx	500	o. n.	3.7 (a)	nd	6.61 ± 0.03	xx	1266 ± 140	xx	20.03 ± 2.11	xx	xx	5	xx
AH-3	500	60	0.16	71	1083	4.2 (a)	>0.80	3.56 ± 0.05	xx	720 ± 236	43 ± 5	22.38 ± 0.85	16.93	0.9946	6	xx
AH-4	500	60	0.17	71	d. r. q.	4.2 (a)	nd	3.97 ± 0.29	xx	130 ± 50	90 ± 14	23.03 ± 2.27	19.69	0.9967	5	NQ
GYC	500	xx	xx	500	o. n.	3.7 (a)	1.03	6.50 ± 0.37	xx	1376 ± 60	xx	0.94 ± 0.93	xx	xx	5	xx
GYC-1	505	40	0.09	65	60	4.2 (a)	>0.74	2.49 ± 0.07	xx	380 ± 85	72 ± 4	2.42 ± 1.66	0.37	0.9980	3	xx
GYC-2	505	5	0.16	71	d. r. q.	4.2 (a)	nd	3.64 ± 0.07	xx	375 ± 100	73 ± 5	1.75 ± 0.75	0.63	0.9989	5	xx
GYC-3	402	5	0.05	70	d. r. q.	4.2 (a)	nd	3.34 ± 0.07	xx	636 ± 116	54 ± 2	1.76 ± 0.67	0.22	0.9985	3	xx
AH-C	450	xx	xx	450	o. n.	3.9 (a)	0.98	7.95 ± 0.48	xx	2703 ± 65	xx	23.21 ± 0.27	xx	xx	5	xx
AHC-1	450	40	0.08	71	120	4.2 (a)	>0.89	3.58 ± 0.05	xx	916 ± 50	66 ± 1	24.27 ± 0.64	22.67	0.9984	3	xx
AHC-3	414	40	0.08	73	900	1.2 (b)	>0.52	3.60 ± 0.06	xx	315 ± 80	88 ± 6	22.84 ± 0.56	23.26	1.0004	3	xx
AHC-4	403	5	0.02	71	d. r. q.	4.2 (a)	nd	3.60 ± 0.08	xx	1190 ± 27	56 ± 1	23.72 ± 2.09	22.82	0.9991	5	xx
SD1	502	xx	xx	502	o. n.	3.6 (a)	>0.85	5.79 ± 0.48	xx	1223 ± 71	xx	-32.22 ± 0.16	xx	xx	3	xx
SD1-300	405	5	0.10	34	d. r. q.	2.8	nd	2.02 ± 0.15	xx	146 ± 64	88 ± 17	-30.93 ± 0.42	-32.39	0.9985	2	xx
SD1-700	410	5	0.10	70	d. r. q.	3.2	(>0.66)	3.90 ± 0.15	xx	170 ± 35	86 ± 4	-30.84 ± 0.19	-32.44	0.9984	2	xx
SD1-1000	389	5	0.10	100	d. r. q.	3.4	(>0.67)	4.97 ± 0.35	xx	274 ± 62	78 ± 4	-31.00 ± 2.01	-32.57	0.9984	3	xx
SD1-1500	404	5	0.10	150	d. r. q.	2.8	>0.86	5.39 ± 0.16	xx	834 ± 117	32 ± 1	-30.09 ± 1.20	-36.78	0.9933	3	xx
GYB	500	xx	xx	500	o. n.	3.6 (a)	0.98	6.33 ± 0.79	xx	1451 ± 70	xx	3.38 ± 0.25	xx	xx	3	xx
GYB-1	420	60	0.07	74	1087	1.2	0.71	3.08 ± 0.09	xx	405 ± 95	72 ± 4	2.91 ± 0.68	3.57	1.0007	3	xx
GYB-3	420	60	0.07	74	1087	1.7	(0.47)	3.78 ± 0.06	xx	260 ± 70	82 ± 6	3.70 ± 0.56	3.32	0.9996	2	xx
SD2	500	xx	xx	500	o. n.	3.3 (a)	nd	4.55 ± 0.09	xx	1167 ± 20	xx	-16.58 ± 1.03	xx	xx	3	xx
SD2-1	410	5	0.10	70	d. r. q.	2.1	0.96	3.82 ± 0.28	xx	329 ± 86	72 ± 5	-20.0 ± 2.4 (d)	-15.25	1.0048	1	xx
SD2-3	404	5	0.02	70	d. r. q.	1.0	nd	3.74 ± 0.09	xx	202 ± 38	83 ± 3	-19.66 ± 1.10	-15.94	1.0037	4	xx
SD2-5b	405	5	0.10	71	60	1.8	(0.22)	3.46 ± 0.39	xx	190 ± 35	84 ± 3	-18.52 ± 2.21	-16.21	1.0023	2	xx
SD2-6	405	5	0.10	70	300	1.6	(0.57)	3.52 ± 0.13	xx	175 ± 20	85 ± 1	-19.29 ± 0.15	-16.11	1.0032	2	xx

Table 2. Experimental results. *Continuation*

Sample ID	p_S [MPa]	t_I [min]	r [MPa/s]	p_E [MPa]	t_A [min]	ΔQFM	$S^{6+}/\Sigma S$	H_2O [wt%]	Cl [wt%]	S [ppm]	%S degass.	$\delta^{34}S_{melt}$ [‰]	$\delta^{34}S_{fluid}$ [‰]	α_{g-m}	n (SIMS)	Comments
GYCIA	508	xx	xx	502	o. n.	0.7	0.09	6.56 ± 0.24	0.103 ± 0.002	1018 ± 188	xx	*7.9 ± 0.7(e)*	xx	xx	*1(+2)(e)*	re-melted (f)
GYCIA-1	412	5	0.10	70	d. r. q.	1.7	(0.37)	3.73 ± 0.06	0.089 ± 0.009	184 ± 60	82 ± 12	6.05 ± 0.69	8.32	1.0023	2	xx
GYCIA-2	404	5	0.10	70	66	1.9	(0.47)	3.56 ± 0.28	0.081 ± 0.007	148 ± 60	85 ± 17	7.08 ± 1.20	8.05	1.0010	3	NQ
GYCIA-3	407	5	0.10	70	300	1.8	(0.29)	3.61 ± 0.07	0.073 ± 0.010	112 ± 52	89 ± 22	5.24 ± 0.48	8.24	1.0030	3	xx
GYCIA-4	415	5	0.10	70	4323.5	1.8	(0.35)	1.98 ± 0.03	0.073 ± 0.009	92 ± 48	91 ± 28	4.63 ± 0.28	8.24	1.0036	2	xx
GYCIA-5	401	5	0.10	71	63	1.9	(0.20)	3.84 ± 0.09	0.078 ± 0.008	124 ± 48	88 ± 16	-0.74 ± 0.62	9.11	1.0099	2	xx
GYMCIA	495	xx	xx	478	o. n.	0.8	0.23	6.29 ± 0.24	0.051 ± 0.001	1043 ± 143	xx	5.09 ± 1.57	xx	xx	6	re-melted (f)
GYMCIA-1	412	5	0.10	70	d. r. q.	1.7	0.33	3.64 ± 0.07	0.047 ± 0.008	356 ± 112	66 ± 8	6.77 ± 1.02	4.22	0.9975	5	xx
GYMCIA-3	407	5	0.10	70	300	1.8	(0.65)	3.62 ± 0.06	0.044 ± 0.006	128 ± 36	88 ± 9	5.53 ± 1.24	5.03	0.9995	3	xx
GYMCIA-4	415	5	0.10	70	4323.5	1.8	(0.25)	3.61 ± 0.06	0.046 ± 0.006	108 ± 48	90 ± 19	5.41 ± 0.89	5.05	0.9996	5	xx
GYMCIA-5	401	5	0.10	71	63	1.9	(0.25)	3.59 ± 0.06	0.045 ± 0.008	176 ± 44	83 ± 7	6.85 ± 1.26	4.73	0.9979	5	xx
RED	495	xx	xx	495	o. n.	0.1	0.03	6.71 ± 0.18	xx	1623 ± 242	xx	7.79 ± 0.20	xx	xx	5	re-melted (f)
RED-1	402	5	0.10	70	60	1.0	(0.33)	3.77 ± 0.09	xx	172 ± 56	89 ± 11	3.25 ± 1.49	8.33	1.0051	3	xx
RED-2	413	5	0.10	71	d. r. q.	1.2	(0.30)	3.45 ± 0.10	xx	284 ± 116	82 ± 16	2.65 ± 1.56	8.88	1.0063	3	xx
RED-3	412	5	0.10	70	300	1.1	(0.25)	3.56 ± 0.06	xx	200 ± 56	88 ± 9	2.69 ± 0.36	8.51	1.0058	3	xx
RED-4	405	5	0.10	70	1204.5	1.1	0.46	3.39 ± 0.41	xx	330 ± 25	80 ± 2	5.11 ± 0.80	8.48	1.0034	4	NQ
QFMCIA	508	xx	xx	509	6 days	0.4	(0.04)	6.58 ± 0.13	0.104 ± 0.002	260 ± 19	xx	4.60 ± 1.42	xx	xx	5	xx
QFMCIA-3	424	5	0.02	70	d. r. q.	0.8	(0.28)	3.48 ± 0.10	0.095 ± 0.002	52 ± 16	80 ± 8	2.04 ± 0.73	5.25	1.0032	3	xx
QFMCIA-4	412	5	0.01	70	d. r. q.	0.9	(0.23)	3.57 ± 0.06	0.097 ± 0.003	69 ± 15	74 ± 4	3.37 ± 0.33	5.04	1.0017	2	xx

Notes: EMP (e.g. S, Cl contents), IR (H_2O contents) and XANES ($S^{6+}/\Sigma S$ ratio) data have also been shown in Chapter I-A.

Sample ID: starting glasses are written in *italic*; p_S: start pressure; t_I: initial annealing time before decompression; r: decompression rate – error of decompression rate ≤ 0.01 MPa/s; p_E: final pressure after decompression / before rapid quench; t_A: annealing time at final conditions; ΔQFM: Nominal oxygen fugacity determined using the *Shaw*-membrane technique or (a) intrinsic redox conditions determined by e.g. Berndt et al.(2002) – (b) experiments without *Shaw*-membrane; fO_2 calculated using the initially loaded H_2 pressure; $S^{6+}/\Sigma S$: error probably >0.1, values in parenthesis refer to samples with very low sulfur content in the melt (<300 ppm) leading to (very) noisy XANES spectra – *italic* font indicates that the $S^{6+}/\Sigma S$ ratios should be equal to 1, see Chapter I-A for details; *%S degass*.: relative fraction of sulfur degassed from the melt upon decompression – determined by mass balance calculations. $\delta^{34}S_{melt}$: SIMS data [‰, V-CDT] – (d) only one spot measured, 2 σ of the 50 analytical cycles is given as error, see Section 3.2 – (e) two of the three SIMS measurements show varying count rates during the measurement and were not considered; 2 σ of the 50 analytical cycles is given as error, see Section 3.2; $\delta^{34}S_{fluid}$: estimated by mass balance calculations [‰, V-CDT]; α_{g-m}: average error ±0.0015, based on the analytical precision of the SIMS measurements; *Comments*: (f): starting glass contained quench related S-globules and was re-melted for ~1 h at ~1030°C and 500 MPa to improve homogeneity, see Chapter I-A for details.

xx: not relevant or 0; o. n.: over night; d. r. q.: direct rapid quench; nd: not determined / no measurement conducted; NQ: normal quench, cooling rate ~150°C/min.

The analytical approach further relies on the measurement of S-bearing glass standards with known S-isotope composition to account for the instrumental fractionation. In-house glass standards at WHOI with major element compositions ranging from basalts to high silica glasses were used for this calibration (Mandeville et al., 2008). The S-isotope composition of these glass standards ($\delta^{34}S_{Std}$) covers a range from about -30 ‰ up to about +20 ‰ and was determined by conventional bulk methods (e.g. KIBA reagent extraction method; Sasaki et al., 1979; Ueda and Sakai, 1984; Mandeville et al., 2009). The linear relation between $\delta^{34}S_{Std}$ and $\delta^{34}S_{SIMS}$ – found by Charles W. Mandeville and Nobumichi Shimizu – clearly indicates that matrix effects related to bulk composition (major element and S-isotope) or the oxidation state of S are negligible.

In addition, to monitor short and long term variations of the instrumental fractionation of the ion probe and to allow a correction of the raw isotopic data (see Appendix II-C for details), at least two measurements on a selected standard glass (usually MORB glass 892-1; $\delta^{34}S = 0.7$ ‰) were conducted after each 2-3 sample measurements. The accuracy of the analytical approach was also tested by using the IAEA standard materials SO6 (BaSO$_4$, $\delta^{34}S = -31.1 \pm 0.14$ ‰) and/or NBS 127 (BaSO$_4$, $\delta^{34}S = +20.3 \pm 0.14$ ‰) as S source for the starting glasses SD1 (SO6) and SD2 (~26.6 % NBS 127 and ~73.4 % SO6; corresponding to a $\delta^{34}S$ of about -17.4 ‰). SIMS measurements indicate a $\delta^{34}S$ of -32.2 ± 0.2 ‰ for SD1 and a $\delta^{34}S$ of -16.6 ± 1.0 ‰ for SD2. Thus, a precision of ~1 ‰ for the SIMS analyses of the στυδιεδ experimental andesitic glasses can be assumed. Details on the processing procedure of the raw SIMS data are given in the Appendix II-C.

Most samples were analyzed 2 to 8 times (Table 2), depending on the quality of the single measurement (e.g. the internal standard deviation) and each measurement consists of 50 cycles for ^{32}S and ^{34}S, respectively. However, sample SD2-1 could only be analyzed once (Table 2) owing to difficulties in identifying bubble-free spots which are large enough for SIMS analyses. Moreover, two of the three measurements conducted on GYClA show varying count rates, probably reflecting an instable primary beam during the analyses. Consequently, only one measurement of GYClA was considered. Hence, the S-isotope data of GYClA and SD2-1 has to be interpreted with caution. The 2 sigma of the 50 analytical cycles is given as error for these two samples (see Table 2).

The corrected S-isotope data of the decompression experiments and the respective starting glass was used – together with the measured volatile contents in the melt – to determine the isotopic composition of the fluid phase and the isotopic fractionation factors via mass balance calculations for various fO_2 (ranging from~QFM+1 to ~QFM+4). In the following sections, the S isotope composition is reported in a conventional delta (δ) notation given in ‰. The Vienna Canyon Diablo Troilite (V-CDT) was used as S-isotope reference standard (Coplen and Krouse, 1998; Ding et al., 2001).

$$\delta^{34}S = (\,[\,(^{34}S/^{32}S_{sample})\,/\,(^{34}S\,/\,^{32}S_{V\text{-}CDT})\,]\,-\,1\,)\cdot 1000 \tag{1}$$

The gas-melt isotopic fractionation factor $\alpha_{g\text{-}m}$ was estimated using the following assumption:

$$\Delta^{34}S_{g\text{-}m} = \delta^{34}S_{gas} - \delta^{34}S_{melt} \approx 10^3\ln\alpha_{g\text{-}m} \tag{2}$$

3.3 Determination of S speciation in melt and fluid using XANES spectroscopy

The S speciation in most starting glasses and glasses of the decompression experiments was already characterized via X-ray absorption near edge spectroscopy (XANES) at the S K-edge (2472 eV) in a previous study (Chapter I-A). Additional measurements were performed with a smaller beam size (~60×60 µm instead of ~250×150 µm) in this study to detect small scale variation in S speciation throughout sample. Details on the XANES measurement can also be found in the Appendix II-D and II-E.

4. RESULTS

The run products obtained after decompression consist of glass and bubbles with quenched fluids (decompression experiments). No crystals could be detected. The experimental conditions and the volatile concentrations of starting glasses and of glasses after decompression are given in Table 2 (same data as in Chapter I-A). The major element concentrations determined by EMP revealed that the glasses are chemically homogeneous and similar to the anhydrous andesite, if volatiles are subtracted and oxides are normalized to 100 wt% (see also Chapter I-A).

4.1 Determination of $S^{6+}/\Sigma S$ and fO_2 in glasses using XANES spectra

The $S^{6+}/\Sigma S$ ratios in glasses determined in Chapter I-A via XANES using the model of Jugo et al. (2010) are listed in Table 2. These values were used in Chapter I-A to estimate the fO_2 inside the capsules [$fO_2(XANES)$] via equation 3 (see Section 5.2). The derived $fO_2(XANES)$ values often differ significantly from the nominal fO_2 in the vessel. Possible reasons for these deviations are discussed in detail in Chapter I-A. As suggested in Chapter I-A the nominal fO_2 is used to discuss and interpret the data obtained. However, $fO_2(XANES)$ of some (reduced) samples is applied (in addition to the nominal fO_2) to create a model predicting the effect of fO_2 on $\alpha_{g\text{-}m}$, in order to account for possible small differences between the nominal fO_2 in the vessel and within the capsule, which may have a significant effect on the S speciation in fluid- and melt-phase, respectively (see Section 5.2).

4.2 Sulfur speciation in the quenched fluid (XANES)

The results of the XANES measurements with a ~60×60 μm beam size are shown in the Appendix II (Fig. II-E.1). Areas containing high volume fraction of bubbles and areas nearly devoid of bubbles were selected and compared. Small differences between the spectra of bubble-bearing and bubble-free areas can be observed. These variations can possibly be assigned to S species from the quench products of the fluid inclusions (see Appendix II-E.). The XANES data indicates that SO_2 may be the prevailing S species in the fluid phase at QFM+4 while significant amounts of H_2S are probably present in the fluid at QFM+1 (see Fig. II-E.1 and description of spectra in Appendix II-E.). Thus, the fluid-melt isotope fractionation of S at oxidizing conditions (> QFM+3) may be dominated by the isotopic fractionation pair $SO_{2\ (gas)} - SO_4^{2-}{}_{(melt)}$, while $H_2S_{(gas)} - S^{2-}{}_{(melt)}$ is probably the most relevant fractionation pair at reducing conditions (< QFM+1). However, XANES spectra do not allow a quantitative estimation of the H_2S/SO_2 ratio in the fluid.

4.3 Sulfur isotope fractionation

Fig. 1 indicates a negative correlation between $\delta^{34}S_{melt}$ and the fraction of S remaining in the melt phase (*f*) under oxidizing conditions (> QFM+2.7). The relative change in $\delta^{34}S_{melt}$ with increasing release of S seems to be independent on the initial isotopic composition which varied between -32‰

and +18‰ (Fig. 1). Hence, the instrumental S isotope fractionation is assumed to be largely independent of the (initial) S-isotope composition of the glass, at least in the studied range of $\delta^{34}S_{melt}$. Thus, in the following, the initial $\delta^{34}S_{melt}$ will not be considered for the discussion and interpretation of detected fluid-melt isotope fractionation trends.

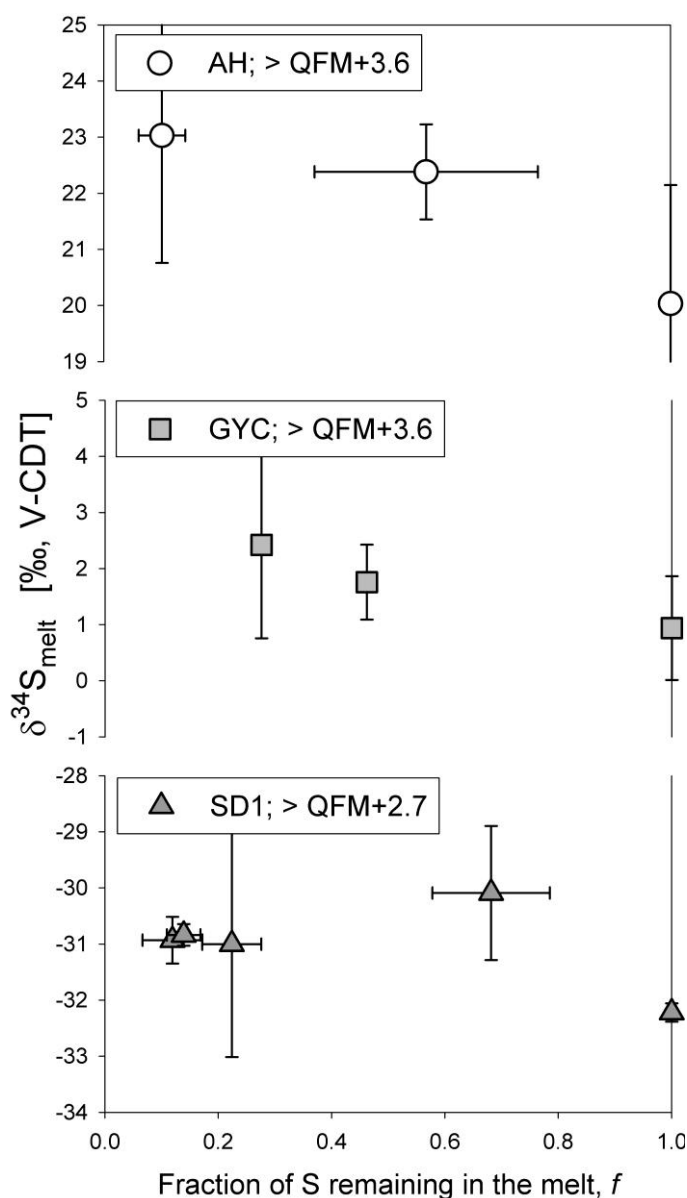**Fig. 1:** S-isotopic composition ($\delta^{34}S_{melt}$) of selected experimental series conducted under oxidizing conditions ($\log(fO_2/\text{bar}) > \text{QFM+2.7}$) plotted against fraction of S remaining in the melt phase (f). The initial $\delta^{34}S_{melt}$ (0% S degassed; $f = 1.0$) was 18.25 ± 1.12 ‰ (AH), 0.93 ± 0.86 ‰ (GYC) or -32.22 ± 0.16 ‰ (SD1), respectively.

Fig. 2 clearly shows a significant influence of fO_2 on the fluid-melt isotope fractionation. Although error bars are large for some experimental products, the dataset (see Table 2) confirms that the fluid-melt isotope fractionation of S is detectable with the applied experimental and analytical approach. In general, $\delta^{34}S_{melt}$ increases upon (S-) degassing at oxidizing conditions (~QFM+3), while it decreases at relatively reducing conditions (~QFM+1). No significant fractionation is observed for the series of experiments performed at intermediate redox conditions (~QFM+1.8). The data in Fig. 1 and 2 clearly indicates that the fluid has a lower $\delta^{34}S$ than the melt from which it exsolved at oxidizing conditions and a higher $\delta^{34}S$ than the melt at reducing conditions, in agreement with the theoretical considerations (see review of Taylor, 1986). It is emphasized that Fig. 2 includes data with different r and t_A but that there is no detectable effect of these parameters on $\alpha_{g\text{-}m}$ (see next Section 4.3.1).

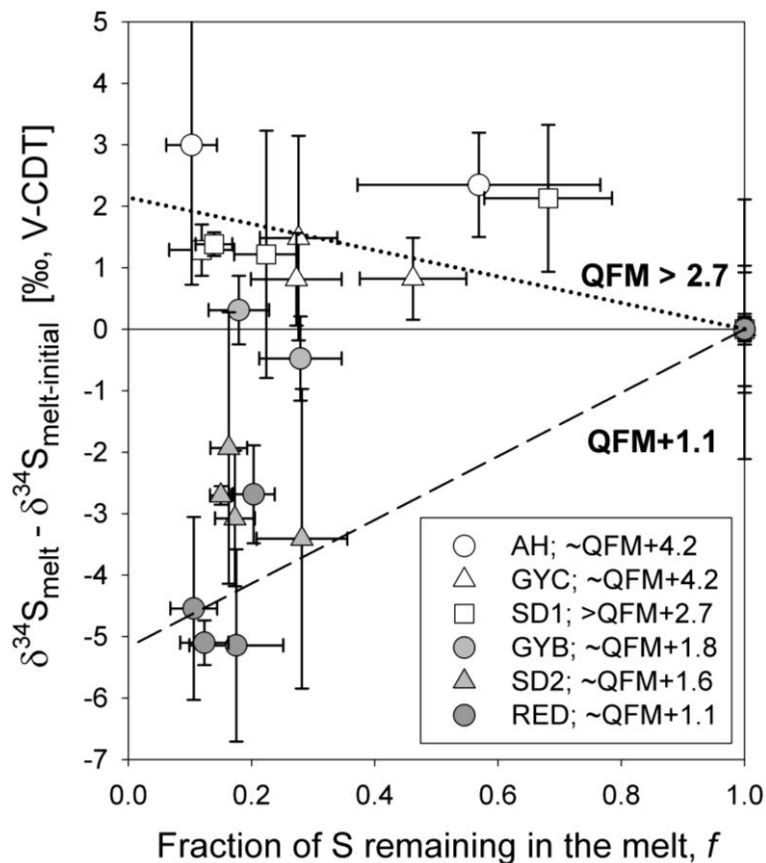**Fig. 2:** Isotopic fractionation of S at various fO_2. The normalized $\delta^{34}S_{melt}$ is plotted against fraction of S remaining in the melt phase (f). The figure shows all Cl free experiments except AHC, because of the varying fO_2 within this experimental series.

4.3.1 Influence of t_A and r on α_{g-m}

In Fig. 3, α_{g-m} values of selected experimental series (GYClA, GYMClA and RED) are plotted against

t_A. The experimental series were chosen because they cover a wide range of t_A (0 h to ~20 h or ~72 h).

The data reveals that t_A has no significant influence on α_{g-m}; i.e. α_{g-m} values of the same experimental

series are similar within error. This is also confirmed by decompression experiments (using starting

glass GYC) performed with varying r, e.g. α_{g-m} = 0.9989 $\pm$ 0.0015 at r ~0.16 MPa/s (experiment

GYC-2) and α_{g-m} = 0.9985 $\pm$ 0.0013 at r ~0.05 MPa/s (GYC-3). Thus, the α_{g-m} values given in Table 2

can be interpreted as reflecting equilibrium fluid-melt fractionation.
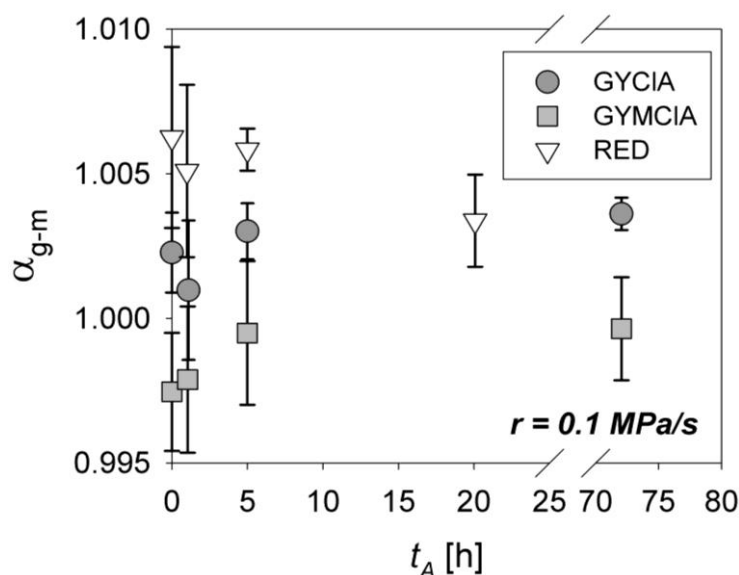
Fig. 3: Influence of t_A on α_{g-m} at constant r of 0.1 MPa/s. The
experiment GYClA-5 was excluded (see Section 4.3.2).

4.3.2 Influence of fO_2 on α_{g-m}

The Fig. 2 and 3 indicate that the fluid-melt S isotope fractionation strongly depends on fO_2. The

whole dataset of α_{g-m} values given in Table 2 is reported as a function of ΔQFM in Fig. 4. It is

emphasized that four points plotted in Fig. 4 need to be interpreted with caution. The data points at

~QFM+4.2 and $\alpha_{g-m} \approx$ 0.9946 as well as 0.9967 (sample AH-3 and AH-4) were determined from the

starting glass AH. The uncertainty on the δ^{34}S of this starting glass is large compared to all other

starting glasses (δ^{34}S of AH has 1 sigma error of ~2 ‰, Table 2), indicating heterogeneous S-isotope

distribution. Thus, the low α_{g-m} values compared to other experiments at ~QFM+4.2 in Fig. 4 is

probably due to a bad estimation of δ^{34}S in the starting glass. Fig. 1 confirms that the δ^{34}S in the starting glass AH is most probably underestimated and may be about 21-22‰ because the linear extrapolation of the points with an f value of ~0.1 and ~0.6 indicates that the δ^{34}S in the initial melt should be ~ +21.8‰. Assuming a δ^{34}S in the range 21-22‰ for the starting glass AH, the calculated α_{g-m} would overlap with the other data at ~QFM+4.2 in Fig. 4. The SIMS analyses of the outliers at QFM+1.9 and $\alpha_{g-m} \approx 1.010$ (grey triangle in Fig. 4; GYClA-5) as well as at QFM+2.7 and $\alpha_{g-m} \approx 0.993$ (open square in Fig. 4; SD1-1500) showed strongly varying count statistics for ^{32}S when measuring on different locations on the sample. In addition, the counts for ^{32}S detected in GYClA-5 are significantly higher than those of comparable experiments (e.g. GYClA-2). Considering that both samples were highly vesiculated, the variation of count statistics may be due to a contribution of S-bearing phases (possibly quench phases from the fluid) at the bubble-melt interface to the detected S-isotope signal. Thus, these two samples (GYClA-5 and SD1-1500) as well as the samples AH-3 and AH-4 are not considered for following discussions.

Excluding these four problematic samples, Fig. 4 reveals that α_{g-m} is > 1 at log(fO_2/bar) < QFM+1.5 and < 1 at log(fO_2/bar) > QFM+2.5. The redox range between QFM+1.5 and QFM+2.5, in which α_{g-m} changes from less than 1 to more than 1, correlates well with the sulfate-sulfide transition in silicate melts (e.g. Jugo et al., 2010; Klimm et al., 2012a).

Three starting compositions also contained Cl and the results show that the presence of Cl in concentrations up to 1000 ppm has a negligible effect on the S isotope fractionation at ~ QFM+1.5. The scattering of the data is mainly due to the analytical precision of the SIMS technique. Based on the experimental data in Table 2, an average α_{g-m} of 0.9985 ± 0.0007 is derived for oxidizing conditions at log(fO_2/bar) ≥ QFM+2.8 (samples AH-3, AH-4 and SD1-1500 excluded) and an α_{g-m} of ~1.0042 ± 0.0024 is calculated for relatively reducing redox conditions at log(fO_2/bar) ≈ QFM+1. It is emphasized that the fractionation factors are identical within error if only experiments with t_A > 5 h or $r \leq 0.05$ MPa/s are considered for the calculation of the mean values (~0.9988 ± 0.0013 at > QFM+4 and ~1.0032 ± 0.0027 at ~QFM+1), indicating that equilibrium isotopic distribution was attained in the experiments.

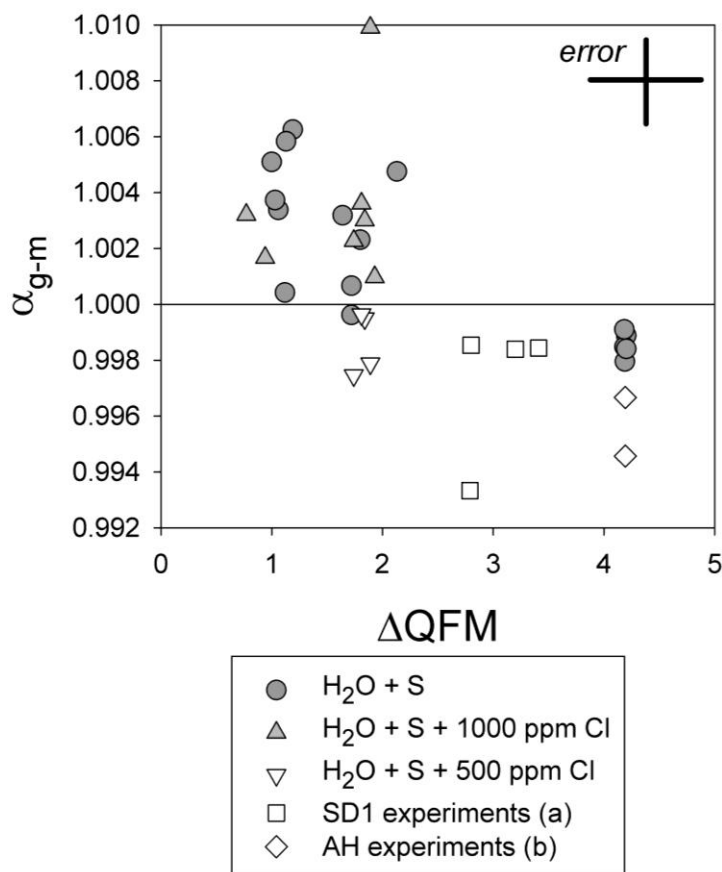**Fig. 4:** S-isotope fractionation factor α_{g-m} plotted against fO_2. For clarity, the typical errors for α_{g-m} and fO_2 are illustrated by the black cross in the upper right corner. The final p of the decompression experiments was typically 70 MPa (see Table 2).
(a) SD1 experiments: quenched at final p of 30, 70, 100 or 150 MPa (see Table 2).
(b) AH experiments: uncertainty on the δ^{34}S of the AH starting glass is large compared to other starting glasses due to heterogeneous S-isotope distribution (see Section 4.3.2).

5. DISCUSSION

The experimental results presented in this study provide first constraints on the fractionation of S-isotopes between H_2O-S-(Cl)-fluids and silicate melts during magma degassing at geologically relevant conditions. As mentioned above, the influence of r and t_A at final p on S-isotope fractionation is negligible within the investigated redox range. Hence, the observed influence of fO_2 on α_{g-m} may reflect equilibrium isotope fractionation effects occurring upon closed system degassing, even if experiments were directly quenched after decompression ($t_A = 0$ h). This is not surprising as kinetically controlled isotopic fractionation processes are rare in high T processes occurring in magmatic systems (O'Neil, 1986). Thus, our results indicate that S-isotopic equilibrium between fluid and andesitic melt

is reached during a degassing controlled by an r ranging from ~0.01 to 0.16 MPa/s. On the other hand, based on the same set of experiments, kinetically controlled degassing mechanisms were revealed in Chapter I-A for the release of S from oxidized andesitic melt upon fast decompression. In Chapter I-A it is noted that equilibrium distribution of S between fluid and melt was only reached after a t_A of ≥ 5 h at oxidizing conditions, whereas the same isotopic distribution was observed independently of t_A in this study, indicating that fluid-melt S-isotopic fractionation is not affected by the kinetics of S degassing.

5.1 Comparison with the de Hoog et al. (2001) model

In the following discussion, the new data is compared to the model of de Hoog et al. (2001), which is based on experimental data and theoretical considerations from the 70s and early 80s (summarized by Taylor, 1986). The $\Delta^{34}S_{g-m}$ values for each experiment, calculated following equation 2, were used to determine average $\Delta^{34}S_{g-m}$ values for each experimental series at a given fO_2 (GYB, GYC, etc., see Table 2). Fig. 5 shows the relationbship between (average) $\Delta^{34}S_{g-m}$ and fO_2. The $\Delta^{34}S_{g-m}$ value of the AH experiments is different from other values at ~QFM+4.2 due to the large uncertainty on the $\delta^{34}S_{melt}$ in the AH starting glass (see Section 4.3.2). The effect of fO_2 on $\Delta^{34}S_{g-m}$ calculated for 1030°C following the model of de Hoog et al. (2001) is plotted for comparison. The *de Hoog*-model relies basically on T dependences of α_{g-m} provided by Miyoshi et al. (1984) and Taylor (1986) as well as on equations of Marini et al. (1998) and Wallace and Carmichael (1992) linking fO_2 to the speciation of S in the fluid and in the melt, respectively. The *de Hoog*-model underestimates the isotopic fractionation at reducing conditions by about one order of magnitude. In addition, the extrapolation of the *de Hoog*-model to $\log(fO_2/\text{bar}) >$ QFM+2.1 leads to unrealistic low $\Delta^{34}S_{g-m}$ values. The discrepancies, especially those observed for oxidizing conditions, may be related to the modeling approach in the *de Hoog*-model. An accurate model for the evaluation of α_{g-m} and, thus, of $\Delta^{34}S_{g-m}$ must include the four predominant S-isotope fractionation pairs: *i) $SO_2\,_{gas} - SO_4^{2-}{}_{melt}$, ii) $H_2S\,_{gas} - SO_4^{2-}{}_{melt}$, iii) $SO_2\,_{gas} - S^{2-}{}_{melt}$ and iv) $H_2S_{gas} - S^{2-}{}_{melt}$* (Mandeville et al., 2009). However, the model proposed by de Hoog et al. (2001) does not account for two of these fractionation pairs (*i* and *ii*). These pairs are mainly

controlling the isotope fractionation under oxidizing conditions, explaining the problems of the *de Hoog*-model to predict accurately $\Delta^{34}S_{g\text{-}m}$ for $\log(fO_2/\text{bar}) > \text{QFM}+2.1$. Moreover, the differences observed at ~QFM+1 indicate that the T dependence of $\Delta^{34}S_{g\text{-}m}$ determined by Miyoshi et al. (1984) in the T range of 600 to 1000°C and used by de Hoog et al. (2001) for the estimation of $\alpha(H_2S_{gas} - S^{2\text{-}}{}_{melt})$ is probably not applicable for silicate melts at high T conditions (i.e., > 1000°C). The experimental data of Miyoshi et al. (1984) have to be applied with caution to silicate systems considering that the S-isotope fractionation factor $\alpha(SO_4^{2\text{-}}{}_{melt} - H_2S_{gas})$ was determined between $SO_4^{2\text{-}}$ in NaCl or LiCl-KCl melts and H_2S in an aqueous fluid and that $\alpha(SO_4^{2\text{-}}{}_{melt} - S^{2\text{-}}{}_{melt})$ was determined by decomposing anhydrous Na_2SO_3 in NaCl and LiCl-KCl melts. In a first approximation, the T dependence determined for $\alpha(SO_4^{2\text{-}}{}_{melt} - H_2S_{gas})$ may be more realistic, considering that the fluid composition is similar to that expected in natural systems.
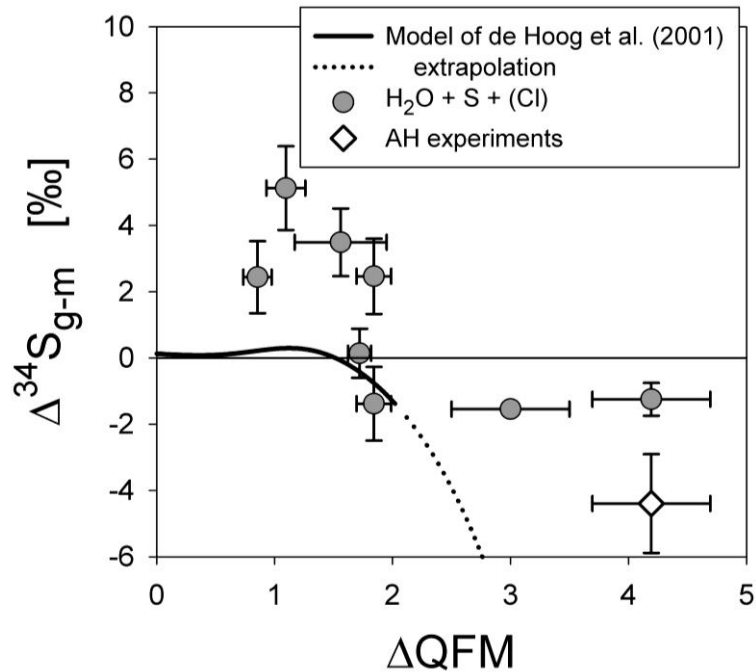
Fig. 5: $\Delta^{34}S_{g\text{-}m}$ of all experimental series plotted against fO_2. The displayed trend line was calculated for 1030°C following the approach of de Hoog et al. (2001) and is plotted for comparison. The dotted trend represents an extrapolation of the de Hoog et al. (2001) model. The AH data is distinguished from other results due to the large isotopic variation detected in the AH starting glass. GYClA-5 and SD1-1500 were excluded for the calculation of the $\Delta^{34}S_{g\text{-}m}$ values (see Section 4.3.2).

5.2 Modeling of the fluid-melt S-isotope fractionation

The comparison of the new experimental data with the *de Hoog*-model shows that an improved model for the evaluation of α_{g-m} is barely needed. Our experimental data has been used to develop such a model for $T \approx 1030°C$. A good knowledge of the S speciation in the melt and the coexisting fluid at given *p-T-fO$_2$* is required for the calculations.

Sulfur speciation in melt: The *fO$_2$* of each experiment can be utilized to estimate the molar fraction of S dissolved as sulfate-species in the melt, $x(SO_4^{2-})_{melt}$, using equation 3 provided by Jugo et al. (2010).

$$x(SO_4^{2-})_{melt} = S^{6+} / \Sigma S = 1 / (1 + 10^{(2.1 - 2 \cdot \Delta QFM)}) \tag{3}$$

where ΣS is the sum of S dissolved as sulfide (S^{2-}) and sulfate (S^{6+}) in the melt and $x(SO_4^{2-})_{melt} = 1 - x(S^{2-})_{melt}$.

Sulfur speciation in fluid: The H_2S/SO_2 molar fraction in the gas phase was calculated using the program *DCompress* provided by Alain Burgisser (CNRS, Orleans, France) which is based on data of Burgisser et al. (2008) to model the degassing of rhyolitic melts and on unpublished data of Burgisser et al. to model the degassing of basaltic melts. The program allows us the estimation of the H_2S/SO_2 molar fraction in a S-O-H fluid coexisting with basaltic (at 1000 to 1400°C) or rhyolitic melts (at 710 to 910°C) for given *fO$_2$*. The decompression (from 3000 to 700 MPa) of a rhyolitic (at 900°C) and a basaltic melt (at 1030°C) containing initially 6 wt% H_2O, 1000 ppm S and 0.1 wt% gas was simulated for *fO$_2$* ranging from QFM-1 to QFM+5. The modeled molar H_2S/SO_2 fractions in the fluid phases were used to determine the fraction of SO_2 [$x(SO_2)_{fluid}$ = (mol SO_2) / (mol SO_2 + mol H_2S)] and H_2S [$x(H_2S)_{fluid}$ = 1 − $x(SO_2)_{fluid}$] in the fluid phase as a function of *fO$_2$* for a rhyolitic and basaltic composition.

The main assumptions for the new model are: *a)* The fluid-melt isotope fractionation can be described by $\alpha(SO_{2\ gas} - SO_4^{2-}{}_{melt})$ at very oxidizing conditions and *b)* by $\alpha(H_2S_{\ gas} - S^{2-}{}_{melt})$ at very reducing redox conditions. The average α_{g-m} of ~0.9985 derived from experiments conducted under oxidizing conditions (log(*fO$_2$*/bar) > QFM+2.8) is assumed to represent the fractionation pair $SO_{2\ gas} - SO_4^{2-}{}_{melt}$, considering that $x(SO_4^{2-})_{melt}$ and $x(SO_2)_{fluid}$ are nearly 1 at log(*fO$_2$*/bar) > QFM+2.8. Furthermore, an

average α_{g-m} of ~1.0042 was estimated for $\log(fO_2/\text{bar}) \approx \text{QFM+1.1}$ (experiments RED-1 to RED-4; AHC-3), corresponding to $x(SO_4^{2-})_{melt}$ and $x(SO_2)_{fluid}$ of ~0.5 in basaltic systems. The values of $x(SO_4^{2-})_{melt}$ and $x(SO_2)_{fluid}$ are calculated using the model of Jugo et al. (2010) and the *DCompress* program, respectively. The α_{g-m} fractionation factor of ~1.0042, and the determined value for $\alpha(SO_{2\ gas} - SO_4^{2-}{}_{melt})$, are used to estimate a value of $\alpha(H_2S_{\ gas} - S^{2-}{}_{melt})$ for basaltic systems. The same approach can be used to estimate a value of $\alpha(H_2S_{\ gas} - S^{2-}{}_{melt})$ at QFM+1.1 for rhyolitic systems if $x(SO_2)_{fluid}$ is modeled using *DCompress* for rhyolite melts. The estimated $\alpha(H_2S_{\ gas} - S^{2-}{}_{melt})$ values are 1.0099 and 1.0050 for basaltic and rhyolitic systems (Table 3). The calculations were repeated using the $S^{6+}/\Sigma S$ ratio estimated from the XANES spectra to account for the observed discrepancies between the prevailing fO_2 in the vessel and $fO_2(XANES)$. In this case, the estimated $\alpha(H_2S_{\ gas} - S^{2-}{}_{melt})$ values are 1.0073 and 1.0046 for basaltic and rhyolitic systems. The fractionation factor $\alpha(H_2S_{\ gas} - SO_4^{2-}{}_{melt})$ was estimated using the results of Miyoshi et al. (1984) who used Na_2SO_4 melt and (aqueous) H_2S fluid in their experiments. Subsequently, $\alpha(SO_{2\ gas} - S^{2-}{}_{melt})$ can be calculated using equation 4.

$$\alpha(SO_{2\ gas} - S^{2-}{}_{melt}) = \alpha(SO_{2\ gas} - SO_4^{2-}{}_{melt}) + \alpha(H_2S_{\ gas} - S^{2-}{}_{melt}) - \alpha(H_2S_{\ gas} - SO_4^{2-}{}_{melt}) \qquad (4)$$

The application of the data of Miyoshi et al. (1984) to extract $\alpha(H_2S_{\ gas} - SO_4^{2-}{}_{melt})$ for silicate systems may be problematic (see Section 5.1), but can be tested using the *T* dependence of $\alpha(SO_{2\ gas} - H_2S_{gas})$ given by Taylor (1986) based on theoretical calculations of Richet et al. (1977). If the average values derived for $\alpha(H_2S_{gas} - S^{2-}{}_{melt})$ and $\alpha(SO_{2\ gas} - S^{2-}{}_{melt})$ (Table 3) are used to calculate the fractionation between H_2S and SO_2 in a fluid phase, a value of $\alpha(SO_{2\ gas} - H_2S_{gas})$ of 1.0023 is obtained, which is similar to the value calculated using the data in Taylor (1986).

The fluid-melt fractionation factors used for the modeling of the isotopic fractionation are summarized in Table 3. They were applied to calculate fractionation factors at given fO_2 [$\alpha_{g-m}(fO_2)$] using the S speciation in the fluid- (estimated using *DCompress*) and melt-phase (estimated using XANES data and the model of Jugo et al., 2010); see Appendix II-F for details.

Fig. 6 shows the modeled isotopic fractionation trends. All four trends correlate well with the experimental data. The trends calculated for a basaltic melt composition (blue lines) seem to show a better correlation with the measured $\Delta^{34}S$ values when compared to rhyolite trends (red lines). However, the *T* for the calculations in rhyolitic system using *DCompress* is limited to 900°C, and the observed differences between the measured $\Delta^{34}S$ values and the modeled trends may be related to both, compositional and *T* differences (i.e. differences between those applied for the *DCompress* modeling and those of the conducted experiments).

The differences between the modeled trends and the experimental data can also be explained by a (slight) shift of the sulfide-sulfate transition in the studied andesitic system when compared to the basaltic samples used by Jugo et al. (2010) to determine equation 3 which was applied to estimate $x(SO_4^{2-})_{melt}$. In fact, Baker and Moretti (2011) noted that the dependence of $S^{6+}/\Sigma S$ on fO_2 is significantly affected (e.g.) by *T*, *p* and melt composition. Nevertheless, as mentioned above, $fO_2(XANES)$ shows a good correlation with nominal fO_2 (if doubtful XANES data is excluded). Fig. 4A in Chapter I-A also indicates that the sulfide-sulfate transition in the studied dacitic andesite glasses may be shifted by ~ +0.5 log units. According to the data shown in Fig. 5 the sulfide-sulfate transition in dacitic andesite glasses is suggested to be at an fO_2 of about QFM+1.8. However, a clear determination of the sulfide-sulfate transition in dacitic andesite glasses is needed to (possibly) improve our model.

In general, the fluid-melt S-isotope fractionation at oxidizing conditions is very well constrained by our data. Noteworthy, an extrapolation of the S-isotope data presented in Mandeville et al. (2009) for natural samples of the climactic eruption of Mt. Mazama (relevant degassing *T* estimated for the samples range from 840 to 975°C) indicates an α_{g-m} of about 0.9982 at 1030°C and fairly oxidizing conditions (~QFM+1.7 to QFM+1.9 log units), which is within error of our experimental data for oxidized systems. In contrast, the lack of experimental data at $\log(fO_2/\text{bar}) \ll$ QFM+1 leads to a large error on the estimation of $\alpha(H_2S_{gas} - S^{2-}_{melt})$. However, considering that equilibrium (S-)isotope fractionation effects refer to the effect of atomic mass on bond energy (e.g. O'Neil, 1986) and assuming that differences in bonding energies of S-isotopes in melts are negligible when comparing

different silicate melt compositions, the average $\alpha(H_2S_{gas} - S^{2-}_{melt})$ of 1.0067 ± 0.0026 determined on

the basis of our data can be applied to a wide range of reduced magmatic systems at 1030°C.
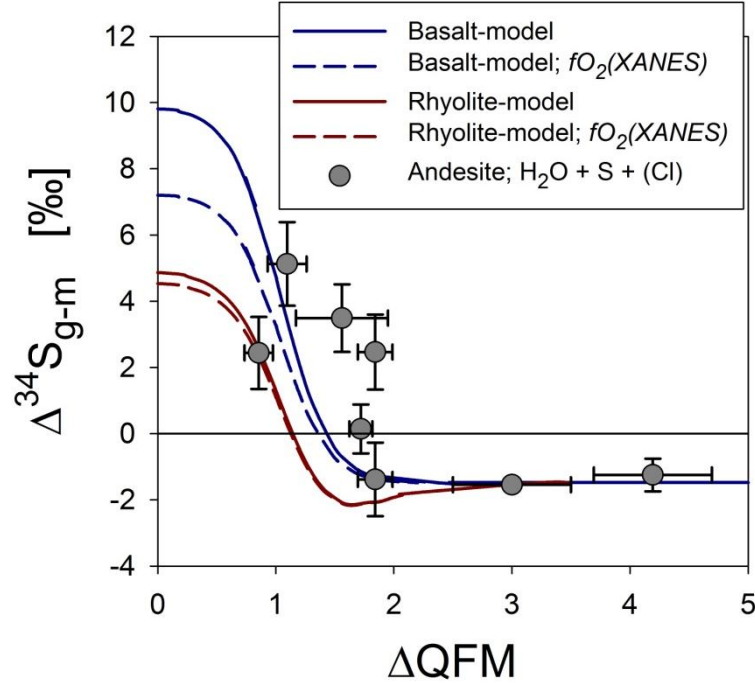
Fig. 6: Modeled dependence of $\Delta^{34}S_{g-m}$ on fO_2 for rhyolitic and basaltic melt. $\Delta^{34}S_{g-m}$ values of all experimental series are plotted for comparison.
AH experiments excluded, due to the large uncertainty on $\delta^{34}S_{melt}$ in the AH starting glass (see Section 4.3.2).

Table 3: Estimated fluid-melt S-isotope fractionation factors for 1030°C.

Method	$\alpha(SO_{2\ gas} - SO_4^{2-}{}_{melt})$	$\alpha(H_2S_{gas} - S^{2-}{}_{melt})$	$\alpha(SO_{2\ gas} - S^{2-}{}_{melt})$	$\alpha(H_2S_{gas} - SO_4^{2-}{}_{melt})$
oxidized experiments	0.9985	-	-	-
basalt / fO_2	-	1.0099	1.0122	-
basalt / XANES	-	1.0073	1.0095	-
rhyolite / fO_2	-	1.0050	1.0072	-
rhyolite / XANES	-	1.0046	1.0069	-
Miyoshi et al. (1984)	-	-	-	0.9963
average	*0.9985± 0.0007*	*1.0067 ± 0.0023*	*1.0090 ± 0.0025*	*0.9963 ±0.0002*

Notes: oxidized experiments: average α_{g-m} derived from experiments conducted at $\log(fO_2/\text{bar}) > \text{QFM}+2.8$
basalt / fO_2: used basaltic melt composition for the *DCompress* calculations and the nominal fO_2 (Table 2)
basalt / XANES: used basaltic melt composition for the *DCompress* calculations and the XANES data (Table 2)
rhyolite / fO_2: used rhyolitic melt composition for the *DCompress* calculations and the nominal fO_2 (Table 2)
rhyolite / XANES: used rhyolitic melt composition for the *DCompress* calculations and the XANES data (Table 2)
Miyoshi et al. (1984): $10^3 \ln \alpha(SO_4^{2-}{}_{melt} - H_2S_{gas}) = 6.3 \cdot (10^6 / T^2)$

5.3 Modeling S-isotope composition of volcanic gasses

The isotopic composition of volcanic gases released from a melt can be estimated using the equations

given by Holloway and Blank (1994) for closed and open system degassing, respectively:

$$\delta^{34}S_{\text{m-f}} \approx \delta^{34}S_{\text{m-i}} - (1 - f) \cdot 10^3 \cdot \ln \alpha_{\text{g-m}} \qquad \textit{closed system} \qquad (5)$$

$$\delta^{34}S_{\text{m-f}} \approx (\delta^{34}S_{\text{m-i}} + 10^3) \cdot (f^{\alpha(\text{g-m}) - 1}) - 10^3 \qquad \textit{open system} \qquad (6)$$

where f is the fraction of S remaining in the melt as well as $\delta^{34}S_{\text{m-i}}$ and $\delta^{34}S_{\text{m-f}}$ are the initial and the

final isotopic composition in the melt phase, respectively. Subsequently, the isotopic composition of

the released fluid phase ($\delta^{34}S_{fluid}$) can be determined using equation 7:

$$\delta^{34}S_{\text{m-i}} = (1 - f) \cdot \delta^{34}S_{\text{fluid}} + (f) \cdot \delta^{34}S_{\text{m-f}} \qquad (7)$$

The fractionation factor $\alpha_{\text{g-m}}$ for a given fO_2 can be estimated applying the model described in Section

5.2 and using the average $\alpha_{\text{g-m}}$ values of the four fractionation pairs listed in Table 3. The derived $\alpha_{\text{g-m}}$

values (listed in the figure captions of Fig. 7) can be used to model the isotopic composition of a

released fluid ($\delta^{34}S_{\text{fluid}}$) upon open and closed system degassing (Fig. 7). Significant differences

between the modeled trends for closed system and open system degassing are only observed if less

than 30% of the S in the melt is released. Thus, distinguishing between closed and open system

degassing based on the S isotope signature of a volcanic gases may only be possible for a moderate

decompression event or at the beginning of an intense decompression (e.g. initial phase of a volcanic

eruptions). Fig. 7a and 7b also indicate that even under intermediate redox conditions (~QFM+1.5) a

remarkable fluid-melt S-isotope fractionation should be expected.

Most importantly, the data reveals that the first fluid released by open system degassing may be up to

~10 ‰ lighter (oxidized magmas) or up to ~35 ‰ heavier (reduced magmas) than the $\delta^{34}S$ of the

source magma. Considering that fast decompression combined with open system degassing often

occurs during explosive, hazardous volcanic events, a distinct change in $\delta^{34}S_{fluid}$ detected in the volcanic gas should be expected prior or during the initial phase of the eruption.
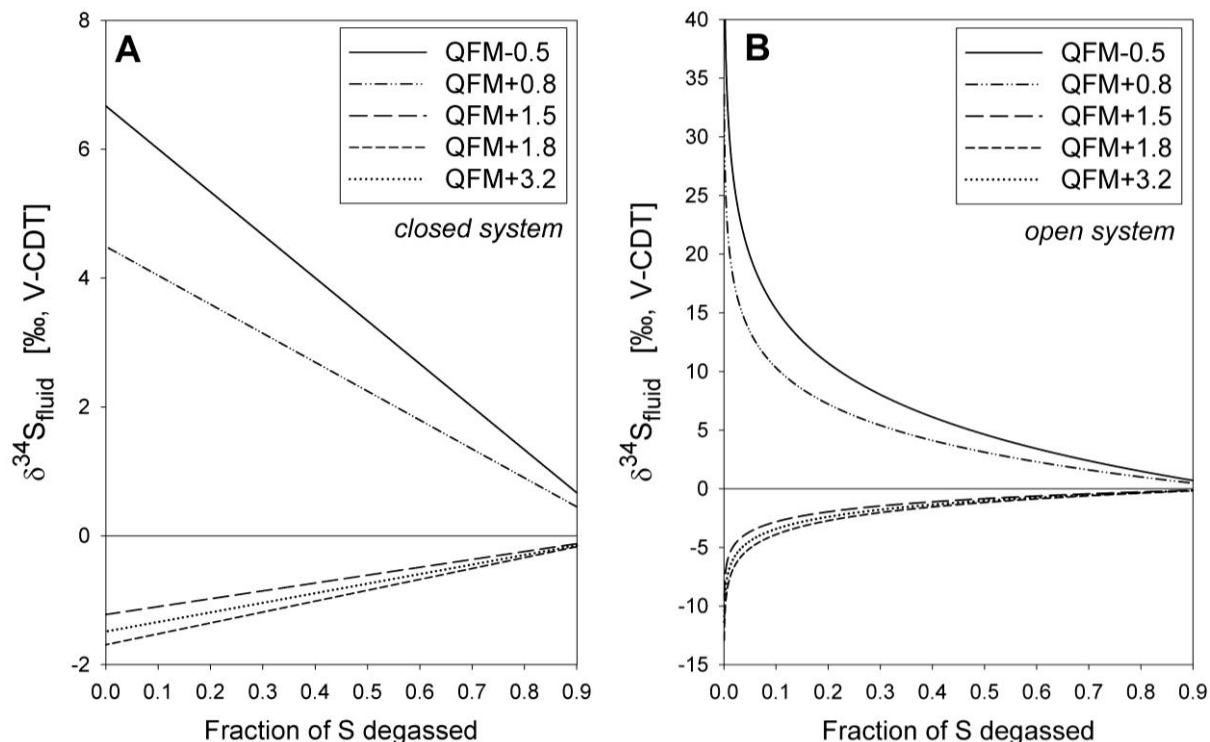
Fig. 7a/b: $\delta^{34}S_{fluid}$ plotted against the relative fraction of S degassed from the melt at log(fO_2/bar) ranging from QFM-0.5 to QFM+3.2. **a)** Closed system degassing. **b)** Open system degassing.
The α_{g-m} values for given fO_2 were estimated using our model for the dependence of α_{g-m} on fO_2.
(α_{g-m} = 1.0067 for QFM-0.5; 1.0045 for QFM+0.8; 0.9988 for QFM+1.5; 0.9983 for QFM+1.8 and 0.9985 for QFM+3.2)

5.4 Implications to studies on natural systems

The new experimental data presented in this study is of great value for a better interpretation of natural S-isotope compositions detected e.g. in pumices, scoria or volcanic gases. Ohba et al. (2008), for instance, applied the chemical trap method (using KOH solution) to monitor the volcanic gas signature at Miyakejima (Japan). The authors estimated a $\Delta^{34}S_{gas-magma}$ of about -0.3 to -1.0 ‰ for two degassing periods (2001 to summer 2002; summer 2002 to 2005). Ohba et al. (2008) noted that the fO_2 required to produce the observed fractionation may be about QFM+1.3 to QFM+1.9 and, thus, ~0.5 log units higher than estimated petrologically by Yasuda et al. (2001). Ohba et al. (2008) proposed a fluid-melt disequilibrium in terms of fO_2 to explain the observed discrepancies. However, the results of Ohba et al. (2008) rely on calculation procedures of Marini et al. (1998) for the estimation of α_{g-m} for a given

fO₂, *fH₂O* and *T*. The Marini et al. (1998) model is comparable to that of de Hoog et al. (2001) and also lacks for two of the predominant S-isotope fractionation pairs (see Section 5.1). Considering the new experimental results presented in this study, the isotopic fractionation determined by Ohba et al. (2008) may be explained by comparable redox conditions as determined by Yasuda et al. (2001). This example shows that our findings need to be considered for the interpretation of magmatic S-isotope signature. However, the *T* dependence still needs to be verified to allow the application to a wide range of magmatic systems.

6. CONCLUSION

A new experimental approach was applied to investigate S-isotope fractionation between fluid and silicate melt. The obtained results provide, for the first time, constraints on fluid-melt S-isotope fractionation at geologically relevant *p-T* condition with close to natural fluid-melt compositions.

The data shows that previous models (e.g. de Hoog et al., 2001) based on experiments using simple compositions (e.g. molten salt Na_2SO_4 and Na_2S analogies), theoretical or compilation type studies from the 70s and 80s (summarized by Taylor, 1986) may significantly underestimate the isotopic fractionation. Reasons for the observed discrepancies may be *i)* fundamental mistakes of previously published models and *ii)* the very limited data available in literature on S-isotope fractionation, which is probably not applicable to magmatic systems.

In general, measuring S-isotope compositions of volcanic material can be of great importance to investigate degassing processes (e.g. distinguish between open and closed system degassing), understand atmospheric transport processes of volcanic gas-ash-clouds and/or assess the source(s) of volatiles in magmatic systems. The presented data will help to understand and interpret related S-isotope signatures and especially isotopic data of reduced systems may need to be re-interpreted. The observed independence of α_{g-m}, on the bulk Cl content indicates that the estimated fractionation factors and trends may be applicable to complex multi-component fluid-melt systems.

CHAPTER III

DISTRIBUTION OF S AND S-ISOTOPES BETWEEEN H$_2$O-S±CL FLUIDS AND BASALTIC MELT

ABSTRACT

Decompression experiments (from 400 to 70 MPa) were conducted to investigate the sulfur (S) distribution and S-isotope fractionation between basaltic melts and coexisting fluids. Volatile-bearing [~3 to ~7 wt% water (H$_2$O), ~300 to ~1200 ppm S, 0 to ~3600 ppm chlorine (Cl)] basaltic glasses were used as starting material. The MgO content in the melt was either ~1 wt% (Mg-poor basalt) or ~10 wt% (alkali basalt) to investigate the role of compositional changes on S distribution. The experiments were performed in internally heated pressure vessels (IHPV) at 1050°C to 1250°C, variable oxygen fugacities (fO_2; ranging from log(fO_2/bar) ~QFM to ~QFM+4; QFM = quartz-fayalite-magnetite buffer) and at a constant decompression rate (r) of 0.1 MPa/s. The annealing time (t_A) at final pressure (p) and temperature (T) after decompression was varied from 0 to 5.5 h to study the fluid-melt equilibration process.

S and H$_2$O contents in the melt decreased significantly during decompression, while the Cl contents in the melt remained almost constant. No changes in H$_2$O and Cl content were observed with t_A, while S decreased slightly with t_A < 2 h; i.e. fluid-melt near-equilibrium conditions were reached within ~2 h after decompression, even in experiment performed at the lowest T of 1050°C. Thus, fluid-melt partitioning coefficients of S ($D_S^{fl/m}$) were determined from experiments with $t_A \geq 2$ h.

The experiments showed that MgO (~1 to 10 wt%), H$_2$O (~3 to ~7 wt%) and Cl content (< 0.4 wt%) in the melt have no significant effect on $D_S^{fl/m}$. Consistent with previous studies, $D_S^{fl/m}$ decreased strongly with increasing fO_2; e.g. at ~1200°C $D_S^{fl/m} \approx 180$ at QFM+1 and $D_S^{fl/m} \approx 40$ at QFM+4. A positive correlation was observed between $D_S^{fl/m}$ and T in the range of 1150 to 1250°C at both oxidizing (QFM+4; $D_S^{fl/m} = 52 \pm 27$ to 76 ± 30) and intermediate (QFM+1.5; $D_S^{fl/m} = 94 \pm 20$ to 209 ± 80) redox conditions. Data compiled at 1050°C and reducing conditions (~QFM; $D_S^{fl/m} = 58 \pm 18$) indicated that the trends may be extrapolated to 1050°C, at least for intermediate to reducing conditions.

The S-isotope composition in glasses of selected samples was measured by secondary ion mass spectrometry (SIMS). Gas-melt isotopic fractionation factors (α_{g-m}) were calculated via mass balance. At 1200°C an average α_{g-m} of 0.9981 ± 0.0015 was determined for oxidizing conditions (~QFM+4), while an average α_{g-m} of 1.0025 ± 0.0010 was estimated for fairly reducing conditions (~QFM+1). Under reducing conditions (~QFM) and 1050°C an average α_{g-m} of 1.0037 ± 0.0009 was determined. The data showed that equilibrium fractionation effects during closed system degassing of basaltic melts at T relevant for magmatic systems (1050 to 1250°C) can induce an S-isotope fluid-melt fractionation of about +4 ‰ in reduced systems and of about -2 ‰ in oxidized systems.

1. INTRODUCTION

S is the third most abundant volatile in natural silicate melts (besides H_2O and CO_2) and the highest concentrations are found in basaltic magmas which often contain >>1000 ppm S (e.g. Perfit et al., 1983; le Roux et al., 2006; Moune et al., 2007; Wallace and Edmonds, 2011). During crystallization, S is mainly incorporated in accessory phases (mainly sulfides, e.g. Parat et al., 2011) but a significant fraction of S is also released to the fluid phase in late stage crystallization processes or upon decompression due to high fluid-melt partitioning coefficients ranging from 1 to 2800 (Keppler, 1999; Newman and Lowenstern, 2002; Lesne et al., 2011; Webster and Botcharnikov, 2011; Witham et al., 2012). Such magmatic S-bearing fluids have a crucial role in the formation of high T ore deposits (e.g. porphyry-type) or can be responsible for the release of high amounts of S to the atmosphere in case of volcanic eruptions, leading e.g. to climate impact (see review of Oppenheimer et al., 2011).

The distribution of S between fluid and basaltic melt at (near-) equilibrium conditions has been investigated in a few studies within the last decades; however, the dataset is still patchy. The existing data on basaltic melt compositions (and other compositions) has been summarized in the review of Webster and Botcharnikov (2011). The available S fluid-melt partitioning dataset is obtained in basaltic melts for T ranging from 1050 to 1150°C, fO_2 varying from $\log(fO_2/\text{bar}) \approx$ QFM to QFM+3.2 [hereafter differences of $\log(fO_2/\text{bar})$ to the quartz-fayalite-magnetite (QFM) buffer are given to

specify fO_2] and a p range of 25 to 800 MPa (Teague et al., 2008; Moune et al., 2009; Beermann et al., 2011; Lesne et al., 2011; Webster and Botcharnikov, 2011). Additional experiments of Gorbachev (1990) conducted at 500 MPa and 1100°C are difficult to interpret because fO_2 is not reported.

None of the available studies systematically investigated the influence of T on the fluid-melt partitioning coefficient of S ($D_S^{fl/m}$) in basaltic systems. Noteworthy, Lesne et al. (2011) observed a significant compositional effect on $D_S^{fl/m}$ in basaltic systems implying that the data obtained in different studies at T of 1050 to 1150°C for different compositions cannot be compiled to extract a general temperature effect on $D_S^{fl/m}$.

The influence fO_2 on $D_S^{fl/m}$ in basaltic systems was investigated by Beermann (2010). The author observed, for instance, that $D_S^{fl/m}$ increases from 27 ± 7 at QFM+3.2 to 200 ± 51 at QFM+0.7 in Cl-bearing (~0.05 to ~0.55 wt% Cl) trachybasaltic systems at 200 MPa and 1050°C. The only systematic work investigating the influence of p on $D_S^{fl/m}$ in basaltic systems was published by Lesne et al. (2011). The experiments were conducted under intermediate to oxidizing conditions (QFM+1.7 to QFM+3.1), at 1150°C and 25 to 400 MPa and reveal that $D_S^{fl/m}$ increases strongly from ~10 to ~40 at 100 MPa to ~600 to ~3000 at 25 MPa in basaltic systems.

Recent studies show that the role of other volatiles present in the melt phase may influence significantly $D_S^{fl/m}$. A strong influence of H_2O content in the systems on $D_S^{fl/m}$ is indicated by the results of Moune et al. (2009), but was not yet confirmed by systematic experimental investigations. Beermann (2010) observed a significant increase of $D_S^{fl/m}$ along with increasing Cl content in the basaltic systems, e.g. under oxidizing conditions (~QFM+2) $D_S^{fl/m}$ increases from ~1 at 0.05 wt% bulk Cl in the system to ~96 at ~3.5 wt% Cl. A similar positive correlation between Cl content and $D_S^{fl/m}$ was observed for phonolitic (Webster et al., 2009) and andesitic melts (Chapter I-A), while data Botcharnikov et al. (2004) for rhyodacitc systems indicate a slight negative correlation between Cl content and $D_S^{fl/m}$. The influence of Cl on $D_S^{fl/m}$ is not fully understood, however, the authors suggested that this effect can possibly be attributed to changes in fluid and melt properties, to non ideal mixing in the fluid phase and/or to interactions between the volatiles (e.g. H_2O, Cl, S) as well as between volatiles and cations within the melt and the coexisting fluid phase.

More experimental data and thermodynamic models on equilibrium distribution of S between fluid and (basaltic) melt are crucially needed to interpret the composition of gases released on top of active volcanoes and to relate magmatic processes at depths with the response at the surface (via changes of the gas composition). However, two additional types of information are necessary to fully interpret the S signatures in volcanic gases: *i)* kinetic studies are required to check for the conditions (e.g. decompression rate) at which equilibrium fluid-melt S distribution is occurring during degassing of ascending magmas and *ii)* the S-isotope fractionation between fluid and silicate melt must be known to interpret the isotopic composition of volcanic gases.

Although disequilibrium distribution of S between fluids and melts may be of minor importance in basaltic systems due to the low melt viscosity and fast diffusion of volatiles within the melt, kinetic effects may be expected in basaltic systems with very fast ascent rates (e.g. ≥ 0.1 MPa/s). However, all available studies on fluid-melt distribution of S in basaltic systems are based on equilibrium experiments and kinetic experiments are needed to evaluate whether kinetic degassing effects of S occur in basaltic systems or not.

Degassing of S is accompanied with S-isotope fractionation effects between fluid and silicate melt. The isotopic fractionation depends mainly on *T* (e.g. Mandeville et al., 2009) and on speciation of S in both phases (Mandeville, 2010) but the isotopic fractionation between S species in fluid and (silicate) melt at magmatic conditions is not well constrained. The existing models (e.g. Marini et al., 1998; de Hoog et al., 2001) are based on one experimental study of the S-isotope fractionation between fluid and melt conducted by Miyoshi et al. (1984) as well as on theoretical data of Richet et al. (1977). However, Miyoshi et al. (1984) used molten salt as melt phase and the applicability of the data to silicate melt systems can be questioned because the tendency to retain ^{34}S in salt melts upon decompression is probably not equivalent to that in silicate melts. Fiege (Chapter II) performed experiments using an andesitic system and determined a fluid-melt S-isotope fractionation of about +4 to +10 ‰ at 1030°C (i.e. melt becomes enriched in ^{34}S upon degassing) at reducing conditions and of about -2 ‰ (i.e. melt becomes depleted in ^{34}S upon degassing) at oxidizing conditions. The large scatter at reducing conditions is attributed to the lack of data at very low fO_2, at which S in the fluid-melt system is fully reduced (~QFM); i.e. the existing data were extrapolated from ~QFM+1 to

~QFM. Thus, more experimental data are urgently required to constrain the fractionation factor at reducing conditions, to determine the T dependence of the fractionation and to verify the applicability of the fractionation factors determined for an andesitic melt by Fiege (Chapter II) to other silicate melt compositions.

In this study, degassing of basaltic melts containing up to 1200 ppm S was simulated by decompression experiments to study the influence of fO_2 on $D_S^{fl/m}$ and α_{g-m} as well as of T on $D_S^{fl/m}$ and α_{g-m} in basaltic systems. The experiments were performed at different oxygen fugacities with $\log(fO_2/\text{bar})$ ranging from ~QFM to ~QFM+4 and at T of 1050 to 1250°C. The initial H_2O and Cl content in the melt varied in the range of 3 to 7 wt% and 0 to 3600 ppm, respectively, which allows us to determine the influence of bulk H_2O and Cl content on $D_S^{fl/m}$. To understand the possible influence of melt polymerization and, thus, of S-diffusivity and kinetics of S-degassing, the MgO content in the anhydrous starting glasses was either ~1 or ~10 wt%; i.e. $X_{Mg} = MgO/(MgO+FeO_{tot})$ molar ratio in the melt ranges from ~0.2 to ~0.7 (FeO_{tot} = total iron concentration in the glass given in FeO). The variation of the MgO content allows us to study possible effects of changes in basaltic melt composition on $D_S^{fl/m}$ at almost constant FeO_{tot} content (note: FeO is known to have a strong influence on S-solubility; see e.g. review of Wallace and Edmonds, 2011).

Decompression experiments using volatile bearing basaltic melts were carried out at a constant continuous r of 0.1 MPa/s and with t_A ranging from 0 to ~5 h to study fluid-melt equilibration processes. Experiments quenched directly after decompression ($t_A = 0$ h) may represent disequilibrium conditions, while decompression experiments followed by annealing for ~5 h at constant T and p may represent equilibrium or at least near-equilibrium conditions. Possible kinetic effects may be preserved in samples with $t_A = 0$ h. On the other hand, determined $S_{(fluid)}/S_{(melt)}$ ratios of samples with $t_A = 5$ h may represent the partitioning coefficient $D_S^{fl/m}$, i.e. a thermodynamic quantity.

Finally the S-isotope composition of selected starting glasses and partially degassed glasses was analyzed by SIMS to allow us to estimate the fluid-melt S-isotope fractionation during decompression.

2. EXPERIMENTS

2.1 Improvement of experimental strategy for basaltic systems

A primary objective of this study is to investigate the kinetics of S and S-isotope degassing in basaltic systems at geologically relevant T (e.g. ~1050 to ~1250°C) via decompression experiments. However, conducting (decompression) experiments with S-bearing melts at $T > 1050$°C (i.e. close or above the melting point of Au) is problematic because typical noble metal containers for higher T (Pt, AuPd) are known to react with a S-bearing fluid-melt system. Containers such as olivine (Beermann et al., 2011) or quartz glass (Fleet et al., 1991) are useless for continuous decompression experiments as differences between p inside the capsules and p inside the vessel during decompression cannot be ruled out. Lesne et al. (2011) developed a new experimental approach using AuPd capsules, which allows one to conduct experiments at $T > 1050$°C and which is based on the mixture of carbonate and oxide powders, a decarbonization step and the addition of H_2O as brucite. However, this method is constrained by a major disadvantage since the starting composition of the melt is calculated via weighed in properties and may vary significantly between each synthesis. In addition, AuPd was found to be not flexible enough to conduct continuous decompression at rates of ~0.1 MPa/s; i.e. the capsules usually fail during decompression. Hence, a new experimental approach was developed to allow us to conduct continuous decompression experiments at $T > 1050$°C.

Several experimental methods were tested. For instance, preliminary syntheses conducted in AuPd or Pt capsules usually failed after very short time (< 10 min), probably due to the reaction of a high-T acidic S-rich fluid with the capsule material. Such a reaction was mentioned in previous studies and is directly related to the siderophile character of Pd and Pt (e.g. Webster and Botcharnikov, 2011). Beyond that, the addition of H_2O as brucite [$Mg(OH)_2$] in order to delay the formation of a aggressive S-rich fluid during heating (see Lesne et al., 2011) was also quite unsuccessful. In addition, Fe can diffuse into the AuPd or Pt capsule material (e.g. Barr and Grove, 2010), which may lower the melting point of the capsule material significantly and can cause capsule failure. However, Fe-loss to a Pt-capsule wall was found to be of minor importance if run durations are short (< 6 h, see Section 4). Moreover, test decompression experiments showed that the Pt-capsule will not fail (or lose significant

amounts of iron) if H_2O and S were already dissolved in the melt before conducting the experiment. Based on these experiences, the following experimental procedure was successfully applied.

2.2 Experimental procedure

In a *first step* a synthetic anhydrous MgO-free glass with a composition typical for an alkali basalt (composition OB93 used by Freise et al., 2009) was prepared by melting a mixture of oxide (Al_2O_3, SiO_2, TiO_2, Fe_2O_3, MgO, Mn_2O_3) and carbonate (Na_2CO_3, $CaCO_3$, K_2CO_3) powders in a $Pt_{90}Rh_{10}$ crucible at 1600°C and 1 atm. for 2 h. The crucible was quenched in a water bath. The glass was ground, melted (1600°C, 1 atm., 2 h) and quenched again to improve homogeneity. Part of this glass was enriched in Mg (using dried MgO powder), following the same procedure, to produce *i)* a Mg-poor basaltic glass (~1 wt% MgO added) and *ii)* a Mg-rich alkali basaltic glass (~10 wt% MgO added). The Mg-poor basalt and the alkali basalt served as starting material for the following decompression experiments. The compositions of the obtained anhydrous starting glasses are listed in Table 1.

In a *second step* volatile enriched [H_2O, S, (Cl)] starting glasses were synthesized in IHPV using either the Mg-poor basalt or the alkali basalt. These syntheses were conducted in Au capsules (6 mm inner diameter; 0.2 mm wall thickness) at 1050°C (sub-liquidus), ~500 MPa and fO_2 ranging from ~ QFM+0 to ~QFM+4. Water was added using deionized H_2O, Cl using 10 wt% HCl_{aq} and S using gypsum ($Ca[SO_4] \times 2H_2O$); added volatile contents: ~3 to ~7 wt% H_2O, ~300 to ~1200 ppm S; 0 to ~3600 ppm Cl. The mixtures were filled stepwise into Au-capsules and compressed by a piston to minimize entrapped air and welded shut. The obtained glasses contain significant amounts (about 10 vol%) of S-free crystals (typically olivine (ol), clinopyroxene (cpx) and (titano-) magnetite (mt), depending e.g. on fO_2) as they were carried out at sub-liquidus conditions.

Third, ~200 mg of crushed and grounded glass were loaded into Pt capsules (diameter = 4 mm; wall thickness = 0.2 mm), compressed with a piston and welded shut. The samples were placed in an IHPV and annealed for ~10 min at 400 MPa, 1150 or 1200°C and ~QFM+0 to ~QFM+4 to dissolve the crystals in the melt and determine the starting conditions (e.g. melt composition including H_2O, S and

Cl content as well as S-isotope composition). This step only applies for experimental series conducted at T above the melting point of Au (i.e. it does not applied to the series ABLA and ABLClA, Table 2). In a *fourth* step, isothermal decompression experiments were conducted in IHPV at 1050 to 1250°C in Au (1050°C) or Pt capsules (>1050°C) at fO_2 ranging from ~QFM to ~QFM+4. The capsules had a length of ~18 mm (diameter = 4 mm; wall thickness = 0.2 mm) to allow expansion of the loaded material (~150 mg of crushed and ground glass) during decompression. Again the material was compressed with a piston to minimize entrapped air and welded shut. Thus, almost cylindrical melt reservoirs are generated during the experiment (diameter: ~2.5 to 4.5 mm; height: ~4 mm) which minimizes the influence of the capsule wall on the fluid-melt system in the center of the cylinder. The samples were annealed for short term (~10 min) prior to decompression and, subsequently, p was released continuously from ~400 to ~70 MPa at a constant rate of ~0.1 MPa/s. The samples were either directly quenched (isobaric, rapid-quench technique) after decompression to preserve fluid-melt non-equilibrium conditions or annealed for various times (t_A = 0 to ~20 h for 1050°C experiments and t_A = 0 to ~5 h for experiments at T > 1050°C) at final p-T conditions before quenching to approach fluid-melt near-equilibrium conditions. The experimental conditions of the conducted syntheses and decompression experiments are listed in Table 2.

Table 1: Composition [wt%] of the anhydrous MgO-free, MgO-poor basalt, alkali basalt glasses. The composition was measured via EMP (see Section 3.1.1)

[wt%]	SiO$_2$	TiO$_2$	Al$_2$O$_3$	FeO$_{tot}$†	MnO	MgO	CaO	Na$_2$O	K$_2$O	P$_2$O$_5$	Total
MgO-free	54.30	2.89	16.42	11.86	0.14	-	10.06	3.37	1.01	0.44	100.48
basalt	*0.29*	*0.05*	*0.16*	*0.24*	*0.10*	-	*0.07*	*0.13*	*0.02*	*0.04*	*0.44*
MgO-poor	52.46	2.80	16.14	10.98	0.15	0.94	10.55	3.31	1.03	0.41	98.79
basalt	*0.41*	*0.05*	*0.14*	*0.15*	*0.11*	*0.03*	*0.08*	*0.08*	*0.02*	*0.03*	*0.62*
alkali	46.78	2.72	14.87	10.57	0.14	10.52	9.80	2.93	0.92	0.40	99.64
basalt	*0.49*	*0.05*	*0.18*	*0.31*	*0.08*	*0.45*	*0.15*	*0.47*	*0.06*	*0.05*	*1.19*

Notes: italic values: standard deviations (1 sigma) based on microprobe analyses; number of EMP analyses per sample: 20
† FeO$_{tot}$: total iron concentration in the glass given as FeO

Table 2: Experimental conditions and results.

Sample ID	X_{Mg}	T [°C]	t_A [h]	ΔQFM	$Fe^{3+}/\Sigma Fe$ corr.	$S^{6+}/\Sigma S$	S [ppm]	H_2O [wt%]	Cl [wt%]	$D_S^{fl/m}$
ABWB-0x #			†	3.4 (a)	0.51	*1.04*	1181 ± 23	4.73 ± 0.09	xx	xx
ABWB-1 ¶			0	4.1 (a)	0.53	*1.03*	967 ± 32	2.24 ± 0.10	xx	9 ± 1
ABWB-2 ¶	~0.7	1200	2	4.1 (a)	0.51	*1.05*	886 ± 23	2.45 ± 0.10	xx	14 ± 1
ABWB-3 ¶			5	4.1 (a)	0.50	*1.04*	840 ± 43	2.36 ± 0.09	xx	17 ± 1
ABWB-4 ¶			1	4.1 (a)	0.53	*1.02*	923 ± 17	2.43 ± 0.08	xx	12 ± 1
ABWClE-0x #			†	3.5 (a)	nd	*1.04*	1160 ± 18	4.84 ± 0.10	0.131 ± 0.006	xx
ABWClE-1 ¶			0	4.1 (a)	nd	*1.04*	941 ± 46	2.39 ± 0.09	0.158 ± 0.006	10 ± 1
ABWClE-2 ¶	~0.7	1200	2	4.1 (a)	nd	*1.05*	959 ± 22	2.53 ± 0.09	0.145 ± 0.004	9 ± 1
ABWClE-3 ¶			5	4.1 (a)	nd	*1.03*	854 ± 10	2.49 ± 0.09	0.150 ± 0.006	15 ± 1
ABWClE-4 ¶			1	4.1 (a)	nd	*1.04*	991 ± 14	2.42 ± 0.09	0.135 ± 0.004	7 ± 1
ABWCl-F0x #			†	2.9 (a)	nd	*1.03*	992 ± 27	2.97 ± 0.12	0.090 ± 0.004	xx
ABWCl-F1 ¶			0	4.1 (a)	nd	*1.03*	894 ± 14	2.23 ± 0.09	0.098 ± 0.005	15 ± 1
ABWCl-F2 ¶	~0.7	1200	2	4.1 (a)	nd	*1.04*	871 ± 36	2.14 ± 0.09	0.099 ± 0.003	17 ± 1
ABWCl-F3 ¶			5	4.1 (a)	nd	*1.04*	826 ±14	2.23 ± 0.09	0.088 ± 0.003	25 ± 3
ABWCl-F4 ¶			1	4.1 (a)	nd	*1.03*	936 ± 34	2.23 ± 0.09	0.088 ± 0.004	8 ± 1
ABWClDx-0x #			†	3.7 (a)	nd	0.97	1156 ± 20	5.75 ± 1.03	0.048 ± 0.005	xx
ABWClDx-2 ¶	~0.2	1200	2	4.1 (a)	nd	*1.03*	650 ± 10	3.29 ± 1.27	0.053 ± 0.005	31 ± 14
ABWClDx-4 ¶			1	4.1 (a)	nd	*1.03*	654 ± 22	2.45 ± 1.11	0.047 ± 0.009	23 ± 12
ABLC36-0 #		1150	†	3.6 (a)	nd	1.00	704 ± 9	4.92 ± 0.88	xx	xx
ABLC36-1 ¶	~0.2	1150	5	4.1 (a)	nd	*1.01*	291 ± 18	1.89 ± 0.60	xx	46 ± 17
ABLC36-2 ¶		1250	5.5	4.1 (a)	nd	0.98	247 ± 31	2.09 ± 0.84	xx	64 ± 29
ABLB-0 #		1150	†	3.6 (a)	nd	0.87	811 ± 11	5.62 ± 1.22	xx	xx
ABLB-1 ¶		1150	5	4.1 (a)	nd	*1.09*	296 ± 36	2.03 ± 0.69	xx	48 ± 20
ABLB-2 ¶	~0.2	1250	5.5	4.1 (a)	nd	0.95	211 ± 12	2.46 ± 0.34	xx	88 ± 23
ABLB-3 ¶		1200	5	4.1 (a)	nd	*1.06*	287 ± 14	2.04 ± 0.89	xx	50 ± 25
ABLClD-0 #		1150	†	3.5 (a)	nd	0.94	786 ± 12	4.94 ± 0.91	0.219 ± 0.012	xx
ABLClD-1 ¶	~0.2	1150	5	4.1 (a)	nd	0.95	268 ± 45	1.94 ± 0.64	0.197 ± 0.009	63 ± 26
ABLClD-3 ¶		1200	5	4.1 (a)	nd	0.97	270 ± 15	2.07 ± 0.80	0.208 ± 0.010	65 ± 28
Ba12 *			†	0.58	nd	nd	895 ± 62	4.87 ± 0.56	xx	xx
Ba12-1 ¶	~0.7	1150	0	1.64	nd	0.03	357 ± 57	3.07 ± 0.20	xx	81 ± 18
Ba12-2 ¶			0	1.64	nd	0.04	428 ± 17	2.93 ± 0.23	xx	55 ± 9
AB36A-0 #		1150	†	1.17	0.29	0.02	790 ± 26	6.52 ± 0.42	xx	xx
AB36A-1 ¶		1150	5	1.78	0.31	0.79	130 ± 21	1.62 ± 0.09	xx	102 ± 19
AB36A-3 ¶	~0.7	1250	5	1.59	0.30	0.65	80 ± 20	2.42 ± 0.98	xx	212 ± 103
AB36A-4 ¶		1200	5.5	1.00	0.17	0.04	111 ± 11	2.28 ± 0.12	xx	142 ± 20
AB36ClA-0 #		1150	†	1.81	nd	*-0.02*	689 ± 17	6.04 ± 0.42	0.361 ± 0.010	xx
AB36ClA-1 ¶		1150	5	1.78	nd	0.64	163 ± 27	2.32 ± 0.12	0.369 ± 0.012	86 ± 17
AB36ClA-3 ¶	~0.7	1250	5	1.59	nd	0.63	70 ± 12	1.83 ± 0.63	0.330 ± 0.006	206 ± 80
AB36ClA-4 ¶		1200	5.5	1.00	nd	0.01	146 ± 12	2.20 ± 0.17	0.370 ± 0.007	96 ± 13
ABLC-0x #			†	0.78	nd	0.01	772 ± 63	4.18 ± 0.36	xx	xx
ABLC-2 ¶	~0.2	1200	0	0.82	nd	0.01	118 ± 21	2.37 ± 0.15	xx	123 ± 27
ABLC-3 ¶			2.1	1.17	nd	0.13	74 ± 15	2.66 ± 0.48	xx	272 ± 82

Table 2: Experimental conditions and results. *Continuation*

Sample ID	X_{Mg}	T [°C]	t_A [h]	ΔQFM	$Fe^{3+}/\Sigma Fe$ corr.	$S^{6+}/\Sigma S$	S [ppm]	H_2O [wt%]	Cl [wt%]	$D_S^{fl/m}$
ABLClF-0 #			†	0.83	nd	0.10	532 ± 13	5.03 ± 0.95	0.192 ± 0.003	xx
ABLClF-2 ¶			0	0.82	nd	0.03	177 ± 18	2.23 ± 0.15	0.178 ± 0.007	71 ± 16
ABLClF-3 ¶	~0.2	1200	2.1	1.17	nd	0.13	64 ± 9	2.48 ± 0.52	0.195 ± 0.020	283 ± 93
ABLClF-4 ¶			5.5	0.80	nd	0.15	68 ± 9	2.38 ± 0.16	0.180 ± 0.011	252 ± 63
ABLClF-5 ¶			2	0.49	nd	0.12	80 ± 7	2.05 ± 0.13	0.183 ± 0.004	188 ± 42
ABGA-0 #	~0.2	1200	†	-0.30	nd	*-0.02*	317 ± 10	3.23 ± 0.15	xx	xx
ABGA-1 ¶			0	1.20	nd	nd	191 ± 19	2.28 ± 0.13	xx	68 ± 9
ABGAx-0x #			†	0.63	0.28	*-0.02*	717 ± 51	5.83 ± 0.35	xx	xx
ABGAx-1x ¶			0	1.19	0.21	0.08	207 ± 20	2.48 ± 0.13	xx	73 ± 11
ABGAx-2x ¶	~0.2	1200	2	0.96	0.35	0.10	121 ± 7	2.75 ± 0.80	xx	157 ± 49
ABGAx-3 ¶			5	1.14	0.33	0.09	92 ± 8	2.02 ± 0.68	xx	175 ± 63
ABGAx-4 ¶			1	0.98	0.22	*-0.02*	164 ± 13	2.54 ± 0.49	xx	100 ± 23
ABGClA-0 #	~0.2	1200	†	-0.01	nd	*-0.01*	441 ± 26	3.01 ± 0.19	0.044 ± 0.006	xx
ABGClA-1 ¶			0	1.20	nd	nd	238 ± 12	2.53 ± 0.13	0.039 ± 0.004	167 ± 33
ABGClAx-0x #			†	0.78	nd	*-0.02*	864 ± 19	7.07 ± 0.47	0.090 ± 0.002	xx
ABGClAx-1x ¶			0	1.19	nd	0.00	407 ± 41	2.91 ± 0.15	0.083 ± 0.005	27 ± 4
ABGClAx-2x ¶	~0.2	1200	2	0.96	nd	0.10	102 ± 11	2.44 ± 0.87	0.084 ± 0.004	159 ± 61
ABGClAx-3 ¶			5	1.14	nd	0.09	135 ± 16	2.09 ± 0.63	0.083 ± 0.002	107 ± 36
ABGClAx-4 ¶			1	0.98	nd	*-0.02*	211 ± 8	2.43 ± 0.56	0.088 ± 0.004	65 ± 16
ABGClB-0 #	~0.2	1200	†	0.19	nd	*-0.01*	403 ± 23	3.75 ± 0.16	0.098 ± 0.006	xx
ABGClB-1 ¶			0	1.20	nd	0.08	186 ± 13	2.45 ± 0.20	0.098 ± 0.004	88 ± 13
ABGClBx-0x #			†	0.63	nd	*-0.01*	881 ± 21	6.73 ± 0.46	0.103 ± 0.005	xx
ABGClBx-1x ¶			0	1.19	nd	*-0.01*	218 ± 76	2.93 ± 0.15	0.086 ± 0.004	78 ± 29
ABGClBx-2x ¶	~0.2	1200	2	0.96	nd	0.13	114 ± 9	2.67 ± 0.75	0.095 ± 0.004	163 ± 50
ABGClBx-3 ¶			5	1.14	nd	0.11	124 ± 15	2.26 ± 0.80	0.092 ± 0.003	135 ± 52
ABGClBx-4 ¶			1	0.98	nd	0.01	223 ± 16	2.68 ± 0.61	0.090 ± 0.005	72 ± 19
ABGClC-0x #			†	0.87	nd	*-0.02*	802 ± 15	6.74 ± 0.36	0.222 ± 0.013	xx
ABGClC-1x ¶			0	1.19	nd	*-0.02*	331 ± 65	2.76 ± 0.13	0.203 ± 0.019	35 ± 8
ABGClC-2x ¶	~0.2	1200	2	0.96	nd	0.16	113 ± 7	3.01 ± 0.84	0.237 ± 0.006	162 ± 48
ABGClC-3 ¶			5	1.14	nd	0.11	96 ± 10	2.76 ± 0.81	0.224 ± 0.008	182 ± 59
ABGClC-4 ¶			1	0.98	nd	*-0.01*	202 ± 28	2.24 ± 0.51	0.204 ± 0.008	65 ± 18
ABLA §			†	0.01	0.20	0.01	581 ± 13	6.12 ± 0.26	xx	xx
ABLA-1 §			5.1	-0.03 (b)	0.23	*-0.01*	241 ± 96	2.89 ± 0.29	xx	43 ± 18
ABLA-2 §	~0.6	1050	0	-0.03 (b)	0.15	*-0.01*	216 ± 18	2.86 ± 0.20	xx	51 ± 6
ABLA-3 §			0	-0.06 (b)	0.17	0.03	210 ± 23	2.81 ± 0.20	xx	53 ± 7
ABLA-5 §			2	-0.15 (b)	0.18	0.09	177 ± 11	3.04 ± 0.17	xx	73 ± 7
ABLClA §			†	0.29	nd	nd	617 ± 24	6.10 ± 0.43	0.132 ± 0.004	xx
ABLClA-1 §			5.2	-0.07 (b)	nd	nd	231 ± 30	2.73 ± 0.18	0.143 ± 0.012	49 ± 9
ABLClA-3 §	~0.6	1050	0	-0.06 (b)	0.16	0.11	270 ± 17	2.77 ± 0.18	0.129 ± 0.002	38 ± 5
ABLClA-5 §			2	-0.15 (b)	nd	0.07	200 ± 12	2.90 ± 0.16	0.133 ± 0.006	64 ± 8

Notes: Sample ID: starting glasses are written in *italic*; t_A: annealing time at final conditions; *ΔQFM:* Nominal fO_2 determined using the *Shaw*-membrane technique or (a) intrinsic redox conditions determined by Berndt et al. (2002), see Section 2.3 – (b) *Shaw*-membrane blocked, fO_2 calculated using the initially loaded H_2 pressure; $Fe^{2+}/\Sigma Fe$ *corr.*: analytical error < 0.12 (2 σ), raw data was corrected for Fe^{3+} reduction by S^{2-} during sample digestion (see Section 3.2); $S^{6+}/\Sigma S$: error probably > 0.1 values in parenthesis refer to samples with very low sulfur content in the melt (< 300 ppm) leading to (very) noisy XANES spectra (see text); *italic* font indicates that the estimated $S^{6+}/\Sigma S$ ratios should be equal to 1 when > 1 or 0 when < 0;

Table 2: Experimental conditions and results. *Continuation*

Synthesized in Au capsules and annealed for 10 min in Pt capsules (see Section 2.2); ¶ Pt capsules; *AuPd capsules; § Au capsules; †: see Section 2.2 for details on the run durations of the syntheses; xx: not relevant or 0; nd: not determined / no measurement conducted;

Initial p of the decompression experiments was 400 MPa. Samples were annealed for ~10 min prior to decompression. The p was released continuously to 70 MPa ($r \sim 0.1$ MPa/s); see Section 2.2 for details on experimental procedure. Most partially degassed samples contain Au- or Pt-globules depending on capsule material.

2.3 Redox conditions

The fO_2 prevailing in the capsules of syntheses and experiments were indirectly adjusted via the hydrogen fugacity (fH_2) of the pressure vessel, considering that hydrogen (H_2) diffuses through the capsule wall and controls fO_2 by reaction with H_2O: $H_2 + \frac{1}{2} O_2 \leftrightarrow H_2O$. Oxidized syntheses and experiments were carried out in IHPV without *Shaw*-membrane using pure Ar gas. These IHPV contain H_2 as an impurity and the intrinsic redox conditions were estimated to be QFM+3.9 at a H_2O activity $a(H_2O)$ of 1 (Berndt et al., 2002; Wilke et al., 2002; Schuessler et al., 2008). Intermediate to reducing redox conditions were adjusted using an Ar-H_2 gas mixture as pressure-medium and the prevailing fH_2 during the experiment was continuously recorded using a *Shaw*-membrane (Berndt et al., 2002). After quenching the sample, fH_2 in the vessel was measured while maintaining the final p-T conditions. Noteworthy, the *Shaw*-membrane was partly obstructed during decompression experiments of the series ABLA and ABLClA conducted at 1050°C and under reducing conditions (~QFM). Thus, in a first approximation the initially loaded H_2-pressure (~13 bars) was used to roughly estimate the fO_2 in the vessel. However, these values may only represent a lower limit of the fO_2 adjusted in the capsule due to expected H_2 loss from the vessel upon p release (see below, this Section).

The $a(H_2O)$ of all syntheses was calculated using the approach of Burnham (1979) to account for the influence of H_2O on the redox conditions inside the capsules. The equation 1 in Chapter I-A was applied to estimate the nominal fO_2 of the starting glasses for given $a(H_2O)$ (see also Jugo et al., 2010). On the other hand, $a(H_2O)$ of the decompression experiments was always close to one (fluid phase contains minor amounts of S and Cl only) and fO_2 was calculated assuming $a(H_2O) = 1$.

Noteworthy, decompression induced changes in redox conditions within the vessel and inside the capsule are to be expected, e.g. due to increasing $a(H_2O)$ in the melt and decreasing fH_2 in the vessel

during decompression (see Chapter I-A and references therein). In addition, consistent with observations in Chapter I-A, a preferential loss of H_2 through the decompression valve was observed which also leads to a significant decrease of fH_2 in the vessel during p release. Thus, fO_2 cannot be kept absolutely constant during decompression. Nevertheless, syntheses and experiments of one experimental series were always carried out under similar redox conditions; i.e. the estimated fO_2 values are typically identical within error (± 0.5 log units; see Table 2).

To account for the expected loss of H_2, selected experiments (experimental series labeled with ABG, see Table 2) were conducted with higher H_2 partial pressures than would be required for isobaric experiments (i.e. the loaded H_2-pressure was a factor ~1.6 higher than the H_2-pressure applied for the isobaric synthesis of starting glasses). From the determination of the H_2-pressure at the end of the experiment, a loss of H_2 by a factor of 1.2 to 12.3 (average 6.7) is observed for experiments carried out at T $\geq$ 1150°C. This loss is slightly higher than that observed in Chapter I-A for decompression experiments conducted at 1030°C. The higher loss can be explained by the high initial H_2-pressure loaded into the vessel for the experiments of this study (typically 5 to 20 bars). It is emphasized that the loading of H_2 in excess to the vessel cannot fully compensate the H_2 loss upon decompression. However, the nominal fO_2 values of these decompression experiments are relatively close to the nominal fO_2 of the starting glasses (difference is typically < 0.5 log units).

The decompression induced changes of fH_2 in the vessel and of fO_2 inside the capsule imply that a re-adjustment via H_2 diffusion through the capsule wall and within the sample occurs during the experiment. The time required for fH_2 and fO_2 equilibration significantly depends on T and capsule material. The permeability of H_2 is significantly lower through Au (by a factor of ~2) than through Pt (Chou, 1987). Considering the influence of T on the permeability, H_2 may be transported about 5 times faster through the Pt capsule wall of experiments conducted at 1200°C than through the Au wall of the 1050°C experiments. The equation provided by Zhang and Ni (2010) based on the H_2 diffusion data of Shelby (1977) and Shang et al. (2009) can be used to roughly estimate the time required for fH_2 equilibration within the melt (see also Chapter I-A). However, the estimation may provide minimum durations, as the solubility of H_2 in the melt plays a crucial role to H_2 mobility (e.g. Gaillard et al., 2003). The calculations indicate that the time needed for H_2 to diffuse from the wall to the center of

the capsule will decrease by a factor of ~1.5 if T increases from ~1050 to ~1200°C. Hence, the fO_2 equilibration after decompression may be significantly faster (by a factor of > 7) for experiments conducted at $T \geq 1150$°C in Pt-capsules in comparison to those performed at 1050°C in Au-capsules.

Noteworthy, decompression experiments with andesitic melt performed at 1030°C in Au-capsules (Chapter I-A) indicate that (near-) redox equilibrium conditions between the vessel and the fluid-melt system inside the capsule are already achieved during or shortly after decompression a an r of ~0.1 MPa/s. Thus, redox equilibrium is assumed for all experimental results presented in this study.

In addition to the estimation of fO_2 from the H_2-pressure [$fO_2(nominal)$], S and Fe speciation data obtained for selected run products were used to estimate the fO_2 in the experiments. The derived values are compared to the estimated $fO_2(nominal)$ to evaluate the accuracy and applicability of $fO_2(nominal)$; see Section 4.1. However, if not specified differently, the fO_2 values reported in the following sections refer to $fO_2(nominal)$.

3. ANALYTICAL METHODS

3.1 Glass composition

3.1.1 Electron microprobe (EMP)

The glass compositions of the quenched samples (except for the H_2O content) were determined using a Cameca SX-100 electron microprobe (EMP, 15 keV acceleration voltage; 20 μm beam size). Na was analyzed at a beam current of 5 nA for 4 s (counting time). This setting was applied to minimize the Na migration during EMP measurements (Morgan and London, 1996, 2005). The major constituents (Si, Ti, Al, Fe, Mn, Mg, Ca, K, P) were measured with a beam current of 10 nA and a counting time of 10 s. Counting time and beam current were further increased to 120 s and 35 nA for Cl and to 240 s and 35 nA for S to improve counting statistics (detection limit: ~32 ppm for S, ~50 ppm for Cl). NIST (U. S. National Institute of Standards and Technology) standard glasses 610 and 620 were measured during each microprobe sessions to evaluate the accuracy of the measurements and to allow a correction of the raw S data. The relative deviation of S contents from the value given for the standard glasses is < 5 % [NIST 610 contains ~560 ppm S (Evans et al., 2008; Guillong et al., 2008; Webster et al., 2009) and NIST 620 ~1120 ppm; see https://www-s.nist.gov/srmors/].

3.1.2 H₂O determination

Near infra-red (NIR) measurements were conducted on doubly polished glass chips to determine the H_2O concentrations in the glasses. The thickness of the prepared sections ranges from ~50 to ~300 μm, depending on the translucency of the respective samples. The NIR spectra were collected using a Bruker IFS 88 FTIR spectrometer equipped with a Bruker IRscope II IR microscope. A tungsten light source, a CaF_2 beam splitter, and a mercury-cadmium-tellur (MCT) narrow range detector were used in the measurements. 100 scans were accumulated for each spectrum (spectral resolution: 4 cm^{-1}) and 3 spots were analyzed on each glass sample. The concentrations (in wt%) of OH groups *c(OH)* and molecular H_2O *c(H₂O)* dissolved in the basaltic glasses was determined using the heights (absorbances) of the bands at 4500 cm^{-1} (OH groups) and 5200 cm^{-1} (H_2O) respectively and applying the following equations (Lambert-Beer law):

$$c(H_2O) = \frac{1802 \cdot A(H_2O)}{d \cdot \rho} \cdot \frac{1}{\varepsilon(H_2O)} \qquad (1)$$

$$c(OH) = \frac{1802 \cdot A(OH)}{d \cdot \rho} \cdot \frac{1}{\varepsilon(OH)} \qquad (2)$$

where *d* is the thickness of the section in cm and *ρ* is the density of the glass in g/L. *A(H₂O)* and *A(OH)* refer to the absorbance of molecular H_2O and OH groups, respectively. *ε(H₂O)* and *ε(OH)* are the linear molar absorption coefficient in L mol^{-1} cm^{-1} of the respective NIR peak. The total H_2O content is the sum of *c(H₂O)* and *c(OH)*.

The densities (*ρ*) of the glasses were estimated using the relationship provided by Ohlhorst et al. (2001) for basaltic melts. Densities calculated using the empirical equation given by Shishkina et al. (2010) for basaltic glasses are consistent with the calibration of Ohlhorst et al. (2001); i.e. densities differ by < 3 % for water contents ranging from 0 to 10 wt%. To verify the applicability of the equation given by Ohlhorst et al. (2001) to melt compositions of this study, the densities were also calculated from glass compositions using the Gladstone-Dale rule (Gladstone and Dale, 1863; see Chapter I-A for details). The deviation of the densities estimated using the linear relation given by

Ohlhorst et al. (2001) from the *Gladstone-Dale* densities was found to be $\ll 1\%$, independent of the melt composition (i.e. Mg-free, Mg-poor or alkali basalt).

Tangential baseline correction was applied to determine the heights of the water bands. Absorption coefficients can change as a function of melt composition (Silver et al., 1990). To test the applicability of the coefficients given in the literature, selected starting glasses were analyzed by Karl-Fischer titration (KFT, see methods in Behrens, 1995; Leschik et al., 2004; Behrens et al., 2009). For the determination of absorption coefficients, additional water-bearing glasses with water contents ranging from 1.7 to 8.5 wt% were synthesized (~1200°C, 500 MPa) and measured by KFT and NIR. These glasses contain 0, ~1 and ~8 wt% MgO, corresponding to a X_{Mg} of 0 to ~0.7, to account for a possible influence of Mg content on the calibration.

In Fig. 1 the normalized absorbances of both NIR bands are plotted against each other (relevant data is listed in Table III-A1 in the Appendix III) together with the calibrations for basaltic glasses proposed by Ohlhorst et al. (2001) and Shishkina et al. (2010). The samples with X_{Mg} of ~0.7 correlate well with the regression line of Ohlhorst et al. (2001) indicating that this calibration is applicable to all experimental glasses with alkali basaltic composition ($\varepsilon(H_2O) = 0.56$ L mol^{-1} cm^{-1} and $\varepsilon(OH) = 0.56$ L mol^{-1} cm^{-1}). This observation is confirmed by Fig. 2a showing that the total water content (based on KFT measurements) is well reproduced in the range of ~2 to ~6 wt% H_2O. Noteworthy, the basaltic melt studied by Ohlhorst et al. (2001) is characterized by a similar X_{Mg} of ~0.7. On the other hand, starting glasses synthesized at 1050°C, showing a X_{Mg} of ~0.55 in the melt, plot perfectly on the calibration line of Shishkina et al. (2010) for basaltic melts with similar X_{Mg} of ~0.6, indicating that the linear molar absorption coefficient given by these authors can be used to determine the H_2O contents of experimental samples conducted at 1050°C ($\varepsilon(H_2O) = 0.65$ L mol^{-1} cm^{-1} and $\varepsilon(OH) = 0.69$ L mol^{-1} cm^{-1}). In contrast, the data of glasses containing 0 to 1 wt% MgO (X_{Mg}: 0 to ~0.2) cannot be described by the calibrations of Ohlhorst et al. (2001) and Shishkina et al. (2010). Thus, regressions were performed for all Mg-free and Mg-poor (~1 wt% MgO) samples, respectively. A third regression was determined based on both sets of glasses (Mg-free and Mg-poor). The absorption coefficients derived from this regression ($\varepsilon(H_2O) = 0.848$ L mol^{-1} cm^{-1} and $\varepsilon(OH) = 1.161$ L mol^{-1} cm^{-1}) were used to estimate the water content by NIR in the Mg-poor glasses. The calculated NIR water content

correlates well with the bulk KFT water content (Fig. 2b), at least in the range of 2 to 8 wt% H_2O, and

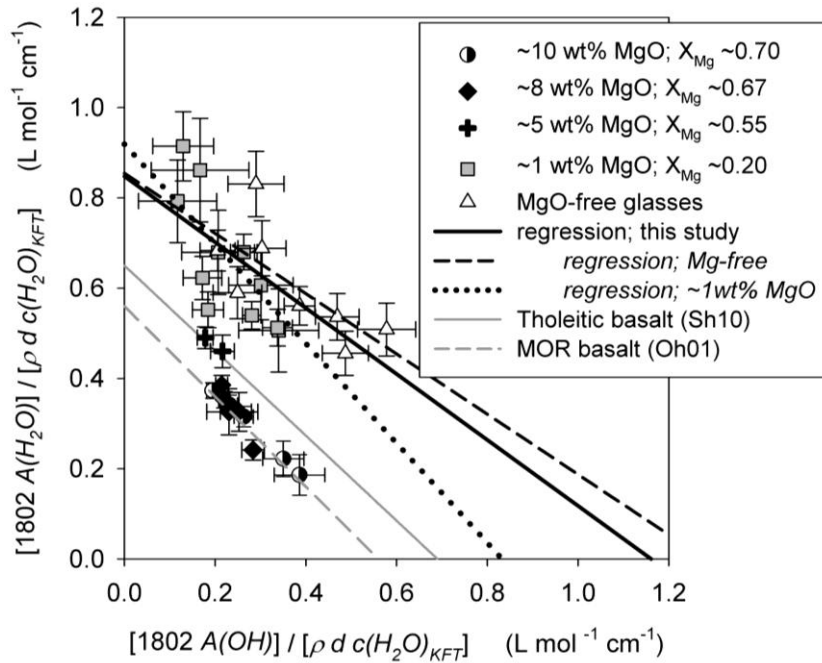the difference between KFT and NIR determination is typically < 0.2 wt% H_2O.

Fig. 1: Calibration plot for the absorption coefficients of the OH and H_2O combination bands in the NIR.
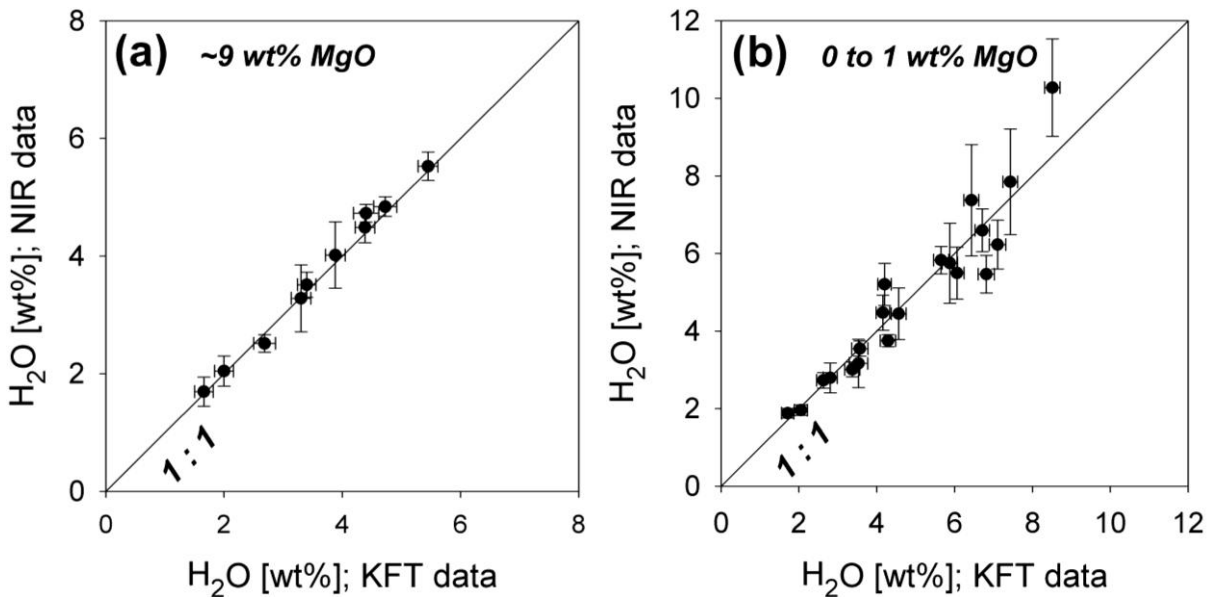Sh02: Shishkina et al. (2010); Oh01: Ohlhorst et al. (2001)

Fig. 2a-b: a) NIR H_2O contents vs. KFT H_2O contents for alkali basalt glasses. **b)** NIR H_2O contents vs. KFT H_2O contents for Mg-poor basalt glasses.
The NIR H_2O contents were calculated using either (**a**) the absorption coefficients provided by Ohlhorst et al. (2001) for basalts or (**b**) the new absorption coefficients determined for Mg-poor and Mg-free basalts (see Section 3.1.2).

3.1 S-isotope composition in the glasses

The $^{34}S/^{32}S$ ratios were measured in selected glasses (prior to decompression and after decompression) using the Cameca IMS 1280 at Woods Hole Oceanographic Institution (WHOI). The analyses were carried out using a 10 µm Cs^+ primary beam with an acceleration voltage of 10 kV and a beam current of 1-2 nA. The secondary ions produced by the primary beam are collected at 10 kV acceleration voltage with a 150 µm field of view and a mass resolving power of 5500. The energy slit is centered and opened to ~50 V. These settings have proven their reliability in previous sessions and allow to determine the S-isotope composition in (silicate) glasses with low S contents (<<1000 ppm) with an external precision of ~0.5 ‰; see Mandeville et al. (2008) and Chapter II.

Measurements of Charles W. Mandeville and Nobumichi Shimizu on silicate glasses with compositions ranging from basaltic to high silica and $\delta^{34}S$ ranging from about -30 ‰ to about +20 ‰ [determined by conventional bulk S-isotope methods, e.g. KIBA reagent extraction method (Sasaki et al., 1979; Ueda and Sakai, 1984; Mandeville et al., 2009)] show that the instrumental fractionation is independent of melt composition and follows a linear trend. Thus, routine measurements of a basaltic glass standard with well known S-isotope composition ($\delta^{34}S$ ~ 0.7 ‰) allow to determine the instrumental fractionation and correcting the raw $^{34}S/^{32}S$ ratios. In order to monitor short (and long) term variations of the instrumental fractionation, this basaltic glass standard was measured (at least) twice before and after 2 to 3 sample measurements. Each sample was analyzed 2 to 5 times depending on the quality of the single measurement (e.g. the internal standard deviation) and each measurement consists of 50 to 60 cycles for ^{32}S and ^{34}S, respectively.

This analytical approach is equivalent to the procedure applied by Fiege (Chapter II) for andesitic melts. Thus, the raw data was processed following the same procedure as described in Chapter II (i.e. see Appendix II-C.).

The S-isotope composition will be reported in a conventional delta (δ) notation given in ‰ (equation 3). The Vienna Canyon Diablo Troilite (V-CDT) was used as S-isotope reference standard (Coplen and Krouse, 1998; Ding et al., 2001). The $\Delta^{34}S_{g-m}$ values as well as the gas-melt isotopic fractionation factors α_{g-m} were estimated using equation 4.

$$\delta^{34}S = (\ [\ (^{34}S/^{32}S_{sample})\ /\ (^{34}S\ /\ ^{32}S_{V\text{-}CDT})\ ]-1\ )\cdot 1000 \tag{3}$$

$$\Delta^{34}S_{g\text{-}m} = \delta^{34}S_{gas} - \delta^{34}S_{melt} \approx 10^3\ ln\ \alpha_{g\text{-}m} \tag{4}$$

3.2 S and Fe speciation

S K-edge (ca. 2.47 keV) XANES analyses were carried out using the SUL-X beamline at the synchrotron radiation source ANKA (Karlsruhe Institute of Technology, Germany) to determine the S speciation in the basaltic glasses. The ANKA storage ring (circumference: 110.4 m) operates at a beam energy of 2.5 GeV and a beam intensity of 200 mA. The SUL-X beamline uses a wiggler as radiation source. The energy of the monochromator was calibrated to the white line of S^{6+} in scotch tape (2481.4 eV). The spectra were collected in fluorescence mode from ~2.45 to ~2.55 keV and with a beam size of about 200 μm × 100 μm. Quick-XAFS scans (bragg axis is continuously running; XAFS: X-ray absorption fine structure) were performed to avoid irradiation damages [relevant details for quick-XAFS: ~330 motorsteps/s; energy increments: 0.3 eV in the edge region (~2.46 to ~2.50 keV) and 1 eV in the pre- and post-edge region].

The energies of the derived spectra were corrected to the white line of the spectrum of gypsum (2482.84) to allow an estimation of fO_2 within the capsule based on the model of Jugo et al. (2010) for basaltic melt. The method relies on the estimation of the $S^{6+}/\Sigma S$ ratio in a first step, followed by the calculation of fO_2. Noteworthy, some $S^{6+}/\Sigma S$ ratios are below 0 or above 1, indicating the limitation of the approach for relatively oxidized or reduced systems (see Table 2). In accordance with the equations provided by Jugo et al. (2010), it is assumed that $S^{6+}/\Sigma S$ ratios ≥ 1 indicate an fO_2 of $\geq$ QFM+4.2 and $S^{6+}/\Sigma S$ ratios ≤ 0 may refer to an fO_2 of $\leq$ QFM-0.8. However, these values have high uncertainty. The approach applied for the fO_2 estimation using S-XANES spectra is described in detail in Chapter I-A.

The bulk Fe speciation of selected experimental samples, conducted at ~QFM+1 to ~QFM+4, was measured by colorimetric wet-chemical analyses (Schuessler et al., 2008). The derived $Fe^{3+}/\Sigma Fe$ values were corrected for Fe^{3+} reduction by S^{2-} during sample digestion according to the findings of Sossi and O'Neill (2011) and using the $S^{6+}/\Sigma S$ ratios determined by XANES (see also Chapter I-A).

The corrected $Fe^{3+}/\Sigma Fe$ ratios are listed in Table 2 and are used to further constrain the redox conditions inside the capsule (see Section 4.1).

4. RESULTS

Syntheses and experiments performed at 1050°C contain significant amounts of crystals, while samples carried out at higher T (1150 to 1250°C) are crystal-free (Fig. 3). All decompression experiments are vesiculated, indicating that volatiles are released to a fluid phase upon decompression. The amount of bubbles decreases upon further annealing after decompression and, simultaneously, the bubbles (or fluid pools) are growing (compare Fig. 3a and 3b) and often migrating to the capsule wall (compare Fig. 3c and 3d). The crystals observed in the samples performed at 1050°C and ~QFM comprise ol (Fo_{80}) and sometimes smaller amounts of cpx ($En_{40}Wo_{48}Fs_{12}$); see Fig. 3e and 3f. The size of the crystals in the starting glasses ranges between 5 and 25 μm in diameter and was found to increase slightly upon decompression (~5 to ~35 μm). The crystal size remains constant during further annealing after decompression. The crystal volume fraction does not change significantly during decompression and upon annealing after decompression (~10.2 ± 2.6 vol%; determined via point counting method).

The bulk composition – analyzed by EMP and IR spectroscopy (H_2O content) – of all volatile-bearing starting glasses and experimental glasses performed at 1150 to 1250°C are similar within error (2 sigma) to the respective anhydrous starting glasses (alkali basalt of Mg-poor basalt) if H_2O, S and Cl are subtracted and oxides are normalized to 100 wt%. Experiments conducted at 1050°C show slight differences in melt compositions when compared to the starting glasses, induced by the crystallization of ol (and cpx). The average MgO and FeO contents re-calculated on an anhydrous basis are ~5.0 wt% and ~9.6 wt%, respectively, and lower than those in the anhydrous alkali basaltic starting glass, while all other constituents show slightly higher concentrations.

The glasses of all samples are chemically homogenous and show typically no detectable concentration gradients between fluid pools or towards the capsule wall. However, the FeO content of some glasses from experiments performed in Pt capsules at $T \geq 1150$°C tends to be slightly lower than in the corresponding starting glass. In addition, EMP data of a few experiments (ABLClF-5, ABGAx-1x,

ABGClC-1x) indicates a small decrease of the FeO content (by < 10 %) from the center to the wall of the capsule. However, the FeO contents of glasses in the center of the capsules are always similar within error to the concentration in the corresponding starting glass. EMP measurements of the Pt capsule materials of decompression experiments (run duration: ~6 h; 1200°C) reveal that the first few μm (< 20 μm) of the capsule wall may contain up to ~3 wt% FeO under reducing conditions (~QFM+1) and up to ~1 wt% FeO under oxidizing conditions. However, the FeO content in the Pt capsule wall decreases to zero 10 to 20 μm away from the melt-wall interface. These profiles can be used to roughly estimate the Fe-loss to the capsule wall using mass balance calculations. The calculations indicate that the Fe-loss to the capsule wall relative to the initial FeO content in the melt is < 1 % for experiments conducted under reducing conditions and < 0.5 % for experiments performed under oxidizing conditions. It is assumed that these minor changes in melt composition, related to the Fe-loss to the capsule wall, are not affecting the degassing processes of H_2O, S and Cl upon decompression.
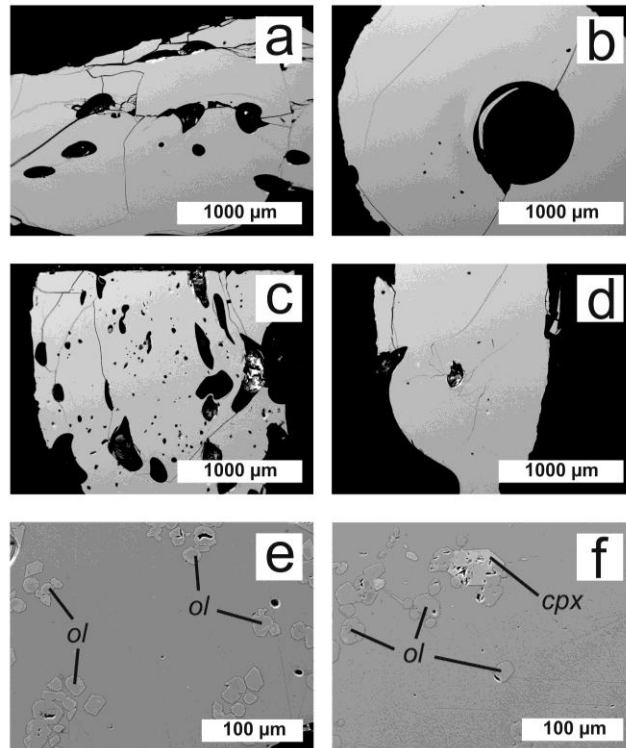

Fig. 3a-f: BSE images of selected decompression experiments ($r = 0.1$ MPa/s). **a)** Experiment ABLClF-2 (T = 1200°C; $t_A = 0$ h); **b)** ABLClF-4 (1200°C; 5.5 h); **c)** ABLA-3 (1050°C; 0 h). **d)** ABLA-1 (1050°C; 5 h); **e)** ABLA-3 (1050°C; 0 h). **f)** ABLClA-1 (1050°C; 5 h).
ol: Olivine; cpx: Clinopyroxene

4.1 Speciation of S and Fe in the melt

The redox equilibrium between vessel and melt interior after decompression can be tested using S and Fe speciation data obtained via S-XANES and Fe-colorimetric analyses. Fig. 4a indicates that the $Fe^{3+}/\Sigma Fe$ ratios of most samples analyzed correlate well with $fO_2(nominal)$, following the trends predicted by computation models (Kress and Carmichael, 1991; Moretti, 2005). Most points plot close to the trends calculated by the model of Kress and Carmichael (1991) and this model is used to estimate the fO_2 inside the capsule based on $Fe^{3+}/\Sigma Fe$ ratios $[fO_2(Fe)]$. Fig. 4b indicates that the derived $fO_2(Fe)$ values show generally a good correlation with $fO_2(nominal)$. The calculated $fO_2(Fe)$ values of five samples (ABLA, -1; ABGAx-0x, -2x, -3) are ~0.8 to ~1.2 log units higher than $fO_2(nominal)$. These discrepancies possibly refer to uncertainties of the computation model used for the estimation of $fO_2(Fe)$; e.g. the influence of p on $Fe^{3+}/\Sigma Fe$ at given fO_2 is probably underestimated by the model of Kress and Carmichael (1991). On the other hand, uncertainties in the $S^{6+}/\Sigma S$ ratio, estimated using XANES spectra, and used to correct the measured $Fe^{3+}/\Sigma Fe$ ratios can easily cause artificially high $Fe^{3+}/\Sigma Fe$ ratios. This is supported by Fig. 4c, indicating that the estimated $S^{6+}/\Sigma S$ ratios are generally in accordance with the $fO_2(nominal)$ at oxidizing conditions, but may differ significantly (by > 1 log unit) at intermediate to reducing redox conditions. The deviations observed for several partially degassed samples performed at < QFM+2 is most likely related to the bad quality of the XANES spectra of glasses with low S contents (< 300 ppm). In addition, the integral method suggested by Jugo et al. (2010) to quantify fO_2 via S-XANES spectra of reduced glasses may only provide a rough estimation of fO_2 because a sharp S^{2-} peak at ~2472 eV is not considered (see also Chapter I-A). Indeed, the glasses of three out of five samples showing significant discrepancies between $fO_2(Fe)$ and $fO_2(nominal)$ contain < 250 ppm S and XANES spectra of all five samples show a distinct S^{2-} feature at about 2472 eV. In addition, according to Baker and Moretti (2011), the fO_2 at which the S^{6+}/S^{2-} ratio in the melt equals 0.5 (sulfide/sulfate transition) can change significantly with changing melt composition, p and T; i.e. the sulfide/sulfate transition (at 100 MPa) may drift by ~1 log unit towards more oxidizing conditions for H_2O saturated melts when compared to H_2O poor melts. Considering that the applied S-XANES calibration provided by Jugo et al. (2010) relies on hydrous but typically not H_2O-saturated basaltic glasses synthesized at 1050°C and 200 MPa, the sulfide/sulfate transition in

the glasses of this study, which are often H_2O saturated, may be at slightly higher fO_2 than suggested

by Jugo et al. (2010). This could also explain the deviations observed in Fig. 4c.

A comparison of the fO_2 calculated using S-XANES spectra [$fO_2(XANES)$] with $fO_2(Fe)$ confirms the

large uncertainty of the XANES data obtained for reduced samples (Fig. 4d). As expected from the

discussion above, $fO_2(XANES)$ and $fO_2(Fe)$ are in good agreement under intermediate to oxidizing

redox conditions ($\geq$ QFM+1.5) but may differ significantly (by ~0.7 to 2.5 log units) under reducing

conditions (< QFM+1). Noteworthy, four out of six samples showing significant deviations between

$fO_2(XANES)$ and $fO_2(Fe)$ refer to XANES spectra from which a $S^{6+}/\Sigma S$ ratio < 0 was extracted, which

is certainly impossible (AB36-0; ABLA-1; ABGAx-0x, -4). Thus, these $fO_2(XANES)$ values have to be

interpreted with caution. In addition, the glasses of the problematic samples often contain < 250 ppm S

and typically show a sharp S^{2-} peak at ~2472 eV.

Furthermore, as mentioned previously, the *Shaw*-membrane was obstructed during experiments of the

series ABLA and ABLClA. It is emphasized that the Fe and S speciation data available for these

experiments (see Table 2) indicate similar fO_2 values (average values: $\log(fO_2(Fe)/\text{bar}) \sim$ QFM+0.3;

$\log(fO_2(XANES)/\text{bar}) \sim$ QFM+0.1) as estimated based on the H_2-pressure initially loaded to the vessel

(~QFM).

To conclude, the good correlation between the prevailing fO_2 in the vessel [$fO_2(nominal)$] and $fO_2(Fe)$

(Fig 4a and 4b) indicates that $fO_2(nominal)$ provides a good estimation of the prevailing fO_2 in the

capsule even for experiments quenched directly after decompression. Hence, re-adjustment between

the redox conditions in the vessel and within the sample is fast and (near-) redox equilibrium between

vessel and melt interior is achieved during decompression, confirming previous estimations based on

H_2 permeability (see Section 2.3 and Chapter I-A). In the following sections, $fO_2(nominal)$ will be

used to interpret and discuss the obtained results.
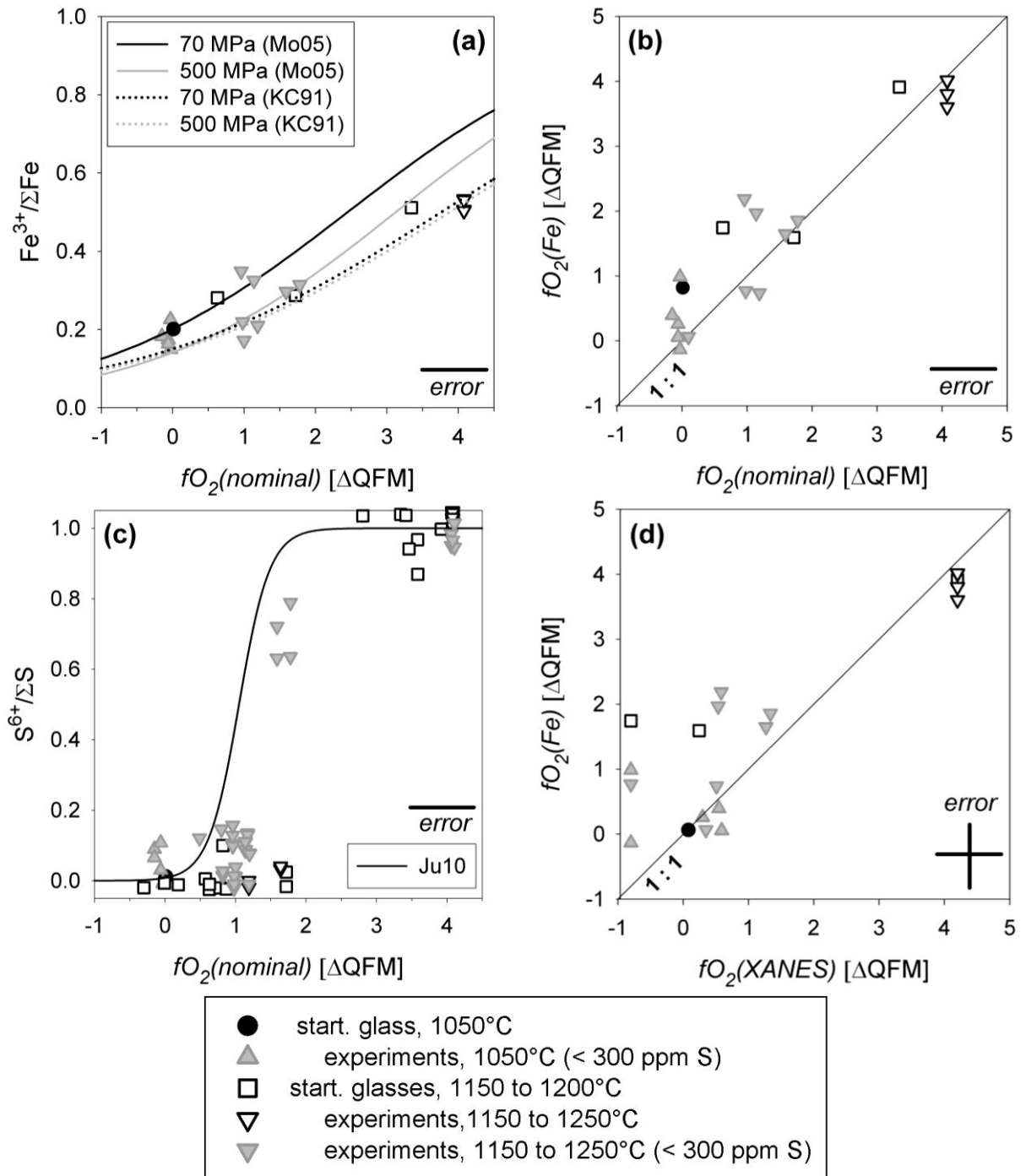
Fig. 4a-d: Comparison of the redox conditions in the vessel with Fe- and S-speciation data. **a)** $Fe^{3+}/\Sigma Fe$ vs. $fO_2(nominal)$ in the vessel. **b)** $fO_2(Fe)$ in the capsule vs. $fO_2(nominal)$ in the vessel. **c)** $S^{6+}/\Sigma S$ vs. $fO_2(nominal)$ in the vessel. **d)** $fO_2(Fe)$ in the capsule vs. $fO_2(XANES)$ in the capsule.
$fO_2(nominal)$, prevailing fO_2 in the vessel determine using either the H_2-pressure measured in the *Shaw*-membrane or the (known) intrinsic redox conditions in the vessel.
$fO_2(Fe)$, calculated using the corrected Fe-colorimetric data and the model of Kress and Carmichael (1991).
$fO_2(XANES)$, based on XANES data, determined using the approach of Jugo et al. (2010).

4.2 Fluid-melt distribution of H_2O, S and Cl

The distribution of volatiles between fluid and melt under fluid-melt equilibrium is described by the partitioning coefficients $D^{fl/m}$ (for S: $D_S^{fl/m}$), where

$$D^{fl/m} = X_{(fluid)} / X_{(melt)} \qquad\qquad (5)$$

and X is the concentration in wt% of the volatile in the fluid and in the melt, respectively. H_2O, S and Cl contents in the starting glasses and in the partially degassed glasses of the decompression experiments were measured (EMP and IR) and used to estimate the volatile contents in the fluid phase by mass balance calculations. The derived $X_{(fluid)}$ / $X_{(melt)}$ ratios may not represent equilibrium conditions. Thus, the term $D*_S^{fl/m}$ is used in the following to describe the S fluid-melt distribution for kinetic experiments, while $D_S^{fl/m}$ (= partitioning coefficient) is used when near-equilibrium conditions are evident.

Noteworthy, the alkali basaltic starting glass was used for most experiments conducted under oxidizing conditions, while most experiments carried out under intermediate (~QFM+1.5) to reducing conditions ($\leq$ QFM+1) have Mg-poor basaltic composition. In the following sections results for Mg-poor basalt with $X_{Mg} \approx 0.2$ and alkali basalt with $X_{Mg} \approx 0.7$ will be compared to evaluate the possible effects of melt composition on fluid-melt distribution of S.

4.2.1 Evolution of H_2O contents during decompression and annealing

The H_2O content in the melt decreases significantly during decompression from 400 to 70 MPa ($r = 0.1$ MPa/s) and remains constant upon further annealing at final p-T conditions ($t_A = 0$ to 5.5 h; see Fig. 5a, 5b and 6a; Table 2). Melt composition (i.e. bulk H_2O, S, Cl and MgO content) and fO_2 have no significant effect on the H_2O content at final p of 70 MPa (values are similar within error). H_2O contents measured in glasses of decompression experiments conducted at 1150 to 1250°C are always between 2.0 and 3.0 wt% H_2O (47 experiments) except for four experiments which are slightly below 2.0 wt% H_2O and three experiment with slightly more than 3.0 wt% H_2O. For these last experiments, the error bar is relatively high because IR-glass sections were thin (< 100 µm). An

average value of 2.4 ± 0.4 wt% H_2O is obtained for data at 1150 to 1250°C and this value is within the error of all analyzed glasses, except for experiment AB36A-1 (see Table 2 and Fig. 5a and 5b). Glasses of decompression experiments conducted at 1050°C show slightly higher H_2O contents with an average of 2.9 ± 0.2 wt% (Fig. 6a; H_2O contents range from ~2.7 to ~3.0 wt% at 1050°C and 70 MPa), when compared to those performed at higher T. This may be due to a slight negative correlation between H_2O solubility and T at 70 MPa, which is in accordance with previous studies (e.g. Holtz et al., 1995), or due to the slightly different melt composition at 1050°C (see Section 4.).

The average H_2O contents estimated for glasses of experiments carried out at 1050°C and 1150 to 1250°C, respectively, are similar within error to the H_2O solubility in basaltic melt at 70 MPa calculated using *VolatileCalc* (Newman and Lowenstern, 2002) and the empirical model of Moore et al. (1998); i.e. a H_2O solubility of ~2.5 to 3.0 wt% is predicted by these models. The constant H_2O contents of the melt, independently on t_A, as well as the good agreement with the H_2O solubility data indicate that H_2O contents in melts from all decompression experiments are close to equilibrium values.

4.2.2 Evolution of Cl contents during decompression and annealing

The Cl contents in the partially degassed glasses of the decompression experiments are similar within error to the starting glasses (Table 2). Thus, only minor amounts of Cl are released into the fluid phase and $D_{Cl}^{fl/m}$ is close to 1, in agreement with previous data on CO_2-free basaltic systems (Webster et al., 1999; Chevychelov et al., 2008), and $D_{Cl}^{fl/m}$ will not be discussed in the following sections. However, the obtained results are used to evaluate the interaction between S and Cl in basaltic systems (see Sections 4.2.3 and 5.3).

4.2.3 Evolution of S fluid-melt distribution during decompression and annealing

The S content in the melt decreases strongly during decompression from 400 to 70 MPa (Fig. 5c, 5d and 6b). As illustrated in Fig. 5c and 5d, the S release depends strongly on the prevailing fO_2. For instance, about 10 to 37 % (average: 21 ± 12 %) of the initial S in the melt is released to the fluid upon decompression at QFM+4 and 1200°C, while about 40 to 75 % (average: 59 ± 12 %) are released at

Fig. 5a-f: Evolution of the H_2O and the S content in the melt and of the S fluid-melt distribution at 1200°C. **a)** H_2O content vs. t_A at oxidizing conditions (~QFM+4). **b)** H_2O content vs. t_A at reducing conditions (~QFM+1). **c)** S content vs. t_A at oxidizing conditions (~QFM+4). **d)** S content vs. t_A at reducing conditions (~QFM+1). **e)** $D^{*}{}_{S}{}^{fl/m}$ vs. t_A at oxidizing condition (~QFM+4). **f)** $D^{*}{}_{S}{}^{fl/m}$ vs. t_A at reducing conditions (~QFM+1).

~QFM+1 and 1200°C. In addition, experiments conducted at oxidizing conditions show that the initial S content (ranging from ~800 to ~1200 ppm) significantly affects the final S content in the melt after decompression (t_A = 0h). The small range of initial S contents in the reduced melts (~690 to ~880 ppm S) does not allow one to identify a possible correlation with the final S content in the melt. Under oxidizing conditions, the Mg content in the melt (X_{Mg}: ~0.2 or ~0.7) influences the final S content. For instance, melts with initial S contents of ~1200 ppm show a final concentration of ~650 ppm when $X_{Mg} \approx 0.2$ and a final concentration of ~930 ppm when $X_{Mg} \approx 0.7$ (all other experimental conditions being identical, Fig 5c). Such an effect of X_{Mg} on final S content in the melt is not observed at reducing conditions. An influence of the initial Cl content in the melt (0 to 3600 ppm) on S content in the melt with t_A is not observable.

The S contents in the glasses remain almost constant upon further annealing at final *p-T* (contents are typically identical within error), independently on fO_2, *T* or melt composition. However, some experimental series indicate a slight decrease of the S content in the melt within the first 2 h of annealing. Thus, it is proposed that fluid-melt near-equilibrium with respect of S fluid-melt distribution is achieved at least for $t_A \geq 2$ h.

In line with observations made for the evolution of the S (this Section), Cl (Section 4.2.2) and H_2O (Section 4.2.1) contents in the melt with t_A, $D*_S^{fl/m}$ was found to increase slightly between t_A = 0 to 2 h (Fig. 5e, 5f and 6c) and to remain constant when $t_A \geq 2$ h. Thus, $D*_S^{fl/m}$ values of experiments with $t_A \geq 2$ h should represent near-equilibrium conditions; i.e. $D*_S^{fl/m} = D_S^{fl/m}$. Changes in initial S and Cl content in the melt have no significant effect on $D*_S^{fl/m}$ in agreement with previous studies (e.g. data in Chapter I-A; Keppler, 2010; Zajacz et al., 2012). An influence of initial H_2O content, ranging from ~3 to ~7 wt%, is also not observed i.e. the derived $D*_S^{fl/m}$ values are typically similar within error (see Fig. 5 and 6 and data Table 2). This indicates that S obeys Henry's law in basaltic systems, at least for the studied range of bulk H_2O and S contents, which is consistent with previously published data for more evolved magmatic systems (e.g. Keppler, 2010; Zajacz et al., 2012); see also Fig. III-B.1 in Appendix III. Under reducing conditions (~QFM+1) no influence of X_{Mg} is indicated by the data (Fig. 5f). Under oxidizing conditions (~QFM+4), the $D*_S^{fl/m}$ values obtained for alkali basalts (X_{Mg}: ~0.7) are slightly lower than those determined for Mg-poor basalts (X_{Mg}: ~0.2) (Fig. 5e). However, the error

bars of the $D*_S^{fl/m}$ values for Mg-poor basalts are large and values obtained for alkali basalts are often identical within error.
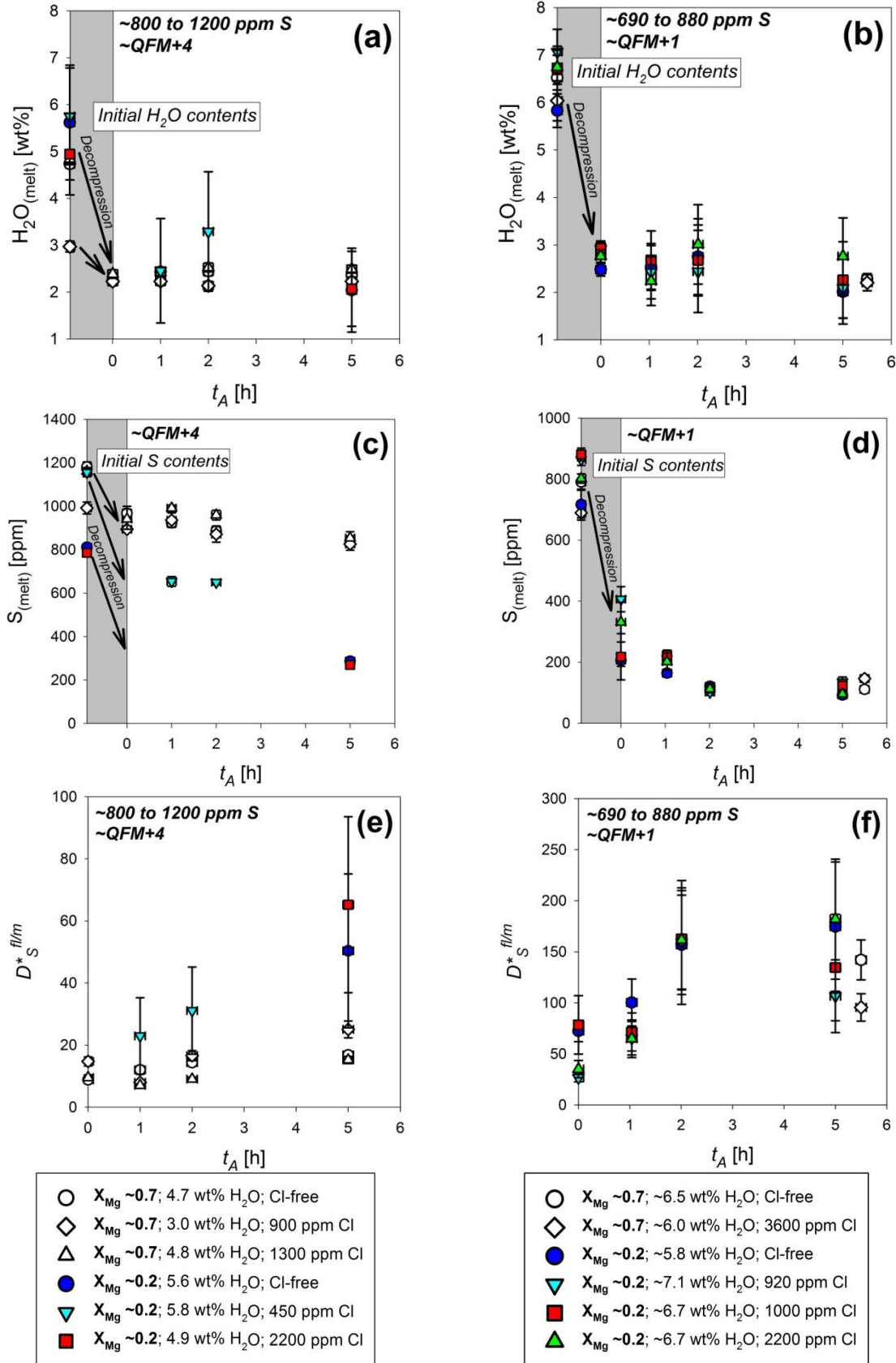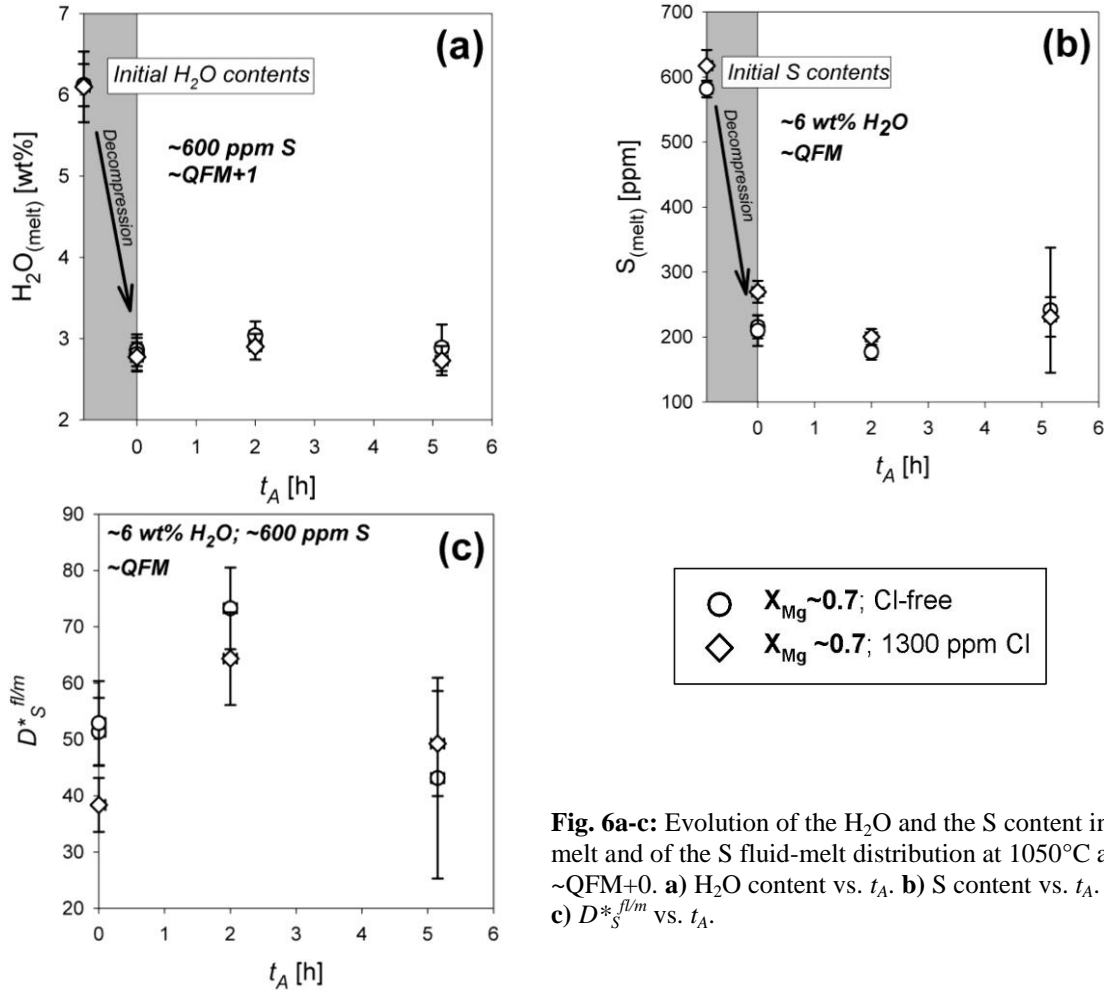

Fig. 6a-c: Evolution of the H_2O and the S content in the melt and of the S fluid-melt distribution at 1050°C and ~QFM+0. **a)** H_2O content vs. t_A. **b)** S content vs. t_A. **c)** $D*_S^{fl/m}$ vs. t_A.

4.2.3.1 Influence of T on S fluid-melt distribution

Fig. 7 illustrates the influence of T on $D_S^{fl/m}$ in the range of 1150 to 1250°C, under oxidizing (~QFM+4; Fig. 7a) and intermediate (~QFM+1.5; Fig. 7b) redox conditions. To avoid possible variations of $D_S^{fl/m}$ as a result of changing X_{Mg} of the melt, only data obtained with X_{Mg} ~0.2 are presented in Fig. 7a (~QFM+4) while data with X_{Mg} ~0.7 is shown Fig. 7b (~QFM+1.5).

Fig. 7a shows that T may have a small effect on $D_S^{fl/m}$ at oxidizing redox conditions (~QFM+4); i.e. $D_S^{fl/m}$ increases slightly from 52 ± 27 at 1150°C to 76 ± 30 at 1250°C. Similar observations are made for intermediate redox conditions (Fig. 7b), although the influence of T on $D_S^{fl/m}$ is more pronounced at ~QFM+1.5; i.e. $D_S^{fl/m}$ increases by a factor of ~2 from 94 ± 20 at 1150°C to 209 ± 80 at 1250°C.

Considering an average $D_S^{fl/m}$ of 58 ± 18, determined from experiments performed at 1050°C and under reducing conditions (~QFM), the observed correlation between T and $D_S^{fl/m}$ may be extrapolated to 1050°C, at least for intermediate redox conditions. These observations contrast with data of Keppler (2010) for haplogranitic systems which indicate a minor effect of T on $D_S^{fl/m}$ in the range of 750 to 850°C at 200 MPa and ~QFM+1.1. The differences between the results of Keppler (2010) for haplogranite and the data obtained in this study for basalt may arise from significant differences in melt composition (i.e. the haplogranitic system is Fe-free, while the basaltic melts of this study contain ~10 wt% FeO; see also Section 5.2).
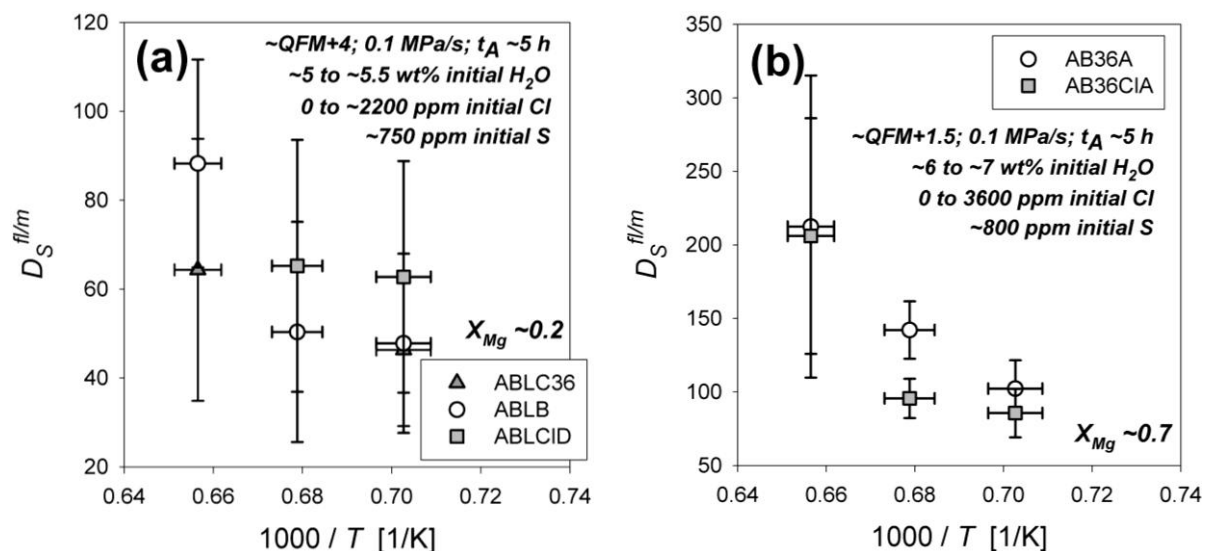
Fig. 7a-b: Influence of T on $D_S^{fl/m}$. **a)** Oxidizing conditions (~QFM+4), X_{Mg} ~0.2. **b)** Intermediate redox conditions (~QFM+1.5), X_{Mg} ~0.7.

4.3 Fluid-melt S-isotope fractionation

The $\delta^{34}S$ values of the glasses ($\delta^{34}S_{melt}$) analyzed with SIMS range from 0.67 ± 0.42 ‰ to 5.76 ± 0.15 (Table 3). Mandeville et al. (2008) and Fiege (Chapter II) have shown that the initial S-isotope composition in the starting glass has no influence on the instrumental S-isotope fractionation, at least in the $\delta^{34}S_{melt}$ range of about -32 ‰ to +18 ‰. Hence, the initial $\delta^{34}S_{melt}$ is not considered for the discussion and interpretation of α_{g-m} values derived from the individual experiments.

Fig. 8 shows that α_{g-m} remains constant within error during further annealing after decompression at given fO_2 and T. This is in agreement with our general knowledge indicating that kinetic isotopic fractionation effects are rare in high T processes (e.g. O'Neil, 1986) and consistent with findings in Chapter II for andesitic systems. It is assumed that the determined α_{g-m} values of all experiments (i.e. independently on t_A) reflect fluid-melt equilibrium fractionation of S-isotopes for given T and fO_2 conditions at which each individual experiment was performed.

In general, $\delta^{34}S_{melt}$ was found to increase under oxidizing conditions and to decrease under reducing conditions upon S degassing (see e.g. Fig. 8), consistent with theoretical considerations (see review of Taylor, 1986). For instance, experiments conducted under oxidizing conditions (~QFM+4) at 1200°C indicate an average α_{g-m} of 0.9981 ± 0.0015, while experiments performed at the same T but under reducing conditions (~QFM+1) reveal an average α_{g-m} of 1.0025 ± 0.0010. Noteworthy, an influence of the Mg content in the melts on the α_{g-m} is not observed.
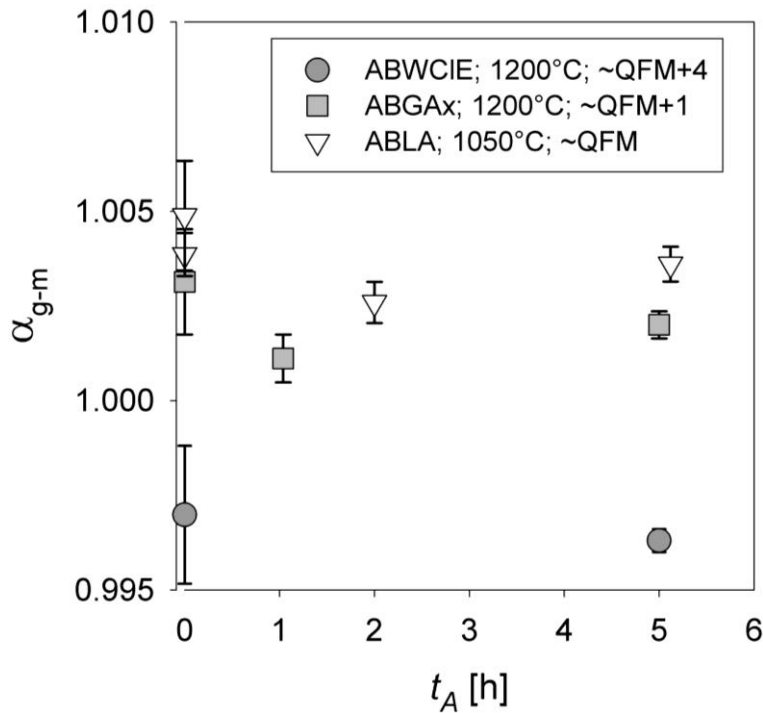

Fig. 8: Evolution of α_{g-m} with t_A.

Table 3: Experimental results. S-isotope data

Sample ID	%S degassed	$\delta^{34}S_{melt}$ [‰, V-CDT]	$\delta^{34}S_{fluid}$ [‰, V-CDT]	α_{g-m}	n (SIMS)
ABWClE-0x	xx	4.78 ± 0.11	-	-	2
ABWClE-1	19 ± 1	5.35 ± 0.91	2.33	0.9970	2
ABWClE-3	26 ± 1	5.76 ± 0.15	2.05	0.9963	2
ABWClDx-0x	xx	3.55 ± 0.36	-	-	2
ABWClDx-1	37 ± 1	3.59± 0.63	3.48	0.9999	2
ABWClDx-3	46 ± 1	3.91 ± 0.07	3.12	0.9992	2
ABLB-0	xx	3.36 ± 0.53	-	-	3
ABLB-1	63 ± 1	4.55 ± 0.87	2.67	0.9981	4
ABLB-2	74 ± 1	5.05 ± 1.45	2.76	0.9977	5
ABLB-3	65 ± 1	4.51 ± 0.98	2.72	0.9982	3
Ba12	xx	3.20 ± 0.13	-	-	2
Ba12-1	60 ± 1	2.69 ± 1.43	3.54	1.0008	2
ABLC-0x	xx	5.39 ± 0.21	-	-	2
ABLC-2	69 ± 2	3.79 ± 0.10	6.10	1.0023	2
ABLC-4	68 ± 2	2.83 ± 0.70	6.60	1.0038	2
ABGAx-0x	xx	4.15 ± 1.00	-	-	3
ABGAx-1x	71 ± 1	1.92 ± 0.46	5.05	1.0031	2
ABGAx-3	87 ± 1	2.41 ± 0.18	4.40	1.0020	2
ABGAx-4	77 ± 1	3.29 ± 0.32	4.40	1.0011	2
ABLA	xx	5.05 ± 0.33	xx	xx	3
ABLA-1	58 ± 9	2.94 ± 0.23	6.54	1.0036	2
ABLA-2	63 ± 1	2.62 ± 0.28	6.48	1.0039	2
ABLA-3	64 ± 1	1.93 ± 0.73	6.80	1.0049	2
ABLA-5	70 ± 1	3.25 ± 0.27	5.83	1.0026	2

Notes: Sample ID: starting glasses are written in *italic*; xx: not relevant or 0

4.3.1 Influence of T on fluid-melt S-isotope fractionation

$\Delta^{34}S_{g-m}$ values are determined for each experiment which was analyzed by SIMS. In case of more than one experiment being conducted at the same T with the same starting glass (i.e. only t_A differs), the derived $\Delta^{34}S_{g-m}$ values are used to estimate an average $\Delta^{34}S_{g-m}$ value (for example, an average $\Delta^{34}S_{g-m}$ of 3.73 ± 0.94 was calculated for 1050°C and ~QFM, based on four experiments of series ABLA). Thus, the data points shown in Fig. 9, illustrating the dependence of $\Delta^{34}S_{g-m}$ on T often refer to more than one experiment.

Under oxidizing conditions (> QFM+2.8) the fluid-melt S-isotope fractionation can be described by the fractionation pair: $SO_{2\ gas} - SO_4^{2-}{}_{melt}$ and thus, by the fractionation factor $\alpha(SO_{2\ gas} - SO_4^{2-}{}_{melt})$. Under reducing conditions (~QFM) H_2S in the fluid and S^{2-} in the melt are the only abundant S species

in a magmatic fluid-melt system and the fractionation factor $\alpha(H_2S_{gas} - S^{2-}_{melt})$ applies to describe the
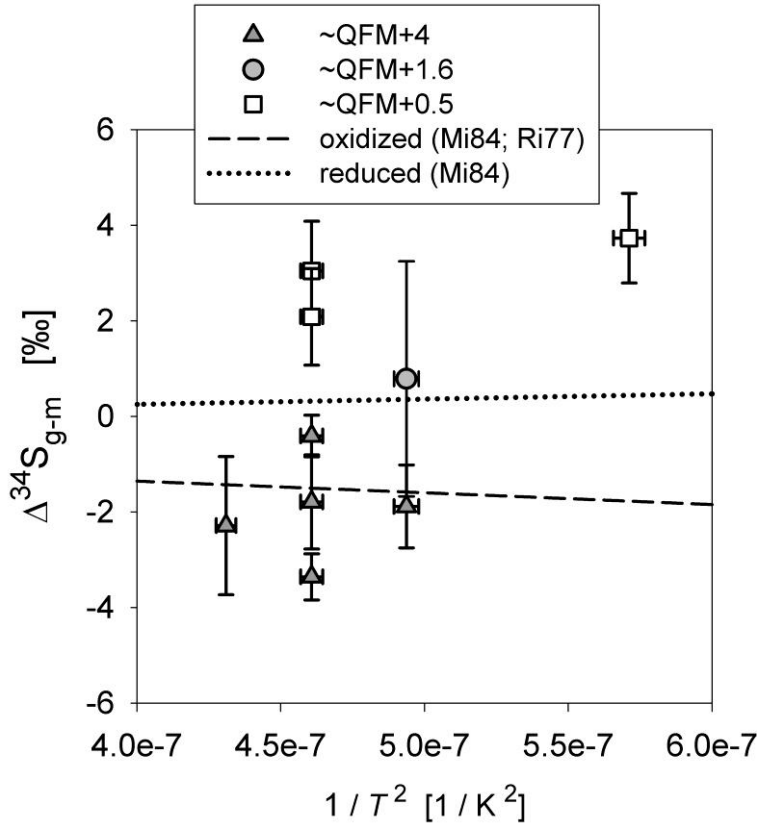
isotopic fractionation upon S-degassing.

Fig. 9: *T* dependence of the S-isotope fluid-melt fractionation. SIMS data derived from the same experimental series conducted at constant *T* were used to calculate a single $\Delta^{34}S_{g-m}$ value; e.g. the data point at $1/T^2 \sim$ 5.7×10^{-7} $1/K^2$ is based on the four experiments of series ABLA. The trend for oxidizing conditions (*dashed line*) was calculated using the *T* dependence for $\alpha(SO_{2\,gas} - H_2S_{gas})$ given by Taylor (1986), based on data of Richet et al. (1977; Ri77), and the *T* dependence for $\alpha(H_2S_{gas} - SO_4^{2-}_{melt})$ provided by Miyoshi et al. (1984; Mi84); see Section 5.5.2, equation 8. The trend for reducing condition (*dotted line*) is based on data of Miyoshi et al. (1984; Mi84); i.e. the *T* dependence provided by the authors for $\alpha(H_2S_{gas} - SO_4^{2-}_{melt})$ and $\alpha(S^{2-}_{melt} - SO_4^{2-}_{melt})$ was used to calculate $\alpha(H_2S_{gas} - S^{2-}_{melt})$ at given *T*.

The *T* dependence for $\alpha(SO_{2\,gas} - H_2S_{gas})$ given by Taylor (1986), based on theoretical considerations

of Richet et al. (1977), as well as the *T* dependence for $\alpha(H_2S_{gas} - SO_4^{2-}_{melt})$ provided by Miyoshi et al.

(1984) based on experiments ($T = 600$ to $1000°C$; atmospheric *p*) are used to estimate a *T* dependence

for $\alpha(SO_{2\,gas} - SO_4^{2-}_{melt})$; see also Section 5.5.2, equation 8. In addition, the *T* dependences determined

by Miyoshi et al. (1984) for $\alpha(H_2S_{gas} - SO_4^{2-}_{melt})$ and $\alpha(S^{2-}_{melt} - SO_4^{2-}_{melt})$ are used to calculate

$\alpha(H_2S_{gas} - S^{2-}_{melt})$ at given *T*. Subsequently, trends for oxidizing [$\alpha(SO_{2\,gas} - SO_4^{2-}_{melt})$] and reducing

[α(H_2S_{gas} − S^{2-}_{melt})] conditions are calculated and plotted for comparison in Fig. 9. The results of this study under oxidizing conditions are in agreement with the calculated trends. On the other hand, under reducing conditions (~QFM+0.5), the experimental data obtained for basaltic systems indicate significantly larger fractionation effects than predicted by the data of Miyoshi et al. (1984). $\Delta^{34}S_{g-m}$ determined in this study is 2.56 ± 1.04 at 1200°C and ~QFM+0.5 while relationships of Miyoshi and co-workers indicate a $\Delta^{34}S_{g-m}$ of 0.57 ± 0.30 for reducing conditions and 1200°C. Comparable observations were made Fiege (Chapter II) for andesitic systems, noting that the *T* dependences of Miyoshi et al. (1984) are probably not applicable to silicate systems (see Section 5.5.1).

5. DISCUSSION

5.1 Kinetics of S degassing: The contrasting behavior of andesite and basalt

The experimental data shows that kinetically controlled transient degassing of large amounts of S do not occur in basaltic systems, at least within the investigated range of *p-T-fO₂* conditions and $r = 0.1$ MPa/s. Fig. 5c and 5d show that the S content in the basaltic glasses does not change significantly as a function of t_A. However, as noted above (Section 4.2.3) a small decrease of S content in the melt may be observed within the first 2 h of annealing after decompression (independent of *fO₂*), but equilibrium fluid-melt partitioning of S is obtained at least after 2 h annealing at reducing as well as oxidizing conditions. This observation made for basaltic systems at oxidizing conditions contrasts with data obtained by Fiege (Chapter I-A) for andesitic systems (Fig. 10). The results presented in Chapter I-A for oxidized andesitic melts show that significant amounts of S are released to the fluid during fast decompression (*r* ~ 0.1 MPa/s) and that part of the S is then diffusing back into the glass during annealing (Fig. 10). Near-equilibrium is reached after ~5 h. This kinetic effect was interpreted to be related to the formation of anhydrite within the fluid phase upon decompression. Noteworthy, crystalline phases (like anhydrite) were not observed in any of the bubbles of the basaltic samples. Differences in fluid composition and, thus, differences in fluid properties when comparing basaltic to andesitic systems may be one explanation for the observed discrepancies. In this hypothesis the fluid coexisting with the basaltic melt would not become saturated in anhydrite upon decompression. However, this is very speculative. It is more reasonable to assume that the lower melt viscosity of

basaltic melts when compared to andesitic melts and, thus, differences in S transport rate within the melt play a crucial role.

Assuming that S transport in the basaltic melts is controlled by diffusion (i.e. convection processes are negligible), the time t [s] required for fluid-melt equilibration with respect to S distribution after decompression can also be estimated via the S diffusivity $D_{(S)}$ [m^2/s] in the basaltic melt and the distance x [m] between fluid pools [with $x = (2 \cdot D_{(S)} \cdot t)^{0.5}$]. The distance between two bubbles was estimated using back scattered electron (BSE) images (collected via EMP) and is typically < 50 µm at 1050°C and < 300 µm at 1200°C for experiments quenched directly after decompression ($t_A = 0$ h; examples are shown in Fig. 3a and 3c).

Behrens and Stelling (2011) found that the empirical Eyring equation (equation 6), relating diffusivity D_η [m^2/s] and viscosity η [Pa·s], is adequate to estimate the S diffusivity in basaltic systems,

$$D_\eta = \frac{k \cdot T}{\lambda \cdot \eta} \tag{6}$$

where k is the Boltzmann constant, T is the temperature [K] and λ is the jumping distance (here: ~0.3 nm). Applying the Eyring relationship to estimate the transport properties of S at 1050°C, using the viscosity model of Hui and Zhang (2007) for the alkali basalt composition, and assuming an initial H$_2$O content in the melt of 6 wt% (prior decompression) and a final content of ~2.5 wt% H$_2$O (after decompression), the derived D_η values are 8 to 16 times higher than those estimated in Chapter I-A for andesitic melts at 1030°C prior to and after decompression, respectively. Noteworthy, most experiments of this study were performed at $T \geq 1150$°C and the differences in D_η between andesitic melts at 1030°C (Chapter I-A) and basaltic melts at ≥ 1150°C (this study) are calculated to be > 25. These differences in D_η between andesitic and basaltic melts can explain the absence of kinetic, transient degassing effects of S upon decompression of basaltic melts.

Assuming a distance between two bubbles of 50 µm the time t required to reach equilibrium conditions in basaltic systems with respect to S fluid-melt distribution ranges between ~4 and ~64 min at 1050°C (depending on Mg and H$_2$O content of the melt) and between ~1 and ~3 min at 1200°C.

Noteworthy, the model of Giordano et al. (2008) predicts slightly higher η values; i.e. run durations of up to 85 min may be required to reach equilibrium conditions at 1050°C. Considering that decompression from 400 to 70 MPa with $r = 0.1$ MPa/s takes 55 min, the estimated timescales indicate that diffusion controlled transport of S is sufficient to achieve fluid-melt near-equilibrium within 1 or 2 h after decompression. This is consistent with the experimental data, i.e. S content in the melts remains almost constant for $t_A \geq 2$ h.
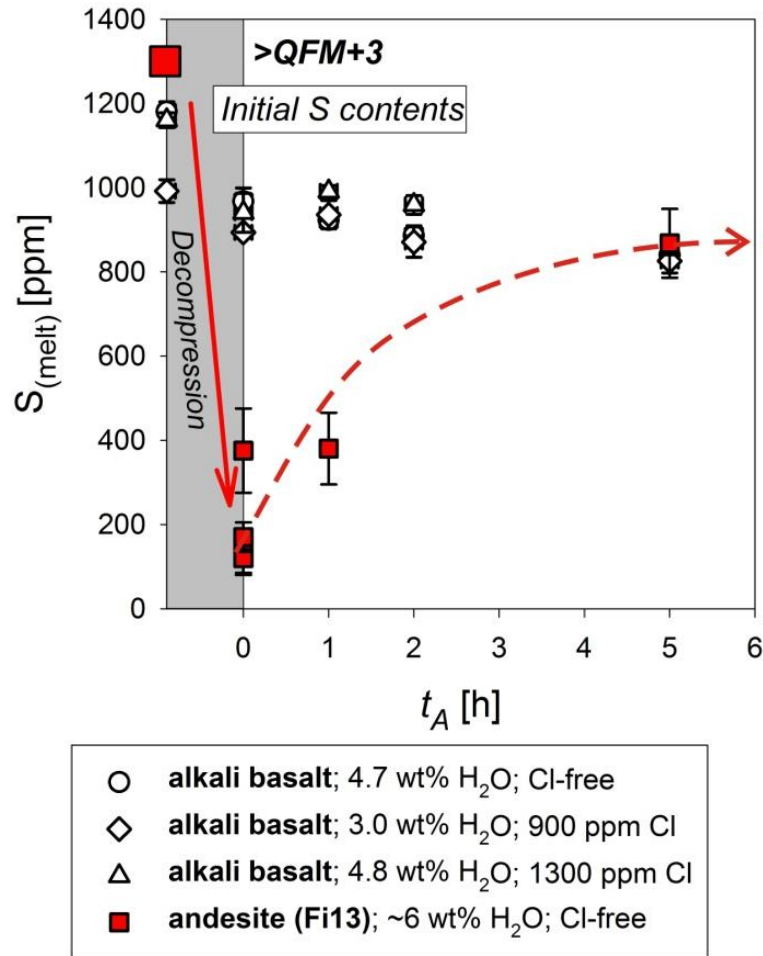
Fig. 10: Evolution of the S content in the melt during decompression ($r \sim 0.1$ MPa/s) and with t_A under oxidizing conditions (> QFM+3). Data of this study for basaltic systems is compared to results presented in Chapter I-A (Fi13) for andesitic systems. The *red arrows* illustrate the evolution of the S content in the andesitic melt.

5.2 Influence of melt composition on $D_S^{fl/m}$

As shown by the collected data, changing the bulk MgO content of the sample and, thus, changing slighly polymerization (and viscosity) of the melt does not affect the fluid-melt distribution of S, H_2O and Cl (Fig. 5) to a significant extend. The slight increase of $D_S^{fl/m}$ with decreasing X_{Mg} observed at

~QFM+4 (Fig. 5e) is probably negligible considering the high uncertainty of the calculated $D_S^{fl/m}$ values at $X_{Mg} = 0.2$; i.e. $D_S^{fl/m}$ values at $X_{Mg} = 0.2$ and $X_{Mg} = 0.7$ are usually identical within error.

Under oxidizing conditions (~QFM+4) and $t_A \geq 2$ h (near-equilibrium), an average $D_S^{fl/m}$ of 39 ± 25 is estimated for basaltic systems at ~70 MPa and ~1150 to ~1250°C. Considering the minor dependence of $D_S^{fl/m}$ on T under oxidizing conditions (see Section 4.2.3.1, Fig. 7a), the estimated average $D_S^{fl/m}$ value is in agreement with observations of Fiege (Chapter I-A) suggesting that an average $D_S^{fl/m}$ of ~50 can be applied to a wide range of p and silicate melt composition under oxidizing conditions.

Based on experiments carried out under reducing conditions (~QFM) at ~1050°C and with $t_A \geq 2$ h (near-equilibrium conditions) a $D_S^{fl/m}$ of 58 ± 18 is estimated for alkali basaltic melts at p of ~70 MPa (see Fig. 6). A similar $D_S^{fl/m}$ of 74 ± 30 was calculated using data from Moune et al. (2009) for similar melt compositions, T (1050°C) and fO_2 (~QFM) but higher p of 200 to 300 MPa. However, p variations in the range of 70 to 400 MPa have no significant effect on $D_S^{fl/m}$ (see data in Chapter I-A; Keppler, 2010; Lesne et al., 2011). In contrast to oxidizing conditions, the change of melt composition from basaltic to rhyolitic may influence strongly $D_S^{fl/m}$ at QFM to QFM+1. In Chapter I-A a $D_S^{fl/m}$ of ~220 was estimated for andesite at ~QFM+1, ~1030°C and ~70 MPa. This value is in good agreement with data of Zajacz et al. (2012) obtained for similar melt composition at ~QFM, 1000°C and 200 MPa. In addition, Keppler (2010) determined a $D_S^{fl/m}$ of about 470 for haplogranitic systems at ~QFM-0.9, 850°C and 200 MPa. The difference of T between the dataset for haplogranite and other systems does not explain this variation of $D_S^{fl/m}$ (see Fig. 7 and Keppler, 2010). Noteworthy, the FeO content in the different melts ranges from ~10 wt% (basalt; this study) to ~5 wt% (andesite; Chapter I-A) to 0 wt% (Fe-free haplogranite; Keppler, 2010). Hence, the contrasting observations made for the influence of melt composition on $D_S^{fl/m}$ under reducing conditions, when compared to oxidizing conditions, refers most likely to the large effect of FeO content in the melt on S^{2-} solubility in reduced systems (see e.g. review of Wallace and Edmonds, 2011). This is also consistent with the observed minor dependence of MgO content on $D_S^{fl/m}$ at almost constant FeO contents indicated by the results of this study and in agreement Zajacz et al. (2012) noting a negative correlation between $D_S^{fl/m}$ and FeO content in andesitic melts under reducing conditions (~QFM).

5.3 Interaction of S and Cl

Previous studies investigating the effect of Cl on $D_S^{fl/m}$ in trachybasaltic (Beermann, 2010), phonolitic (Webster et al., 2009) and andesitic systems (Chapter I-A) showed that $D_S^{fl/m}$ increases with the bulk Cl content. On the other hand, a weak negative correlation between $D_S^{fl/m}$ and bulk Cl content in rhyodacitic systems at ~QFM+0.6, 850°C, and 200 MPa was observed by Webster and Botcharnikov (2011) based on results of Botcharnikov et al. (2004). However, data of Botcharnikov et al. (2004) has a high uncertainty due to the presence of pyrrhotite in most samples. Thus, in a first approach, the absence of a correlation between the initial Cl content in the basaltic melt (0 to ~0.36 wt% Cl) and $D_S^{fl/m}$ indicated by the results in this study seems to be inconsistent with these studies. However, the bulk Cl content in some of the previous studies mentioned above was significantly higher than in this study (Webster et al., 2009; Beermann, 2010). For instance, the bulk Cl content in the trachybasaltic system investigated by Beermann (2010) ranges from ~0.05 to ~3.5 wt% Cl. Noteworthy, the author observed no systematic effect of Cl on $D_S^{fl/m}$ for bulk Cl contents ≤ 0.55 wt%, which is consistent with results of this study. Moreover, considering that the Cl content in basaltic melts of this study remains almost constant during decompression and further annealing after decompression at final p-T conditions, the $D_{Cl}^{fl/m}$ at our investigated conditions is ~ 1, implying that the Cl content in the coexisting fluid phase is negligible. Hence, the data of this study and Beermann (2010) indicate that changing fluid properties, related to changing fluid composition (e.g. changing contents of Cl and charge compensating cations), are responsible for the effect of bulk Cl content on $D_S^{fl/m}$ observed in previous studies. In agreement with interpretations of Webster and Botcharnikov (2011) it is suggested that the effect of Cl on $D_S^{fl/m}$ can be explained by changing activity coefficients of S and Cl in the fluid phase. Hence, Cl content in the system can only affect the distribution of S between fluid and melt if $D_{Cl}^{fl/m} >> 1$, i.e. significant amounts of Cl can be released to a fluid phase upon decompression.

5.4 Influence of fO_2 on $D_S^{fl/m}$

Based on the results gained for 1150 to 1250°C for basaltic systems in this study, an average $D_S^{fl/m}$ of 39 ± 25 is determined for oxidizing conditions (~QFM+4), while a $D_S^{fl/m}$ of 181 ± 86 is calculated for redox conditions of ~QFM+1. Thus, this study confirms that $D_S^{fl/m}$ depends strongly on fO_2 which

influences the S speciation in the melt (e.g. Keppler, 1999; Jugo et al., 2010; Keppler, 2010; Zajacz et al., 2012). The relationship between $D_S^{fl/m}$ and fO_2 (Fig. 11) indicated by the new data is in agreement with results presented in Chapter I-A for andesitic systems (~70 MPa, 1030°C) and data of Beermann (2010) for trachybasaltic systems (100 to 200 MPa, 1050°C). Noteworthy, only anhydrite- and pyrrhotite-free experiments of Beermann (2010) with comparable bulk Cl content ($\leq$ 0.55 wt%) are considered in Fig. 11. The data of Zajacz et al. (2012) for andesitic systems (200 MPa, 1000°C) follow a similar trend but which is slightly shifted towards lower $D_S^{fl/m}$ for a given fO_2 at < QFM+2. Considering that $D_S^{fl/m}$ is rather independent of p in the range of 70 to 400 MPa (see data in Chapter I-A; Keppler, 2010; Lesne et al., 2011) and the small T dependence indicated in Fig. 7, the slightly higher $D_S^{fl/m}$ values obtained for experiments conducted at 1150 to 1250°C (this study) when compared to experiments performed at 1000 to 1050°C (see data in Chapter I-A; Beermann, 2010; Zajacz et al., 2012) may be explained by differences in T. On the other hand, under reducing conditions, differences in melt composition can also explain the lower $D_S^{fl/m}$ determined in previous studies for andesitic systems (see Section 5.2).
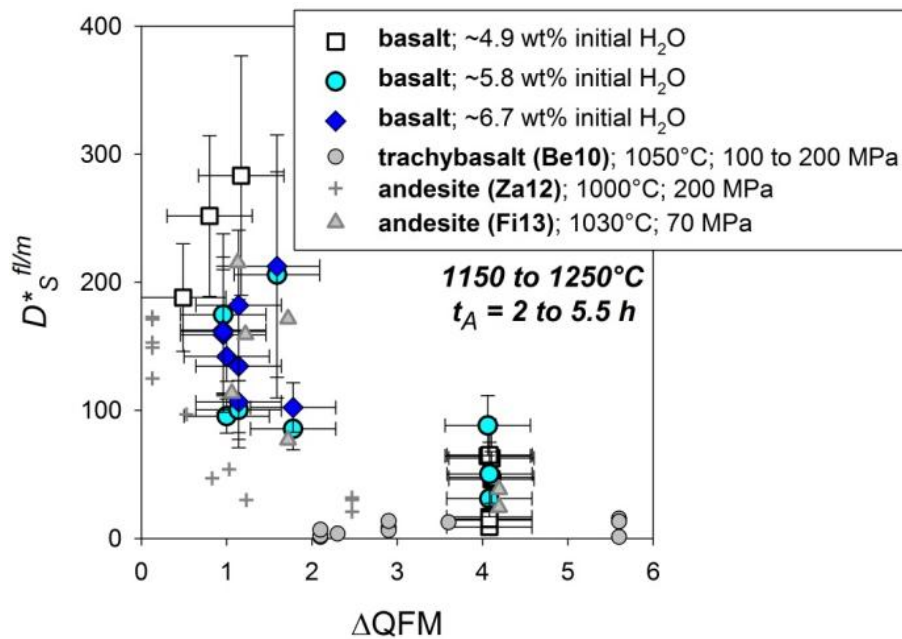

Fig. 11: Influence of fO_2 on $D_S^{fl/m}$ ($t_A \geq$ 2h; near-equilibrium).
Be10: Beermann (2010); equilibrium experiments; only anhydrite- and pyrrhotite-free experiments are considered.
Za12: Zajacz et al. (2012); equilibrium experiments.
Fi13: Data presented previously in Chapter I-A; decompression experiments; $r \approx$ 0.1 MPa/s; $t_A \geq$ 5 h (near-equilibrium).

5.5 S-isotope fractionation

5.5.1 Applicability of previously published T dependences to silicate melts

The large discrepancies observed for reducing conditions between the experimental data of this study and the trend derived from the data of Miyoshi et al. (1984) – (see Fig. 9; Section 4.3.1) – indicate that either the equation given by Miyoshi et al. (1984) for $\alpha(SO_4{}^{2-}{}_{melt} - S^{2-}{}_{melt})$ or for $\alpha(SO_4{}^{2-}{}_{melt} - H_2S{}_{gas})$ or both, are not applicable to silicate systems. The equations of Miyoshi et al. (1984) are based on experiments performed at 600 to 1000°C and atmospheric p, using either anhydrous Na_2SO_3 in melts of NaCl and LiCl-KCl mixture to determine $\alpha(SO_4{}^{2-}{}_{melt} - S^{2-}{}_{melt})$ or molten NaCl analogues and aqueous sodium chloride fluid to determine $\alpha(SO_4{}^{2-}{}_{melt} - H_2S{}_{gas})$. In Chapter II it is suggested that the T dependence determined by Miyoshi et al. (1984) for $\alpha(SO_4{}^{2-}{}_{melt} - H_2S{}_{gas})$ may be applicable to silicate systems, as the composition of the fluid is similar to that expected in natural systems. However, the applicability of the value of $\alpha(SO_4{}^{2-}{}_{melt} - S^{2-}{}_{melt})$ may be questioned. The equilibrium isotope fractionation effects result from the effect of atomic mass on bond energy (e.g. O'Neil, 1986), the differences between $\Delta^{34}S_{g-m}$ observed in this study and predicted by Miyoshi et al. (1984) are most probably related to the significant differences in melt composition and structure when comparing silicate melts to molten salt, i.e. the bonding energy of S^{2-} incorporated in a sodium chloride melt may differ significantly from that of S^{2-} in a silicate melts.

Noteworthy, differences in bonding energies of S^{2-} or S^{6+} in basaltic melts when compared to rhyolitic melts are probably negligible for fluid-melt S-isotope fractionation effects. Hence, it is proposed that the isotopic fractionation factors determined in this study are applicable to a large range of silicate melt compositions. This is also confirmed by the good correlation found between the basaltic data of this study and results for andesitic composition presented in Chapter II; see Section 5.5.2 and Fig. 12 in this Chapter.

5.5.2 Modeling S-isotope fractionation in silicate systems

The isotopic data obtained in this study at 1050°C under reducing conditions (~QFM) and previous data obtained for an andesitic composition at 1030°C in the fO_2 range of ~QFM+1 to ~QFM+4 (see Chapter II) are used to predict the dependence of $\Delta^{34}S_{g-m}$ on fO_2. Changes in melt composition from

andesitic to basaltic as well as slight changes in T from 1030°C (andesite, Chapter II) to 1050°C (basalt, this study) are assumed to have a minor effect on α_{g-m} and data are combined together.

The S-isotope fractionation is controlled by four fractionation factors $\alpha(SO_{2\ gas} - SO_4{}^{2-}{}_{melt})$, $\alpha(SO_{2\ gas} - S^{2-}{}_{melt})$, $\alpha(H_2S_{gas} - SO_4{}^{2-}{}_{melt})$ and $\alpha(H_2S_{gas} - S^{2-}{}_{melt})$, but the factor at very oxidizing, $\alpha(SO_{2\ gas} - SO_4{}^{2-}{}_{melt})$, and at very reducing conditions, $\alpha(H_2S_{gas} - S^{2-}{}_{melt})$, are expected to control mainly the fractionation over the whole fO_2 range (see discussion in Chapter II). Thus, these two factors need to be determined accurately. In Chapter II we constrained the value of $\alpha(SO_{2\ gas} - SO_4{}^{2-}{}_{melt})$ to be 0.9985 ± 0.0007 at 1030°C, but $\alpha(H_2S_{gas} - S^{2-}{}_{melt})$ was not well constrained for reducing conditions and was estimated to be between ~1.0046 and ~1.0099 (*lower* and *upper limit*, respectively, Fig. 12) at 1030°C. The data obtained in this study at ~QFM allow us to improve the value of $\alpha(H_2S_{gas} - S^{2-}{}_{melt})$. S in fluid coexisting with a basaltic melt is almost exclusively present as H_2S at ~QFM and 1050°C, i.e. $SO_2 / (SO_2 + H_2S)$ molar ratio is ~0. This information is obtained using the program *DCompress*, provided by Alain Burgisser (CNRS, Orléans, France) and based on data of Burgisser et al. (2008) and unpublished data of Burgisser et al.. The model of Jugo et al. (2010) shows that S^{2-} is the only relevant species in the basaltic melt at these conditions, i.e. $S^{6+}/\Sigma S \approx 0$. A $\Delta^{34}S_{g-m}$ of 3.73 ± 0.94 was determined for experiments performed at 1050°C and ~QFM. Hence, it is suggested that an α_{g-m} of 1.0037 ± 0.0009 describes the isotopic fractionation between S^{2-} in the silicate melt and H_2S in the fluid at 1050°C.

Following the approach described in Chapter II the effect of fO_2 on $\Delta^{34}S_{g-m}$ was re-calculated for $T \approx 1040$°C using $\alpha(SO_{2\ gas} - SO_4{}^{2-}{}_{melt}) = 0.9985 \pm 0.0007$ estimated by Fiege (Chapter II) for 1030°C in andesitic systems as well as the new value for $\alpha(H_2S_{gas} - S^{2-}{}_{melt})$ of 1.0037 ± 0.0009 determined for basaltic systems at 1050°C. The re-calculated value for $\alpha(SO_{2\ gas} - S^{2-}{}_{melt})$ is ~1.0060 while $\alpha(H_2S_{gas} - SO_4{}^{2-}{}_{melt})$ is estimated to be ~0.9964 at 1040°C.

The evolution of $\Delta^{34}S_{g-m}$ as a function of fO_2 is shown by the solid red line in Fig. 12. Fig. 12 shows that the evolution of $\Delta^{34}S_{g-m}$ is close to that predicted by the model presented in Chapter II if the *lower limit* of $\Delta^{34}S_{g-m}$ is applied. The large difference to the *upper limit* is most likely related to the lack of data for andesites at < QFM+0.8.
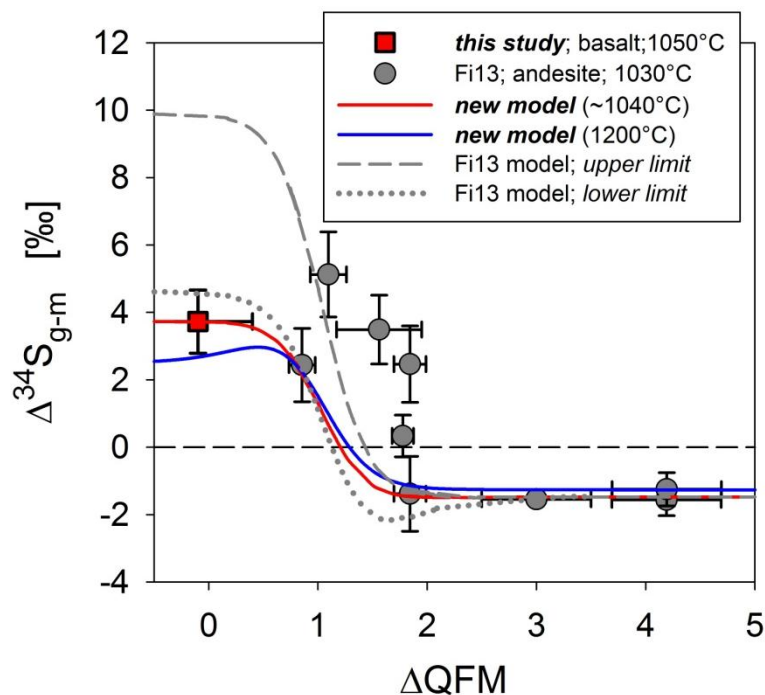
Fig. 12: $\Delta^{34}S_{g-m}$ vs. fO_2. See Section 5.5.2 for details on the calculation
of the *red trend* (1040°C) and the *blue trend* (1200°C).
Fi13: This data was previously presented in Chapter II. The modeling
approach for the *grey trends* is described in Chapter II, Section 5.2.

As mentioned previously (Chapter II, Section 5.2), the significant differences between the calculated
trend(s) and some of the andesitic data at intermediate redox conditions is either related to
uncertainties in the determination of fO_2 in the experiments or to the possible influence of *p*, *T* and
melt compositions on the sulfate/sulfide transition (Baker and Moretti, 2011).

The isotopic data obtained in this study for various *T* is limited (see Table 3), however, it can be used
to estimate a preliminary relationship for the dependence of $\alpha(H_2S_{gas} - S^{2-}_{melt})$ on *T*. Considering only
experiments with $S^{6+}/\Sigma S < 0.1$ conducted at 1200°C and under reducing conditions (i.e. ABL-C-2;
ABG-Ax-1x; -3) a α_{g-m} of 1.0025 ± 0.0011 can be determined, and this value presumably
represent $\alpha(H_2S_{gas} - S^{2-}_{melt})$ at 1200°C in silicate systems. In combination with the $\alpha(H_2S_{gas} - S^{2-}_{melt})$
value determined for 1050°C under reducing conditions (1.0037 ± 0.0009) the following preliminary
equation, based on regression, is proposed to be applicable to silicate melt systems at elevated *T*
(~1000 to 1200°C):

$$10^3 \ln \alpha(H_2S_{gas} - S^{2-}_{melt}) = 10.84 \cdot 10^6 / T^2 - 2.50; \quad T\,[K]; \quad 1\text{ sigma} \sim 0.0010 \qquad (7)$$

Using the T dependence for $\alpha(SO_{2\ gas} - H_2S_{\ gas})$ given by Taylor (1986) based on data of Richet et al. (1977) as well as the T dependence for $\alpha(H_2S_{\ gas} - SO_4{}^{2-}{}_{melt})$ provided by Miyoshi et al. (1984) a T dependence for $\alpha(SO_{2\ gas} - SO_4{}^{2-}{}_{melt})$ is estimated to be:

$$10^3 \ln \alpha(SO_{2\ gas} - SO_4{}^{2-}{}_{melt}) = -0.42\ (10^3/T)^3 - 1.933\ (10^3/T)^2 - 0.105\ (10^3/T) - 0.41; \quad T\ [K] \qquad (8)$$

As shown in Fig. 9, equation 8 reproduces well the data obtained in this study for oxidizing basaltic systems at 1150 to 1250°C (see Fig. 9). Thus, equation 7 and 8 are used to estimate $\alpha(H_2S_{\ gas} - S^{2-}{}_{melt})$ and $\alpha(SO_{2\ gas} - SO_4{}^{2-}{}_{melt})$ for 1200°C. However, considering that a $\Delta^{34}S_{g-m}$ of -1.82 ‰ is predicted by equation 8 for 1030°C and that a $\Delta^{34}S_{g-m}$ of about -1.48 ‰ was determined in Chapter II for the same T in andesitic systems (value is based on 8 experiments), it is assumed, in a first approximation, that ~0.24 ‰ need to be added to the values predicted by equation 8 when studying silicate systems. Subsequently, following the approach described in Chapter II to estimate the missing two fractionation pairs [$\alpha(SO_{2\ gas} - S^{2-}{}_{melt})$ and $\alpha(H_2S_{\ gas} - SO_4{}^{2-}{}_{melt})$] and to calculate the S speciation in the fluid and melt phase at given fO_2, respectively, α_{g-m} is estimated for given fO_2 at 1200°C. The derived trend for 1200°C is shown in Fig. 12 (blue line). The trend indicates that T has a small effect on S-isotope fluid-melt fractionation under oxidizing conditions, while significant changes are to be expected under reducing conditions.

6. CONCLUSION AND IMPLICATIONS TO NATURAL SYSTEMS

The presented experimental results provide first insights on the kinetics of S degassing during decompression in basaltic systems. The experiments show that fluid-melt near-equilibrium with respect to S distribution in basaltic systems is achieved shortly ($t_A < 2$ h) after fast decompression from 400 to 70 MPa ($r = 0.1$ MPa/s). In contrast to previous results for oxidized andesitic systems (Chapter II), no evidence for kinetically controlled transient release of large amounts of S to a fluid phase upon fast decompression of basaltic melts is indicated by the experimental results.

Another important finding of this study is that changes in melt composition from basaltic to rhyolitic have a minor effect on $D_S^{fl/m}$ under oxidizing but a major effect on $D_S^{fl/m}$ under reducing conditions. These differences are presumably related to the large effect of FeO (i.e. Fe^{2+}) content in the melt on S^{2-} solubility.

Furthermore, experimental data obtained for Cl-bearing basaltic systems (this study and Beermann, 2010) indicate that the interaction between S and Cl is of minor importance in basaltic systems containing ≤ 0.55 wt% Cl. Experiments of this study show that only negligible amounts of Cl are released by Cl-bearing basaltic melts (≤ 0.36 wt% Cl) to a fluid phase during decompression. Thus, it is reasonable to assume that changing fluid properties related to changing fluid composition are responsible for the S-Cl interaction at higher bulk Cl contents (> 0.55 wt%). The observed minor release of Cl to a fluid phase upon decompression from 400 to 70 MPa has to be taken into account for the interpretation of volcanic gas signatures. For instance, the Cl/S ratio in volcanic gases released by alkali basaltic magma, ascending from a deep magma reservoir (~10 to 15 km) to a magma chamber at lower levels (~2 to 3 km) is expected to be very low if bulk Cl is ≤ 0.55 wt%.

The S-isotope data confirm observations made in Chapter II indicating that *i)* fluid-melt S-isotope fractionation in reduced magmatic systems may be significantly higher than previously assumed and *ii)* the *T* dependence derived from experiments from the 80s, using molten salt, are probably not applicable to silicate melts at magmatic *p-T* conditions. The combined results of this study and of Chapter II show that closed system degassing of basaltic melts at ~1040°C can induce a fluid-melt S-isotope fractionation of about +3.7 ‰ in reduced systems (~QFM) and of about -1.5 ‰ in oxidized systems (~QFM+4). Furthermore, results presented in this study show that the fluid-melt S-isotope fractionation decreases slightly with increasing *T*; e.g. at 1200°C a fluid-melt fractionation of up to +3.0 ‰ can be expected under reducing. Model calculation indicate that differences of up to ~30 ‰ between $\delta^{34}S$ of the fluid and $\delta^{34}S$ of the source melt can be reached during open system degassing of reduced systems. The results show that monitoring S-isotopes in volcanic gases with modern, high precision techniques can become a powerful tool to improve forecasting of volcanic eruptions.

SUMMARY AND CONCLUSIONS

A new experimental approach was applied to investigate kinetics of S (and Cl) distribution between fluid and H_2O-S±Cl-bearing andesitic and basaltic melt. The data provides first insights into the partitioning of S (and Cl) between fluid and melt upon degassing at disequilibrium conditions.

Experiments, which were conducted under oxidizing conditions (> QFM+3; i.e. when S^{6+} is the only S species) with andesitic melt composition, revealed a strong decrease of the S content in the melt by about 85% during fast decompression (0.1 MPa/s). After fast decompression subsequent annealing for ≥ 5 h resulted in an increase of the S content in the andesitic melt up to ~75% level of the initial S content; i.e. the rapidly released S was partly resorbed by the melt during annealing. On the other hand, at lower fO_2 (QFM+1 to QFM+1.5; i.e. when S^{2-} became abundant), the S content in the andesitic melt was found to be largely independent of t_A after decompression at the same rate ($r = 0.1$ MPa/s). These observations indicate different behaviors of S^{2-} and S^{6+} during kinetically-controlled degassing which need to be considered when modeling decompression induced magma degassing.

Experiments with basaltic melt composition show that fluid-melt near-equilibrium with respect to S distribution is achieved shortly (t_A < 2 h) after decompression from ~400 to ~70 MPa at a rate of ~0.1 MPa/s, largely independent of fO_2 ranging from ~QFM to ~QFM+4. In contrast to data obtained for andesitic systems, no evidence for kinetically controlled transient release of S upon fast decompression of basaltic melts is indicated by the experimental results.

The presented results indicate no distinct correlation between bulk H_2O content, ranging e.g. from ~3 to ~7 wt% in the basaltic system, and $D_S^{fl/m}$. However, a slight negative correlation between the bulk H_2O content in the melt and $D_S^{fl/m}$ indicated by a few experiments with andesitic composition (Chapter I-A, Fig. 6b and 8b) may be due to variations in fO_2 (varying from QFM+1.0 to QFM+2.2 for these experiments) as well as to the low accuracy of $D_S^{fl/m}$ values derived from experiments with low initial H_2O content, which is related to the applied approach (i.e. mass balance calculations). The addition of up to ~1000 ppm Cl to the system has a small but noticeable effect on $D_S^{fl/m}$ in S-enriched (>> 300 to ~3000 ppm S) andesitic systems. On the other hand, data for Cl-bearing basaltic systems (this study; Beermann, 2010) shows that the S-Cl interaction is of minor importance in basaltic systems containing

≤ 0.55 wt% Cl. Noteworthy, our results show that only negligible amounts of Cl are released by Cl-bearing basaltic melts (≤ 0.36 wt% Cl) during decompression (i.e. $D_{Cl}^{fl/m} \sim 1$), while a $D_{Cl}^{fl/m}$ ranging from ~1 to ~13 was determined for andesitic systems. Accordingly, we suggest that changing fluid properties related to changing fluid composition are responsible for the S-Cl interaction at higher Cl contents in the bulk system (> 0.55 wt% Cl; see Beermann, 2010). The minor release of Cl to a fluid phase during decompression (typically from ~400 to ~70 MPa) of basaltic melts has to be considered for the interpretation of volcanic gas signatures; i.e. the Cl/S ratio in volcanic gases released by ascending basaltic magma is supposed to be very low (probably < 1) when bulk Cl is ≤ 0.55 wt%.

Another important finding of this study is that strong changes in bulk melt composition from basaltic to rhyolitic have only a minor effect on $D_S^{fl/m}$ under oxidizing but a major effect under reducing conditions. These differences are supposed to be directly related to the large effect of FeO content in the melt on S^{2-} solubility (see e.g. review of Baker and Moretti, 2011). The data obtained on S (and Cl) fluid-melt distribution at fluid-melt disequilibrium and near-equilibrium, respectively, under varying redox conditions as well as with differing initial volatile content, are of high relevance for developing volcanic degassing scenarios.

Bubble formation was investigated on selected andesitic samples via BSE image analyses. A comparison of the obtained results with data of Cichy et al. (2011) for rhyodacitic systems indicate the high importance of decompression style on *BND*, confirming the observations of Nowak et al. (2011) based on preliminary decompression experiments. In addition, the data shows that even short storage times (≤ 5 h) at shallow depths (~2 to 3 km) interrupting the ascent of a magma, have a significant effect on *BND*; e.g. *BND* decreases by ~1 log unit within 5 h annealing after decompression. Both findings need to be considered when interpreting *BND* values derived from natural (pumice) samples and help to understand explosive (Plinian) eruptions.

Selected samples were analyzed by SIMS to investigate S-isotope fractionation between fluid and silicate melt. The results provide first constraint on S-isotope fractionation between fluid and silicate melt at geologically relevant *p-T* condition and with close to natural fluid-melt compositions. The compiled data for andesitic and basaltic systems shows that previous models (e.g. de Hoog et al., 2001) based on experiments using simple melt compositions (e.g. molten salt Na_2SO_4 and Na_2S

analogies) as well as on theoretical or compilation type studies from the 70s and 80s (summarized by Taylor, 1986) may significantly underestimate the isotopic fractionation in silicate systems, at least under reducing conditions. The observed discrepancies can be explained by *i)* systematic flaws in previously published models and *ii)* the limited (experimental) data available in literature on S-isotope fractionation, which is probably not applicable to silicate melts at magmatic *p-T* conditions. In this study we show that closed system degassing of S-bearing silicate melts at ~1040°C can induce S-isotope fluid-melt fractionation of about +3.7 ‰ under reducing conditions (~QFM to ~QFM+1) and of about -1.5 ‰ under oxidizing conditions (> QFM+3). In addition, the obtained data indicates that the fluid-melt S-isotope fractionation decreases slightly with increasing *T*; e.g. at 1200°C a $\Delta^{34}S_{g-m}$ of up to +3.0 ‰ can be expected under reducing conditions while a $\Delta^{34}S_{g-m}$ of about -1.3 ‰ was estimated for oxidizing conditions. Model calculations based on these experimental results reveal that differences of up to ~30 ‰ between $\delta^{34}S$ of the fluid and $\delta^{34}S$ of the source melt can be reached upon open system degassing of reduced silicate melts. Thus, monitoring S-isotopes signatures in volcanic gases with modern, high precision techniques can help to forecast volcanic events.

REFERENCES

Allard P. (1983) The origin of hydrogen, carbon, sulfur, nitrogen and rare gases in volcanic exhalations: Evidence from isotope geochemistry. In *Forecasting Volcanic Events* (ed. H. Tazieff and J.-C.Sabroux). Elsevier. pp. 337-386.

Armienti P. (2008) Decryption of Igneous Rock Textures: Crystal Size Distribution Tools. *Rev. Mineral. Geochem.* **69**, 623-649.

Arthur M. A. (2000) Volcanic contributions to the carbon and sulfur geochemical cycles and global change. In *Encyclopedia of Volcanoes* (ed. H. Sigurdsson). Academic Press, San Diego. pp. 1045-1056.

Backnaes L., Stelling J., Behrens H., Goettlicher J., Mangold S., Verheijen O., Beerkens R. G. C. and Deubener J. (2008) Dissolution mechanisms of tetravalent sulphur in silicate melts: Evidences from sulphur K edge XANES studies on glasses. *J. Am. Ceram. Soc.* **91**, 721-727.

Bagdassarov N., Dorfman A. and Dingwell D. B. (2000) Effect of alkalis, phosphorus, and water on the surface tension of haplogranite melt. *Am. Mineral.* **85**, 33-40.

Baker D. R. and Moretti R. (2011) Modeling the Solubility of Sulfur in Magmas: A 50-Year Old Geochemical Challenge. *Rev. Mineral. Geochem.* **73**, 167-213.

Barr J. and Grove T. (2010) AuPdFe ternary solution model and applications to understanding the fO_2 of hydrous, high-pressure experiments. *Contrib. Mineral. Petrol.* **160**, 631-643.

Beermann O. (2010) The solubility of sulfur and chlorine in H_2O-bearing dacites of Krakatau and basalts of Mt. Etna. Ph. D. thesis, Leibniz Univ. Hannover

Beermann O., Botcharnikov R. E., Holtz F., Diedrich O. and Nowak M. (2011) Temperature dependence of sulfide and sulfate solubility in olivine-saturated basaltic magmas. *Geochim. Cosmochim. Acta* 75, 7612-7631.

Behrens H. (1995) Determination of water solubilities in high-viscosity melts; an experimental study on $NaAlSi_3O_8$ and $KAlSi_3O_8$ melts. *Eur. J. Mineral.* **7**, 905-920.

Behrens H. and Stelling J. (2011) Diffusion and Redox Reactions of Sulfur in Silicate Melts. *Rev. Mineral. Geochem.* **73**, 79-111.

Behrens H., Zhang Y. X. and Xu Z. G. (2004) H_2O diffusion in dacitic and andesitic melts. *Geochim. Cosmochim. Acta* **68**, 5139-5150.

Behrens H., Misiti V., Freda C., Vetere F., Botcharnikov R. E. and Scarlato P. (2009) Solubility of H_2O and CO_2 in ultrapotassic melts at 1200 and 1250 degrees C and pressure from 50 to 500 MPa. *Am. Mineral.* **94**, 105-120.

Bény C., Guilhaumou N. and Touray J. C. (1982) Native-Sulfur-Bearing Fluid Inclusions in the CO_2-H_2S -H_2O- S-System - Micro-Thermometry and Raman Micro-Probe (Mole) Analysis - Thermochemical Interpretations *Chem. Geol.* **37**, 113-127.

Berndt J., Liebske C., Holtz F., Freise M., Nowak M., Ziegenbein D., Hurkuck W. and Koepke J. (2002) A combined rapid-quench and H_2-membrane setup for internally heated pressure vessels: Description and application for water solubility in basaltic melts. *Am. Mineral.* **87**, 1717-1726.

Binder B. and Keppler H. (2011) The oxidation state of sulfur in magmatic fluids. *Earth Planet. Sci. Lett.* **301**, 190-198.

Bluth G. J. S., Doiron S. D., Schnetzler C. C., Krueger A. J. and Walter L. S. (1992) Global Tracking of the SO_2 Clouds from the June, 1991 Mount-Pinatubo Eruptions. *Geophys. Res. Lett.* **19**, 151-154.

Bondarenko G. V. and Gorbaty Y. E. (1997) In situ Raman spectroscopic study of sulfur-saturated water at 1000 bar between 200 and 500°C. *Geochim. Cosmochim. Acta* **61**, 1413-1420.

REFERENCES

Botcharnikov R. E., Behrens H., Holtz F., Koepke J. and Sato H. (2004) Sulfur and chlorine solubility in Mt. Unzen rhyodacitic melt at 850 degrees C and 200 MPa. *Chem. Geol.* **213**, 207-225.

Botcharnikov R. E., Linnen R. L., Wilke M., Holtz F., Jugo P. J. and Berndt J. (2011) High gold concentrations in sulphide-bearing magma under oxidizing conditions. *Nat. Geosci.* **4**, 112-115.

Burgisser A. and Scaillet B. (2007) Redox evolution of a degassing magma rising to the surface. *Nature* **445**, 194-197.

Burgisser A., Scaillet B. and Harshvardhan (2008) Chemical patterns of erupting silicic magmas and their influence on the amount of degassing during ascent. *J. Geophys. Res.* **113**, B12204, 1-14.

Burnham C. W. (1979) Magmas and hydrothermal fluids. In *Geochemistry of hydrothermal ore deposits* (ed. H. L. Barns). John Willey and Sons, New York. pp. 71-136.

Carroll M. R. and Rutherford M. J. (1985) Sulfide and Sulfate Saturation in Hydrous Silicate Melts. *J. Geophys. Res.* **90**, C601-C612.

Carroll M. R. and Rutherford M. J. (1987) The Stability of Igneous Anhydrite: Experimental Results and Implications for Sulfur Behavior in the 1982 El Chichon Trachyandesite and Other Evolved Magmas. *J. Petrol.* **28**, 781-801.

Carroll M. R. and Rutherford M. J. (1988) Sulfur Speciation in Hydrous Experimental Glasses of Varying Oxidation-State - Results from Measured Wavelength Shifts of Sulfur X-Rays. *Am. Mineral.* **73**, 845-849.

Cashman K. V. (2004) Volatile controls on magma ascent and eruption. In *The State of the Planet: Frontiers and Challenges in Geophysics* (eds. R. S. J. Sparks and C. J.Hawkesworth). American Geophysical Union, Geophysical Monograph series **150**, Washington, pp. 109-124.

Chevychelov V. Y., Bocharnikov R. E. and Holtz F. (2008) Experimental study of chlorine and fluorine partitioning between fluid and subalkaline basaltic melt. *Dokl. Earth Sci.* **422**, 1089-1092.

Chou I-M. (1987) Oxygen Buffer and Hydrogen Sensor Techniques at Elevated Pressures and Temperatures. In *Hydrothermal Experimental Techniques* (eds. G. C. Ulmer and H. L. Barnes). John Willey and Sons, New York. pp. 61-99.

Cichy S. B., Botcharnikov R. E., Holtz F. and Behrens H. (2011) Vesiculation and Microlite Crystallization Induced by Decompression: a Case Study of the 1991–1995 Mt Unzen Eruption (Japan). *J. Petrol.* **52**, 1469-1492.

Coplen T. B. and Krouse, H. R. (1998) Sulphur isotope data consistency improved. *Nature* **392**, 32-32.

de Hoog J. C. M., Taylor B. E. and van Bergen M. J. (2001) Sulfur isotope systematics of basaltic lavas from Indonesia: implications for the sulfur cycle in subduction zones. *Earth Planet. Sci. Lett.* **189**, 237-252.

de Laeter J. R., Bohlke J. K., De Bièvre P., Hidaka H., Peiser H. S., Rosman K. J. R. and Taylor P. D. P. (2003) Atomic weights of the elements: Review 2000 - (IUPAC technical report). *Pure Appl. Chem.* **75**, 683-800.

Delmelle P., Ayris P. S. S. and Dingwell D. (2011) SO_2 and HCl scavenging by ash at high temperature in volcanic eruption plumes: insights from laboratory experiments. *Geophys. Res. Abstr.* **13**, EGU2011-9785.

Ding T., Valkiers S., Kipphardt H., De Bièvre P., Taylor P. D. P., Gonfiantini R. and Krouse R. (2001) Calibrated sulfur isotope abundance ratios of three IAEA sulfur isotope reference materials and V-CDT with a reassessment of the atomic weight of sulfur. *Geochim. Cosmochim. Acta* **65**, 2433-2437.

Evans K. A., O'Neill H. S. C. and Mavrogenes J. A. (2008) Sulphur solubility and sulphide immiscibility in silicate melts as a function of the concentration of manganese, nickel, tungsten and copper at 1 atm and 1400 °C. *Chem. Geol.* **255**, 236-249.

Faure G. (1986) *Principles of Isotope Geology*, John Wiley and Sons, New York.

REFERENCES

Fleet M. E. (2005) XANES spectroscopy of sulfur in earth materials. *Can. Mineral.* **43**, 1811-1838.

Fleet M. E., Stone W. E. and Crocket J. H. (1991) Partitioning of palladium, iridium, and platinum between sulfide liquid and basalt melt: Effects of melt composition, concentration, and oxygen fugacity. *Geochim. Cosmochim. Acta* **55**, 2545-2554.

Freise M., Holtz F., Nowak M., Scoates J. S. and Strauss H. (2009) Differentiation and crystallization conditions of basalts from the Kerguelen large igneous province: an experimental study. *Contrib. Mineral. Petrol.* **158**, 505-527.

Gaillard F., Schmidt B., Mackwell S. and McCammon C. (2003) Rate of hydrogen-iron redox exchange in silicate melts and glasses. *Geochim. Cosmochim. Acta* **67**, 2427-2441.

Gerlach T. M. and Nordlie B. E. (1975) The C-O-H-S gaseous system; Part II, Temperature, atomic composition, and molecular equilibria in volcanic gases. *Am. J. Sci.* **275**, 377-394.

Giordano D., Russell J. K. and Dingwell D. B. (2008). Viscosity of magmatic liquids: A model. *Earth Planet. Sci. Lett.* **271**, 123-134.

Gladstone J. H. and Dale T. P. (1863) Researches on the Refraction, Dispersion, and Sensitiveness of Liquids. *Philos. Trans. R. Soc. London* **153**, 317-343.

Gondé C., Martel C., Pichavant M. and Bureau H. (2011) In situ bubble vesiculation in silicic magmas. *Am. Mineral.* **96**, 111-124.

Gorbachev N. S. (1990) Fluid-Magma Interaction in Sulfide-Silicate Systems. *Intl. Geol. Rev.* **32**, 749-836.

Guillong M., Latkoczy C., Seo J. H., Gunther D. and Heinrich C. A. (2008) Determination of sulfur in fluid inclusions by laser ablation ICP-MS. *J. Anal. Atom. Spectrom.* **23**, 1581-1589.

Hamada M., Laporte D., Cluzel N., Koga K. T. and Kawamoto T. (2010) Simulating bubble number density of rhyolitic pumices from Plinian eruptions: constraints from fast decompression experiments. *Bull. Volcanol.* **72**, 735-746.

Hawthorne F. C., Krivovichev S. V. and Burns P. C. (2000) The Crystal Chemistry of Sulfate Minerals. *Rev. Mineral. Geochem.* **40**, 1-112.

Higgins M. D. (2000) Measurement of crystal size distributions. *Am. Mineral.* **85**, 1105-1116.

Higgins M. D. (2002) Closure in crystal size distributions (CSD), verification of CSD calculations, and the significance of CSD fans. *Am. Mineral.* **87**, 171-175.

Higgins M. D. and Chandrasekharam D. (2007) Nature of Sub-volcanic Magma Chambers, Deccan Province, India: Evidence from Quantitative Textural Analysis of Plagioclase Megacrysts in the Giant Plagioclase Basalts. *J. Petrol.* **48**, 885-900.

Holloway J. R. and Blank J. G. (1994). Application of Experimental Results to C-O-H Species in Natural Melts. *Rev. Mineral.* **30**, 187-230.

Holtz F., Behrens H., Dingwell D. B. and Johannes W. (1995) H_2O solubility in haplogranitic melts: compositional, pressure and temperature dependence. *Am. Mineral.* **80**, 94-108.

Hui H. and Zhang Y. (2007) Toward a general viscosity equation for natural anhydrous and hydrous silicate melts. *Geochim. Cosmochim. Acta* **71**, 403-416.

Hurwitz S. and Navon O. (1994) Bubble nucleation in rhyolitic melts: Experiments at high pressure, temperature, and water content. *Earth Planet. Sci. Lett.* **122**, 267-280.

Jugo P. J., Wilke M. and Botcharnikov R. E. (2010) Sulfur K-edge XANES analysis of natural and synthetic basaltic glasses: Implications for S speciation and S content as function of oxygen fugacity. *Geochim. Cosmochim. Acta* **74**, 5926-5938.

REFERENCES

Katsura T. and Nagashima S. (1974) Solubility of Sulfur in Some Magmas at 1-Atmosphere. *Geochim. Cosmochim. Acta* **38**, 517-531.

Keppler H. (1999) Experimental evidence for the source of excess sulfur in explosive volcanic eruptions. *Science* **284**, 1652-1654.

Keppler H. (2010) The distribution of sulfur between haplogranitic melts and aqueous fluids. *Geochim. Cosmochim. Acta* **74**, 645-660.

Klimm K., Kohn S. C., Botcharnikov R. E. (2012a) The dissolution mechanism of sulphur in hydrous silicate melts. II: Solubility and speciation of sulfur in hydrous silicate melts as a function of fO_2. *Chem Geol.* **322-323**, 250-267.

Klimm K., Kohn S. C., O'Dell L. A., Botcharnikov R. E. and Smith M. E. (2012b) The dissolution mechanism of sulphur in hydrous silicate melts. I: Assessment of analytical techniques in determining the sulphur speciation in iron-free to iron-poor glasses. *Chem. Geol.* **322–323**, 237-249.

Kress V. C. and Carmichael I. S. E. (1991) The compressibility of silicate liquids containing Fe_2O_3 and the effect of composition, temperature, oxygen fugacity and pressure on their redox states. *Contrib. Mineral. Petrol.* **108**, 82-92.

Krishnamurthy N. and Soots V. (1971) Raman Spectrum of Gypsum. *Can. J. Phys.* **49**, 885-896.

Lautze N., Sisson T., Mangan M. and Grove T. (2011) Segregating gas from melt: an experimental study of the Ostwald ripening of vapor bubbles in magmas. *Contrib. Mineral. Petrol.* **161**, 331-347.

le Roux P. J., Shirey S. B., Hauri E. H., Perfit M. R. and Bender J. F. (2006). The effects of variable sources, processes and contaminants on the composition of northern EPR MORB (8–10°N and 12–14°N): Evidence from volatiles (H_2O, CO_2, S) and halogens (F, Cl). *Earth Planet. Sci. Lett.* **251**, 209-231.

Leschik M., Heide G., Frischat G. H., Behrens H., Wiedenbeck M., Wagner N., Heide K., Geissler H. and Reinholz U. (2004) Determination of H_2O and D_2O contents in rhyolitic glasses. *Phys. Chem. Glasses* **45**, 238-251.

Lesne P., Kohn S. C., Blundy J., Witham F., Botcharnikov R. E., Behrens H. (2011) Experimental Simulation of Closed-System Degassing in the System Basalt-H_2O-CO_2-S-Cl. *J. Petrol.* **52**, 1737-1762.

Mandeville C. W. (2010) Sulfur: A Ubiquitous and Useful Tracer in Earth and Planetary Sciences. *Elements* **6**, 75-80.

Mandeville C. W., Webster J. D., Rutherford M. J., Taylor B. E., Timbal A. and Faure K. (2002) Determination of molar absorptivities for infrared absorption bands of H_2O in andesitic glasses. *Am. Mineral.* **87**, 813-821.

Mandeville C. W., Shimizu N., Kelley K. A. and Cheek L. (2008) Sulfur Isotope Variation in Basaltic Melt Inclusions from Krakatau Revealed by a Newly Developed Secondary Ion Mass Spectrometry Technique for Silicate Glasses. *EOS Trans. AGU* **83**(53), Fall Meeting, San Fransisco, #V13-F07(abstr.).

Mandeville C. W., Webster J. D., Tappen C., Taylor B. E., Timbal A., Sasaki A., Hauri E., Bacon C. R. (2009) Stable isotope and petrologic evidence for open-system degassing during the climactic and pre-climactic eruptions of Mt. Mazama, Crater Lake, Oregon. *Geochim. Cosmochim. Acta* **73**, 2978-3012.

Marini L., Chiappini V., Cioni R., Cortecci G., Dinelli E., Principe C. and Ferrara G. (1998) Effect of degassing on sulfur contents and $\delta^{34}S$ values in Somma-Vesuvius magmas. *Bull. Volcanol.* **60**, 187-194.

Metrich N. and Rutherford M. J. (1992) Experimental study of chlorine behavior in hydrous silicic melts. *Geochim. Cosmochim. Acta* **56**, 607-616.

Metrich N. and Mandeville C. W. (2010) Sulfur in Magmas. *Elements* **6**, 81-86.

REFERENCES

Miyoshi T., Sakai H. and Chiba H. (1984) Experimental-Study of Sulfur Isotope Fractionation Factors between Sulfate and Sulfide in High-Temperature Melts. *Geochem. J.* **18**, 75-84.

Moore G., Vennemann T. and Carmichael I. S. E. (1998) An empirical model for the solubility of H_2O in magmas to 3 kilobars. *Am. Mineral.* **83**, 36-42.

Moretti R. (2005) Polymerisation, basicity, oxidation state and their role in ionic modelling of silicate melts. *Ann. Geophys.* **48**, 583-608.

Moretti R., Papale P. and Ottonello G. (2003) A model for the saturation of C-O-H-S fluids in silicate melts. In *Volcanic Degassing*, Special Publication 213 (ed. C. Oppenheimer et al.). Geological Society of London. pp. 81-101.

Morgan G. B. VI and London D. (1996) Optimizing the electron microprobe analysis of hydrous alkali aluminosilicate glasses. *Am. Mineral.* **81**, 1176-1185.

Morgan G. B. VI and London D. (2005) Effect of current density on the electron microprobe analysis of alkali aluminosilicate glasses. *Am. Mineral.* **90**, 1131-1138.

Moune S., Sigmarsson O., Thordarson T. and Gauthier P.-J. (2007) Recent volatile evolution in the magmatic system of Hekla volcano, Iceland. *Earth Planet. Sci. Lett.* **255**, 373-389.

Moune S., Holtz F. and Botcharnikov R. E. (2009) Sulphur solubility in andesitic to basaltic melts: implications for Hekla volcano. *Contrib. Mineral. Petrol.* **157**, 691-707.

Nagashima S. and Katsura T. (1973) Solubility of Sulfur in Na_2O-SiO_2 Melts under Various Oxygen Partial Pressures at 1100 °C, 1250 °C, and 1300 °C. *B. Chem. Soc. Jpn.* **46**, 3099-3103.

Newman S. and Lowenstern J.B. (2002) VOLATILECALC: a silicate melt-H_2O-CO_2 solution model written in Visual Basic for excel. *Comput. Geosci.* **28**, 597-604.

Newton R. C. and Manning C. E. (2005) Solubility of anhydrite, $CaSO_4$, in NaCl-H_2O solutions at high pressures and temperatures: Applications to fluid-rock interaction. *J. Petrol.* **46**, 701-716.

Noguchi S., Toramaru A. and Nakada S. (2008) Relation between microlite textures and discharge rate during the 1991-1995 eruptions at Unzen, Japan. *J. Volcanol. Geoth. Res.* **175**, 141-155.

Nowak M., Cichy S. B., Botcharnikov R. E., Walker N. and Hurkuck W. (2011) A new type of high-pressure low-flow metering valve for continuous decompression: First experimental results on degassing of rhyodacitic melts. *Am. Mineral.* **96**, 1373-1380.

O'Neil J. R. (1986) Theoretical and experimental aspects of isotopic fractionation. *Rev. Mineral. Geochem.* **16**, 1-40.

Ochs F. A. and Lange R. A. (1999) The Density of Hydrous Magmatic Liquids. *Science* **283**, 1314-1317.

Ohba T., Nogami K., Hirabayashi J.-I. and Mori T. (2008) Isotopic fractionation of SO_2 and H_2S gases during the absorption by KOH solution, with the application to volcanic gas monitoring at Miyakejima Island, Japan. *Geochem. J.* **42**, 119-131.

Ohlhorst S., Behrens H. and Holtz F. (2001) Compositional dependence of molar absorptivities of near-infrared OH- and H_2O bands in rhyolitic to basaltic glasses. *Chem. Geol.* **174**, 5-20.

Ohmoto H. and Lasaga A. C. (1982) Kinetics of reactions between aqueous sulfates and sulfides in hydrothermal systems. *Geochim. Cosmochim. Acta* **46**, 1727-1745.

Ohmoto H. and Rye R. O. (1979) Isotopes of sulfur and carbon. In Geochemistry of Hydrothermal Ore Deposits (ed. H. L. Barnes), Wiley. pp. 509-567.

Oppenheimer C., Scaillet B. and Martin R.S. (2011) Sulfur Degassing From Volcanoes: Source Conditions, Surveillance, Plume Chemistry and Earth System Impacts. *Rev. Mineral. Geochem.* **73**, 363-421.

REFERENCES

Parat F., Holtz F. and Klugel A. (2011) S-rich apatite-hosted glass inclusions in xenoliths from La Palma: constraints on the volatile partitioning in evolved alkaline magmas. *Contrib. Mineral. Petrol.* **162**, 463-478.

Perfit M. R., Fornari D. J., Malahoff A. and Embley R. W. (1983) Geochemical Studies of Abyssal Lavas Recovered by Dsrv Alvin from Eastern Galapagos Rift, Inca Transform, and Ecuador Rift: 3. Trace-Element Abundances and Petrogenesis. *J. Geophys. Res.* **88**, 551-572.

Richet P., Bottinga Y. and Janoy M. (1977) A review of hydrogen, carbon, nitrogen, oxygen, sulphur, and chlorine stable isotope enrichment among gaseous molecules. *Annu. Rev. Earth Planet. Sci.* **5**, 65-110.

Sakai H., Casadevall T. J. and Moore J. G. (1982). Chemistry and isotope ratios of sulfur in basalts and volcanic gases at Kilauea volcano, Hawaii. *Geochim. Cosmochim. Acta* **46**, 729-738.

Sarma L. P., Prasad P. S. R. and Ravikumar N. (1998) Raman spectroscopic study of phase transitions in natural gypsum. *J. Raman Spectrosc.* **29**, 851-856.

Sasaki A., Arikawa Y. and Folinsbee R. E. (1979) Kiba reagent method of sulfur extraction applied to isotopic work. *Bull. Geol. Surv. Jpn.* **30**, 241-245.

Scaillet B., Pichavant M., Roux J., Humbert G. and Lefevre A. (1992) Improvements of the Shaw Membrane Technique for Measurement and Control of fH_2 at High-Temperatures and Pressures. *Am. Mineral.* **77**, 647-655.

Scaillet B., Pichavant M. and Roux J. (1995) Experimental Crystallization of Leucogranite Magmas. *J. Petrol.* **36**, 663-705.

Schuessler J. A., Botcharnikov R. E., Behrens H., Misiti V. and Freda C. (2008) Oxidation state of iron in hydrous phono-tephritic melts. *Am. Mineral.* **93**, 1493-1504.

Schwab R. G. and Küstner D. (1981) The equilibrium fugacities of important oxygen buffers in technology and petrology. *Neues Jahrbuch Mineral.* **140**, 112–142.

Shang L. B., Chou I-M., Lu W. J., Burruss R. C. and Zhang Y. X. (2009) Determination of diffusion coefficients of hydrogen in fused silica between 296 and 523 K by Raman spectroscopy and application of fused silica capillaries in studying redox reactions. *Geochim. Cosmochim. Acta* **73**, 5435-5443.

Shaw H. R. (1965) Comments on viscosity, crystal settling, and convection in granitic magmas. *Am. J. Sci.* **263**, 120-152.

Shelby J. E. (1977) Molecular-Diffusion and Solubility of Hydrogen Isotopes in Vitreous Silica. *J. Appl. Phys.* **48**, 3387-3394.

Shishkina T. A., Botcharnikov R. E., Holtz F., Almeev R. R. and Portnyagin M. V. (2010) Solubility of H_2O- and CO_2-bearing fluids in tholeiitic basalts at pressures up to 500 MPa. *Chem. Geol.* **277**, 115-125.

Silver, L. A., Ihinger P. D. and Stolper E. (1990) The influence of bulk composition on the speciation of water in silicate glasses. *Contrib. Mineral. Petrol.* **104**, 142-162.

Smith E. and Dent G. (2005) *Modern Raman Spectroscopy – A Practical Approach*. John Wiley and Sons Ltd, Chichester.

Sossi P. A. and O'Neill H. St. C. (2011) Systematic Underestimation of the Oxidation State of MORB Glasses. *Mineral. Mag.* **75** (3).

Sossi P. A., Foden J. D., Halverson G. P. (2012) Redox-controlled iron isotope fractionation during magmatic differentiation: an example from the Red Hill intrusion, S. Tasmania. *Contrib. Mineral. Petrol.* **164**, 757-772.

Sparks R. S. J., Barclay J., Jaupart C., Mader H. M., Phillips J. C. (1994) Physical aspects of magma degassing - 1. Experimental and theoretical constraints on vesiculation. *Rev. Mineral. Geochem.* **30**, 413-445.

Stelling J., Behrens H., Wilke M., Göttlicher J. and Chalmin-Aljanabi E. (2011) Interaction between sulphide and H_2O in silicate melts. *Geochim. Cosmochim. Acta* **75**, 3542-3557.

REFERENCES

Symonds R. B., Rose W. I., Bluth G. J. S. and Gerlach T. M. (1994) Volcanic-gas studies: methods, results, and applications. *Rev. Mineral.* **30**, 1-66.

Taylor B. E. (1986). Magmatic Volatiles - Isotopic Variation of C, H, and S. *Rev. Mineral.* **16**, 185-225.

Teague A. J., Kohn S. C., Klimm K. and Botcharnikov R. E. (2008) Sulphur solubility in Mount Hood andesites and CO_2 fluids: Implications for volcanic degassing. *EOS Trans. AGU* **89**(53), Fall Meeting, San Francisco, #V21B-2086(abstr.).

Toramaru A. (2006) BND (bubble number density) decompression rate meter for explosive volcanic eruptions. *J. Volcanol. Geoth. Res.* **154**, 303-316.

Turner J. S. and Campbell I. H. (1986) Convection and mixing in magma chambers. *Earth Sci. Rev.* **23**, 255-352.

Ueda A. and Sakai H. (1984) Sulfur isotope study of Quaternary volcanic rocks from the Japanese Islands Arc. *Geochim. Cosmochim. Acta* **48**, 1837-1848.

Wallace P. and Carmichael I. S. E. (1992) Sulfur in Basaltic Magmas. *Geochim. Cosmochim. Acta* **56**, 1863-1874.

Wallace P. J. and Edmonds M. (2011) The Sulfur Budget in Magmas: Evidence from Melt Inclusions, Submarine Glasses, and Volcanic Gas Emissions. *Rev. Mineral. Geochem.* **73**, 215-246.

Watson E. B. (1994) Diffusion in volatile-bearing magmas. *Rev. Mineral.* **30**, 371-412.

Webster J. D. (1992) Fluid-Melt Interactions Involving Cl-Rich Granites - Experimental-Study from 2 to 8 Kbar. *Geochim. Cosmochim. Acta* **56**, 659-678.

Webster J. D. and Botcharnikov R. E. (2011) Distribution of Sulfur Between Melt and Fluid in S-O-H-C-Cl-Bearing Magmatic Systems at Shallow Crustal Pressures and Temperatures. *Rev. Mineral. Geochem.* **73**, 247-283.

Webster J. D., Kinzler R. J. and Mathez E. A. (1999) Chloride and water solubility in basalt and andesite melts and implications for magmatic degassing. *Geochim. Cosmochim. Acta* **63**, 729-738.

Webster J. D., Sintoni M. F. and De Vivo B. (2006) The role of sulfur in promoting magmatic degassing and volcanic eruption at Mt. Somma-Vesuvius. In *Volcanism in the Campania Plain: Vesuvius, Campi Flegrei and Ignimbrites* (ed. B. de Vivo). Elsevier. pp. 219-233.

Webster J. D., Sintoni M. F. and De Vivo B. (2009) The partitioning behavior of Cl, S, and H_2O in aqueous vapor- +/- saline-liquid saturated phonolitic and trachytic melts at 200 MPa. *Chem. Geol.* **263**, 19-36.

Wilke M., Behrens H., Burkhard D. J. M. and Rossano S. (2002) The oxidation state of iron in silicic melt at 500 MPa water pressure. *Chem. Geol.* **189**, 55-67.

Wilke M., Jugo P. J., Klimm K., Susini J., Botcharnikov R., Kohn S. C. and Janousch M. (2008) The origin of S^{4+} detected in silicate glasses by XANES. *Am. Mineral.* **93**, 235-240.

Wilke M., Klimm K. and Kohn S. C. (2011) Spectroscopic Studies on Sulfur Speciation in Synthetic and Natural Glasses. *Rev. Mineral. Geochem.* **73**, 41-78.

Witham F. (2011) Conduit convection, magma mixing, and melt inclusion trends at persistently degassing volcanoes. *Earth Planet. Sci. Lett.* **301**, 345-352.

Witham F., Blundy J., Kohn S. C., Lesne P., Dixon J., Churakov S. V. and Botcharnikov R. (2012) SolEx: A model for mixed COHSCl-volatile solubilities and exsolved gas compositions in basalt. *Comput. Geosci.* **45**, 87-97.

Yasuda A., Nakada S. and Fujii T. (2001) Sulfur Abundance and Redox State of Melt Inclusions from Miyake-jima 2000 Eruption Products. *Bull. Volcanol. Soc. Jpn.* **46**, 165-173.

REFERENCES

Zajacz Z., Candela P. A., Piccoli P. M. and Sanchez-Valle C. (2012) The partitioning of sulfur and chlorine between andesite melts and magmatic volatiles and the exchange coefficients of major cations. *Geochim. Cosmochim. Acta* **89**, 81-101.

Zhang Y. and Ni H. (2010) Diffusion of H, C, and O Components in Silicate Melts. *Rev. Mineral. Geochem.* **72**, 171-225.

Zhang Y., Ni H. and Chen Y. (2010) Diffusion Data in Silicate Melts. *Rev. Mineral. Geochem.* **72**, 311-408.
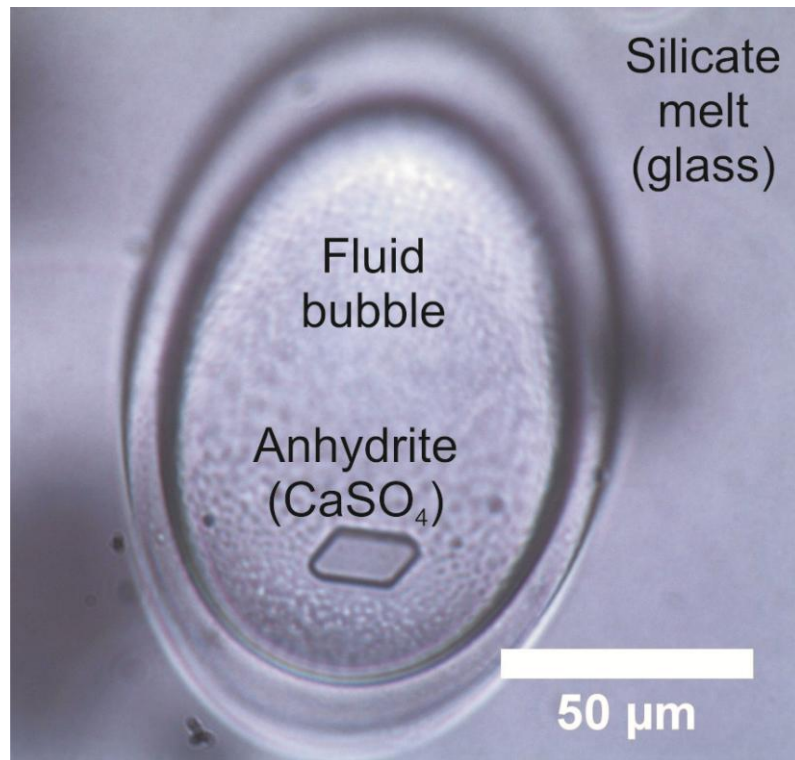
APPENDIX I

I-A. Microscopic investigation

Fig. I-A.1: Microscopic image of a fluid bubble in the quenched andesitic glass. The bubble contains a well-developed translucent crystal with monoclinic shape (anhydrite, according to Raman spectroscopy) and amorphous material quenched from the fluid. This type of anhydrite-bearing fluid inclusion is a typical feature of the decompression experiments conducted at oxidizing conditions ($\log(fO_2/\text{bar}) \sim \text{QFM+4}$) and quenched directly after decompression ($t_A = 0$ h).

I-B. Raman spectroscopy

Confocal Raman spectroscopy was used to determine the S species in the quenched fluid phase and to identify crystals (see Fig. I-A.1). Measurements were carried out on a Bruker Senterra micro-Raman spectrometer equipped with an Olympus BX 51 microscope and an Andor DU420-OE CCD (Settings: 532 nm laser excitation line; 20 mW power; Olympus 50× LWD objective; 20 s accumulation time; 5 acquisition repetitions, 50 µm pinhole). Unpolarized spectra were recorded in the range of 70 to 4455 cm^{-1} with a resolution of ±9 cm^{-1}. The wavelength accuracy and precision is maintained to better than 0.1 cm^{-1}. The as-measured raw sets of Raman spectra were baseline- and *T* corrected, integrated and smoothed twice by the application of adjacent averaging over three points. The applied correction

caused no artificial modification of Raman bands symmetry. For comparison Raman spectra were normalized to the fundamental OH stretching vibration band at ~3550 cm^{-1}.

Bubbles (~50 μm in diameter) near the surface but still closed to the atmosphere were selected for Raman measurements. The laser was focused on the sample surface and depth profiles were measured down to a depth of 50 μm with a step size of 5 μm. Along such a profile the relative contributions of the glass, quenched fluid and (possibly) crystals to the spectra change systematically. Spectra of crystals and bubbles always contain contributions of the glass matrix (Fig. I-B.1). This cannot be avoided even when using a confocal setup. Nevertheless, the characteristic sharp features from crystals and quenched S species can be easily distinguished from the broad bands of the glass (spectrum (d) in Fig. I-B.1).

The spectrum on top (Fig. I-B.1 (a), $QFM+4_{disequi}$) was recorded on a crystal in a bubble formed in an experiment under oxidizing conditions with instantaneous quench after decompression, thus, it represents fluid-melt disequilibrium. The most prominent peak at 1010 to 1014 cm^{-1} fits to the symmetric stretching vibration of sulfate groups in gypsum or anhydrite. Weak peaks at ~434 and ~625 cm^{-1} are consistent with published Raman spectra of gypsum (Sarma et al., 1998; Smith and Dent, 2005), while the peaks at 664 to 676 cm^{-1} and ~1128 cm^{-1} are characteristic for anhydrite (Sarma et al., 1998). An additional weak peak at ~494 to 497 cm^{-1} is expected for anhydrite or gypsum based on literature, but it is overprinted by spectral features of the glass. The absence of OH stretching vibration bands at 3405 and 3490 cm^{-1} originating from crystalline water in gypsum (Krishnamurthy and Soots, 1971) gives clear evidence that the frequently observed monoclinic shaped crystals in the quenched fluids under oxidizing conditions and fluid-melt disequilibrium are most likely anhydrite. Additionally, a small fraction of gypsum is present in the quench products of the fluid as indicated by the peaks at ~434 and ~625 cm^{-1}. The distinct peaks at 150 cm^{-1}, 219 cm^{-1} and 472 cm^{-1} most likely originate from S_8 globules which often occur as quench products in S-rich fluids (Bény et al., 1982). The presence of S_8 globules and gypsum in the quenched products can be explained by dissociation of SO_2 in the fluid upon cooling. These findings indicate that sulfate is the dominating S species in high p fluids (> 200 MPa) while reduced S species (SO_2, elemental S) become predominant in low p fluids (< 100 MPa) under oxidizing conditions (~QFM+4).

Appendix I

If decompression was followed by annealing for $\geq$ 5 h, anhydrite was absent in bubbles, and spectra recorded on bubbles show no systematic variation with annealing time. Since S concentration in the melt also remains constant after 5 h annealing (see Fig. 11 in Chapter I-A), we conclude that near-equilibrium conditions were achieved between fluid and melt. The spectrum (b) for *QFM+4$_{equi}$* in Fig. I-B.1 gives evidence for precipitated sulfate in quench phases in bubbles after annealing at final *p* and *T*. In other spectra (not shown here) features of S_8 globules or an additional weak broad peak close to $\sim$1087 cm^{-1} were observed, the latter is probably caused by vibrations of HSO_4^- (1050 to 1056 cm^{-1}) and/or SO_2 (1148 to 1151 cm^{-1}); (Bondarenko and Gorbaty, 1997; Binder and Keppler, 2011). The different observations result from inhomogeneous distribution of quench phases in bubbles and the instability of such phases under the laser beam.

In experiments under reducing conditions a broad, slightly asymmetric band near 2600 cm^{-1} was observed (spectrum (c), *QFM+1)*. This band is assigned to stretching vibrations of H_2S ($\sim$2588 cm^{-1}) and HS^- ($\sim$2557 cm^{-1}); (Bény et al., 1982; Bondarenko and Gorbaty, 1997). The sharp peak at $\sim$1071 cm^{-1} is probably related to protonated sulfate species (Bondarenko and Gorbaty, 1997; Binder and Keppler, 2011), indicating that S is not entirely reduced under these conditions. No systematic changes in the spectra were observed upon annealing after decompression. This finding is consistent with constant volatile contents of the melts upon annealing (Fig. I-B.1) and indicates near-equilibrium distribution of volatiles between fluid and melt.
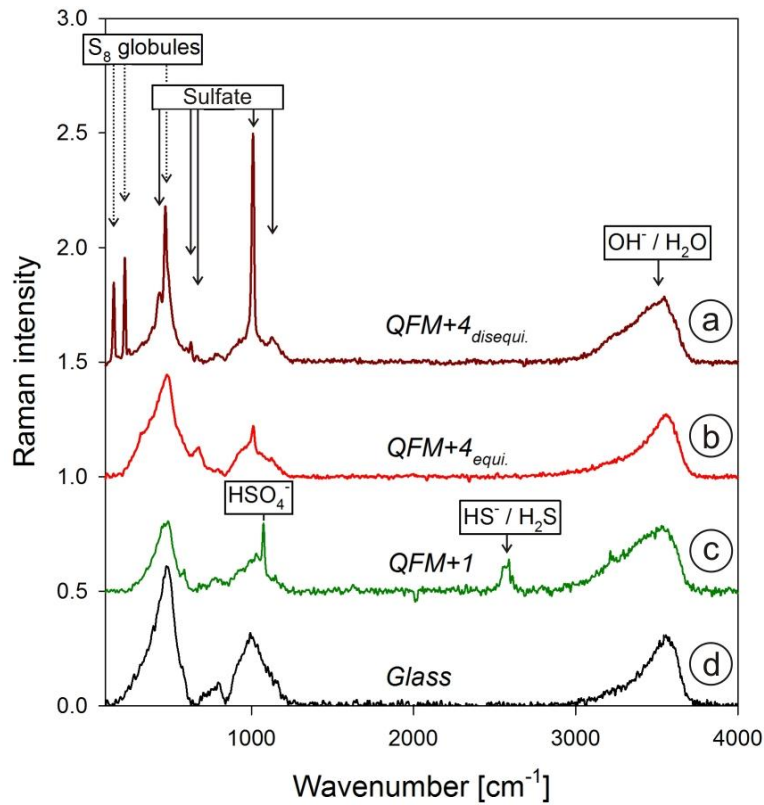
Fig. I-B.1. Raman spectra after decompression experiments with S and H_2O bearing dacitic andesite melts at 1030°C. Decompression was performed at a rate of ~0.1 MPa/s from 400 to 70 MPa. After decompression the samples were either rapidly quenched or further annealed (t_A) for 0 to 48 h at final *p-T* conditions.
(a): Oxidizing conditions (QFM+4), direct quench ($t_A = 0$ h): Fluid-melt disequilibrium
(b): Oxidizing conditions (QFM+4), long term annealing ($t_A = 48$ h): Fluid-melt equilibrium achieved.
(c): Reducing conditions (QFM+1): The spectrum is representative for both, disequilibrium ($t_A = 0$ h) and equilibrium ($t_A = 20$ h) conditions.
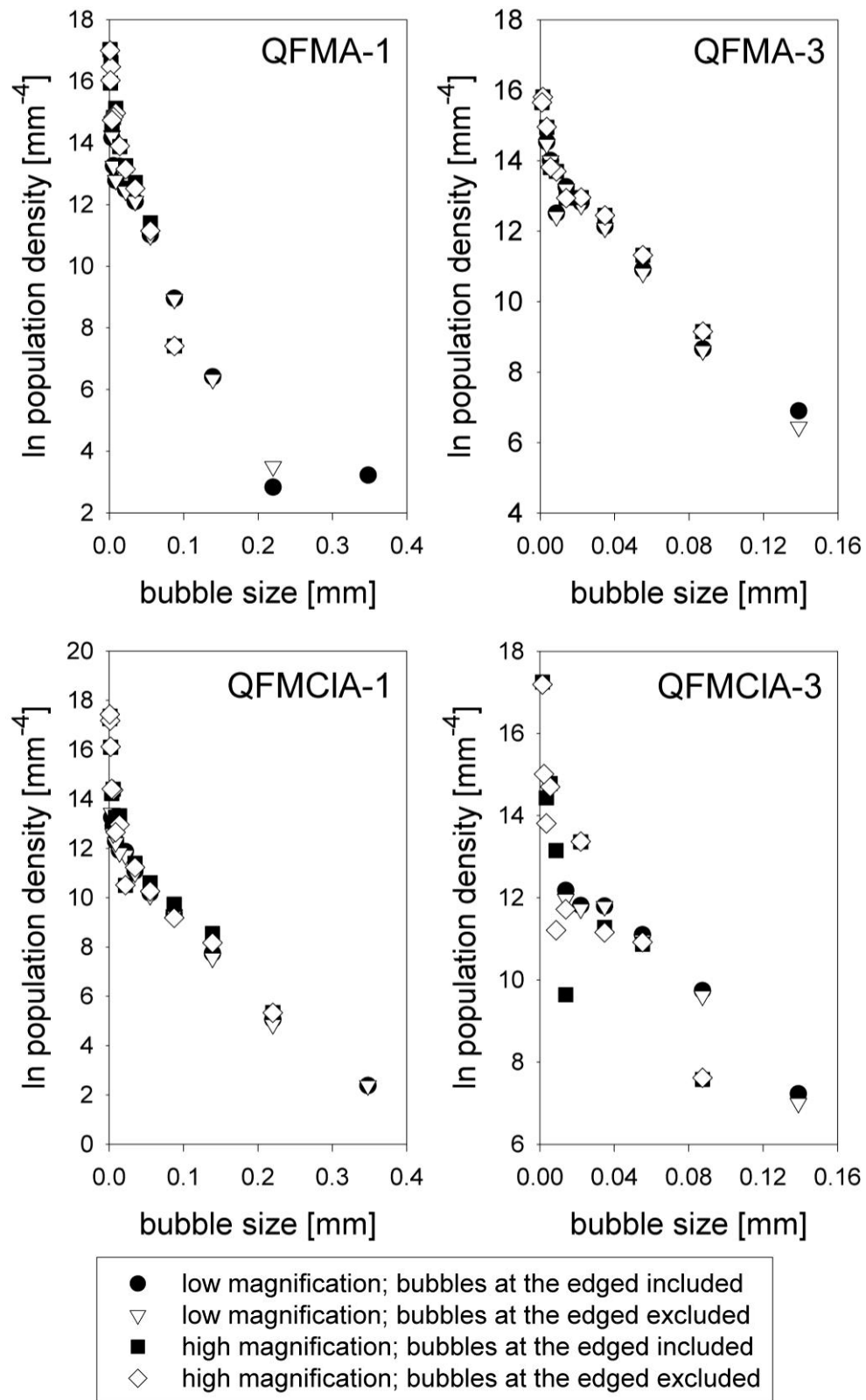(d): Typical spectrum of hydrous glass after decompression.

I-C. Bubble size distribution

Fig. I-C.1. Bubble size distribution of selected samples (QFMA-1; -3; QFMClA-1; -3). Images sizes range between ~600 × ~400 μm (high magnification) and ~2500 × ~1850 μm (low magnification). Bubbles at the edges of the images were either excluded or included during image analyses.

APPENDIX II

II-A. Electron microprobe analyses

The glass composition of all samples was determined using a Cameca SX-100 electron microprobe (EMP; acceleration voltage: 15 keV – beam size: 20 μm). The applied beam current was 5 nA (Na) or 10 nA (Si, Ti, Al, Fe, Mn, Mg, Ca, K) and the counting times range from 4 s (Na) up to 10 s or 30 s for all major constituents (Si, Ti, Al, Fe, Mn, Mg, Ca, K). Beam current and the counting time were increased for the analyses of S (35 or 100 nA; 240 s) and Cl (35 nA; 120 s) to decrease the detection limit and to improve the counting statistics, respectively (detection limits: ~32 ppm S; ~50 ppm Cl). NIST (U. S. National Institute of Standards and Technology) standards 610 and 620 where measured before and after most analyses to constrain the precision of the measurements.

II-B. IR spectroscopy

Near infra-red spectroscopy was conducted to determine the water contents in the glass samples. The spectra were collected using a microscope Bruker IRscope II connected to a FTIR spectrometer Bruker IFS 88 equipped with Mercury-Cadmium-Tellurium narrow range detector, a tungsten lamp and a CaF_2 beam splitter. The spectral resolution was set to 4 cm^{-1} and two to five measurements were collected on each sample.

The measurement of the water content dissolved in glass samples as OH^- groups and molecular H_2O is based on the Beer-Lambert law. Doubly polished glass chips with a thickness of ~120 to ~300 μm, depending on the transmittance of the samples, were prepared for the analysis. The thickness was determined using a conventional micrometer (precision: 3 μm). The absorbances of the IR active bands of molecular water (5200 cm^{-1}) and hydroxyl groups (4500 cm^{-1}) were used for the estimations. The tangential baseline correction described by Ohlhorst et al. (2001) was applied to determine the heights of the H_2O and OH^- bands. The densities of the glasses were calculated following the method of Mandeville et al. (2002) using the known glass composition and the Gladstone-Dale rule (Gladstone and Dale, 1863). The absorption coefficients determined in Chapter I-A for the andesitic melt composition were applied to quantify the water contents in the glasses [$\varepsilon(5200cm^{-1}) = 1.27 \pm 0.07$ L/mol·cm for molecular water; $\varepsilon(4500cm^{-1}) = 0.84 \pm 0.07$ L/mol·cm for hydroxyl groups]. A detailed

description of the NIR measurements and the determination of the absorption coefficients can be found in Chapter I-A.

II-C. Processing procedure of raw SIMS data

In a first step, the raw SIMS data was time interpolated to account for a drift of the instrumental fractionation during a 50-cycles measurement (as ^{32}S and ^{34}S were alternately detected) and ^{34}S/ ^{32}S ratios were filtered for a 2 sigma deviation. In a second step, the raw δ^{34}S values were corrected by the long term analytical drift of the instrumental fractionation, using a time based linear interpolation of all δ^{34}S values of the standard glasses analyzed within one analytical sequence (*analytical sequences* are subdivided by e.g. sample exchanges, ion-beam shut down, software reset). The instrumental fractionation can be described by the fractionation factor $\alpha_{(t-m)}$, calculated using the true (*t*) δ^{34}S$_t$ of 0.7 ± 0.5 ‰ of the monitored basaltic glass standard (MOR basalt 892-1) and the measured (*m*) δ^{34}S$_m$ values of the standard. The instrumental drift within ~6 days of continuous measurement (≜ only short term interruptions between *analytical sequences*; usually < 2 h) is illustrated in Fig. II-C.1, showing that $\alpha_{(t-m)}$ ranges from ~0.9825 to ~1.0044. The figure shows that the instrumental drift can be described by a polynomial function. However, within one *analytical sequence* the applied linear interpolation should be adequate. In a final step, to account for short term variations, the pre-corrected δ^{34}S values of the standards measured right before and after a set of 2-3 sample measurements were used for a time based correction of the δ^{34}S values using linear interpolation. Note, this short term variation between two standard measurement (within ~2.5 h) is typically < 0.5‰.
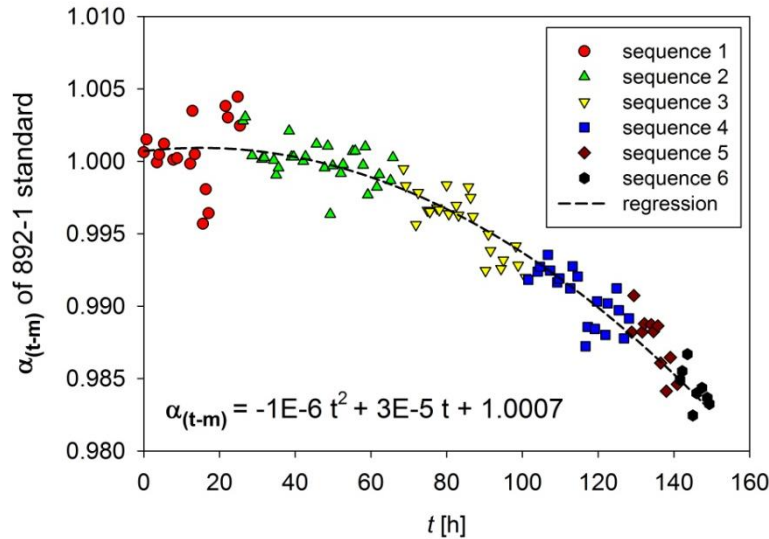
Fig. II-C.1: Drift of the instrumental fractionation. The different analytical sequences are illustrated by different symbols and color.

II-D. S speciation: X-ray absorption near edged spectroscopy (XANES)

XANES at the S K-edge (2472 eV) was performed on most samples to investigate the S speciation in the andesitic glasses and, if possible, in the quenched fluids, using the SUL-X beamline (uses wiggler as radiation source) at the synchrotron radiation source ANKA (Karlsruhe Institute of Technology, Germany). Noteworthy, the data on S speciation in the glasses is shown in Chapter I-A. ANKA operates at a beam energy of 2.5 GeV and a beam intensity of 200 mA. The storage ring has a circumference of 110.4 m. The spectra were collected in fluorescence mode from 2.45 to 2.55 keV. Quick-XAFS scans (XAFS: X-ray absorption fine structure; bragg axis is continuously running) were conducted to avoid irradiation damages (see also Chapter I-A). 5 to 20 spectra were collected on each position, depending on the quality of the single spectrum. The spectra were compared systematically and only spectra showing no evidence for changes in S speciation (e.g. formation of S^{4+}, changes in $S^{6+}/\Sigma S$ ratio), caused by irradiation with the X-ray beam during synchrotron analysis (Wilke et al., 2008), were considered and merged. The energy of the monochromator was calibrated to the white line of sulfate in scotch tape (2481.4 eV).

Two different beam sizes were applied *i)* to evaluate the bulk S speciation in the andesitic glasses (~250×150 μm) and *ii)* to detect small scale variation in S speciation throughout sample (~60×60 μm). These variations can possibly be assigned to S species in the quenched fluid inclusions near the surface (see Appendix II-E.).

Appendix II

The energies of the spectra were corrected to the white line of the spectrum of gypsum (2482.84 eV) to be directly comparable to recent studies (e.g. Jugo et al., 2010; Stelling et al., 2011). The XANES spectra collected with the beam size 250×150 µm were used to estimate the *fO$_2$(XANES)* of the experiments following the approach of Jugo et al. (2010). However, in contrast to Jugo et al. (2010), we applied the fit parameters for andesitic glass compositions determined by Max Wilke (pers. comm.) and used by Botcharnikov et al. (2011), to account for compositional influences.

II-E. S speciation in the quenched fluid

The determination of S species within bubbles using XANES is difficult because the emitted fluorescence decreases exponentially with depth below sample surface. However, the spectra may provide a rough estimation of the prevailing S speciation in the fluid.

The comparison of spectra collected on sample volumes containing no or almost no bubbles with those containing large bubble fractions close to the surface (depth ≤ 10 µm) provides qualitative information on the S-bearing species in the fluid. It is emphasized that the contribution of the S species in the bubbles to the spectra is very small and that the spectra are dominated by contributions of the surrounding S in the glass. However, as shown in Fig. D.1, few spectra reveal significant differences which may be attributed to S-species in the fluid phase. Fig. D.1 displays selected spectra of AHC-2 (~QFM+4, *r*: ~0.1 MPa/s, *t$_A$*: ~20 h) and RED-3 (~QFM+1, ~0.1 MPA/s, ~5 h) collected on areas with very low volume fraction of bubbles (*g*) and on bubble-rich areas (*g+b*). Spectra of reference materials are plotted for comparison.

In general, differences in energy position and peak shape of bands related to S^{4+} and S^{2-} species in glasses (or fluids) when compared to the peak positions and shape observed in the reference materials (sodium sulfite Na$_2$SO$_3$ for S^{4+} and pyrrhotite Fe$_{1-X}$S for S^{2-}) are related to the different stereochemical environment and, thus, depend on the chemical composition of the respective S compound (e.g. Fleet, 2005; Klimm et al., 2012b).

The spectrum of AHC-2 collected on a bubble-poor area (*g*) indicates that nearly all S in the glass is present as sulfate (S^{6+}/ΣS ~1) at oxidizing conditions (~QFM+4). On the other hand, spectra collected on areas with a high volume fraction of bubbles [(AHC-2 (*b+g*)] reveal an additional, small but

143

distinct peak at ~2478.2 eV. This peak most likely refers to sulfite S^{4+} (see reference material; Backnaes et al., 2008; Wilke et al., 2008). Noteworthy, Backnaes et al. (2008) as well as Wilke et al. (2008) noted that S^{2-} and S^{6+} are the only significant S species observed in quenched silicate glasses. Furthermore, it is unlikely that the observed sulfite peak is caused by irradiation as the applied analytical approach allows us to distinguish between original and artificial features (see above; Section II-D). Hence, the peak at ~2478.2 eV can most probably be attributed to SO_2 in the closed bubbles. Although the contribution of the S^{4+} peak is small in the spectra, it indicates that SO_2 may be the dominant S species in the fluid phase at QFM+4.
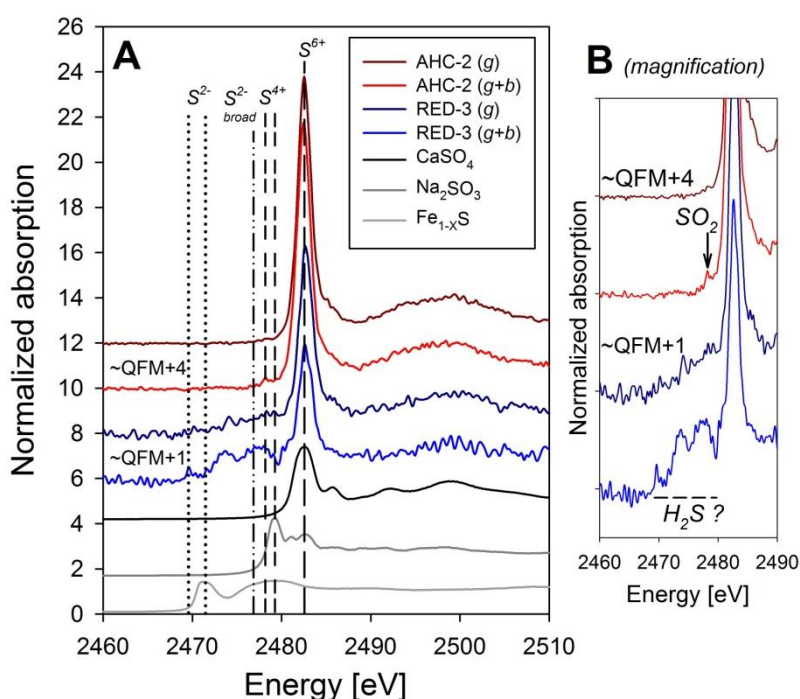

Fig. II-E.1 a/b: S Kα XANES spectra of selected experimental glasses and reference materials. **a)** The vertical lines mark the positions of the observed sulfur species. The spectra were collected with a beam size of about 60×60 μm, either on bubble free parts of the experimental samples (*g*; glass only) or on areas with a large volume fraction of bubbles close to the surface (*g+b*; glass and bubbles). The sharp peaks at 2482.2 eV, present in most displayed spectra, correspond to sulfate (S^{6+}, *long dashes*). The sharp but remarkably less prominent peak at 2478.2 eV (AHC-2 *g+b*) and 2479.2 eV (reference material: Na_2SO_3), respectively, indicates the presence of sulfite (S^{4+}, *short dashes*). The broad peak with a maximum at ~2477 eV can be attributed to sulfide (RED-3 *g*; RED-3 *g+b*; $Fe_{1-X}S$). The sharp peak observed at 2469.6 eV (RED-3 *g+b*) and at 2471.5 eV (reference material: $Fe_{1-X}S$) also refers to sulfide. The spectrum of sodium sulfite (Na_2SO_3, *dark grey*) indicates the presence of sulfate in the reference material, most likely related to irradiation caused by the X-ray beam (Wilke et al., 2008).
b) Magnification of plot (A). The bands which may indicate the presence of SO_2 (at QFM+4) or H_2S (~QFM+1) in the fluid phase are marked by black arrow (SO_2) or dashed line (H_2S).

Under reducing conditions (~QFM+1; RED-3 spectra) the $S^{6+}/\Sigma S$ ratio was found to be remarkably lower in areas with high volume fraction of bubbles closed to the surface ($g+b$) when compared to bubble poor/free areas (g). The high abundance of the broad peak at ~2477 eV observed in the vesiculated area is probably related to S^{2-} species in the fluid phase. Hence, it is suggested that significant amounts of H_2S are present in the fluid phase at QFM+1.

II-F. Modeling of S-isotope fractionation

The estimated fractionation pairs $\alpha(SO_{2\ gas} - SO_4^{2-}{}_{melt})$, $\alpha(SO_{2\ gas} - SO_4^{2-}{}_{melt})$, $\alpha(H_2S_{\ gas} - S^{2-}{}_{melt})$ and $\alpha(H_2S_{\ gas} - SO_4^{2-}{}_{melt})$ are listed in Table 3 of Chapter II. These values were applied to calculate an average fractionation factors describing the S-isotope fluid-melt fractionation for a given fO_2 at 1030°C [$\alpha_{g\text{-}m}(fO_2)$] using the following equation:

$$\alpha_{g\text{-}m}(fO_2) = \quad A \cdot \alpha(SO_{2\ gas} - SO_4^{2-}{}_{melt}) + B \cdot \alpha(H_2S_{gas} - S^{2-}{}_{melt})$$
$$+ C \cdot \alpha(SO_{2\ gas} - S^{2-}{}_{melt}) + D \cdot \alpha(H_2S_{\ gas} - SO_4^{2-}{}_{melt}) \quad \text{(eqn. A1)}$$

$A = x(SO_2)$ if $x(SO_2) \leq x(SO_4^{2-})$	otherwise $A = x(SO_4^{2-})$	(eqn. A1-1)
$B = x(H_2S)$ if $x(H_2S) \leq x(S^{2-})$	otherwise $B = x(S^{2-})$	(eqn. A1-2)
$C = 0$ if $x(SO_2) \leq x(SO_4^{2-})$	otherwise $C = x(SO_2) - x(SO_4^{2-})$	(eqn. A1-3)
$D = 0$ if $x(H_2S) \leq x(S^{2-})$	otherwise $D = x(H_2S) - x(S^{2-})$	(eqn. A1-4)

where $x(SO_4^{2-})$ is the molar fraction of sulfate in the melt, $x(S^{2-})$ the molar fraction of sulfide in the melt, $x(SO_2)$ the molar fraction of SO_2 in the fluid and $x(H_2S)$ the molar fraction in the fluid.

APPENDIX III

III-A. Data for calibration of NIR absorption coefficients

Table III-A1: Data for calibration of NIR absorption coefficients and concentrations of hydrous species in the glasses.

Sample ID	X_{Mg}	fO_2 [ΔQFM]	H_2O [wt%] KFT †	d [cm]	ρ [g/L]	A(OH)	A(H_2O)	c(OH)	c(H_2O)
AB-A		0.3	3.30 ± 0.17	0.0127	2751	0.015	0.021	1.36	1.92
AB-Cl-A		0.5	3.88 ± 0.17	0.0130	2735	0.019	0.025	1.75	2.26
ABW-B-0x	~0.7	3.4	4.40 ± 0.22	0.0330	2717	0.047	0.085	1.74	3.14
ABW-Cl-E-0		3.5	4.73 ± 0.19	0.0318	2718	0.050	0.080	1.86	2.98
ABWCl0*		3.5	2.69 ± 0.18	0.0310	2767	0.036	0.031	1.36	1.16
BW-Mg-0*		1.0	1.66 ± 0.16	0.0219	2784	0.022	0.010	1.14	0.55
BW-Mg-1*		1.2	2.00 ± 0.16	0.0215	2777	0.023	0.015	1.25	0.79
BW-Mg-2*	~0.65	1.9	3.40 ± 0.16	0.0227	2746	0.031	0.037	1.60	1.91
BW-Mg-3*		2.1	4.38 ± 0.17	0.0227	2726	0.035	0.051	1.81	2.68
BW-Mg-4*		2.4	5.45 ± 0.17	0.0225	2704	0.036	0.069	1.89	3.63
ABL-A	~0.55	0.0	6.04 ± 0.17	0.0162	2621	0.025	0.071	1.56	4.56
ABL-Cl-A		0.3	5.97 ± 0.17	0.0039	2619	0.007	0.016	1.87	4.23
ABW-Cl-Dx-0x		3.7	5.88 ± 0.20	0.0060	2699	0.011	0.036	1.05	4.70
ABG-Ax-0x		0.6	5.65 ± 0.19	0.0134	2698	0.030	0.077	1.28	4.54
ABG-Cl-A-0		0.0	3.37 ± 0.19	0.0177	2756	0.031	0.047	0.98	2.03
ABG-Cl-B-0		0.2	4.29 ± 0.19	0.0316	2741	0.058	0.111	1.03	2.72
ABGCl0*		0.9	6.82 ± 0.21	0.0158	2705	0.030	0.088	1.07	4.39
ABG-0*	~0.2	0.9	7.10 ± 0.21	0.0165	2690	0.031	0.108	1.05	5.18
BW1Mg-1*		1.5	2.81 ± 0.18	0.0082	2761	0.015	0.019	1.03	1.76
BW1Mg-2*		1.7	3.53 ± 0.24	0.0084	2753	0.015	0.023	1.04	2.12
BW1Mg-3*		2.0	4.56 ± 0.19	0.0080	2727	0.017	0.033	1.18	3.26
BW1Mg-5*		2.3	6.43 ± 0.19	0.0067	2666	0.011	0.055	0.91	6.46
BW1Mg-6*		2.5	7.43 ± 0.19	0.0081	2656	0.010	0.071	0.77	7.08
BW1Mg-8*		2.6	8.51 ± 0.20	0.0073	2605	0.012	0.083	0.96	9.31
BW-1n*		0.4	1.71 ± 0.16	0.0203	2780	0.031	0.027	0.85	1.03
BW-2n*		0.6	2.05 ± 0.17	0.0209	2778	0.032	0.030	0.86	1.10
BW1*		0.8	2.63 ± 0.17	0.0110	2762	0.021	0.024	1.06	1.66
BW2*	MgO	1.1	3.56 ± 0.21	0.0122	2745	0.026	0.037	1.19	2.36
BW3*	free	1.3	4.16 ± 0.18	0.0118	2726	0.023	0.051	1.09	3.38
BW4*		1.6	6.06 ± 0.18	0.0112	2705	0.025	0.060	1.30	4.20
BW5*		1.3	4.20 ± 0.17	0.0119	2711	0.022	0.063	1.06	4.15
BW6*		1.7	6.71 ± 0.18	0.0122	2682	0.025	0.083	1.19	5.41

Notes: † H_2O content measured by Karl-Fischer titration; *glass sample was synthesized for the KFT–NIR calibration but not used for decompression experiments.

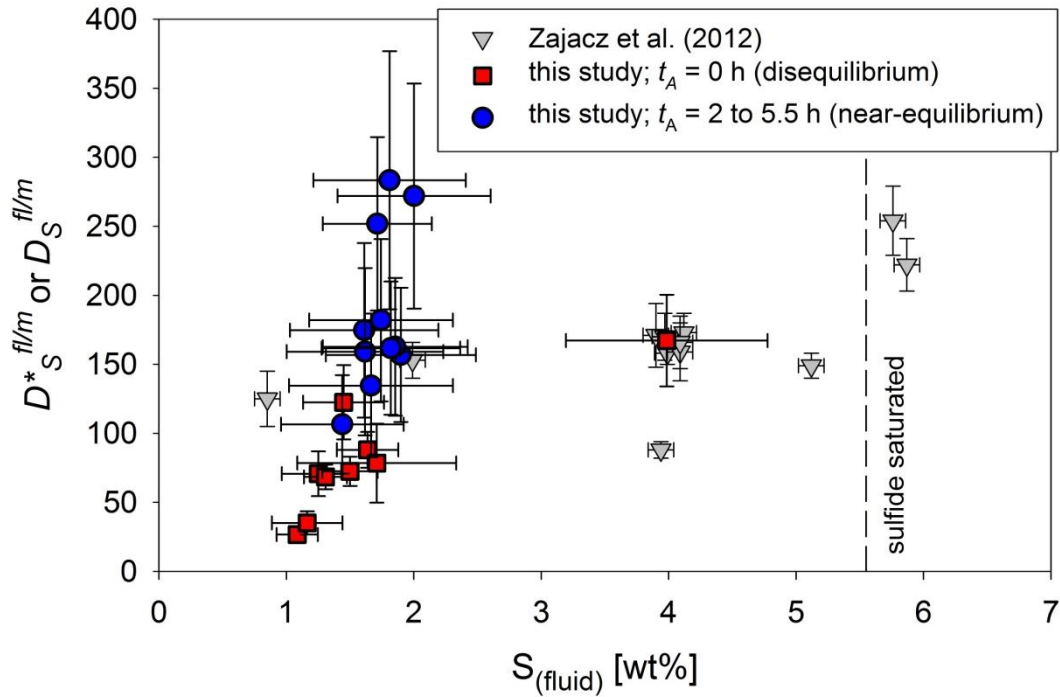*III-B. Data for calibration of NIR absorption coefficients*

Fig. III-B.1: $D*_S^{fl/m}$ or $D_S^{fl/m}$ as a function of $S_{(fluid)}$ [wt%]. The $D*_S^{fl/m}$ values obtained from experiments directly quenched after decompression ($t_A = 0$ h, disequilibrium, red squares) indicate a slight increase of $D*_S^{fl/m}$ with increasing $S_{(fluid)}$. For $t_A \geq 2$ h (near-equilibrium, blue circles) such a dependence of $D_S^{fl/m}$ on $S_{(fluid)}$ is not observed; i.e. the determined $D_S^{fl/m}$ are identical within error. This is in agreement with data of Zajacz et al. (2012) based on equilibrium experiments; i.e. S obeys Henry's law for fluid-melt near-equilibrium conditions and S contents below sulfide saturation.

CURRICULUM VITAE

Personal details

name:	Adrian Fiege	*phone:*	+49 178 542 00 87
address:	Wittekindstraße 37	*date of birth:*	09/27/1982
	30449 Hannover, Germany	*place of birth:*	Hessisch Lichtenau (Germany)
e-Mail:	a.fiege@mineralogie.uni-hannover.de	*Family status:*	unmarried

Research interests

- experimental petrology and geochemistry
- isotopic fractionation in magmatic processes (fluid-melt-mineral; especially sulfur)
- degassing processes and fluid-melt interactions
- formation of ore deposits (e.g. metal partitioning and mobility; fluid-melt-mineral)

Awards/Grants

since 03/2010:	PhD fellow of the German National Academic Foundation
12/2009 – 02/2010:	Assistance in the compilation of the proposal for the NTH Graduate School *GeoFluxes*
08/2010:	DAAD funding for Island excursion
10/2007 - 03/2009:	Diploma fellow of the German National Academic Foundation
05/2005:	DAAD travel funding for an internship in Bristol

Work Experiences and internships:

since 12/2009:	Scientific assistant at the Institute of Mineralogy, Department of Petrology; Leibniz Universität (LU) Hannover
04/2009 - 11/2009:	Lecturer at the Institute of Mineralogy, LU Hannover
05/2008 - 04/2009:	Student research assistant at the Institute of Mineralogy, Department of Petrology, LU Hannover
11/2007 - 04/2008:	Exploration-Geologist, Fluorspar Mine Vergenoeg, Republic of South Africa
04/2006 - 09/2007:	Tutor of „Physics for Geoscientists", LU Hannover
07/2006 - 09/2006:	Internship, Fluorspar Mine Vergenoeg, Republic of South Africa
10/2005 - 03/2007:	Technical Assistant at the Department of „Geochemistry, Rocks and Ores" at the Federal Institute for Geosciences and Natural Resources (BGR), Hannover
09/2005:	Internship at the Department of Earth Sciences, University of Bristol, UK
03/2005:	Internship at the Departments of „Geochemistry, Rocks and Ores" and „Petrology and Isotopic-Geology" at the BGR , Hannover
04/2004 - 09/2007:	Student research assistant at the Institute of Mineralogy, Department Crystallography, LU Hannover
11/2003 - 03/2004:	Student research assistant at the Institute for Sanitary Environmental Engineering and Waste Engineering, LU Hannover

Education:

since 03/2010:	PhD student at the Institute of Mineralogy, LU Hannover
03/2009:	Diploma Geoscience; LU Hannover (*overall grade*: 1.0 "sehr gut") Topic: The influence of F, Li, B and P at variable fO_2 and T on the solubility of Mn-Columbite and Mn-Tantalite in natural rhyolitic melts.
10/2003 - 03/2009:	Diploma student of Geoscience, LU Hannover
04/2003 - 09/2003:	Diploma student of Physics at the Friedrich-Schiller-Universität Jena
06/2002 - 03/2003:	Civil service at the *Jugendburg Ludwigstein*, Witzenhausen
06/2002:	German secondary school leaving examination (*Abitur*) at the Otto-Hahn Gymnasium, Göttingen

Additional activities:

since 2012	Member of the advisory board of the German Mineralogical Society (DMG)
10/2009 - 09/2011:	Member of the board of the Graduate Academy, LU Hannover
10/2005 - 03/2009:	Member of the Student Representatives "Geosciences", LU Hannover
04/2006 - 03/2008:	Member of the Student Representatives of the Faculty of Natural Sciences, LU Hannover
04/2006 - 03/2008:	Member of the Student Council, LU Hannover

Additional skills:

- *Analytical methods* (a selection): ion microprobe (Cameca IMS 1280), electron microprobe (Cameca SX100), XANES (ANKA, Karlsruhe, Germany), LA-ICP-MS (basic experiences made in Hannover)

- *Geoscience software* (a selection): Surpac, GIS, AnalySIS, Mathlab (basics), Surfer (basics)

- *Languages*: German (native); English (excellent); French (some); Spanish (some)

References:

Prof. Francois Holtz, Leibniz Universität Hannover, Germany
Phone: +49 511 762 5281; Email: f.holtz@mineralogie.uni-hannover.de

Prof. Harald Behrens, Leibniz Universität Hannover, Germany
Phone: +49 511 762 8054; Email: h.behrens@mineralogie.uni-hannover.de

Dr. Nobumichi Shimizu, Woods Hole Oceanographic Institution, USA
Phone: +1 508 289 2963; Email: nshimizu@whoi.edu

Dr. Charles W. Mandeville, U.S. Geological Survey, Reston, USA
Phone: +1 703-648-4773; Email: cmandeville@usgs.gov

LIST OF PUBLICATIONS

Journals

Fiege A., Behrens H., Holtz F., Adams F. (----) Kinetic vs. thermodynamic control of degassing of H_2O-S±Cl-bearing andesitic melts. *Geochim. Cosmochim. Acta*, (submitted).

A. Fiege, C. Kirchner, F. Holtz, R. L. Linnen, W. Dziony (2011) Influence of fluorine on the solubility of manganotantalite ($MnTa_2O_6$) and manganocolumbite ($MnNb_2O_6$) in granitics melts – An experimental study. *Lithos* **122**, 165-174

T. Graupner, A. Kassahun, D. Rammlmair, J. A. Meima, D. Kock, M. Furche, **A. Fiege**, A. Schippers, F. Melcher (2007) Formation of sequences of cemented layers and hardpans within sulfide-bearing mine tailings (mine district Freiberg, Germany). *Appl. Geochem.* **22**, 2486-2508

Extended Abstracts

A. Fiege, T. Graupner (2007) Characterisation of mineral distribution and remaining pore spaces in fi ne laminated, partially cemented mine tailings. 9th Biennial SGA Meeting; Mineral Exploration and Research: Digging Deeper; Dublin, Ireland. *Talk*

Abstracts

Fiege, A., Behrens, H., Holtz F., Mandeville C., Shimizu N. (2012) Sulphur Isotopes: An important geochemical tracer in fluid-melt system? EMC Vol.1, Frankfurt, Germany. *Talk*

Crede, L., **Fiege, A.**, Behrens, H. (2012) Degassing kinetics of sulphur upon decompression in basaltic systems. EMC Vol.1, Frankfurt, Germany. *Poster*

A. Fiege, H. Behrens, F. Holtz, C. Mandeville, N. Shimizu (2012) Degassing of andesitic and basaltic melts: fluid/melt distribution of sulfur and S-isotope fractionation. EMPG XIV, Kiel, Germany. *Talk*

M. Dietrich, **A. Fiege**, H. Behrens (2011) Interaction between fluids and silicate melts: Characterization of sulfur species using Raman spectroscopy. 9th Silicate Melt Workshop 2011, La Petite Pierre, Alsace, France. *Poster*

A. Fiege, H. Behrens, F. Holtz, C. Mandeville, N. Shimizu (2011) S partitioning and S-isotope fractionation upon continuous decompression of a hydrous andesitic melt. MSA Short Course: Sulfur in Melts 2011, Goslar, Germany. *Poster*

M. Dietrich, **A. Fiege**, H. Behrens (2011) Characterization of sulfur species in fluids using Raman spectroscopy. MSA Short Course: Sulfur in Melts 2011, Goslar, Germany. *Poster*

A. Fiege, H. Behrens, C. Mandeville, N. Shimizu (2011) Partitioning of S(-Cl) and S-isotopes between fluid and andesitic melt. Goldschmidt Conference Abstract. Goldschmidt Meeting 2011, Prague, Czech Republic. *Poster*

C. Mandeville, N. Shimizu, K. Kelley, N. Metrich, **A. Fiege**, H. Behrens (2011) Progress in Understanding of Sulfur in Subduction Zone Magmas. Goldschmidt Meeting 2011, Prague, Czech Republic. *Talk by C. Mandeville*

R.L. Linnen, A. Aseri, **A. Fiege**, F. Holtz (2011) The role of fluorine on the solubility of high field strength element in silicate melts. GAC-MAC annual meeting 2011, Ottawa, Canada. *Poster*

A. Fiege, H. Behrens, F. Holtz, C. Mandeville (2010) Partitioning of sulphur and sulphur isotopes between andesitic melt and fluids. International Conference, Experimental Mineralogy Petrology Geochemistry XIII, EMPG 2010, Toulouse, France. *Poster*

A. Fiege, C. Kirchner, A. Bartels, F. Holtz, R. L. Linnen (2009) Influence of fluorine on the solubility of manganotantalite ($MnTa_2O_6$) and manganocolumbite ($MnNb_2O_6$) in natural rhyolitic, synthetic haplogranitic and pegmatitic melts. 87. Tagung der Deutschen Mineralogischen Gesellschaft, Halle, Germany. *Talk*

A. Fiege, S. Germerott, F. Holtz, U Schwarz-Schampera, P. Schuette, H. Terblanche (2008) Lithology and genesis of Plattekop hill as an extension of the Vergenoeg fluorspar deposit. 33rd International Geological Congress, Oslo, Norway. *Poster*

A. Fiege, K. Fromme, S. Germerott, K. Möller (2007) Klimaschwankungen – Auslöser für Naturkatastrophen? 175 Jahre Universität Hannover, Nacht der Wissenschaften, Hannover, Germany. *Poster*

Rüscher, C. H., **Fiege**, A., Ren, L., Wark, M., Feldhoff, A. (2006) Investigations of the template-wall interaction of $[Pt(NH_3)_4](HCO_3)_2$ designed SiO_2 nanotubes. 18. Deutsche Zeolith-Tagung und Tagung des Arbeitsausschusses Adsorption, Hannover, Germany. *Poster*

C. H. Rüscher, **A. Fiege**, N. Salman (2006) Temperature dependent infrared (TIR) experiments on the formation and reaction of microporous materials. 18. Deutsche Zeolith-Tagung und Tagung des Arbeitsausschusses Adsorption, Hannover, Germany. *Poster*